Dissertation

SUBMITTED TO THE

Combined Faculty of Natural Sciences and Mathematics
of Heidelberg University, Germany

FOR THE DEGREE OF

Doctor of Natural Sciences

Put forward by

Lukas Robert Gustav Wolff

Born in: Berlin, Germany

Oral examination: November 28th, 2023

Detecting nonlinear and many-body dynamics in nuclear quantum optics

Referees:

apl. Prof. Dr. Jörg Evers

Prof. Dr. Maurits W. Haverkort

Zusammenfassung

In dieser Arbeit werden verschiedene Ansätze der Messung und Auswertung von Daten zur Charakterisierung von kollektiven Kernniveauschemata, die im Niedriganregungssektor von Röntgenkavitäten auftreten, diskutiert. Der erste dieser Ansätze verwendet Fouriertransformationen, um zeit- und frequenz-aufgelöste Spektren zu analysieren, die mithilfe von nuklearen Referenzabsorbern aufgenommen werden. Dies erlaubt, die resonante Kernantwort der zu untersuchenden Probe phasenaufgelöst zu extrahieren. Anschließend wird eine Dichte-Matrix Störungstheorie vorgestellt, die es ermöglicht Vielniveau- und Vielteilchendynamik im Niedriganregungssektor der Wechselwirkung zwischen Kernen und Röntgenstrahlung zu untersuchen. Diese erlaubt es, die induzierte Kerndynamik durch unterschiedlich geformte Röntgenpulse zu betrachten. Die vorgestellte Methode wird verwendent, um Ergebnisse numerischer Simulationen für verschiedenen experimentelle Szenarien zu interpretieren: Zunächst wird diese verwendet, um die Äquivalenz der Intensität von kohärent und inkohärent gestreuten Röntgenstrahlen in Kernresonanzexperimenten herzuleiten. Diese fungiert als Kriterium zur Charakterisierung von nichtlinearer Anregung von Kernensembles durch kohärente Röntgenquellen. Im Anschluss werden verschiedene experimentelle Signaturen von Kopplungen zwischen kollektiv angeregten Kernzuständen in Dünnschichtkavitäten angeregt durch verschiedenartig geformte Röntgenpulse vorgeschlagen und diese dann in Zeitfrequenzspektren identifiziert. Zuletzt wird die Umsetzbarkeit eines bestimmten Methode der kohärenten Doppelpuls-Spektroskopie im Niedriganregungssektor diskutiert und numerisch berechnete Spektren für verschiedene Pulssequenzen werden verglichen.

Abstract

In this thesis, different measurement and data evaluation approaches for the detection and characterization of collective nuclear level schemes arising in the low-excitation regime of thin-film x-ray cavities are discussed. The first approach uses Fourier transforms to analyze time- and frequency-resolved spectra recorded using nuclear reference absorbers. This allows for the extraction of the phase-resolved nuclear resonant response of the sample under investigation. Next, to study the dynamics of nuclear ensembles upon suitably-shaped x-ray light, a density matrix perturbation theory is presented that allows for the study of multi-level and many-body dynamics in the low-excitation regime of the x-ray-nuclei interaction. This method is used to interpret numerical data simulating several experimental scenarios: First, it is used to derive an equivalence between coherently and incoherently scattered x-ray intensity detectable in nuclear resonant scattering experiments, which serves as a criterion for nonlinear excitation of nuclear ensembles at coherent x-ray sources. Second, signatures of couplings between collective excited nuclear states in thin-film cavities upon differently-shaped x-ray pulses are proposed and identified in time-frequency-spectra. Finally, the feasibility of a specific coherent double pulse spectroscopic method under low-excitation conditions is discussed and numerically simulated spectra upon different double pulse sequences are compared.

Within the framework of this thesis, the following articles were published in refereed journals:

[WE23a] ***Unraveling time- and frequency-resolved nuclear resonant scattering spectra***
L. Wolff and J. Evers
Physical Review Research **5**, 013071 (2023)

The following articles are accepted by refereed jounrals and are available as preprints:

[WE23b] ***A characterization and detection method for x-ray excitation of Mössbauer nuclei beyond the low-excitation regime***
L. Wolff and J. Evers
accepted by *Physical Review A*
arXiv:2308.07644 [quant-ph]

Contents

Chapter 1

Introduction

1.1 Motivation

The study and control of quantum systems is key to numerous applications and technical developments as well as fundamental research questions in physics. This dates back to the days of the *first quantum revolution* [Asp23] in the first half of the 20th century where fundamental questions about the structure and stability of atoms lead to the development of quantum theory which revolutionized the understanding of such seemingly different fields of physics as condensed matter physics, electrodynamics and optics, to name but a few. It was crucial in the development of economically and scientifically essential fields such as semiconductor and laser physics. With steady progress in the development of coherent radiation sources, first in the long-wavelength regime, and the discovery of nuclear magnetic resonance (NMR) in 1938 by Isidor Rabi [Rab+39] following the Stern-Gerlach experiment [GS22], studies of few-level quantum systems could be carried out with applications in spectroscopy which created the field of *Quantum Optics* as the study of interactions between coherent light and quantum matter. Especially the second half of the last century saw a rising interest in microscopic quantum systems down to single atoms and photons due to both fundamental questions of quantum mechanics such as entanglement theory as well as applications in laser cooling, atom trapping, atomic clocks and laser spectroscopy [SM85; Chu+86; Ber+86; Bru+96; Jon+00; Hol+00]. These advances, also known as *second quantum revolution* [Asp23], started off the fields of quantum information theory and quantum computing [Pan+98; ADR82; FC72; Cla+69]. These developments demonstrate the power and potential that lies in the study and control of quantum systems using coherent electromagnetic fields.

In a separate development, the study of interactions and correlations in many-body quantum systems became important in many areas of physics: Collective ultra-low temperature phenomena such as superconductivity and -fluidity rely on particle correlations. The theory of optical coherence studies photon correlations and the statistical properties of light [Gla06] with applications, e.g., in stellar interferometry [BT54]. Finally, the understanding of magnetic [Aue98] and other strongly-correlated systems [Mor+12; Ani10; Jia15] in solid state physics are key for the design of new materials. Since the early days of Rabi and the development of NMR spectroscopy using coherent radio-frequency fields, ever more complex spectroscopic techniques using coherent light of different wave lengths were developed to study structure and dynamics of complex systems: starting with microwave fields that are employed as time-keeping standards in atomic clocks [Ram90] to infrared and optical fields [Lud+15] for the study of molecular [HZ11; McH17] and atomic structure [Par07; Cho19] to core-electron spectroscopy [Sie82; DGK08] requiring x-ray excitations in the short wavelength regime. Many techniques for the time- and frequency-resolved studies of quantum dynamics such as photon-echo experiments [KAH64; AKH66; BPW98], pump-probe [Fus08] and multi-dimensional spectroscopy require phase-coherent control fields which can nowadays be provided for a large part of the electromagnetic spectrum [Ern92; ABE76; Muk95; HZ11; Cho19; Wit+20].

The extension and application of such techniques to the hard x-ray regime would open up a complete new world of time- and frequency-resolved experiments with high spatial resolution. However, their practical implementation becomes more challenging towards shorter wavelengths due to the high requirements for coherence-preserving optics and the difficulty of providing coherent control fields [Lu+18; Pag06; Shv04]. Apart from a one-to-one translation of quantum optical methods from the longer wavelength regime into the x-ray domain, x-ray quantum optics comes with its own specific advantages, for instance, the high quantum efficiency and low noise of x-ray detection [Ada+13a], precise focussing and deeper penetration of x-rays into materials [KK17a]. Further, resonance frequencies of quantum systems in the hard x-ray regime promise long coherence times ideally suited for many quantum optical applications involving coherence and interference. With the advent of novel high-brilliance coherent x-ray sources [Emm+10; Ama+12; Ish+12; Ino+19; Dec+20; Nam+21; Liu+; Ada+19a], quantum optics will become an important tool to study, probe and control the coherence

properties of these machines [RES20a].
One particular platform for quantum optical studies at hard x-ray energies are Mössbauer nuclei that feature remarkably narrow linewidths combined with extraordinary coherent scattering properties under robust experimental conditions, i.e. room temperature and ambient pressure. These features, originating in the small size of the atomic nucleus in combination with recoilless scattering of radiation by the nuclei [HT99a], render these nuclei ideal candidates for high-precision hyperfine spectroscopy, fundamental research such as tests of fundamental theories [PR60; KK12] or other applications that require high quality factors such as atomic or nuclear clocks [Shv+23]. Complementary to these narrow nuclear resonance widths are the long lifetimes of nuclear excited states compared to electronic resonances and the time scales of typical x-ray excitation pulses provided by accelerator-based x-ray sources. This allows for a convenient separation of resonantly and nonresonantly scattered radiation in the time-domain and the observation of coherent scattering phenomena that can be used to study the chemical and magnetic environment of Mössbauer nuclei. Moreover, the coherence of the nuclear scattering in combination with the longevity of nuclear excited states enables time-domain control of the nuclear resonances via transient [Boc+21] or static magnetic fields [Shv+96; LPK12], via optical control [KKR99] as well as linear or nonlinear mechanical sample motion [Vag+14; Hee+17; Hee+21] that can be used to directly control the nuclear dynamics [Hee+21] or shape the radiation released by the nuclei [Hee+17]. In addition, with various theoretical proposals and experimental realizations of gating of the coherently emitted radiation by nuclear ensembles [Shv94; Lee23; Ger21] and the commissioning of hard x-ray split-and-delay lines [Lu+18], the realization of suitably-shaped x-ray pulses for multi-pulse coherent spectroscopy with Mössbauer nuclei comes within reach. Applications include studies of nuclear nonlinear, many-body and non-equilibrium phenomena [She12; Ada+19a; RES20b].
In this context, recent years have seen a rising interest in ensembles of Mössbauer nuclei embedded as nano-film layers in planar x-ray waveguides [RES20b; Röh+10; Röh+12; Hee+13; Hee+15a; Hee+15c; Hee+15a; Hab+17; Che+22; HE13; HE15a; Len+20; DLE22b; DLE22a] to study quantum-optical and many-body phenomena [Ada+13b; RE21a; RES20b; KK17b; Ada+19b; SS89a; Vag90; Hel+91; Tit+93; Lip+95; Shv+96; Chu+97; HT99b; Sch+02a; Smi+07; Röh+10; Röh+12; Hee+13; Vag+14; Hee+15c; Hee+15b; Hab+16; Hee+17; Sak+17; Hab+17; Boc+21; Hee+21; SS22; Hee+22; Ma+22]. The nuclei in this experimental platform experience radiation-induced couplings leading to collective frequency shifts and modified cooperative decay rates that can be studied owing to the high sensitivity of nuclear resonant scattering (NRS) and well-separated nuclear resonances. These many-body effects can be controlled by tailoring waveguide materials and structure [DLE22b; DLE22a]. The physical concept underlying these phenomena is the excitation of collectively-excited nuclear states known as nuclear excitons [HT99a; Kag99; Smi99; Röh04] that determine the dynamics and the coherent scattering properties of nuclear ensembles under low-excitation conditions. It was demonstrated both theoretically [HE13; HE15a; Len+20; DLE22a; RES20b] and experimentally [Röh+12; Hee+13; Hab+17; Hee+15a; Röh+10] that this concept allows for the interpretation of resonant scattering experiments in x-ray waveguides in terms of effective quantum-optical few-level schemes. Important milestones in this direction were experimental observations of the collective Lamb shift [Röh+10] of spontaneously-generated coherences [Hee+13], electromagnetically-induced transparency (EIT) [Röh+12], slow light [Hee+15c] and Rabi oscillations associated with coherent couplings between such collectively excited states [Hab+17].
It is a widely unanswered question how these two developments, i.e. the coherent control of nuclear resonances and subsequent shaping of x-ray light, on the one hand, and the study and engineering of effective nuclear few-level schemes, on the other hand, can be brought together. It has been shown that standard measurement and evaluation approaches are insufficient to retrieve the relevant information from nuclear resonant scattering data for an unambiguous interpretation of the underlying dynamical, quantum optical and many-body physics in a number of important cases [Hee+21; DLE22a] and that advanced measurement techniques are required to retrieve this information [Goe+19; Ger21; Hee+21]. Spectroscopic techniques based on the coherent control of the x-ray scattered light off of nuclear resonances bear a great potential to guide this development in future experiments and unlock the observation of phenomena that could not be investigated using established methods. Similarly, the interpretation of data at new high-brilliance x-ray sources such as x-ray free electron lasers (XFELs) [Jae+16; MT10] and x-ray free electron laser oscillators (XFELOs) [Ada+19a] requires guidance from theory to measure and interpret data under nonlinear and many-photon excitation conditions that will be achieved with these sources and go beyond the low-excitation regime (LER) that one was restricted to at synchrotron radiation sources.

1.2 Goals of this thesis

The major goal of this thesis to bring together the possibilities offered by the coherent control of nuclear resonances in terms of advanced coherent spectroscopic techniques and the engineering and investigation of dynamics and collective phenomena in nuclar quantum optics. To this end, theoretical tools are developed that allow for the study and interpretation of nuclear few-level many-body dynamics measured in NRS experiments to study phenomena that require both time- and frequency resolution. These tools go beyond existing approaches in that they enable studies of these dynamics upon suitably-shaped x-ray driving fields and coherent pulse sequences, in principle, even beyond the LER. Apart from providing a theoretical framework for the investigation of nuclear dynamics upon time-dependent x-ray-nucleus interactions, specific signatures for the observation of nonlinear, quantum optical and many-body phenomena are proposed, that allow for a direct comparison with near-future experiments at coherent x-ray sources given that the proposed data acquisition and measurement techniques are mostly already available. Complementing this, a simple and powerful data evaluation technique based on Fourier transforms of time- and frequency-resolved NRS spectra is proposed that facilitates the interpretation and extraction of nuclear dynamics and level structure data obtained in such measurements. Futher, the role that phase control and suitably-shaped x-ray pulses can play to improve the access to the desired experimental signatures will be discussed. We expect our results to help devise future experiments using tailored x-ray pulses to probe nuclear dynamics and characterize quantum optical phenomena and help to interpret the data taken in such experiments. This can unlock all the intriguing features and possibilities coherent spectroscopic techniques offer at the longer wavelength regime to advance the field of Mössbauer science as a whole.

1.3 Thesis outline

Chapter 2 introduces the basic concepts of nuclear resonant scattering and x-ray quantum optics. First, the particular features of nuclear transitions are discussed followed by a presentation of the role of the Mössbauer effect in these fields. A brief overview over polarization effects is followed by a description of features important for experiments at coherent accelerator-based light sources, including time- and frequency-resolved detection methods. This is followed by a summary of the basic aspects of phase control of nuclear resonances. The final two Sections of this Chapter deal with the motivation of a Hamiltonian approach to nuclear resonant scattering before the experimental and theoretical aspects of thin-film x-ray cavities is reviewed.

Chapter 3 describes how heterodyne detection schemes using single-line nuclear reference absorbers can be used to detect time- and frequency-resolved NRS spectra. These spectra are transferred into Frequency-frequency correlation (FFC) spectra via Fourier transformation along the time axis. The structures appearing in these spectra in the linear response regime are interpreted one-by-one and related to interference effects in the scattering setup. As one highlight it is shown how the nuclear target response can be retrieved from these spectra, including phase information. Finally, the controlled suppression of undesired scattering paths is demonstrated using a phase-cycling-type approach, which emphasizes the role of phase control can play for the interpretation and evaluation of NRS data.

In Chapter 4 two variants of density matrix perturbation theory are introduced that form the basis for the interpretation of aspects of many-body and nonlinear nuclear dynamics discussed in the remainder of this thesis: First, self-consistent solutions to the equations of motion of nuclear two-level systems are derived for the excited state population and coherence that allow one to study the excitation dynamics of effective two-level systems in the low-excitation regime and beyond for a wide range of x-ray excitation pulse shapes. As an important extension of this concept a more general perturbative expansion of the nuclear many-body density matrix is presented that allows to study many-body dynamics and more complex level structures.

This formalism is subsequently applied to N interacting two-level systems in Chapter 5. It is shown that the coherently and incoherently scattered intensity associated with the x-ray-induced coherences and the nuclear excited state populations, respectively, become equivalent in the low-excitation regime, largely independent of the details of the nuclear ensemble and the time- and frequency structure of the exciting x-ray pulse. As a consequence, as an experimentally-accessible signature, the ratio of both observables becomes essentially time-independent at low excitations. Experimental signatures for excitations beyond the LER are discussed for non-impulsive and impulsive x-ray excitations.

Chapter 6 studies the dynamics of effective three-level schemes realized in x-ray wave guides containing two layers of resonant nuclei that are coupled by the field inside the cavity as an example of

collective few-level dynamics in thin-film cavities. Experimental signatures of the coupling dynamics in such systems upon impulsive and non-impulsive x-ray excitations are studied numerically and analytically using the perturbation theory of Chapter 4.
Finally, in Chapter 7 the dynamics of effective two- and three-level systems upon double pulse excitations are investigated. The feasibility of experiments typically associated with nonlinear light-matter interactions is discussed under low-excitation conditions. The implications of different shapes of coherent double pulses for experiments involving time-dependent perturbations of nuclear resonances and couplings between excited nuclear states are compared analytically and numerically.
A summary of the results and a conclusion with respect to the findings of this thesis is given in Chapter 8.

1.4 Acknowledgments

I want to thank all the colleagues, friends and family for their active and passive support over the past four years of my PhD. Not all can be mentioned here by name, so I just pick a few that I consider as particularly important: First of all, I would like to thank my group for a friendly and relaxed working environment and especially Dominik Lentrodt, Piet Hein van den Heuvel, Oliver Diekmann, Miriam Gerharz and Jörg Evers for reminding me in weekly Zoom sessions in two years of home office that I was not alone and that even the most frustrating times will finally have and end. I thank Dominik Lentrodt for encouraging discussions from the start of my PhD until the present day and Miriam Gerharz for emotional support before conference talks, explaining obscure experimental details to me, for discovering life crises before submitting papers and, of course, for always sharing the latex command of the week. Of my friends I am especially grateful to David Buhrke for scientific input from a completely different perspective that at least once lead me back onto the right path when I lost it, to Julia Müller for pointing out to me that a PhD is a marathon and not a sprint, to María Rodriguez Luengo por ayudarme a ver la conexión profunda entre el Jazz y la física. Also, to Dr. Martin Preuß for positively-critical comments from a semi-outsider perspective since the days of my master thesis, to Maksym Gachkivskji for voting for me in the first place and taking over from me a year later and I thank Hannah Rühe for being such a great fan of Onkel Lukas. Last but not least I want to give special thanks to Jörg Evers, who takes his role as a supervisor very serious, which I learnt to appreciate especially in the last year, as many scientifc results and the quality of their presentation would not have been possible without his guidance. And, well, thanks to the MPIK summer band. That was fun.

Chapter 2

Background

2.1 Nuclear resonant scattering

After the discovery of the Mössbauer effect in 1958 [Mös12], the potential of ultranarrow nuclear resonances for tests of fundamental theories [PR60] an hyperfine and vibrational spectroscopy was soon realized [KK12; Röh04]. Starting in the 1980s resonant scattering of short coherent pulses of synchrotron off of Mössbauer resonances [GW99] was a rapidly growing and flourishing field that in recent years also layed the foundation to nuclear quantum optics discussed in this thesis. The basic aspects of this *nuclear resonant scattering* (NRS) are reviewed in this Section.

First, the general properties of nuclear resonances compared to atomic transitions are reviewed, followed by an introduction into the Mössbauer effect. Subsequently, polarization effects are briefly discussed. Important concepts and properties of NRS at coherent accelerator-based light sources are introduced and time- and frequency-resolved detection methods are reviewed. Finally, our approach to phase control of light scattered off of nuclear resonances is outlined.

2.1.1 Comparison of nuclear and atomic scattering

To introduce the specific properties and advantages of Mössbauer nuclei, we start by comparing scattering off of atomic and nuclear resonances at hard x-ray energies. The scattering cross section f of x-rays off of an atom or nucleus consists of three parts

$$f = f^0 + f' + if'' \,. \tag{2.1}$$

The first part f^0 describes Thomson scattering that is proportional to the classical electron radius $r_0 = e^2/m_e c^2$ in atomic scattering. Close to an atomic or nuclear resonance, the scattering behaviour is strongly modified, which is taken into account via the so-called *anomalous scattering* $f' + if''$. The resonant contribution to the anomalous scattering can be written as

$$f_{\text{res}} \sim \frac{1}{k_0} \sum_m \frac{\gamma_{\text{rad}}/2}{(\omega_m - \omega_g) - \omega_p - i\gamma/2} \,, \tag{2.2}$$

where, for simplicity, we neglect polarization effects of resonant scattering for the moment, which are discussed in Sec. 2.1.3. The sum in Eq. (2.2) runs over all resonances that participate in the resonant scattering process, k_0 denotes the resonant scattering wave number, ω_g the ground state frequency, ω_m the excited state frequencies and ω_p the frequency of the scattered photon. γ_{rad} takes into account radiative decay processes only while γ is the total linewidth of the transition that incorporates both radiative and nonradiative decay processes. In case of electronic scattering, this includes, e.g., *Auger emission* where excitation energy is transferred to the outer electron shell and released via the emission of an electron. In nuclear scattering this transfer and release of nuclear excitation via emission of an electron is known as *internal conversion*. The branching ratio

$$\alpha = \frac{\gamma}{\gamma_{\text{rad}}} - 1 \tag{2.3}$$

describes the number of excitations released via nonradiative processes divided by the number of excitations released via photon emission. In the context of nuclear resonant scattering this ratio is also called *internal conversion coefficient*.

Several aspects of nuclear resonant scattering distinguish it from electronic scattering:

i) The total linewidth γ of a resonance is proportional to the absolute square of the dipole moment of that transition, i.e. $\gamma \sim |\langle g| \, x \, |e_m\rangle|^2$ and, thus, nuclear transitions feature extraordinary narrow linewidths compared to atomic transitions due to their orders-of-magnitude smaller spatial extent x. Typical atomic energy-widths at hard x-ray photon energies are of the order of $1 - 10$eV while nuclear transitions of the order of neV [HT99a]. Thus, nuclear resonances are about eight to nine orders of magnitude narrower than typical atomic transitions in the same frequency range.

ii) The branching ratio α is typically much smaller for atomic transitions such that the nuclear scattering amplitude on resonance

$$f^n_{\text{res}}(\omega_p = \omega_m - \omega_0) = \frac{i}{k_0(1+\alpha)} \tag{2.4}$$

can be very large compared to electronic scattering. For example, for the archetypical Mössbauer isotope ^{57}Fe with a resonance energy of 14.4 keV and an internal conversion coefficient of $\alpha = 8.56$, this amounts to $|f^n_{\text{res}}| \approx 440 r_0$ [HT99a].

iii) Compared to resonant scattering, Thomson scattering is suppressed by the ratio of electron and proton mass $f^0_n \sim m_e/m_p$ in case of nuclear scattering such that it can be usually neglected, in particular close to resonance where resonant scattering dominates.

iv) While atomic resonances at hard x-ray energies involve continuum states and therefore experience strong resonance broadening [Jam58], typical nuclear resonances at these energies are separated by several 10s or 100's of keV and thus feature isolated Lorentzian line-shapes [HT99a].

Especially the narrow-line widths and the clear separation of nuclear resonances offer specific advantages over the scattering off of atomic resonances, which strongly suggests such transitions for a number of applications: They are very sensitive to tiny changes in the configuration of the electronic environment and via hyperfine interactions to small magnetic and electric fields [KK12; Röh04] and other perturbations of the nuclear resonance which makes them a versatile tool in hyperfine spectroscopy and for fundamental tests that require very high sensitivity [PR60]. Further, they are suitable for quantum-optical applications as they constitute almost ideal two-level or, in case of hyperfine interactions, few-level systems. This aspect of nuclear resonant scattering is discussed in more detail in Sec. 2.2. Finally, the narrow linewidth and the corresponding long coherence times of nuclear transitions allow for control of these resonances in the time- and frequency-domain with applications in spectroscopy, x-ray pulse-shaping and coherent control of nuclear dynamics as further discussed in Secs. 2.3 and 7.1.1.

One disadvantage of the extremely narrow linewidth of nuclear transitions for coherent scattering and spectroscopic applications is the nuclear recoil associated with nuclear x-ray absorption and emission. This particular problem, which was solved by the discovery of the Mössbauer effect in 1957 [Mös58], is briefly discussed in the following Subsection.

2.1.2 Nuclear recoil and the Mössbauer effect

When searching for the γ-ray analogue of resonance fluorescence by studying γ-ray emission and absorption from radioactive sources starting in the late 1920s [Mös12], these attempts first proved to be unsuccessful due to the effect of nuclear recoil: If a hard x-ray photon is emitted or absorbed by a single nucleus this process is accompanied by a momentum transfer of

$$\Delta E = E_0^2/2Mc^2 \tag{2.5}$$

from the photon to the nucleus [Mös12]. Here, M is the mass of the nucleus, E_0 the energy of the photon and c the velocity of light. Consequently, the observed resonance line is shifted away from the actual nuclear resonance by the amount ΔE towards higher[lower] energy in the absorption[emission] process. While this effect is often not of relevance for optical resonance fluorescence, it becomes significant at hard x-ray energies and mass scales of atomic nuclei and can typically lie in the order of 10^{-2} to 10^{2} eV [Mös12]. The typical linewidth of nuclear resonances, in comparison, is typically of the order neV such that the observation of resonance fluorescence of a nuclear isotope excited by the same

isotope becomes very challenging. Moreover, this recoil also breaks spatial coherence of the scattering off of nuclear ensembles, which is crucial for nuclear resonant scattering using accelerator-based x-ray sources corresponding applications, as is discussed in Sec. 2.1.4.
Rudolf Mössbauer discovered that, if the nuclei are embedded in a solid, the recoil is absorbed by the entire crystal and becomes negligible. While the resonance shift due to the nuclear recoil can be neglected, the absorption or emission line can be shifted by a change in internal energy in the crystal, i.e. by the creation or annihilation of phonons. Now, in 1957 [Mös58] Rudolf Mössbauer discovered that their is a high probability that the hard x-ray photon is absorbed by a nucleus without creation of a phonon, i.e. without the change of the internal energy of the crystal, if the average recoil energy is small compared to the Debye frequency of the crystal. For the discovery and explanation effect of this effect, which increases when the temparature is lowered due to a reduction in the occupation number of higher-lying phonon modes, Mössbauer shared half of the Nobel prize in 1961. Clearly, the probability of these zero-phonon excitations reduces with higher photon frequencies such that only isotopes with resonance energies below 150 keV experience a significant contribution owing to this effect [Mös12]. Its influence on nuclear resonant scattering can be calculated by transforming the resonant scattering amplitude Eq. (2.2) for a single transition into the time domain which yields [Tra62; HT99a]

$$f_{\text{res}} = \frac{\gamma_{\text{rad}}}{2ik_0} \int_0^\infty dt e^{i(\omega_e - \omega_g)t} e^{-\frac{\gamma}{2}t} f_{\text{LM}}(t) \tag{2.6}$$

where we introduced the resonant scattering wave number $k_0 = \frac{2\pi}{\lambda_0}$. The factor $f_{\text{LM}}(t)$ takes into account vibrations of the scatterer around its mean position and, for resonant scattering, is given by a statistical average over a Gibbs ensemble of the relative position-dependent phase of the scatterer upon excitation $e^{-i\mathbf{k}_0\mathbf{r}(t)}$ and deexcitation $e^{-i\mathbf{k}_f\mathbf{r}(0)}$. Here, $\mathbf{r}$ denotes the position of the scatterer, $\mathbf{k}_0$ the wave vector of the incident photon and $\mathbf{k}_f$ the wave vector of the released photon. The full expression thus reads

$$f_{\text{LM}}(t) = \langle e^{-i\mathbf{k}_f\mathbf{r}(t)} e^{i\mathbf{k}_0\mathbf{r}(0)} \rangle \tag{2.7}$$

For fast scattering processes such as atomic scattering which proceed on femtosecond time scales compared to picosecond vibration time scales [HT99a], this becomes essentially time-independent and reduces to the Debye-Waller factor (see, e.g., [AM22]). In contrast, for nuclear resonant scattering the scattering time scales are much longer, typically on the nanosecond scale, such that the nuclear motion at time $t = 0$ of excitation and time $t \approx \infty$ of deexcitation become essentially uncorrelated [HT99a], i.e.

$$f_{\text{LM}} \approx \langle e^{-i\mathbf{k}_f\mathbf{r}} \rangle \langle e^{i\mathbf{k}_0\mathbf{r}} \rangle \tag{2.8}$$

which is the so-called *Lamb-Mössbauer factor* describing the fraction of nuclei participating in recoilless scattering in nuclear resonant scattering which is crucial for applications with Mössbauer nuclei that require coherence of the scattering process.

2.1.3 Polarization effects

Another important feature of nuclear resonant scattering is the well-defined multipolarity of Mössbauer transitions and, thus, a strong dependence of the scattering cross sections on the polarization of the incident radiation [Röh04; SBH99; HT99a]. Typically, being electric dipole (E1), magnetic dipole (M1) or electric quadrupole transitions (E2)[1], Mössbauer transitions are very sensitive to local magnetic or crystal fields, which renders them ideal candidates for hyperfine spectroscopy due to Zeeman and electric quadrupole splitting of the nuclear resonances.

As an example, the Zeeman splitting of the M1 nuclear transition of ^{57}Fe with internal hyperfine field of $B = 33.3$ T is shown in Fig. 2.1. The energy splitting $\Delta_E(m_e, m_g)$ between the unsplit resonance $E_0 = 14.4$ keV and a transition $E(m_e, m_g)$ with magnetic quantum numbers m_e, m_g is given by

---

[1] In this notation EL refers to *electric* 2^L-pole transitions, while ML refers to *magnetic* 2^L-pole transitions

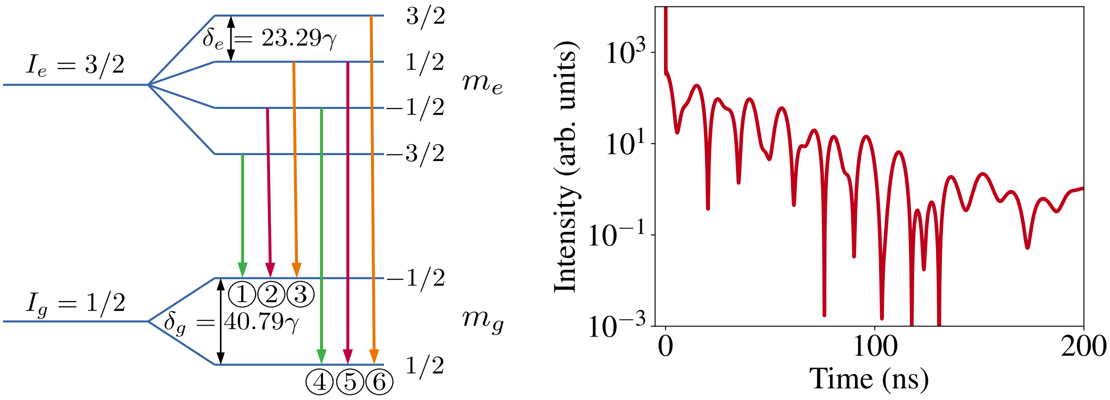

Figure 2.1: Zeeman splitting of the nuclear resonance of ^{57}Fe upon a hyperfine field of $B = 33.3$T: The left panel shows the six allowed transtions with for ground and excited spins I_g and I_e and corresponding magnetic quantum numbers m_g and m_e. The green, red and orange lines refer to transitions that can be driven by right-circularly, linearly and left-circularly polarized light, respectively. The right panel shows the quantum beats arising from interference between the coherently scattered intensity off of all six transitions in an ^{57}Fe sample of 2μm thickness as described in Sec. 2.1.5. The time-dependent intensity was calculated using PYNUSS [Hee19].

$$\Delta E = E(m_e, m_g) - E_0 = -\left(\mu_e \frac{m_e}{I_e} - \mu_g \frac{m_g}{I_g}\right) B\,. \tag{2.9}$$

Here, $I_{e/g}$ denotes the spin of the excited and ground state $|e\rangle$ and $|g\rangle$, respectively. For ^{57}Fe their values are $I_e = 3/2$ and $I_g = 1/2$. The ground and excited state magnetic moments μ_g and μ_e are tabulated in Ref. [Röh04]. Apart from the different transition energy of each of these six hyperfine transitions, only x-rays of distinct polarization scatter off of each of these transitions: Transitions (1) and (4), marked in green in Fig. 2.1, only scatter right-circularly polarized light, (2) and (5), marked in red in Fig. 2.1, only scatter linearly polarized light and transitions (3) and (6), marked in orange, only left-circularly polarized light. This polarization-dependence of the nuclear resonant scattering determines which hyperfine transitions participate in a given scattering experiment depending on the relative orientation of the x-ray polarization and magnetic field which can be used to selectively drive specific transitions [Röh04; SBH99] or even control the polarization of the scattered x-ray light [Ger19].

The relative weights of the nuclear scattering amplitudes of each hyperfine transition are related to the Clebsch-Gordan coefficients and, in principle, can be calculated analytically in a number of important cases [Röh04; SBH99; HT99a] due to the well separated sharp nuclear resonance lines, compared to atomic transitions at hard x-rays that involve continuum modes and corresponding broadening [Röh04]. However, the discussion of polarization effects and hyperfine interactions is mainly out of the scope of this thesis, the only exception being the discussion of the hyperfine splitting of ^{57}Fe discussed in this Section as an example for the evaluation of time- and frequency-resolved spectra in Sec. 3.3.2. The reason for this is two-fold: Nuclear reference absorbers, which is used in heterodyne measurement techniques to scan nuclear resonances in frequency space throughout the thesis (see, Sec. 2.1.5 for a more detailed introduction into this concept), require unsplit resonance lines to serve as frequency references. The second reason is that, in most parts of the thesis, we consider thin-film x-ray cavities containing thin layers of Mössbauer nuclei as targets due to their relevance in nuclear quantum optics (cf. Sec.2.2.2). These thin layers can be manufactured with nanometer thickness. Long-range magnetic order and magnetic hyperfine fields can not build up in such effective two-dimensional nuclear ensembles such that no splitting occurs if the resonant layers consist of only one or two-atomic layers (see, e.g., [Röh+10]). For this reason, scattering amplitudes important for the calculation of the nuclear response functions and coherent and incoherent emission characteristics throughout the thesis simplify considerably and are essentially given by Eq. (2.2) for a single nuclear resonance, only corrected for the spin degeneracy by a prefactor $\frac{2I_e+1}{2(2I_g+1)}$. For a more detailed discussion of polarization effects, the reader is referred to Refs. [Röh04] and [SBH99] and references therein.

2.1.4 Nuclear resonant scattering at accelerator-based light sources

A particularly interesting application of nuclear resonant scattering in combination with Mössbauer-active isotopes is that of the excitation of nuclear ensembles with short broadband coherent x-ray pulses as provided by state-of-the-art synchrotron [BEW05] and x-ray free electron (XFEL) sources [Jae+16]. This has found numerous applications in the field of hyperfine spectroscopy and is also crucial for the coherent control of nuclear dynamics and x-ray pulse-shaping as discussed in Secs. 2.3 and 7.1.1 and to get experimental access to nuclear quantum-optical and many-body phenomena described in Sec. 2.2. The excitation of a nuclear ensemble by an x-ray pulse of which both the pulse duration and the time for propagation through a solid state sample is short compared to the nuclear lifetime allows one to treat the excitation and deexcitation of the nuclear ensemble as separate processes, the formation of collective nuclear excited states known as *nuclear excitons* and the strong enhancement of spatially coherent scattering with important applications in spectroscopy, interferometry and x-ray pulse-shaping.

As discussed in Sec. 2.1.1, nuclear resonant scattering typically proceeds on time scales of nanoseconds or longer[2] while typical pulse durations at accelerator-based coherent x-ray sources are of the order of picoseconds (synchrotron) or even femtoseconds (XFELs). Propagation times of (unscattered) photons through 10's of micrometer thick films or below, typical for nuclear resonant scattering experiments, are of the order of picoseconds or below. This justifies the assumption of near-instantaneous or *impulsive* excitation typically made in theoretical descriptions of nuclear resonant scattering [Röh04; Smi99; Shv99; Hee+17; Hee+21], as also done throughout this thesis. Such short pulses excite all nuclei in the sample with the same temporal phase, which leads to the creation of collective nuclear excited states of the form [HT99a; Smi99; Röh04; RE21a; Len+20; Len21; HE13; Hee14b]

$$|\psi(\mathbf{k}_{in})\rangle = \frac{1}{\sqrt{N}} \sum_{n=1}^{N} e^{i\mathbf{k}_{\mathrm{in}}\mathbf{r}_n} |g_1 \dots e_n \dots g_N\rangle \ , \tag{2.10}$$

where, for simplicity, we assumed an ensemble of N two-level nuclei indexed by n with ground state $|g_n\rangle$ and excited state $|e_n\rangle$ without additional hyperfine splitting. This type of collective delocalized excitation was coined *nuclear exciton* [HT99a; Röh04] and corresponds to a so-called *timed Dicke state* [Scu09a; HE13] due to the inclusion of the phase factor $e^{i\mathbf{k}_{\mathrm{in}}\mathbf{r}_n}$ of each nucleus n at position $\mathbf{r}_n$ excited by a plane-wave x-ray field with incident resonant wave vector $\mathbf{k}_{\mathrm{in}}$. These states feature strong enhancement of the spatially coherently scattered intensity in Bragg directions of the crystal or grazing incidence for thin-film cavities and in propagation direction of the exciting x-ray pulse. The latter type of strong coherent emission is known as *nuclear forward scattering* [Smi99; Röh04] and is of special importance for spectroscopic applications discussed in Sec. 2.1.5 and for coherent control methods discussed in Sec. 2.3.

Coherent emission in forward direction

Two aspects of nuclear forward scattering that can only be explained by the delocalized nature of the nuclear exciton and the corresponding spatial coherence of the scattered radiation are the speed-up of the coherent decay channel [HT99a; Smi99; Röh04] and the appearance of quantum beats [HT99a; Smi99; Röh04]. The former effect is accompanied by intra-resonance interference that leads to characteristic propagational or dynamical beats in the time spectrum measured in forward scattering geometry. The latter effect occurs in case of hyperfine splitting of the nuclear resonance line and can be used to extract spectroscopic information from the nuclear sample as discussed in more detail in Sec. 2.1.5.

For later use, we briefly discuss the shape and origin of the coherently scattered radiation in forward direction of a single-line nuclear absorber, i.e. without resonance splitting due to hyperfine interactions. These concepts are crucial for the development of coherent control of nuclear excitons and the emitted radiation as well as for the interpretation of time and frequency domain features of nuclear resonant scattering discussed in Sec. 2.1.5 and later Chapters of this thesis. For a more detailed presentation of this topic see, e.g., Ref. [Smi99]. For different calculation approaches of the scattered field see, e.g. [Shv99; Röh04]. A particularly simple and clear derivation of the scattering response off of a single resonance line in forward direction consistent with experimental observations in the *linear* excitation regime can be given in the frequency-domain: The propagation of light through a thick

---

[2] For a list of Mössbauer isotopes and their defining parameters, including lifetime, see Appendix A.7 of Ref. [Röh04]

resonant medium is described by Maxwell's equations. An incident electromagnetic field induces a nuclear dipole moment or current which, in turn, acts as a source term for the radiation field. This propagating coupled entity of nuclear excitation and x-ray photon propagation is sometimes called a *nuclear polariton* [Smi+07]. In the frequency domain, this source term is related to the frequency-dependent refractive index $n(\omega)$ of the material and thus to the nuclear resonant scattering amplitude Eq. (2.2)[Röh04; Lax51]. Upon a broadband initial excitation in the linear excitation regime the propagation equation for the total response function $T(z, \omega)$ in direction z of the incident field neglecting absorption can be written as [Röh04]

$$\frac{dT}{dz} = ik_0 n(\omega) T(z,\omega) = ik_0 \left(a_0 f_{\mathrm{coh}}(\omega) + 1\right) T(z,\omega) \quad a_0 = \frac{2\pi\rho}{k_0^2} \tag{2.11}$$

where ρ denotes the number density of resonant nuclei in the sample. The prefactor a_0 relates the forward scattering amplitude to the total coherent scattering amplitude

$$f_{\mathrm{coh}}(\omega) = \frac{1}{2k_0} \frac{f_{\mathrm{LM}}}{(1+\alpha)} \frac{2I_e + 1}{2I_g + 1} \frac{\gamma/2}{\omega_e - \omega_g - \omega - i\gamma/2} \tag{2.12}$$

by virtue of the optical theorem [New82]. Note, that the prefactor $\frac{f_{\mathrm{LM}}}{(1+\alpha)}$ takes into account that only the recoilless fraction of the radiatively scattered photons contributes to the x-ray emission in the coherent channel. The spin degeneracy of the transition in absence of hyperfine splitting is accounted for by the factor $\frac{2I_e+1}{2I_g+1}$. With this, the linear frequency response of a single-line nuclear sample of thickness d in forward scattering can be obtained as

$$T(\omega) = T_0 e^{ik_0 z} \exp\left(\frac{-ib}{\omega - \omega_0 + i\gamma/2}\right) = T_0 e^{ik_0 z} \sum_n \frac{1}{n!} \left(\frac{-ib}{\omega - \omega_0 + i\gamma/2}\right)^n \tag{2.13}$$

where we defined the nuclear transition frequency $\omega_0 = \omega_e - \omega_g$ and the thickness thickness parameter

$$b = \frac{\pi\rho}{2k_0^2} \frac{f_{LM}}{(1+\alpha)} \frac{2I_e + 1}{2I_g + 1} \gamma d\,. \tag{2.14}$$

The series expansion of the exponential in Eq. (2.13) describes multiple scattering events in a thick sample with the nth addend describing n scattering events of a single photon in the target off of a single nuclear resonance. This leads to a characteristic broadening and splitting of the nuclear resonant frequency response in forward direction, which is known as *Double-hump profile* [Smi99]. The splitting is caused by the interference of waves propagating with different group velocities in the crystal [Röh04].

The time-domain analogue of this double-hump profile can be obtained via a Fourier transform of Eq. (2.13) and reads

$$T(t) = \delta(t) + S(t) = \delta(t) - \sqrt{\frac{b}{t}}\, e^{-\frac{\gamma}{2}t}\, e^{-i\omega_0 t} J_1(2\sqrt{bt})\Theta(t)\,. \tag{2.15}$$

Here, J_1 denotes the Bessel function of the first kind, Θ the Heaviside Θ-function and δ the Dirac δ distribution. This expression demonstrates some important features of the time domain response of a thick nuclear sample: First, the lowest scattering order is given by a δ function which corresponds to the $n = 0$ scattering order in the frequency-domain response Eq. (2.13). It corresponds to a radiation contribution that passes the nuclear sample without resonant interaction with the nuclei. The second contribution $S(t)$ including the Bessel function describes the higher scattering orders $n > 0$ in the frequency domain response Eq. (2.13). This response features characteristic beats that are known as *propagational beats* or *dynamical beats* [B̈99; Smi99; Röh04] corresponding to the double-hump profile in the frequency-domain[3]. In addition to these characteristic oscillations shown in the left panel of Fig. 2.2, the nuclear response features an accelerated decay compared to the response of a single nucleus, which is given by a an exponentially-decaying dipole of transition frequency ω_0 and decay

---

[3] For the observation of propagational beats in the optical domain, also see Ref. [Fr91]

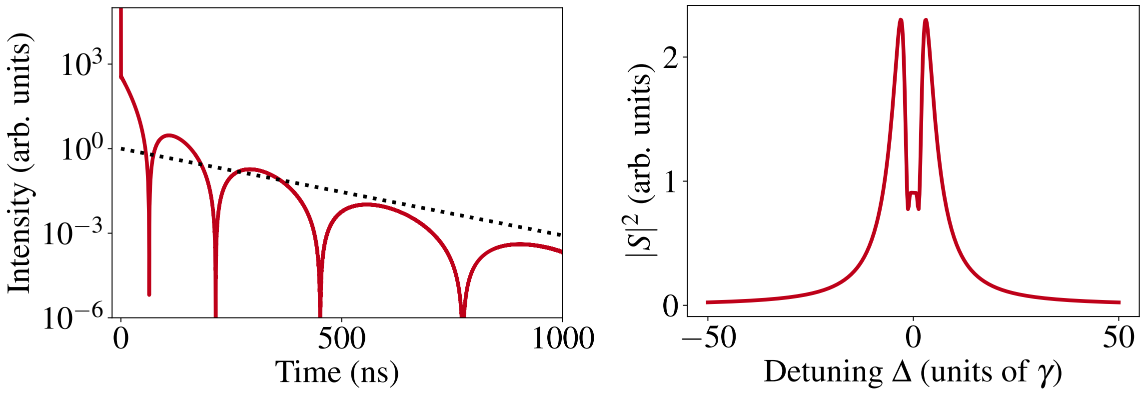

Figure 2.2: Time and nuclear resonant spectrum of a 2μm thick α-iron sample enriched in the resonant isotope ^{57}Fe probed in forward scattering. The left panel shows the dynamical beats described by the Bessel function in Eq. (2.15) as a red solid line. The black dotted line shows the exponential decay of a single nucleus. The faster decay of the dynamical beats compared to the single-nucleus decay is related to the speed up described in the main text. The right panel shows the splitting of the resonance line in the nuclear resonant response due to interference between different frequency components of the propagating nuclear polariton known as double-hump profile.

rate $\Gamma = \gamma/2$. To see this, we perform the early-time approximation of the time-domain response Eq. (2.15), valid if $bt \ll 1$, by comparing the first expansion orders of the Bessel and exponential functions such that

$$\sqrt{\frac{b}{t}}J_1(2\sqrt{bt}) \approx be^{-\frac{b}{2}t} \tag{2.16}$$

and, hence, the early-time nuclear resonant part of the response can be written as

$$S(t) \approx -be^{-i\omega_0 t}e^{-\frac{\gamma+b}{2}t}\,. \tag{2.17}$$

Clearly, with increasing sample thickness, this response becomes stronger via the prefactor b and features enhanced decay via the thickness parameter entering in the exponential. This effect is known as *speed up* [Röh04; Smi99; HT99a] and is a consequence of the cooperative spatially coherent emission of radiation by the nuclear ensemble.

Incoherent nuclear resonant scattering

In the last Section, the effects of coherent enhancement and speed-up of the nuclear emission due to spatially coherent scattering off of nuclear ensembles was discussed. Its application in time-domain forward scattering experiments in form of quantum beats will be discussed in more detail in Sec. 2.1.5. These effects require the atoms to return to their initial ground state after the scattering process such that the path indistinguishability is not broken, which is crucial for spatial coherence like in a multi-slit experiment. If an atom returns to a different state after the scattering process, it can be distinguished from the remaining atoms and cannot interfere with the scattered waves from other atoms. The subsequent scattering is spatially *incoherent* and does not experience the features of enhancement, speed-up or other interference-related effects. There are basically three processes that lead to a change of the state of the atoms:

a) The nucleus does not return to its original ground state and the nuclear wave function changes. This can occur, for instance, if the nucleus returns into a degenerate ground state with a different spin, i.e. a spin-flip. The latter process, therefore, describes *elastic* incoherent nuclear resonant scattering.

b) The nucleus returns to its initial ground state but the excitation energy is transferred to the electronic shell and is released via the ejection of an electron, a process known as *internal conversion*, and via fluorescence radiation from the electronic shell. This changes the atomic wave function and thus singles out the site of the nucleus.

c) The emission of the a photon by the nucleus is not recoilless, i.e. one or several phonons are created after the scattering process. This changes the vibrational state of the crystal. While this process, in principle, can also proceed coherently, this channel is typically strongly suppressed [SK99; Röh04]. This incoherent process can be used to probe the phonon density of the crystal in a technique going under the names nuclear inelastic scattering (NIS) [Röh04] or nuclear resonant inelastic x-ray scattering (NRIXS) [Alp+03] among others.

The spin flip of the nuclear ground state is the only *elastic* of these processes. All other incoherent scattering processes described above are *inelastic* and proceed via a change of energy of either a single atom or the crystal. While the spatially coherent emission is highly directional, i.e. an enhancement of emission is seen in the Bragg and forward channels, the incoherent one is not as the emission from single scatterers is isotropic and thus proceeds into the entire solid angle of 4π. Note that, while spatially coherent emission can only occur if the *absorption* of an x-ray photon by a nucleus is recoilless, absorption with recoil and creation of phonons can lead to incoherent emission and all three channels described above can contribute both after absorption with and without recoil. More detailed descriptions of incoherent nuclear resonant scattering can be found in Refs. [SK99] and [Smi+07].
Within the scope of this thesis, incoherent emission and its relation to the coherent scattering channel in thin-film cavities with special focus on the low-excitation regime will be discussed in Chapter 5. Conversion electron Mössbauer spectroscpy (CEMS) [Nom99; SP84; Fro+85; Fry+08] and fluorescence radiation detection [Smi+07] related to scattering channel (b) are here the preferred methods due to the high detection efficiency of electron detection and its depth-sensitivity as further discussed in Chapter 6.

2.1.5 Detection methods in nuclear resonant scattering

In this Section we discuss basic aspects of time and frequency domain nuclear resonant scattering experiments which are crucial for time-resolved, frequency-resolved and time- and frequency resolved spectra as discussed extensively in Chapters 3-5 to interpret quantum optical and many-body phenomena in thin-film cavities.

Time-domain methods

For a long time, time-domain detection dominated nuclear resonant scattering experiments with synchrotron radiation [Ger+85a; Has+91]. The reason for this is the high temporal resolution of avalanche photodiodes below 1 ns and the translation of small frequency differences on the neV scale, caused by hyperfine splittings of the nuclear resonance, into observable beatings in the temporal response of the nuclear sample, known as *quantum beats*, as shown in the right panel of Fig. 2.1. Two main reasons allow for an observation of these quantum beats: First, the nonresonant response and nuclear resonant response of nuclear samples as discussed, e.g., in Eq. (2.15) are separated well in the time domain since the duration of x-ray pulses from accelerator-based light sources typically is on the picosecond time scale or below and the electronic scattering also proceeds on time scales below picoseconds. In contrast, the nuclear response and the beating periods between nuclear hyperfine transtions are typical of the order of the nuclear lifetime, which, typically, is orders of magnitude longer than the pulse duration. This can be seen in the right panel of Fig. 2.1, which shows the time spectrum of a 2μm α-iron sample enriched in ^{57}Fe, probed in forward scattering. The sharp initial peak at time zero is the nonresonant scattering contribution while the beating pattern dominating the spectrum from about 1 ns onwards is caused by nuclear resonant scattering. This allows for a clear discrimination nuclear resonant scattering and electronic scattering in the time domain.
The second important reason for the observation of a quantum beat pattern is the spatial coherence of the nuclear scattering in the sample: The phase-coherence of the nuclear excitonic state excited in the sample allows for interference between radiation scattered from different resonances of different nuclei. In this sense, the quantum beat pattern like Fig. 2.1 can be interpreted like a time-domain analogue of a multiple-slit experiment where the spatial coherence of the scattering from the multiple-slit leads to an observable interference pattern on the screen [Röh04]. In this sense, the spatial coherence of the scattering is crucial for the observation of quantum beats.
However, time-domain detection also comes with its disadvantages: The interpretation of the time spectra relies on fitting procedures and they may be ambiguous. For example, different hyperfine field configurations may lead to the same beating pattern [Röh04]. Further, in a time-domain measurement the phase information is lost such that a Fourier transform to extract the frequency spectrum cannot

be performed [Cal+05]. This phase information can also be crucial for the interpretation of the nuclear dynamics [Hee+21]. Thus, more advanced detection methods are required.

Frequency-domain methods

In addition to the measurement of quantum beats and related methods [Röh+00] as a time-domain technique, frequency-domain methods are in use.
Many of these methods employ frequency-tunable single-line reference absorbers. Due to the ultranarrow linewidth of Mössbauer resonances and little broadening in thin forward scattering targets, these reference absorbers can be employed in a heterodyne detection scheme: The resonantly scattered radiation in a Mössbauer target interferes with the resonantly scattered radiation off of the reference absorber. By Doppler shifting the resonance frequency ω_a of this *analyzer*, by moving it with a constant velocity v, an effective detuning

$$\Delta = \omega_a \left(1 + \frac{v}{c}\right) , \tag{2.18}$$

where c denotes the velocity of light, can be created. This is achieved using a known as Mössbauer drives [KK12]. By measuring the intensity scattered off of the reference absorber and the target as a function of the detuning Δ, a frequency-resolved spectrum of the target can be obtained [CCL96; Ney+98]. This method is widely used in the field of Mössbauer science (see, e.g., [L'a+00; Röh+10; Hee+13] and Chapter 3). A related method is known as stroboscopic detection, which only records the intensity in certain periodic time intervals [Cal+03]. By recording the arrival time of photons at the detector in addition to the detuning, these methods can be generalized to detect time- and frequency-resolved NRS spectra [Hee+17; Hee+21; Hee14a]. A more detailed account of this measurement approach is given in Chapter 3.
Another approach to measure frequency-resolved NRS spectra at accelerator-based x-ray sources is the production of highly monochromatized radiation at synchrotron sources using pure nuclear Bragg reflections [Smi+97a]. As discussed in Sec. 2.2.2, nuclear Bragg scattering features an exponentially-decaying response and is therefore an ideal candidate for the production of such highly monochromatized x-ray radiation as it can feature narrow Lorentzian radiation responses. Commissioned at synchrotron facilities, these devices are known as *synchrotron Mössbauer source*.

2.2 Nuclear quantum optics

As discussed in Sec. 2.1, nuclear transitions feature extraordinary narrow resonance lines and well-separated transitions [HT99a]. Quality factors, characterizing the number of optical cycles within the lifetime of a specific transition ω_0/γ, of the Mössbauer resonances can be of the order 10^{12} (^{57}Fe) [Röh04] or even up to 10^{19} (^{45}Sc) [Shv+23], which does not only suggest these transitions for high precision spectroscopy and fundamental tests but also for quantum optical applications that build on coherence and interference of quantum states. In addition, the spatial coherence of the excitation and deexcitation of ensembles of nuclei associated with nuclear excitons Eq. (2.10) in combination with the high sensitivity to phase and frequency changes of Mössbauer resonances also makes them an excellent tool for studies of cooperative and many-body phenomena. In recent years, thin-film x-ray cavities have seen a rising interest as a particular platform for nuclear and x-ray quantum optics. The reason is two-fold: First, ensembles of Mössbauer nuclei embedded in these multi-layer structures feature particularly a simple cooperative radiative response with a high degree of controllability of radiatively-induced nucleus-nucleus interactions that allows for the engineering of effective collective level schemes. Second, the dynamics and emission from such multilayer systems in grazing incidence is particularly well understood and can be conveniently studied with existing theoretical methods [R9̈9; Röh04; HE13; HE15a; Len+20].
In this Section, we will first motivate the transition from the nuclear scattering theory outlined in Sec. 2.1 into a Hamiltonian description of nuclear dynamics that can conveniently be studied using density matrix theory and Master equation approaches. Next, thin-film x-ray cavities are introduced as an excellent platform to realize collective nuclear level schemes and to study and engineer nuclear quantum-optical and many-body phenomena. Theoretical aspects and important experimental observations are briefly reviewed.

2.2.1 Hamiltonian approach to nuclear resonant scattering

In Sec. 2.1, we introduced the basics concepts of Mössbauer science and, in particular, nuclear resonant scattering based on scattering theory. Here, we cast theses concepts into a semiclassical Hamiltonian formulation which is an ideal starting point for studying nuclear dynamics and quantum optics using density matrix descriptions of the nuclear ensembles driven by classical light fields. The concepts introduced here, form the basis for the quantum optical descriptions of the dynamics of nuclear ensembles embedded in thin-film cavities and their interactions with x-ray fields in Chapters 4-5.

The general Hamiltonian of a nuclear system interacting with a coherent light field can be written as

$$\hat{H} = \hat{H}_{\text{nuc}} + \hat{W}(t)\,. \tag{2.19}$$

As discussed in Sec. 2.1, nuclear resonances without hyperfine splitting constitute almost ideal two-level systems due to their narrow linewidth and the well-separated nuclear transitions. For this reason, the nuclear part $\hat{H}_{\text{nuc}}$ of the Hamiltonian $\hat{H}$ for a single nucleus is written as

$$\hat{H}_{nuc} = \hbar\omega_0 \left|e\right\rangle \left\langle e\right| \,, \tag{2.20}$$

whith the reduced Planck constant $\hbar = 1.055 \cdot 10^{-34}$ Js. Here and in the following the nuclear ground and excited states are denoted with $|g\rangle$ and $|e\rangle$.

Throughout this thesis we treat the x-ray light field semi-classically, which is consistent with earlier theoretical approaches [Smi99; Shv99; R9̈9; Röh04; LPK11; LPK12] and experimental observations [Shv+96; Shv+98; R.C+00; Smi+07; Röh+10; Röh+12; Hee+17; Hee+21] in the low-excitation regime.

For a single two-level nucleus, we write the interaction Hamiltonian in the dipole approximation [SZ97; HT99a]

$$\hat{W}(t) = -\frac{\hbar}{2}\left(\Omega(\mathbf{r}_n,t)\hat{\sigma}^+ + h.c.\right) \tag{2.21}$$

with the nuclear raising/lowering operators $\hat{\sigma}^+ = \left|e\right\rangle\left\langle g\right|$ and $\hat{\sigma}^- = \left|g\right\rangle\left\langle e\right|$. Here, *h.c.* denotes the hermitian conjugate. The (time-dependent) Rabi frequency $\Omega(\mathbf{r}_n,t)$ is given by

$$\Omega(\mathbf{r},t) = \frac{\mathbf{d}\mathbf{E}(\mathbf{r},t)}{\hbar} \tag{2.22}$$

with the effective nuclear dipole moment $\mathbf{d}$ and the electric field at position $\mathbf{r}$ of the nucleus and time t

$$\mathbf{E}(\mathbf{r}_n,t) = \mathbf{e}\mathcal{E}(t)e^{i\nu t - i\mathbf{k}\mathbf{r}} \tag{2.23}$$

with polarization vector $\mathbf{e}$, a temporal field envelope $\mathcal{E}(t)$, carrier frequency ν and wave vector k. Throughout this thesis, we will consider unfocussed plane wave x-ray fields only, which is a valid assumption in nuclear resonant scattering experiments due to the ultranarrow line width of Mössbauer transitions such that only a very narrow range of field modes interacts resonantly with the nuclear transition (cf. [Len21]).

We briefly comment on the choice the interaction Hamiltonian $\hat{W}(t)$: The dipole interaction Eq. (2.22), formally, corresponds to an electric dipole. However, as discussed in Sec. 2.1.3, nuclear transitions feature multipolarity. While in this thesis we mainly focus on unsplitted single-line systems, the effective nuclear electric dipole moment $\mathbf{d}$ for M1 transitions in free space such as the archetypical ^{57}Fe can be calculated for plane wave fields Eq. (2.23) and the correspondingly defined $\mathbf{B}$ via the Maxwell equation [Len21]

$$-\partial_t\mathbf{B} = \nabla \times \mathbf{E} \tag{2.24}$$

and the magnetic dipole interaction

$$\Omega_{\mathrm{M1}}(\mathbf{r}, t) = \frac{\mathbf{mB}(\mathbf{r}, t)}{\hbar}\,, \tag{2.25}$$

which yields [Len21]

$$\mathbf{d} = -\frac{1}{\nu}\mathbf{m} \times \mathbf{k}\,. \tag{2.26}$$

With this result we restrict ourselves to E1 transitions for the rest of this work without loss of generality. A more rigorous treatment of effective dipole Hamiltonians including higher order multipole moments and beyond the approximations of plane wave fields and free space is given in Ref. [Len21]. Heuristically, we can now relate the effective dipole moment $\mathbf{d}$ to the resonant scattering amplitude discussed in Sec. 2.1 by calculating the linear response of the Hamiltonian $\hat{H}$. For simplicity, we consider a dipole parallel to the electic field such that polarization effects can be neglected. A dipole d driven by an external field E creates a polarization that, in turn creates an electric field, which is given by

$$E_{\mathrm{d}} = \frac{1}{\epsilon_0}\langle \hat{d} \rangle, \tag{2.27}$$

Here, the expectation value of the dipole operator of a single nucleus, given by

$$\hat{d} = d\hat{\sigma}^+ + h.c.\,, \tag{2.28}$$

can be calculated by introducing the nuclear density matrix $\hat{\rho}(t)$ that describes the nuclear state at time t such that

$$E_{\mathrm{d}} = \frac{1}{\epsilon_0}\mathrm{Tr}\left[\hat{d}\hat{\rho}(t)\right] = d\rho_{ge}(t) + c.c.\,, \tag{2.29}$$

where *c.c.* indicates the complex conjugate and $\rho_{ge}(t) = \langle g|\,\hat{\rho}(t)\,|e\rangle$ is called the *coherence* of the density matrix since it is related to coherent dipole emission in the way shown above. To obtain the coherence at time t, the dynamics of the density matrix $\hat{\rho}(t)$ can be described by a Master equation

$$\frac{d}{dt}\hat{\rho} = \frac{1}{i\hbar}\left[\hat{H}, \hat{\rho}\right] + \mathcal{L}\left[\hat{\rho}\right]\,, \tag{2.30}$$

where $\left[\hat{A}, \hat{B}\right] = \hat{A}\hat{B} - \hat{B}\hat{A}$ denotes the commutator between operators $\hat{A}$ and $\hat{B}$. The nonunitary part of the dynamics are described by the Lindbladian

$$\mathcal{L}\left[\hat{\rho}\right] = \frac{\gamma}{2}\left(2\hat{\sigma}^-\hat{\rho}\hat{\sigma}^+ - \left\{\hat{\sigma}^+\hat{\sigma}^-, \hat{\rho}\right\}\right)\,, \tag{2.31}$$

where γ denotes the full linewidth of the nuclear transition and $\left\{\hat{A}, \hat{B}\right\} = \hat{A}\hat{B} + \hat{B}\hat{A}$ the anticommutator of the operators $\hat{A}$ and $\hat{B}$. The Lindbladian Eq. (2.31) describes the incoherent or non-unitary dynamics that has its origin in the (quantum mechanical) interaction between the nuclear ensemble and modes of an electromagnetic bath or continuum [SZ97; MS07; FS05].

Projection of the Master equation Eq. (2.30) onto the ground $|g\rangle$ and excited state $|e\rangle$ of the two-level nucleus yields the optical Bloch equations [MS07; SZ97]

$$\dot{\rho}_{ee} = \langle e|\,\frac{d}{dt}\hat{\rho}\,|e\rangle = -\gamma\rho_{ee} + \frac{i}{2}\left[\Omega(t)\rho_{ge} - \Omega^*(t)\rho_{eg}\right]\,, \tag{2.32a}$$

$$\dot{\rho}_{ge} = \langle g|\,\frac{d}{dt}\hat{\rho}\,|e\rangle = \left(i\omega_0 - \frac{\gamma}{2}\right)\rho_{ge} + \frac{i\Omega^*(t)}{2}\left(2\rho_{ee} - 1\right)\,, \tag{2.32b}$$

$$\rho_{eg} = \rho_{ge}^*\,, \qquad \rho_{gg} = 1 - \rho_{ee}\,, \tag{2.32c}$$

Eq. (2.32b) shows that the lowest-order contribution in the Rabi frequency $\Omega(t)$ to the coherence ρ_{ge} is in first order via the last term while a population ρ_{ee} is first created in second order according to Eq. (2.32a) since the coherence contribution is minimum first order. Thus, since we are interested in the linear dipole response, we only keep contributions up to first order in the coherence. To this end, we set $\rho_{ee} = 0$ in Eq. (2.32b), which can subsequently be solved conveniently in frequency space via a Fourier transformation leading to

$$\rho_{eg}(\omega) = -\frac{1}{2\hbar}\frac{d}{(\omega - \omega_0 + i\gamma/2)}E(\omega). \tag{2.33}$$

With this, the linear susceptibility of the single nucleus $\chi(\omega)$ can be obtained from

$$E_{\mathrm{d}}(\omega) = \chi(\omega)E(\omega)\,, \tag{2.34}$$

which yields

$$\chi(\omega) = -\frac{1}{2\hbar\epsilon_0}\frac{|d|^2}{\omega - \omega_0 + i\gamma/2}\,. \tag{2.35}$$

Using the relation between the susceptibility and the refractive index $n = \sqrt{1+\chi} \approx 1 + \frac{1}{2}\chi$ (see, e.g., [BP08; MS07]), the dipole response of a single nucleus, that experience both scattering with and without recoil, can be related to the nuclear resonant index of refraction in Eq. (2.11), which yields

$$|d| = \sqrt{\frac{2\pi\hbar\epsilon_0}{k_0^3}\frac{\gamma}{1+\alpha}\frac{2I_e+1}{2I_g+1}}\,, \tag{2.36}$$

which is consistent with the result found in Ref. [Len21] taking into account the different definitions of the dipole Hamiltonian $\hat{W}(t)$.

With this, we showed that the dipole moments of a dipole-interaction Hamiltonian $\hat{W}(t)$ Eq. (2.21) can be related to the nuclear resonant scattering amplitude discussed in Sec. 2.1. Hence, for computational and interpretational convenience, we switch to a description of nuclear ensembles and their dynamics in a density matrix formalism the dynamics of which can be described by master equations of the form Eq. (2.73). For these types of equations numerical and in a number of important cases even analytical solutions can be obtained. Similar master equations also form the basis of the perturbative density matrix expansions introduced in Chapter 4 of this thesis.

More rigorously than presented here, effective many-body nuclear master equations in thin-film cavities incorporating effective nucleus-nucleus interactions and cross-damping terms can be derived in the framework of macroscopic quantum electrodynamics [Len+20]. This approach is summarized in the last part of the next Subsection.

2.2.2 Mössbauer ensembles embedded in thin-film cavities

Thin-film x-ray cavities containing one or several nanometer thick layers of nuclei as depicted in Fig. 2.3 are an excellent platform for studying and engineering cooperative and quantum-optical effects. Among the quantum-optical effects oberserved in these structures are superradiant decay, the collective Lamb shift [Röh+10], Fano line shapes [Hee+15a], electromagnetically-induced transparency (EIT) [Röh+12], spontaneously generated coherences [Hee+13], slow light [Hee+15a] and Rabi oscillations between nuclear ensembles [Hab+17]. The reason for this is the tunability of the x-ray-nucleus and the nucleus-nucleus interaction mediated by the cavity in these photonic environments. This can be achieved via control of the angle of incidence, external magnetic fields and the manufacturing of specific layer structures. In these cavities one or several layers of Mössbauer nuclei of nanometer thickness are put in between guiding layers of low electronic density featuring low absorption that allow to sustain different standing electromagnetic field modes. X-rays can couple in and out of this wave guide via cladding layers that act as mirrors and typically feature a reflectance close to one. The total height of these multilayer structures is typically only a few 10s of nanometers to sustain only a few modes of the electromagnetic field in the wave guide structure probed

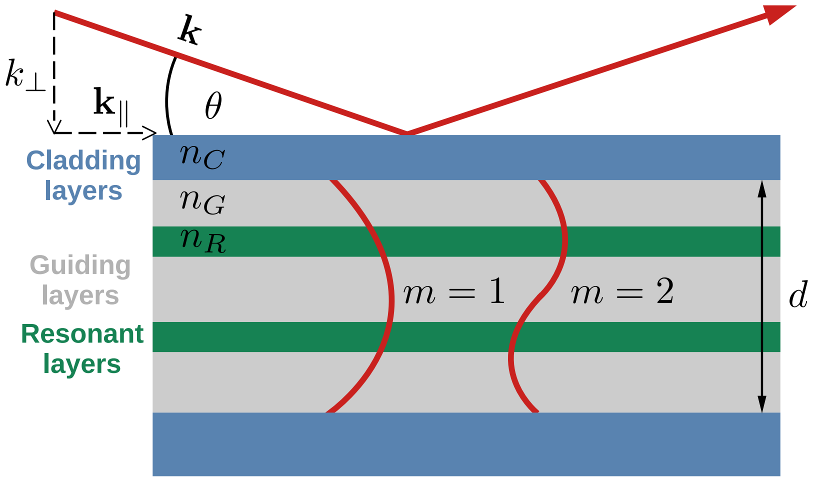

Figure 2.3: Scattering off of thin film cavities and multilayer structures: An x-ray of wave vector $\mathbf{k}$ impinging on a cavity surface at small angle of incidence θ is reflected from the surface layer (cladding) of refractive index n_C and coupled in into the wave guide structure of height d, where standing wave modes of length $\lambda_\perp = d/2m$ are sustained of which the first two are depicted. These modes interact with the nuclei forming resonant layers of refractive index n_R, which are embedded in between materials of low electronic absorption forming guiding layers of refractive index n_G. After repeated transmission and reflection through the layer structure, the x-rays are coupled out again and intefere with the reflected radiation.

at grazing incidence. The scattering off of these structures works as follows (cf. Fig. 2.3): X-rays impinging with angle of incidence θ onto the cladding layer of this multilayer structure. The angle of incidence has to be small such that the x-rays feature total reflection and evanescent coupling into the waveguide [RE21a]. Within the cavity, standing wave modes are sustained that determine the field strength at position of the resonant layers of nuclei. To sustain such modes these resonant layers are put in between the guiding layers. The x-ray field after repeated reflection and transmission from the different layers in the cavity is eventually coupled out of the cavity and superimposed with the reflected x-rays.

To give an intuition on how collective effective quantum optical level schemes arise in x-ray cavities and how this is related to the geometry of the wave guide structure, we give a brief introduction into the radiative normal mode analysis of Bragg reflections in nuclear scatterers as described in Refs. [RE21a; HT99a]. This analysis is related to planar wave guide structures like thin-film cavities using the following argument [RE21a]: The Bragg condition for constructive interference in a multi-layer crystal is given by

$$m\lambda = 2d \sin\theta \,, \tag{2.37}$$

where θ denotes the Bragg angle, d the separation of the crystal layers, λ the wavelength of the scattered x-rays and m the scattering order for constructive interference. Now, the angle of incidence θ of the x-ray radiation relative to the cavity surface in a grazing incidence experiment can be related to the wave number k of the incident radiation and the component normal to the cavity surface via

$$\sin\theta = \frac{k_\perp}{k} \,. \tag{2.38}$$

Inserting this relation into the Bragg condition yields

$$m\lambda_\perp = 2d \,, \tag{2.39}$$

which is the condition for a standing wave of wavelength $\lambda_\perp$ in a resonator of length d (cf. Fig.2.3). Thus, x-ray scattering off of an x-ray wave guide, like a thin-film cavity, of height d can be interpreted as Bragg scattering off of a lattice with lattice spacing d folded into a single layer by the repeated reflection by the cavity mirrors. This way, we motivate the following analysis of normal modes for nuclear Bragg scattering and the extension of the argument about the radiative properties of Bragg reflection to grazing incidence reflection.

We have seen in Sec. 2.1.4 that, in general, collective nuclear excited states upon excitation by impulsive x-ray pulses in the LER take the form of nuclear excitons $|\psi \mathbf{k}_{in}\rangle$ Eq. (2.10). Subsequently, we found that the emission of radiation in nuclear forward scattering even in presence of a single resonance line features beatings in its time response (cf. Fig. 2.2) indicating interference effects. In fact, it can be shown by a detailed radiative normal mode analysis [HT99a] that nuclear excitons $|\psi(\mathbf{k}_{in})\rangle$ are not eigenmodes of the Hamiltonian in the intermediate excited state of the nuclei after x-ray excitation and deexcitation. Instead, the nuclear exciton is a superposition of normal or eigen modes $|\psi_\alpha\rangle$ of the nuclear Hamiltonian

$$\hat{H}_{\text{rad}} = \hbar \sum_n \left(\omega_0 - \frac{i}{2}\gamma\right) |\phi_n\rangle \langle\phi_n| - \hbar \sum_{n \neq m} \frac{\gamma_{\text{rad}}}{2} c_{nm} \frac{e^{ik_{in} r_{nm}}}{k_{in} r_{nm}} |\phi_n\rangle \langle\phi_m| \tag{2.40}$$

with the relative distance between two nuclei $r_{nm} = |\mathbf{r}_n - \mathbf{r}_m|$ the single-excitation product states

$$|\phi_n\rangle = |g_1 \dots e_n \dots g_N\rangle \ . \tag{2.41}$$

The coupling terms arise from a radiative coupling between the different nuclei that can be written as [Röh+12; HT99a]

$$c_{nm} = \begin{cases} \frac{3}{2}(3\cos^2\varphi - 1)\left[\frac{1}{(k_{in} r_{nm})^2} - \frac{i}{k_{in} r_{nm}}\right] & \text{if} \quad r_{nm} k_{in} \ll 1 \\ \frac{3}{2}\sin^2\varphi & \text{if} \quad r_{nm} k_{in} \gg 1 \end{cases} \tag{2.42}$$

where φ is the angle between the polarization of the outgoing and incoming radiation the latter of which determines the direction of the nuclear dipole moment in the intermediate exciton state. A general form of this interaction in terms of nuclear currents or dipole moments can be found in Ref. [HT99a].

The normal modes $|\psi_\alpha\rangle$ can be obtained as eigenstates of $\hat{H}_{\text{rad}}$. By construction, these modes experience an exponential decay, i.e.

$$|\psi_\alpha(t)\rangle = e^{-i\tilde{\omega}_\alpha t} |\psi(0)\rangle = e^{-i\omega_\alpha t} e^{-\frac{\gamma}{2}t} |\psi(0)\rangle \ , \tag{2.43}$$

where we introduced the complex eigenfrequencies $\tilde{\omega}_\alpha = \omega_\alpha + \frac{i}{2}\gamma_\alpha$ of normal mode α.

Note, that the Hamiltonian $\hat{H}_{\text{rad}}$ is symmetric and not Hermitian and therefore the left and right eigenmodes are transposed vectors instead of complex adjoints of each other. Due to the invariance of the trace under the similarity transformation that diagonalizes $\hat{H}_{\text{rad}}$ we find that the real and imaginary parts of the complex eigenfrequencies $\tilde{\omega}_\alpha$ obey

$$\sum_\alpha (\omega_\alpha - \omega_0) = 0 \tag{2.44}$$

$$\sum_\alpha (\gamma_\alpha - \gamma) = \sum_\alpha \left(\gamma_{\text{rad}}^{(\alpha)} - \gamma_{\text{rad}}\right) = 0 \, . \tag{2.45}$$

Where we used that only the radiative part γ_{rad} of the nuclear linewidth is modified by the radiative coupling between the nuclei. Without specifying the form the complex eigenfrequencies, this indicates two things: First, in general, the (real) eigenfrequencies ω_α are shifted away from the original nuclear resonance frequency ω_0 with some modes shifted above and others below the single-nucleus value ω_0. Second, the decay rates of some eigenmodes have increased decay rates $\gamma_{\text{rad}}^{(\alpha)} > \gamma_{\text{rad}}$ (superradiant modes) while other feature reduced decay $\gamma_{\text{rad}}^{(\alpha)} < \gamma_{\text{rad}}$ (subradiant modes). By solving the eigenvalue problem of $\hat{H}_{\text{rad}}$ explicitely [HT99a] one can now show that the nuclear exciton state Eq. (2.10) is *not* an eigenstate of the Hamiltonian $\hat{H}_{\text{rad}}$ in forward scattering and that interference between different normal modes leads to the dynamical beats observed in this geometry (cf. left panel of Fig. 2.2). In contrast, in Bragg scattering off of translationally invariant crystals in the layer plane, if the Bragg condition Eq. (2.37) is fulfilled, only the symmetric (n even) or antisymmetric (n odd) Dicke state [Gar11] in the direction normal to the layer plane are driven, which are normal modes of $\hat{H}_{\mathrm{rad}}$ and feature strong superradiant enhancement [HT99a]. Therefore, the nuclear response $S(\omega)$ of an ensemble of two-level nuclei in Bragg scattering features an exponential decay in the time-domain and a corresponding Lorentzian line shape

$$S(\omega) \sim \frac{1}{\omega - \omega_0 - \Delta_{\mathrm{CLS}} + i(\gamma + \gamma_s)/2} \tag{2.46}$$

in the frequency domain, which is shifted by the collective Lamb shift Δ_{CLS} and broadened by the superradiant decay rate $\gamma/2$ compared to the single-nucleus linewidth γ. This behaviour was both calculated theoretically [HT99a; Man10] and observed experimentally both with synchrotron [SS89b] and the superradiant decay also with XFEL sources [Chu+18] and also forms the basis of the synchrotron Mössbauer source [Smi+97a] described in Sec. 2.1.5.
In agreement with the earlier argument that thin-film cavities can be interpreted as special cases of Bragg scattering, single-resonant layer cavities without hyperfine splitting also feature exponentially-decaying nuclear responses like Eq. (2.46) [Röh+10]. In fact, there are more rigorous approaches to calculate the reflectivity including the superradiance and the collective Lamb shift of nuclear ensembles embedded in thin-film cavities. Three of these approaches we will briefly discuss here: The transfer matrix or layer formalism, the phenomenological quantum optical model and the ab-initio Green's function method.

Layer formalism

The transfer matrix or layer formalism, the application of which to x-ray scattering and, in particular, nuclear resonant scattering is described in great detail in Refs. [R9̈9; Röh04], relates the incoming and outgoing field amplitudes of a stack or multilayer, like the one shown in Fig. 2.3, via reflection and transmission coefficents r'_{ij} and t'_{ij} of the layer boundaries. The propagation within one layer is described via a phase accumulated by the field during propagation given by [Hee14a; Len21]

$$\phi_m = k_{\perp}^{(m)} d_m \,, \tag{2.47}$$

where d_m is the thickness of layer m and $k_{\perp}^{(m)}$ the wave vector component in layer m normal to the layer surface given by

$$k_{\perp}^{(m)} = k^2 \sqrt{n_m^2 - \cos^2\theta} \tag{2.48}$$

One can see, that the layer formalism is a semiclassical method in the sense that it uses the materials refractive index n_m to describe propagation through the material, and reflection and transmission at the interfaces. The transfer matrix at the layer boundaries can be described in terms of the Fresnel coefficients and the complete transfer matrix of the full multilayer structure is given by the product of the transfer matrices of the single layers. A more detailed account of this method is given in Refs. [Hee14a; Len21]. Prominently, the transfer matrix or layer formalism was succesfully used to calculate the cavity reflectivities in Refs. [Röh+10; Röh+12] and to interpret the results in terms of collective phenomena like superradiance, collective Lamb shift and EIT. In particular, explicit values for the collective Lambshift, the superradiant decay rates and the cavity-mediated control fields in the case of EIT could be retrieved by comparison with expected quantum-optical responses. The method is implemented in the software packages CONUSS [Stu00b] and PYNUSS [Hee19], to both calculate cavity and forward scattering responses. Both have been demonstrated to be in excellent agreement with experimental observations at synchrotron light sources. The data evaluated in this Chapter and Chapter 3 have been calculated using PYNUSS.

Phenomenological quantum-optical model

The observation of quantum-optical phenomena like the collective Lamb shift, superradiance and EIT in thin-film cavities and their successful calculation within the semi-classical layer formalism suggests fully quantum-optical few-level descriptions of the system dynamics. The first full quantum-optical model to describe (nonlinear) nuclear dynamics and effective level schemes in thin-film cavities and to derive superradiant decay rates and the collective Lamb shift was introduced in Ref. [HE13]. Here, we give a brief summary of its results for effective two-level systems. For simplicity, we neglect the effects of electromagnetic field polarization as we are mainly interested in nuclear transitions without magnetic hyperfine splitting.

First, we discuss the reflection response of the empty cavity without nuclei. As discussed earlier by relating the model of Bragg scattering to the response of wave guide resonators, the cavity depicted in Fig. 2.3 sustains only standing wave modes satisfying the condition Eq. (2.39) in the direction normal to the cavity surface. In the following, we restrict ourselves to only on guided mode $n = 1$. The standing wave condition Eq. (2.39) is satisfied even if the incidence angle θ changes from the resonance condition

$$k_{\perp}^{c} = k_0 \sin\theta_0 \,, \tag{2.49}$$

where θ_0 is the incidence angle satisfying the standing wave condition for a given resonant wave number k_0. In contrast, if the incidence angle deviates from θ_0, the parallel wave vector component in the cavity is not fixed and for a given wave vector $\mathbf{k}$ of the driving external x-ray field is given by

$$k_{\parallel}^{c} = k \cos\theta \,. \tag{2.50}$$

Thus, the detuning Δ_c between cavity mode frequency $\omega_c = ck_c$ and external x-ray frequency $\nu = ck$ for small angles of incidence is given by

$$\Delta_c = \sqrt{\nu^2 \cos^2\theta + \omega_c^2 \sin^2\theta_0} - \nu \approx -\nu\theta_0\Delta\theta \,, \tag{2.51}$$

where $\Delta\theta = \theta - \theta_0$ characterizes the deviation of the incidence angle θ from the resonant angle θ_0. This results that not only standing wave order but also the cavity detuning can be controlled by the angle of incidence θ. Due to the orders-of-magnitude larger bandwidth of the cavity resonance compared to the nuclear resonance width, this detuning can usually be neglected on frequency scalles typical for NRS experiments but it is worthwile to note that the incidence angle can have a significant influence on the cavity mode structure and the cavity response as we will see below.

The Heisenberg equation of motion for the cavity field creation and annihilation operators $\hat{a}^\dagger$, $\hat{a}$ can be written as [HE13]

$$\frac{d}{dt}\hat{a} = \frac{1}{i\hbar}\left[\hat{a}, \hat{H}_c\right] - \kappa\hat{a} \,, \tag{2.52}$$

where κ denotes the cavity decay constant related to losses of the cavity into the continuum of external field modes. The cavity Hamiltonian $\hat{H}_c$ in the interaction picture oscillating with the external mode frequency ν is given by [HE13]

$$\hat{H}_c = \Delta_c \hat{a}^\dagger\hat{a} + i\sqrt{\kappa_R}\left(a_{in}\hat{a}^\dagger - a_{in}^{*}\hat{a}\right) \,. \tag{2.53}$$

Here, $\sqrt{\kappa_R}a_{in}$ accounts for the coupling of the incident x-ray field with the cavity mode, which can be adjusted by, e.g. changing the material or thickness of the cladding layer.

Explicit evaluation of Eq. (2.52) leads to the explicit expression for the stationary state cavity field mode, defined by the condition $\frac{d}{dt}\hat{a}^{SS} = 0$, [RE21a; HE13]

$$\hat{a}^{SS} = \frac{\sqrt{2\kappa_R}a_{in}}{\kappa + i\Delta_c} \,. \tag{2.54}$$

The empty-cavity reflectance can be calculated using the input-output relations $a_{out} = -a_{in} + \sqrt{2\kappa_R}\hat{a}$ [RE21a; Len21] as

$$T_c = \frac{\langle \hat{a}_{out}\rangle}{a_{in}} = \frac{2\kappa_R}{\kappa + i\Delta_c} - 1 \tag{2.55}$$

On resonance $\Delta_c = 0$ and the so-called critical coupling $2\kappa_R = \kappa$, the empty-cavity response vanishes, which can be interpreted as destructive interference between the the radiation reflected at the cavity surface and the radiation coupled out of the cavity in direction of the reflected beam.
If the nuclei are included, the nuclear polarization modifies the cavity response. In the so-called bad cavity regime [MS07] of fast dissipation κ typical for thin-film x-ray cavities, the cavity modes $\hat{a}$ can be expressed in terms of the incoming field modes and the nuclear source currents in a method called adiabatic elimination by calculating the stationary solution of the Heisenberg equation of motion for the cavity mode operators $\hat{a}$ including the nuclear source terms [HE13]. In the low-excitation regime, where nuclear collective states are given by the nuclear excitons

$$|\psi(\mathbf{k}_c)\rangle = \frac{1}{\sqrt{N}} \sum_{n=1}^{N} e^{i\mathbf{k}_c\mathbf{r}_n} |g_1 \dots e_n \dots g_N\rangle \ , \tag{2.56}$$

an effective Master equation for the nuclei only can be written down, which leads to a modified cavity reflectance [RE21a]

$$T(\Delta) = T_c - \frac{i}{a_{in}} \frac{2\kappa_R}{\kappa + i\Delta_c} g^* \sqrt{N} \langle\psi(\mathbf{k}_c)| \hat{\rho} |G\rangle \ , \tag{2.57}$$

where g denotes the coupling between a single cavity mode and nucleus, $\hat{\rho}$ the nuclear density matrix and

$$|G\rangle = |g_1 \dots g_n \dots g_N\rangle \tag{2.58}$$

is the collective ground state with all nuclei in their respective ground state $|g_n\rangle$. Eq. (2.57) shows that the nuclear coherence $\rho_{EG} = \langle\psi(\mathbf{k}_c)| \hat{\rho} |G\rangle$ strongly modifies the cavity response. From the effective Master equation the effective nuclear dynamics can be obtained by projection onto the collective ground and excited states $|G\rangle$ and $|\psi(\mathbf{k}_c)\rangle$, which yields effective Bloch equations similar to Eqs. (2.32) but now involving collective parameters instead of single-particle ones. Like for the solution of Eqs. (2.32), in the linear regime defined by $\langle G| \hat{\rho} |G\rangle$ only the coherence ρ_{EG} has a nonvanishing contribution while the population ρ_{EE} remains zero. The equation of motion for the coherence within the phenomenological model reads [HE13]

$$\frac{d}{dt} \langle\psi(\mathbf{k}_c)| \hat{\rho} |G\rangle = -i\sqrt{\frac{2}{3}} N g \frac{\sqrt{2\kappa_R} a_{in}}{\kappa + i\Delta_c} + i \left[\Delta - \Delta_{\mathrm{CLS}} + i\frac{\gamma + \gamma_s}{2}\right] \langle\psi(\mathbf{k}_c)| \hat{\rho} |G\rangle \tag{2.59}$$

with collective frequency shifts Δ_{CLS} and superradiant line broadening γ_s defined as

$$\Delta_{\mathrm{CLS}} = \frac{2}{3} N |g|^2 \mathrm{Im}\left[\frac{1}{\kappa + i\Delta_c}\right] \ , \tag{2.60}$$

$$\gamma_s = \frac{4}{3} N |g|^2 \mathrm{Re}\left[\frac{1}{\kappa + i\Delta_c}\right] \ . \tag{2.61}$$

Finally, by inserting the stationary state solution $\frac{d}{dt} \langle\psi(\mathbf{k}_c)| \hat{\rho} |G\rangle = 0$ into Eq. (2.57) one obtains the final form of the cavity reflectance including an ensemble of two-level nuclei as

$$T(\Delta) = \alpha_t - i(\alpha_t + 1) \frac{\left(\frac{\gamma_s}{2} + i\Delta_{CLS}\right)}{\Delta - \Delta_{CLS} + i\frac{\gamma + \gamma_s}{2}} \tag{2.62}$$

with

$$\alpha_t = \frac{2\kappa_R}{\kappa + i\Delta_c} - 1 \, . \tag{2.63}$$

Remarkably, the line shape observed in the cavity reflectance is *not* a simple Lorentzian but is modified by interference with the cavity reflectance T_c. This leads to an effective Fano line shape that can be modified by changing the angle of incidence as was studied in experiments [Hee+15a].
Regarding the nuclear resonant part of the response $T(\Delta)-T_c$ in Eq. (2.62), we were able to derive the collective Lamb shift Δ_{CLS} and the superradiance γ_s observed in thin-film x-ray cavities employing a quantum-optical model. Within this approach, these parameters are associated with a collective effective two-level scheme with states corresponding to nuclear excitons of the form Eq. (2.56) and with modified collective decay rate $\Gamma_c = \frac{\gamma+\gamma_s}{2}$ and renormalized transition frequency $\omega_0+\Delta_{\mathrm{CLS}}$. Similar approaches were used to also derive more complex level schemes including magnetic hyperfine splittings of the nuclear level [HE13] to study spontaneously generated coherences [Hee+13] and three-level systems [HE15a] including effective coherent control fields between the excited states [DLE22a] to realize EIT [Röh+12] and coherent couplings to observe Rabi oscillations between these states [Hab+17]. As a consequence of these results, we can write down an effective few-level master equation (see, e.g., Refs. [Len+20; DLE22a])

$$\frac{d}{dt}\hat{\rho} = \frac{1}{i\hbar}\left[\hat{H}_{\mathrm{eff}}, \hat{\rho}\right] + \mathcal{L}_{\mathrm{eff}}\left[\hat{\rho}\right] \tag{2.64}$$

with full Hamiltonian

$$\hat{H}_{\mathrm{eff}} = \hat{H}_{\mathrm{nuc}} + \hat{W}(t) \tag{2.65}$$

can be written down with a few-level Hamiltonian

$$\hat{H}_{\mathrm{nuc}} = \hbar\sum_{l}\omega_l \left|l\right\rangle\left\langle l\right| - \hbar\sum_{ll'}\Delta_{ll'}\hat{\sigma}_l^{+}\hat{\sigma}_{l'}^{-}\ , \tag{2.66}$$

where ω_l denotes the single-nucleus transition frequencies of effective level l and Δ_{ll} the collective Lamb shifts while $\Delta_{ll'}$ for $l \neq l'$ describes coherent couplings between the excited states. The effective raising and lowering operators $\hat{\sigma}_l^{\pm}$ describe excitation/deexcitation of level l from or into the ground state. The effective interaction Hamiltonian can be written as

$$\hat{W}(t) = -\frac{\hbar}{2}\sum_{l}\left(\Omega(t)\hat{\sigma}_l^{+} + h.c.\right) \tag{2.67}$$

with Rabi frequency

$$\hat{\Omega}(t) = \frac{\mathbf{d}_l\hat{\mathbf{E}}_l(t)}{\hbar} \tag{2.68}$$

and an effective dipole moment $\mathbf{d}_l$ between states $|0\rangle$ and $|l\rangle$ and an effective field $\hat{\mathbf{E}}_l$, that can be quantized or classical, driving that transition. Finally, the effective Lindbladian can be written as

$$\mathcal{L}\left[\hat{\rho}\right] = \sum_{ll'}\Gamma_{ll'}\left[2\hat{\sigma}_{l'}^{-}\hat{\rho}\hat{\sigma}_l^{+} - \left\{\hat{\sigma}_l^{+}\hat{\sigma}_{l'}^{-}, \hat{\rho}\right\}\right]\ , \tag{2.69}$$

where $\Gamma_{ll'}$ includes potential cross-decay terms for $l \neq l'$ and (superradiant) effective decay rates of level l as Γ_{ll}. These types of effective few-level models will be employed to study the cooperative dynamics upon the excitation of time-dependent x-ray pulses of different shape in the LER in Chapters 6 and 7. Further, some implications for dynamics beyond the LER within these effective few-level descriptions are discussed in Chapter 5.

Ab initio Green's function approach

In the previous two Subsections we have seen how effective collective few-level schemes naturally arise in thin-film cavities both in experiment and employing phenomenological quantum-optical models.

However, the validity of these models is limited for different reasons: The semi-classical layer formalism is based on linear response theory and, thus, is only valid in the LER. For future observations at novel coherent x-ray light sources such as XFELs and XFELOs with higher number of resonant photons it cannot be expected to yield accurate results. Further, as based on an effective description based on the nuclear refractive index, it does not provide access to the underlying nuclear dynamics of the system. Finally, quantum-optical effects of the electromagnetic field such as photon correlations can not be studied in this semi-classical model. The phenomelogical quantum-optical model, while in principle solving all these issues, is not complete as important deviations from the layer formalism experimentally-observed quantum-optical effects such as EIT, even if additional heuristic extensions are made to the model, are found [HE15a; Len+20]. To solve these problems ab initio quantum models were developed to account for the effects of high-loss cavities and overlapping cavity modes [Len+20; LE20] were developed. Apart from resolving disagreements with experiments found in the phenomenological model, these ab initio models also offer more fundamental insights into the interactions between bath and cavity modes and the nuclear ensemble.
Most relevant for this thesis is the ab initio Green's function approach developed for thin-film x-ray cavities in Ref. [Len+20]. The reason for this is that it provides rigorous derivations of both many-body nuclear master equations in the cavity evironment as employed in Chapter 5 and of the effective few-level master equation Eq. (2.64). With this, exact expressions for the effective nuclear and few-level parameters can be given within this approach and become computable in an efficient way. In this approach, the full Hamiltonian of the coupled nuclei and electromagnetic field is given by [Len+20]

$$\begin{aligned}\hat{H} = &\int d^3\mathbf{r} \int_0^\infty d\omega \hbar\omega \hat{f}^\dagger(\mathbf{r},\omega)\hat{f}(\mathbf{r},\omega) \\ &+ \sum_{ln} \hbar\omega_{nl}\hat{\sigma}^+_{ln}\hat{\sigma}^-_{ln} - \sum_{ln}\left[\hat{\sigma}^+_{ln}\mathbf{d}^*_l + \hat{\sigma}^-_{ln}\mathbf{d}_l\right]\cdot\hat{\mathbf{E}}(\mathbf{r}_{ln})\end{aligned} \tag{2.70}$$

with bosonic mode operators $\hat{f}(\mathbf{r},\omega)$ and the electromagnetic field operator $\hat{\mathbf{E}}_(\mathbf{r}_{ln})$ at position $\mathbf{r}_{ln}$ of a nucleus n in layer l given by

$$\hat{\mathbf{E}}(\mathbf{r}) = i\sqrt{\frac{\hbar}{\pi\epsilon_0}}\int_0^\infty d\omega \int d^3\mathbf{r}' \sqrt{\mathrm{Im}\left[\varepsilon(\mathbf{r}')\right]}\mathbf{G}(\mathbf{r},\mathbf{r}',\omega)\cdot\hat{f}(\mathbf{r}',\omega) \tag{2.71}$$

where the Green's tensor is defined as the solution to Maxwell's equation

$$\left[\nabla\times\nabla\times\mathbf{G}(\mathbf{r},\mathbf{r}',\omega) - \frac{\omega^2}{c^2}\varepsilon(\mathbf{r},\omega)\mathbf{G}(\mathbf{r},\mathbf{r}',\omega)\right] = \delta(\mathbf{r}-\mathbf{r}')\,. \tag{2.72}$$

with the complex-valued frequency-dependent dielectric permittivity ε accounts for both absorption an dispersion. This approach that describes the quantized electrimagnetic field Eq. (2.71) in terms of the classical Green's tensor $\mathbf{G}(\mathbf{r},\mathbf{r}',\omega)$ is known as macroscopic quantum electrodynamics (QED) [Len+20; SB09]. Starting from the Hamiltonian an effective master equation for the nuclei can be derived using the common steps of Born-Markov and rotating wave-approximation by tracing out the bath modes [FS05; Aga74]. The result reads [Len+20; AG+17]

$$\frac{d}{dt}\hat{\rho} = \frac{1}{i\hbar}\left[\hat{H},\hat{\rho}\right] + \mathcal{L}[\hat{\rho}]\,. \tag{2.73}$$

with the Hamiltonian $\hat{H}$ separated into parts

$$\hat{H} = \hat{H}_{nuc} + \hat{W} \tag{2.74}$$

with nuclear Hamiltonian

$$\hat{H}_{nuc} = \hbar\sum_{nl}\omega_{nl}\hat{\sigma}^+_{nl}\hat{\sigma}^-_{nl} - \hbar\sum_{nn'll'} J_{nn'll'}\hat{\sigma}^+_{nl}\hat{\sigma}^-_{n'l'}\,. \tag{2.75}$$

where the coherent couplings are related to the Green's tensor via [Len+20]

$$J_{nn'll'} = \frac{\mu_0 \omega_{nl}^2}{\hbar} \mathbf{d}_l^* \cdot \mathrm{Re}\left[\mathbf{G}(\mathbf{r}_{ln}, \mathbf{r}_{l'n'}, \omega_{nl})\right] \cdot \mathbf{d}_{l'} \tag{2.76}$$

with the vacuum permeability μ_0. The nucleus-field coupling part reads

$$\hat{W} = -\frac{\hbar}{2} \sum_{nl} \left(\hat{\Omega}_{nl} \hat{\sigma}_{nl}^+ + h.c. \right) . \tag{2.77}$$

Here, the Rabi frequency is given by

$$\hat{\Omega}_{nl} = \frac{\mathbf{d}_{nl} \hat{\mathbf{E}}_{nl}}{\hbar} . \tag{2.78}$$

Finally, the Lindbladian describing the non-unitary or incoherent part of the dynamics is given by

$$\mathcal{L}[\hat{\rho}] = \sum_{n,l} \sum_{n',l'} \left(\Gamma_{nn'll'} + \delta_{nn'} \delta_{ll'} \Gamma_{nl}^{\mathrm{IC}} \right) \left(2 \hat{\sigma}_{n'l'}^- \hat{\rho} \hat{\sigma}_{nl}^+ - \left\{ \hat{\sigma}_{nl}^+ \hat{\sigma}_{n'l'}^-, \hat{\rho} \right\} \right) \tag{2.79}$$

with cross-decay terms

$$\Gamma_{nn'll'} = \frac{\mu_0 \omega_{nl}^2}{\hbar} \mathbf{d}_l^* \cdot \mathrm{Im}\left[\mathbf{G}(\mathbf{r}_{ln}, \mathbf{r}_{l'n'}, \omega_{nl})\right] \cdot \mathbf{d}_{l'} . \tag{2.80}$$

With this, effective master equations for interacting nuclei in thin-film cavities with one or more resonant nuclear layers as discussed in Chapters 4 and 5 are put on a solid ground via the ab initio theory developed in Ref. [Len+20]. Using this approach one can also derive effective LER master equations featuring effective few-level schemes as introduced in the previous Subsection. This is done by assuming that the excited state of the nuclei is unpopulated, i.e. $\langle \hat{\sigma}_{nl}^+ \hat{\sigma}_{nl}^- \rangle \approx 0$ and via a Fourier transformation of all relevant quantities the layer plane of the cavity using the in-plane translational invariance of thin-film cavities. Then, the collective parameters defining the effective Hamiltonian Eq. (2.66) and Lindbladian (2.69) can be calculated via

$$\Delta_{ll'} = \frac{N}{A_\parallel} \frac{\mu_0 \omega_l^2}{\hbar} \mathbf{d}_l^* \cdot \mathrm{Re}\left[\mathbf{G}(z_l, z_{l'}, \mathbf{k}_\parallel, \omega_l)\right] \cdot \mathbf{d}_{l'} , \tag{2.81}$$

$$\Gamma_{ll'} = \frac{N}{A_\parallel} \frac{\mu_0 \omega_l^2}{\hbar} \mathbf{d}_l^* \cdot \mathrm{Im}\left[\mathbf{G}(z_l, z_{l'}, \mathbf{k}_\parallel, \omega_l)\right] \cdot \mathbf{d}_{l'} , \tag{2.82}$$

where $A_\parallel$ is the area covered by the nuclei in the planar cavity, z_l is the depth of the resonant layer l and the parallel wave space Green's operator ist related to the position-space Green's tensor via [Len+20]

$$\mathbf{G}(\mathbf{r}_{ln}, \mathbf{r}_{l'n'}, \omega_{nl}) = \int \frac{d^2\mathbf{k}_\parallel}{(2\pi)^2} \mathbf{G}(z_l, z_{l'}, \mathbf{k}_\parallel, \omega_l) e^{i\mathbf{k}_\parallel \cdot (\mathbf{r}_{\parallel,n} - \mathbf{r}_{\parallel,n'})} , \tag{2.83}$$

where the subscript $\parallel$ denotes the component of the wave vector and position in the layer plane of the cavity.

Nuclear quantum optics under nonlinear excitation conditions

Another aspect of the narrow linewidth of nuclear transitions is that it makes strong driving challenging, which is required for nonlinear excitations associated with many quantum-optical phenomena and related spectroscopic techniques. At synchrotron sources, typically less than one photon of the orders-of-magnitude broader pulse spectrum is resonant with the nuclear resonance such that experiments at these sources are restricted to the linear or low-excitation regime. New coherent x-ray sources such as XFELs and XFELOs with significantly higher resonant photon numbers, thus, can open up a completely new regime of nonlinear optics and quantum optics with Mössbauer nuclei. Further, higher excitations and even inversion of nuclear ensembles were predicted theoretically in x-ray wave guides [Che+22] or cavities using suitable focussing, tailoring of the cavity environment and specific isotopes [HKE16a; Len21; DLE22b]. From a theoretical perspective, this raises the question how low-excitation descriptions of nuclear ensembles and corresponding quantum-optical phenomena as introduced in this Section change at higher excitations and under multi-photon excitation conditions. In principle, nonlinear excitations of the nuclear ensemble can be studied in the phenomenolgical model [Hee14a] and the Green's function formalism [Len21]. However, it remains the question how to detect nonlinearities if the LER is only slightly surpassed and indications of strong driving [HKE16a] can not be observed yet. Another related question is which pulse structure of the x-ray driving field should be used to observe specific nonlinear dynamics and whether and, if yes, which advanced data analysis techniques are required to observe these effects. This question will be discussed in more detail in Chapter 5.

2.3 Phase control of the nuclear resonant response

We have seen in the previous Sec. 2.1 that the essential features of experiments with Mössbauer nuclei are related to the long lifetimes and corresponding sharp linewidths of nuclear transition in combination with the Mössbauer effect. These features lead to strong spatially coherent scattering that, for example, enables hyperfine spectroscopy in the time domain related to the observation of quantum beats (cf. Sec. 2.1.5). In Sec. 2.1.5 we explained how the narrow linewidth of Mössbauer nuclei can be exploited to perform frequency-resolved measurements using single-line nuclear reference absorbers. This technique is based on Doppler shifting the nuclear resonance frequency, which leads to a detuning in the nuclear resonant response compared to the static case. Here, we generalize this concept to imprint arbitrary time-dependent phases $\phi(t)$ onto the nuclear resonant response $S(t)$. Consider first the dipole response Eq. (2.29) of a single nucleus where the time evolution for the coherence is given by the Bloch equation Eq. (2.32b). Now, if the nuclear resonance frequency ω_0 is shifted in time by an amount $-\dot{\phi}(t)$, the equation of motion for the coherence in the linear response regime, where $\rho_{ee} = 0$, is modified to

$$\dot{\rho}_{eg} = \left(-i(\omega_0 - \dot{\phi}(t)) - \frac{\gamma}{2}\right) \rho_{ge} + \frac{i\Omega(t)}{2} \,. \tag{2.84}$$

The solution of this equation is

$$\rho_{eg}(t) = \frac{i}{2} \int_{t_0}^{t} dt' e^{-i\omega_0(t-t')} e^{i\phi(t-t')} e^{-\gamma(t-t')} \Omega(t') \tag{2.85}$$

as can be easily verified by inserting it into the complex conjugate of Eq. (2.84). From Eq. (2.85), the linear response of a single nucleus including a time-dependent shift of its transition frequency by the function $\dot{\phi}(t)$ can be read off as

$$S_{\mathrm{sn}}(t) \sim \frac{i}{2} e^{i\phi(t)} e^{-i\omega_0 t} e^{-\gamma t} \tag{2.86}$$

by comparison with the defining relation of the resonant response function [Smi99]

$$E_{out}(t) = \int_{t_0}^{t} dt' S(t-t') E_{in}(t') \,, \tag{2.87}$$

and by noting that the nuclear coherence is related to the outgoing field via Eq. (2.29). The response function technique will be discussed in more detail in Chapter 3. Here, it is important that the linear response of the single nucleus acquires a time-dependent phase shift $\phi(t)$ via the time-dependent phase shift $\dot{\phi}(t)$ of its resonance frequency. This time-dependent shift caused, for instance, by a linear motion in propagation direction of the incident field in forward scattering, i.e.

$$\dot{\phi}_{\mathrm{MB}}(t) = \frac{v}{c}\omega_0 = \Delta \,, \tag{2.88}$$

like in the case of a Mössbauer drive, which leads to a linear phase shift $\phi(t) = \Delta t$ associated with a detuning that can be used to detect frequency-resolved spectra as discussed in Sec. 2.1.5. Like for the Mössbauer drive, if the time-dependent frequency-shift affects all the nuclei at the same time, this frequency-shift is also reflected in the intermediate exciton state and the response function of the entire nuclear ensemble will acquire a phase shift in its full response function

$$T(t, \phi) = e^{i\phi(t)} T(t) \,. \tag{2.89}$$

Such phase shifts in praxis can, for example, be induced fast piezo motion of the sample in propagation direction of the incident field in forward scattering [Vag+14; Hee+17; Hee+21]. Other techniques can be the fast time-dependent change of the magnitude of an external magnetic field [Boc+21] or of the direction of the magnetic hyperfine field [Shv94; LPK12]. The latter method can only provide phase shifts of $\phi = \pi$ of hyperfinge transitions by a 180 flip of the magnetic field. These methods can be realized experimentally due to the long lifetimes of nuclear excitons. Typically, however, these techniques are not fast enough to be applicable to the nonresonantly scattered radiation which proceeds on the time scale of the excitation pulse with a duration of ps or shorter as discussed in Sec. 2.1.4. Thus, the time-dependent phase shift effectively is only applied to the nuclear resonant part $S(t)$ of the sample response, i.e.

$$T(t) = \delta(t) + e^{i\phi(t)} S(t) \,, \tag{2.90}$$

which allows for the interpretation of the forward scattering response as a phase-coherent double pulse as the relative phase $\phi(t)$ can be tuned by, e.g., sudden phase jumps after the excitation pulse has passed the sample. In the past, this technque has successfully be used to flip the relative sign of the resonant and nonresonant part of a single line reference absorber to both turn destructive interference between both parts into constructive interference thus enhancing the resonant part of the radiation [Hee+17]. A similar method is employed in our numerical studies in Sec. 7.3.1 In another experiment, such a sign flip was used to control the dynamics of a nuclear exciton from enhanced emission to enhanced excitation [Hee+21]. One can envision such phase control techniques to realize phase coherent multi-pulse techniques such as Ramsey interferometry, photon echo spectroscopy or multidimensional spectroscopy to study, e.g., coherent couplings between nuclear excited states. In Sec. 3.4 we show that such phase control can be used to disentangle different contributions of NRS spectra by measuring various phase combinations, which subsequently are subtracted or added to each other. This technique is inspired by similar approaches in collinear multidimensional spectroscopy, called phase-cycling, where the response functions of different excitation order of the driving electric field are separated by measuring and combining the intensities for different values of the driving pulse phases [Tan08; Cho19]. For a more detailed discussion of double-pulse applications to study nuclear dynamics, the reader is referred to Chapter 7.

Chapter 3

Evaluation of nuclear resonant scattering experiments using frequency-frequency correlation spectra

This chapter is based on the following publication:

Unraveling time- and frequency-resolved nuclear resonant scattering spectra
L. Wolff and J. Evers
Physical Review Research **5**, 013071 (2023)

The author of this thesis is the main author of this publication. The content has been reproduced almost verbatim with permission of the journal (© 2023 American Physical Society) and coauthors. The manuscript has undergone minor changes to adapt to the thesis style and structure. The results and content compared to the above-mentioned publication is not altered.

3.1 Advanced measurement and data analysis techniques

Exploring the regime of nonlinear [HKE16b; Che+22; BS97] and non-equilibrium phenomena [SR08] using novel coherent x-ray sources, which has only started to be explored experimentally [Chu+18], will require advanced measurement and data analysis techniques to access a broader range of observables, and to compare theoretical predictions with experimental observations. Examples include spectroscopy beyond the linear response regime [Muk95], photon-correlation measurements [Gla63], or methods to study the time-resolved sample dynamics after external stimuli, potentially on a per-shot basis [She12].

As a first step towards this goal, recent experiments employed a time- and frequency-resolved measurement of the scattered x-ray intensity [Hee+17; Hee+21; SS22; Hee+22], as compared to the established approaches of measuring time-resolved or frequency-resolved spectra separately [KK12], the latter of which can be obtained, for instance, by probing the nuclear absorption using pure nuclear Bragg reflections to produce highly monochromatic x-ray light on the scale of the nuclear line-width [Smi+97a]. Alternatively, the frequency-selectivity can be achieved using a heterodyne approach by adding an additional single-line reference absorber, in the following referred to as analyzer, on a velocity drive up- or downstream of the target under investigation [CCL96; Ney+98], see Fig. 3.1. This method is also used to perform time- and frequency-resolved data acquisition, which provides a number of significant advantages over other detection schemes using single-line reference absorbers, even though it does not require changes to the experimental setup apart from the electronics. On the one hand, it allows one to apply several established data analysis methods using a single experimental data set only. For example, late-time integration methods established as a standard analysis approach for x-ray cavities probed in reflection [CCL96; Deá+06; Röh+10] or related stroboscopic methods [Cal+02; Cal+03; Röh+12] can be employed by integrating the two-dimensional data set along part of the time axis. Importantly, the time- and frequency-resolved spectra allow one to improve the recovery of the target spectra by optimizing the integration range throughout the data analysis [R.C+00; HE20]. Similarly, off-resonant methods can be employed in spectral regions with large detuning between analyzer and target, which may even provide access to the complex-valued target response [Cal+05; Cal+02; Cal+03; Goe+19]. These methods typically exploit the interference between particular scattering pathways, which can be studied in the time [Cal+05]- or frequency domain [Goe+19]. However, these established methods share the drawback that they only make use of select regions of the recorded two-dimensional spectra. On the other hand, the two-dimensional

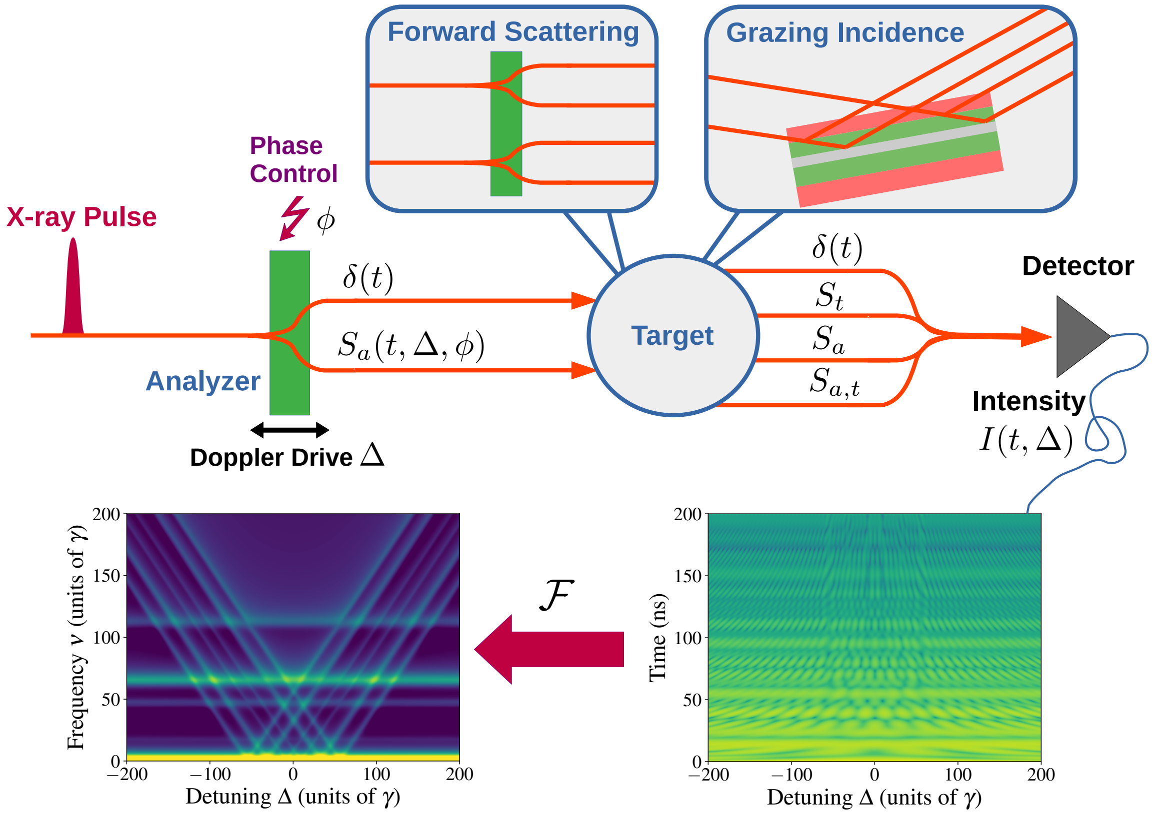

Figure 3.1: Schematic of a setup to record time- and frequency-resolved Nuclear Resonant Scattering spectra in forward and grazing incidence geometry. The goal is to characterize the resonant target response. An additional single-line analyzer mounted on a Doppler drive is used to introduce a variable frequency dependence. Resonant and non-resonant scattering in analyzer and target lead to four interfering scattering pathways contributing to the detection signal. An example for the experimentally accessible scattered intensity as function of analyzer frequency and arrival time of the scattered photons is shown in the lower right panel. The corresponding frequency-frequency correlation (FFC) spectrum studied in this work is obtained via a Fourier transform along the time axis. An example FFC spectrum for the data in the lower-right panel is shown in the lower-left panel. It exhibits clear horizontal and diagonal linear structures which can be interpreted in terms of spectral correlations within the combined analyzer-target-system. In the second part of this work, an additional phase control between resonant and non-resonant response of the analyzer is considered to disentangle the different scattering pathways.

data set allows for a much more stringent comparison between theory and experiment. One reason for this are the rich interference structures, which are lost in the usual one-dimensional data by the integration over the other axis (see bottom-right panel of Fig. 3.1 for an example). Interestingly, these structures encode intensity and phase of the target response. In Refs. [Hee+17; Hee+21], the complex-valued target response was determined by fitting theory models to the entire two-dimensional spectrum, thereby using all recorded data rather than only parts of it. However, this approach is computationally demanding as compared to other methods, and requires model fits in order to extract the desired target properties.

This raises the question, if the two-dimensional spectra can also be analyzed in different ways, which ideally provide access to the desired target properties in a more transparent way, without requiring global fits to the entire spectra, but still allow one to exploit the time- and energy correlations in the spectra, and to make use of large parts or even the entire experimental data set in the analysis.

Motivated by this, here, we develop spectroscopy and analysis techniques which are based on the Fourier transform of experimentally accessible time- and frequency-resolved intensities along the time axis. The resulting complex-valued frequency-frequency correlation (FFC) spectra exhibit particularly simple signatures comprising horizontal and diagonal structures, which can be associated to different contributing scattering processes. These signatures (see the bottom-left panel of Fig. 3.1 for an example) facilitate a selective analysis of the different scattering contributions. We in particular focus on two analysis approaches. First, we discuss linear fits to the diagonal structures in the frequency-

frequency correlation spectra, which allow one to extract nuclear resonance energies, as well as spectral line features such as collective energy shifts and superradiant line broadenings. Second, we show that horizontal or vertical sections through the diagonal structure provide access to amplitude and phase of the nuclear resonant part of the target response, cross-correlated with the analyzer response. This retrieval of the response without contributions from the off-resonant scattering in the target is of particular interest for x-ray cavity targets containing Mössbauer nuclei, since their spectra typically are strongly affected by the interference of electronic and nuclear response, in dependence on the x-ray incidence angle. We further show that an additional control of the relative phase between the electronic and nuclear response of the analyzer allows one to disentangle different scattering pathways, thereby facilitating their selective analysis without imposing additional constraints such as a large analyzer-target detuning. All approaches are illustrated using examples of practical relevance.

This Chapter is structured as follows: The next Section briefly describes a generic experimental setup used to record time- and frequency-resolved spectra including phase- and frequency-control of the nuclear reference absorber. Further, we derive expressions for the frequency-frequency correlation spectra in linear response theory, and discuss them in particular limiting cases. Section 3.3 presents the two analysis approaches for the diagonal structures, including numerical examples in forward scattering and cavity reflection. Section 3.4 introduces the phase control of the analyzer as an additional control parameter, and discusses its implications for the analysis of the diagonal structure. Finally, Sec. 3.5 summarizes the results.

3.2 Linear-response formalism and spectral correlations in nuclear resonant scattering

For our analysis, we consider the setup shown schematically in Fig. 3.1. A temporally short and spectrally broad x-ray pulse delivered by an accelerator-based x-ray source is used to probe a target containing Mössbauer nuclei. Both, forward scattering geometries and reflection from x-ray cavities will be considered. Additional frequency information is gained by introducing a single-line reference absorber, which can be tuned in frequency by Δ via a Doppler drive. Throughout this paper, frequencies are given in units of the target single-nucleus line-width γ. Each target features a near-instantaneous electronic response $\propto \delta(t)$, and a delayed nuclear response, which we denote as $S_i(t)$, with $i \in \{a, t\}$ for analyzer and target [LHH60a; KAK79; Smi99; Shv+98; Röh04; HT99a]. The two-stage setup thus gives rise to four different scattering channels [Smi+05; Cal+05], as illustrated in Fig. 3.1. In the experiment, the time- and frequency-resolved intensity of the scattered light is measured, which gives rise to two-dimensional spectra as illustrated in the bottom right panel of Fig. 3.1 [Hee+17; Hee+21]. A Fourier transform along the time axis then leads to the frequency-frequency correlation spectra considered here. We note that Ref. [Goe+19] employed a similar Fourier transform in order to select a particular frequency region for a subsequent analysis in the time domain. The bottom left part of Fig. 3.1 shows the real value as an example, clearly exhibiting the horizontal and diagonal structures. In Sec. 3.4, we will further consider the possibility of controlling the relative phase ϕ between the electronic and nuclear response of the analyzer.

3.2.1 Time- and frequency resolved spectra in the linear response formalism

A theoretical description of time- and frequency-resolved Nuclear Resonant Scattering spectra can be given employing the linear response formalism (see e.g. [Smi99; HT99a]) which is justified by the narrow line-width characteristic of Mössbauer transitions that typically leads to low excitation in state-of-the-art experiments, even at high-brilliance third-generation synchrotron sources. Neglecting polarization effects [SBH99], each target i in the beam path can be described by a scalar transfer function $\hat{T}_i(\omega)$ in the frequency domain or (impulse) response function $T_i(t)$ in the time domain. Here and in the following, the "hat" denotes quantities in the frequency domain. Then, the outgoing field is given by

$$\hat{E}_{out}(\omega) = \hat{T}_i(\omega)\hat{E}_{in}(\omega)\,, \tag{3.1}$$

$$E_{out}(t) = (T_i * E_{in})(t) \tag{3.2}$$

in the frequency- or time domain, respectively. Next to the convolution $*$ in Eq. (3.2), we also define the cross-correlation $\star$,

$$(f * g)(x) = \int_{-\infty}^{\infty} dy f(x-y)g(y)\,, \tag{3.3}$$

$$(f \star g)(x) = \int_{-\infty}^{\infty} dy f^*(y-x)g(y)\,, \tag{3.4}$$

for two complex-valued functions f, g of frequency or time variables x, y. The convolution can be interpreted as applying a filter f to g, or a propagation of an input g at point y to the final output $f * g$ at point x by virtue of the response function f. The cross-correlation $f \star g$ on the other hand can be thought of as scanning the functions f and g for similarities by introducing relative shifts x between them. Both quantities and their interpretations will turn out to be instrumental for understanding the diagonal and horizontal structures appearing in Fourier-transformed time- and frequency-resolved spectra, the real part of which is shown in the lower left plot of Fig. 3.1 as an example.

The responses of nuclear targets in forward scattering and grazing incidence geometry comprise two fundamentally different scattering processes: Prompt scattering nonresonant with the nuclear transition and coherent resonant scattering delayed by the slow decay of the nuclear transition. On the time scale of the nuclear decay, the prompt radiation can be described by a Dirac-$\delta(t)$-like pulse and thus the outgoing field in Nuclear Resonant Scattering is of the form

$$E_{out}(t) = \alpha[\delta(t) + S_i(t)] * E_{in}(t)\,. \tag{3.5}$$

Here, the prefactor α accounts for attenuation and dispersion imposed by the surrounding nonresonant material and $S_i(t)$ denotes the nuclear resonant part of the target's response. A two-target setup formed by a reference absorber foil T_a (analyzer) and an unknown target T_t in forward scattering geometry as depicted in Fig. 3.1 can be described by the total response function $T(t) = (T_t * T_a)(t)$. The response of the reference absorber with tunable transition frequency $\omega_a + \Delta$ and relative phase ϕ between the prompt and scattered part can be written as

$$T_a(t, \Delta, \phi) = \alpha_a \left[\delta(t) + e^{-i\Delta t} e^{i\phi} S_a(t)\right]\,. \tag{3.6}$$

Note that, typically, we will consider thin reference absorbers whose spectral features are more narrow than those of the target absorber. However, the subsequent analysis does not employ approximations of the reference absorber's response function based on this thin-analyzer limit, and our numerical results below will exhibit effects beyond this limit. In the following, for notational brevity, we will absorb the detuning and phase dependence into the nuclear scattering response as

$$S_a(t, \Delta, \phi) = e^{-i\Delta t} e^{i\phi} S_a(t)\,, \tag{3.7}$$

and suppress the dependence on ϕ throughout this Section as phase control will become of relevance only later in Sec.3.4.

With these considerations, the experimentally accessible time- and frequency-dependent intensity at the detector can be expressed in terms of response functions as

$$I(t, \Delta) = |(T * E_{in})(t)|^2 = (T * E_{in})^*(t)\,(T * E_{in})(t)\,, \tag{3.8}$$

where the Δ-dependence arises via T_a in the response function T. Such two-dimensional time- and frequency-resolved spectra allow for a much more stringent comparison of experimental data to theory predictions than the corresponding one-dimensional time-spectra or energy-spectra alone, and have been measured in recent experiments [Hee+13; Hee+17; Hee+21]

3.2.2 Frequency-frequency correlation spectrum

In order to discuss spectral correlations, we define the frequency-frequency correlation (FFC) spectrum as the Fourier-transform of the experimentally accessible intensity Eq. (3.8) along the time axis,

$$\mathcal{I}(\nu, \Delta) = \int_{-\infty}^{\infty} dt\, e^{i\nu t}\, I(t, \Delta) \tag{3.9}$$

$$= E_0^2 \int_{-\infty}^{\infty} dt\, e^{i\nu t}\, T^*(t)\, T(t) = \frac{E_0^2}{2\pi} (\hat{T} \star \hat{T})(\nu)\,, \tag{3.10}$$

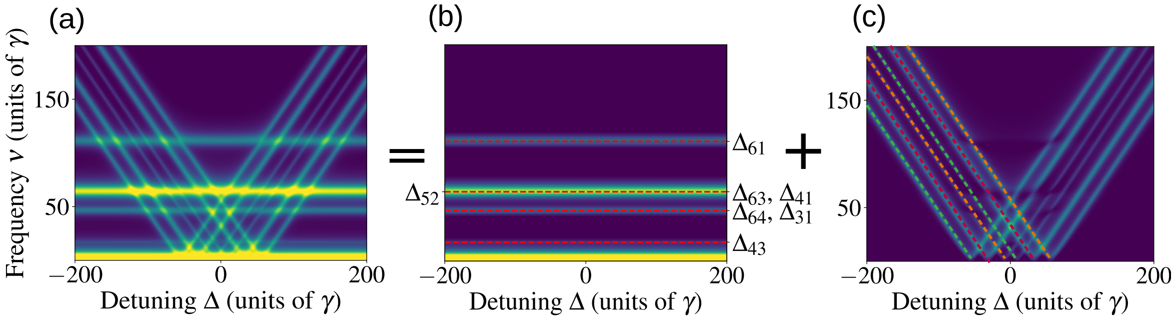

Figure 3.2: Decomposition of FFC spectra into single-target and two-target contributions. (a) shows the real part of the FFC spectrum $\mathcal{I}(\nu, \Delta)$ after removal of the off-resonant background. It can be separated into two parts shown in (b) and (c). The first part in (b) is the sum of the individual responses of target and analyzer, corrected for the non-resonant absorption. The horizontal structures are due to quantum beats in the target. As guide to the eye, the relevant mutual detunings between the target transitions are indicated by dashed red lines. (c) is the difference between the spectra in (a) and (b). This spectrum is dominated by diagonal structures, which originate from the interference of the resonant scattering off of the different target resonances with the resonant analyzer response. These results are obtained for a 2μm thick enriched $\alpha - {}^{57}$Fe target with hyperfine field $B = 33.3$ T and a stainless-steel single-line analyzer as described in the main text. The corresponding level structure and the relevant transitions in the target are shown in Fig. 2.1. The orange, red and green transitions describe the scattering of left-circularly, linearly and right-circularly polarized light, respectively.

where the initial pulse was written as $E_{in}(t) = E_0\delta(t)$ as it is typically orders of magnitude shorter than the nuclear evolution time scales. Note that $I(t, \Delta)$ vanishes for times $t < 0$ since the excitation occurs at $t = 0$. However, the symmetric integration will allow us to derive simple analytical expressions for the case with detection time gating in Sec. III D. Interestingly, the FFC spectrum Eq. (3.9) can be expressed as the (spectral) auto-correlation of the total response function $\hat{T}$. The result Eq. (3.10) can thus be regarded as a frequency-domain instance of the Wiener-Khinchin theorem which relates the Fourier transform of the power spectral density $|T(t)|^2$ to the autocorrelation $(\hat{T} \star \hat{T})(\nu)$ (see, e.g., [Eng07]). As we will see in the following, the Fourier transformation in Eq. (3.9) translates temporal interference effects into spectral correlations from which spectral features and the phase information of the nuclear target can be extracted. However, it is important to note that the FFC spectrum itself is not an intensity, as it is complex-valued for general Fourier frequencies ν. The reason is that it is derived via the Fourier transform from the experimentally accessible real-valued intensity. Regarding previous detection schemes using single-line reference absorbers as mentioned in the introduction, we note that the FFC spectrum reduces to the real-valued time-integrated spectrum for $\nu = 0$ (cf. [CCL96]). By only integrating over certain parts of the time-axis, late-time and stroboscopic spectra (see, e.g. [Cal+03]) can be recovered from the same $\nu = 0$ contribution. In this sense, the FFC spectrum can be regarded as a generalization of these methods to arbitrary Fourier frequencies ν using the same data set. The case where the signal at early times is discarded, is discussed in more detail in Sec. 3.3.4 and appendix A.1. In the following, we focus on the ideal case in which all times are available for data analysis in order to derive analytical expressions for the most relevant features of these spectra.

A numerical example for the FFC spectrum in Eq. (3.9) is given in Fig. 3.1. The bottom-right panel shows the experimentally accessible time- and frequency-resolved intensity $I(t, \Delta)$ in Eq. (3.8). The bottom-left panel shows the real part of the FFC spectrum in Eq. (3.9), which is dominated by a set of horizontal and diagonal spectral features in the $\Delta-\nu$-plane. Note, that throughout this paper, we only plot and analyze the positive ν branch of the FFC spectrum since the inversion of the Fourier frequency $\nu \to -\nu$ leads to complex conjugation of the FFC signal. The main part of our FFC analysis, however, will be carried out on its real part or absolute value and thus the negative ν branch contains only redundant information.

For an interpretation of these diagonal features, we rewrite the spectral auto-correlation function Eq. (3.10) using the Fourier-domain response functions

$$\hat{T}(\omega) = \hat{T}_t(\omega)\hat{T}_a(\omega)\,, \quad \hat{T}_a(\omega, \Delta, \phi) = \alpha_a \left[1 + \hat{S}_a(\omega, \Delta, \phi)\right] \tag{3.11}$$

as

$$\mathcal{I}(\nu,\Delta) = \frac{E_0^2|\alpha_a|^2}{2\pi}\left[(\hat{T}_t \star \hat{T}_t)(\nu) + (\hat{T}_t \star \hat{T}_t\hat{S}_a)(\nu) + (\hat{T}_t\hat{S}_a \star \hat{T}_t)(\nu) + (\hat{T}_t\hat{S}_a \star \hat{T}_t\hat{S}_a)(\nu)\right] . \tag{3.12}$$

Eq.(3.11) shows the clear separation of nonresonant (electronic) scattering, which is approximately constant on the scale of the nuclear resonances, and the frequency-dependent nuclear resonant scattering in form of the nuclear resonant response $S_a(\omega,\Delta,\phi)$ in the frequency-domain. This separation is crucial for the evaluation of the FFC spectrum in the form of Eq.(3.12), the single parts of which can be interpreted as follows: the first term describes spectral correlations between different transitions in the target, as will be further discussed below. The other three terms contain the contribution $\hat{T}_t\hat{S}_a = \alpha_t[\hat{S}_a + \hat{S}_a\hat{S}_t]$ combining target and analyzer. Its first addend $\sim \hat{S}_a$ arises from the aforementioned nonresonant (electronic) scattering in the target followed by resonant (nuclear) scattering processes in the analyzer foil. It forms the basis of the heterodyne-type detection schemes which determine the target response using interference between radiation emitted from the target and analyzer, respectively (cf. [Cal+05; R.C+00]). It will turn out to be the main origin of the diagonal structure found in FFC spectra. The second addend $\sim \hat{S}_a\hat{S}_t = \hat{S}_{a,t}$, known as radiative coupling [Smi99; HT99a; Sch+02b; Smi+05], describes processes with resonant scattering in both analyzer and target. In the following, we will exploit that these two scattering contributions are naturally separated owing to their different scattering amplitudes as a function of detuning between analyzer and target and will focus on the first contribution, as it dominates the FFC spectra in the large analyzer-target detuning limit.

3.2.3 Large analyzer-target detuning limit

The resonantly scattered part of the analyzer response $\hat{S}_a(\omega)$ is nonzero in the vicinity of the resonance frequency $\omega = \omega_a + \Delta$ only. For the same reason, the full target response becomes spectrally flat far-off nuclear resonance, i.e., $\hat{T}_t(\omega) \approx \alpha_t$. As a result, we can approximate

$$\hat{T}_t(\omega)\hat{S}_a(\omega) \approx \alpha_t\hat{S}_a(\omega) \tag{3.13}$$

in the limit of large detunings $\Delta + \omega_a - \omega_t$ between the analyzer and target transitions with frequencies ω_t. In this approximation, the spectral auto-correlation function can be written as

$$\mathcal{I}_{\text{off}}(\nu,\Delta) \approx \frac{E_0^2|\alpha_a|^2}{2\pi}\left[(\hat{T}_t \star \hat{T}_t)(\nu) + |\alpha_t|^2(\hat{S}_a \star \hat{S}_a)(\nu) + \alpha_t(\hat{T}_t \star \hat{S}_a)(\nu) + \alpha_t^*(\hat{S}_a \star \hat{T}_t)(\nu)\right] . \tag{3.14}$$

The first two terms correspond to the full target response $\mathcal{F}[|T_t(t)|^2]$ and the resonantly scattered part of the analyzer response $\mathcal{F}[|S_a(t)|^2]$, where $\mathcal{F}$ denotes the Fourier transform. These contributions can be determined from separate measurements of the time-dependent scattered intensity of the target and the analyzer alone, i.e., in the absence of the respective other target. Their complex-valued contributions to Eq. (3.14) then follow from a Fourier transformation analogous to Eq. (3.9).

This separation of the single-stage contributions $\hat{T}_t \star \hat{T}_t$ and $\hat{S}_a \star \hat{S}_a$ from the FFC spectrum is illustrated in Fig. 3.2. The full FFC spectrum in panel (a) decomposes into the single-stage response parts shown in (b) and the residual two-target contributions in (c). Clearly, the single-stage responses correspond to the horizontal lines in (a) since they do not depend on Δ, whereas the two-target parts give rise to the diagonal lines. Note that, if the single-stage contributions are removed by subtracting the time-resolved analyzer and target intensities, the count rates of the three measurements of the time- and frequency-resolved spectrum, the time-resolved target spectrum and the time-resolved analyzer spectrum, have to be adjusted to each other, e.g. by adapting the count rates such that after subtraction the horizontal lines have been removed. Alternatively, the horizontal lines can be removed directly from the FFC spectrum by determining their vertical position and shape far away from the diagonal structure. As these contribution to the FFC spectrum are detuning-independent, a subtraction of the result directly clears the horizontal lines from the entire spectrum without the need of additional measurements. We pursue the first approach in the numerical analysis in Sec. 3.3, while the second one is applied to the horizontal lines appearing in the sum spectrum $\mathcal{I}_{inv}$ in Sec. 3.4.1.

After subtracting the single-stage contributions, we remove the constant off-resonant background contribution to $\hat{T}_t$, which can be written in the same form as Eq. (3.11), i.e. the part proportional to $|\alpha_t|^2$ in the second line of Eq. (3.14), to study the nuclear resonant part $\hat{S}_t$ of the response alone. This can be done, e.g. by rejecting the first few nanoseconds after pulse arrival at the detector. Then, finally, the spectral auto-correlation function in the large analyzer-target detuning limit Eq. (3.14) can be written as

$$\mathcal{I}_{Dia}(\nu,\Delta) = \frac{I_0^{\rm NR}}{2\pi}\left[(\hat{S}_a \star \hat{S}_t)(\nu) + (\hat{S}_a^* \star \hat{S}_t^*)(-\nu)\right] , \tag{3.15}$$

where we used $(f \star g)(\nu) = (g^* \star f^*)(-\nu)$. Further, we defined $I_0^{\rm NR} = E_0^2|\alpha_a\alpha_t|^2$ which describes the intensity at the detector after the two-target setup in the absence of nuclear scattering.

It is important to note that throughout the derivation of Eq. (3.15), no assumptions were made on the analyzer and target response functions, except for the general features that the scattering contributions to the response functions cover only a limited spectral region, and that the full response function is spectrally flat outside this nuclear resonance region. Therefore, the expression Eq. (3.15) holds for general nuclear targets.

The interpretation of Eq. (3.15) will be discussed in more detail in Sec. 3.2.5 which also reveals its relation to the diagonal structures in the FFC spectrum and how it can be employed to extract the complex-valued nuclear resonant part of the target response from experimentally accessible FFC spectra.

3.2.4 Relation to off-resonant methods in the time domain

The derivation of Eq. (3.15) relied on the large analyzer-target detuning, in order to isolate a single scattering channel of interest. In the literature, several methods have been reported which employ a similar parameter regime in order to study time- and frequency-resolved Nuclear Resonant Scattering spectra, specifically for the recovery of the complex-valued target response function [Cal+05; Goe+19]. These latter methods operate in the time-domain, and we can connect our energy-domain result Eq. (3.15) to them via the so-called cross-correlation theorem [Wei] as

$$\begin{aligned}\mathcal{I}_{RM}(\nu,\Delta) =& \frac{I_0^{\rm NR}}{2\pi}\left[(\hat{S}_t \star \hat{S}_a)(\nu) + (\hat{S}_a \star \hat{S}_t)(\nu)\right] \\ =& \frac{I_0^{\rm NR}}{2\pi}\left\{\Big(\mathcal{F}[S_t^*(t)] * \mathcal{F}[S_a(t)]\Big)(\nu) + \Big(\mathcal{F}[S_a^*(t)] * \mathcal{F}[S_t(t)]\Big)(\nu)\right\} \\ =& 2I_0^{\rm NR}\int_{-\infty}^{\infty} dt e^{i\nu t}\mathrm{Re}\left[S_t^*(t)S_a(t)\right] .\end{aligned} \tag{3.16}$$

We see that the spectral cross-correlation between target and analyzer response are mapped to the interference between the corresponding time-domain responses and thus, studying the diagonal structure in the FFC spectrum is analogous to studying the hyperbolic interference pattern appearing in the time- and frequency-resolved intensities.

Our analysis below exploits specific features of the energy-domain representation, and extends the previous results in several ways. Most notably, we will discuss the spectroscopy of thin-film cavities probed in grazing incidence, and show that the off-resonant approaches allow one to access the nuclear target response alone, without the usual interference with the electronic scattering on the cavity structure.

Further, it is important to note that both the energy- and time-domain approaches discussed so far are restricted to off-resonant spectral regions, in which the radiative coupling contributions are negligible. Hence, data recorded near resonance between analyzer and target cannot be employed for the analysis and, as a consequence, these spectroscopy methods do not allow one to access the interesting regime in which radiative couplings substantially modify the target dynamics [Sch+02b; Smi+05; Hee+21; SS22; Hee+22]. To overcome these limitations, below in Sec. 3.4, we will discuss a method to suppress different scattering channels to become more independent of the large analyzer-target detuning limit or related approximations, and will demonstrate its advantages by comparison to the off-resonant method.

A brief comparison of the off-resonant methods to the so-called late-time integration spectroscopy methods is given in Appendix A.1.

3.2.5 Interpretation of the frequency-frequency correlation spectrum

After having derived the spectral auto-correlation function Eq. (3.10) in the large analyzer-detuning limit Eq. (3.15), and hence a representation of the FFC spectrum in terms of response functions in this limit, we now turn to its interpretation, which will form the basis for further analysis below.

Thin-analyzer limit

To this end, we for the moment assume an idealized case of a single-line analyzer with negligible linewidth and absorption α_a and resonance frequency $\omega_a + \Delta$ given by the scattering response function

$$\hat{S}_a(\omega, \Delta) = \delta(\omega - \Delta - \omega_a). \tag{3.17}$$

Then, Eq. (3.15) simplifies to

$$\mathcal{I}_{\text{id}}(\nu, \Delta) = \frac{I_0^{\text{NR}}}{2\pi} \left[\hat{S}_t(\omega_a + \Delta + \nu) + \hat{S}_t^*(\omega_a + \Delta - \nu) \right] . \tag{3.18}$$

Thus, in this idealized ("id") analyzer case, the FFC spectrum provides direct access to the desired nuclear resonant target response $\hat{S}_t$. Interestingly, the two contributions of $\hat{S}_t$ in Eq. (3.18) are centered around $\omega_a + \Delta \pm \nu$. This can be understood by noting that the analyzer response at $\omega_a + \Delta$ is shifted by the Fourier frequency $\pm\nu$ in the cross correlation. We can thus identify the two contributions as the origin of the two branches of the diagonal structures with positive or negative slopes in the FFC spectrum.

Below, we will also consider analyzers with finite thickness, in which case Eq. (3.18) generalizes to Eq. (3.15), i.e., the target response is additionally cross-correlated with the analyzer response function.

As a final remark, we note that, while the diagonal structure is directly related to the nuclear resonant target response $\hat{S}_t$, the FFC spectrum in principle also allows to study the full target response $\hat{T}_t$ if the nonresonant background is not removed in the derivation of Eq.(3.15), at the cost of retaining a large nonresonant background in the FFC spectrum. This approach, however, is out of the scope of this publication.

Extracting information on the target response from the diagonal structures in the FFC spectrum

As a result of Eq. (3.18), the target can be characterized via the diagonal structures in the FFC spectrum in two different ways. First, the diagonals are governed by the relation

$$\nu(\Delta) = \pm(\Delta - \omega_t + \omega_a) , \tag{3.19}$$

which defines lines in the ν-Δ-plane with slope ± 1 and offset $\pm(\omega_a - \omega_t)$. Thus, upon extrapolating the diagonals in the FFC spectrum, they both cross the $\nu = 0$ coordinate axis at $\Delta = \omega_t - \omega_a$, and thereby provide access to the target transition frequency. Note that this argument generalizes to multiple target transitions as discussed below.

Second, one may analyze the spectral shape of the diagonals in the FFC spectrum as function of Δ or ν. From Eq. (3.18) it follows that in both cases, this shape corresponds to the desired shape of the nuclear resonant target response. Note that the FFC spectrum is complex-valued, and thereby provides access to the amplitude and the phase of the resonant response $\hat{S}_t$. This "phase problem" of extracting the phase of a target response is an ubiquitous problem in spectroscopy, imaging and diffraction experiments [ANM11; Tay03; Stu01; Cal+05].

Both approaches will be discussed in Sec. 3.3. There, the more realistic situation with a finite analyzer width in Eq. (3.15) will be considered. Then, the target spectrum is broadened and modified in amplitude through the correlation with the analyzer spectrum. Therefore, in practice, analyzers with a spectrum narrow as compared to the desired target spectrum should be employed. Further, different horizontal and vertical cuts through the diagonals can be combined in order to reduce uncertainties in the recovery of the target response.

Horizontal structures in the FFC spectrum

The horizontal lines appearing in the FFC spectrum (c.f. Fig. 3.2) can be attributed to a beating of light scattered on target transitions with different resonance frequencies. The different scattering channels interfere due to the coherent nature of the scattering, giving rise to the so-called quantum beats [Smi99; HT99a; Röh04]. As in the case of the diagonal structures in the FFC spectrum, the Fourier-transform of the time- and frequency resolved intensity of this beating pattern will peak whenever the Fourier frequency ν equals one of the detunings between a pair of interfering hyperfine transitions (Fig.3.2 (b)). Note, however, that not all detunings between hyperfine transitions, which are indicated in Fig.3.2 (c), appear as horizontal lines in the spectrum. This is due to the fact that in our calculation the sample is irradiated by an unpolarized beam and the hyperfine field is oriented perpendicularly to the beam direction. Hence, photons scattered off the $\Delta m = 0$ and $\Delta m = \pm 1$ are orthogonally polarized and do not interfere with each other (cf. [SBH99]) and thus the corresponding peaks/lines do not appear in Fig.3.2.

3.3 Analysis of the diagonal structure

In the previous Sec. 3.2.5, we have shown that the diagonal structure in the FFC spectrum is formed by correlations of analyzer and target responses centered around positions $\nu(\Delta) = \pm(\Delta - \omega_t + \omega_a)$. This allows for the determination of spectral target parameters by extrapolating the diagonals towards the crossing point with the ν- or Δ-axis. Furthermore, horizontal or vertical cuts through the diagonals provide access to the complex-valued nuclear resonant part of the target response function $\hat{S}_t$ (cross-correlated with the analyzer response function). In this Section, we demonstrate the practical feasibility of both of these approaches, by evaluating representative model data of nuclear forward scattering targets and thin-film cavities.

3.3.1 Computational details on the analysis

The model data evaluated in this Section are calculated using the software package PYNUSS [Hee19], which features methods to evaluate Nuclear Forward Scattering and cavity reflection spectra, similar to the software package CONUSS [Stu00a], but is written in the language Python [VRD09] and features substantial extensions for the analysis of quantum optical applications in Nuclear Resonant Scattering. In PYNUSS, forward scattering and cavity reflection spectra are calculated using the transfer matrix and layer formalism, respectively [Röh04; Stu00a]. Our model system is the Mössbauer isotope ^{57}Fe with transition energy $\hbar\omega_t = 14.4$keV and single-nucleus decay rate $\hbar\gamma = 4.7$neV. As analyzer, an enriched stainless steel sample ($^{57}\mathrm{Fe}_{55}\mathrm{Cr}_{25}\mathrm{Ni}_{20}$) of thickness 1μm with the same transition frequency $\omega_a = \omega_t$ (the isomeric shift is neglected for simplicity, without loss of generality) and single-nucleus line-width is used for the calculation. Different targets will be considered in the analysis, as specified below.

Following Sec. 3.2, the diagonal analysis is then performed on the complex-valued quantity

$$\mathcal{I}_{\mathrm{bc}}(\nu, \Delta) = \mathcal{F}\left[\left(I(t,\Delta) - |\alpha_t|^2 I_a(t) - |\alpha_a|^2 I_t(t)\right)\Theta(t - t_1)\right] , \tag{3.20}$$

where $I(t,\Delta)$ is the experimentally accessible time- and frequency-resolved intensity, $I_a(t)$ and $I_t(t)$ are the individual time-spectra of analyzer and target, respectively, and α_a, α_t the prefactors describing electronic absorption. Compared to the discussion of the FFC spectrum in the Sec. 3.2, these two terms correspond to the single-stage contributions $\hat{T}_t \star \hat{T}_t$ and $\hat{S}_a \star \hat{S}_a$ in the first line of Eq. (3.14) In the following discussion we will refer to $\mathcal{I}_{\mathrm{bc}}(\nu, \Delta)$ as the background-corrected FFC spectrum.

In practice, this quantity can be measured in different ways. One approach is to measure $I(t, \Delta)$, $I_a(t)$ and $I_t(t)$ separately. One then has to consider possible variations in the total number of resonant incident photons contributing to the different spectra in order to perform the subtraction. Alternatively, one can measure $I(t, \Delta)$ only, and then determine the Δ-independent background to be subtracted directly in the FFC spectrum in regions far away from the diagonal structures. This latter approach will be discussed in more detail in Sec. 3.4.

As discussed in Sec. 3.2.3, the background correction in Eq. (3.20) removes the horizontal lines and low-frequency background as shown in Fig. 3.2. Further, the Heaviside Θ-function serves to exclude the first few nanoseconds of the recorded intensity after the nuclear excitation, mainly for two reasons: First, from a theoretical point of view, it is desirable to exclude the contribution from the prompt pulse from the analysis since it is orders of magnitude more intense than the nuclear resonant response and thus leads to a large background in the Fourier spectrum. This lower cutoff can, in principle, be set during data evaluation if the spectrum has been measured reliably at all times. However, the second reason for rejecting the intensity at early times is the fact that the prompt radiation leads to a detector overload during the first few nanoseconds after pulse arrival. Thus, typically the first few ns are not available for data evaluation. Throughout the analysis, we will first consider the ideal case with all times available for data analysis and then discuss the effect of a finite measurement time range in Sec. 3.3.4.

Regarding the discussion of the FFC spectrum and diagonal structure around Eq. (3.14) and Eq. (3.15), the background removal via the time-gating $\Theta(t-t_1)$ in Eq.(3.20) removes the off-resonant

Table 3.1: Magnetic hyperfine splittings of ^{57}Fe extracted using the line fits to the off-resonant FFC spectrum's diagonal structures. The results compare results with and without optimization of the fit range, and corresponding data for two different time gatings. The first column indicates reference values obtained from a calculation using PYNUSS. All results are given in units of the single-nucleus line-width γ.

PYNUSS Ref.	Off-resonant	Off-resonant (opt.)	Gating (20ns)	Gating (40ns)
8.7596	8.652(25)	8.719(12)	8.83(32)	9.32(39)
32.0605	31.956(27)	32.053(17)	32.35 (51)	32.32(52)
55.3406	55.159(42)	55.267(15)	56.00(55)	55.1(1.1)

background proportional to $|\alpha_t|^2$ in the second line of Eq. (3.14) (for details, the reader is referred to the discussion in Sec. 3.2.3) and thus the background-corrected FFC spectrum is expected to be described well by Eq. (3.15) in the large analyzer-target detuning limit, which will be exploited to reconstruct the complex-valued nuclear resonant target response in Sec. 3.3.3.

3.3.2 Extracting spectral parameters via linear fits to the diagonal structure

We start by performing linear fits to the diagonal structure, which we then extrapolate towards the crossing points with the ν- or Δ-axes, in order to extract spectral information on the target such as resonance energies. In spectroscopic applications of Nuclear Resonant Scattering, the spectra often feature multiple splitted, broadened and shifted resonances, e.g., due to magnetic or electric hyperfine fields. In such a multi-resonance case, the condition Eq. (3.19) generalizes to

$$\nu_j(\Delta) = \pm(\Delta - \omega_{\text{hf}}^{(j)} + \omega_a) \tag{3.21}$$

with slope ± 1 and points of intersection $(\omega_a - \omega_{\text{hf}}^{(j)})$ with the ν-axis for each transition resonance frequency $\omega_{\text{hf}}^{(j)}$ separately. In order to extract these resonance frequencies via linear fits to the diagonal structures in the FFC spectrum, one has to determine points along the diagonals through which the lines should be fitted. In the following, we discuss two approaches to perform such linear fits, based on horizontal or vertical sections through the FFC spectrum. Note that in both cases, each resonance frequency $\omega_{\text{hf}}^{(j)}$ is obtained via a fit of a diagonal line with the offset as the single free parameter, which combines data over a broad range of detunings values, thereby reducing the detrimental effect of statistical or systematic uncertainties. These fits do not require prior knowledge about the target systems, and in this sense are model-independent. This suggests the diagonal analysis of FFC spectra as a versatile spectroscopic technique at pulsed x-ray sources.

As a specific example, we extract the magnetic hyperfine splittings of ^{57}Fe with internal hyperfine field $B = 33.3$T from the FFC spectra. As a reference to compare the linear fit results to, we determine the three positive hyperfine transition frequencies as peak maxima of the nuclear resonant target spectrum calculated with PYNUSS for a 0.3µm thin target foil. The results are tabulated as a function of the single-nucleus line-width γ in Table 3.1 in the column "PYNUSS Ref.".

Figure 3.3(a) shows the real part of the background-corrected FFC spectrum of a 2μm thick α–^{57}Fe foil irradiated by linearly polarized light in forward scattering geometry as given in Eq. (3.20). The magnetic hyperfine field is oriented perpendicular to the beam propagation direction and tilted by an angle of 45 degrees with respect to the beam polarization axis to ensure that all hyperfine transitions are adressed during the scattering process. In computing the FFC spectrum, we first consider the ideal case, by including intensities from times slightly after the x-ray excitation in order to suppress the prompt non-resonant contribution, up to measurement times larger than $10\gamma^{-1}$ to ensure high resolution along the ν-axis. The effect of more restricted measurement time intervals will be discussed in Sec. 3.3.4 below. Further, we choose the real part of the (complex-valued) FFC spectrum for the peak evaluation since it is more symmetric and spectrally narrower than its absolute value, as the imaginary part features a broad asymmetric line shape.

Vertical cuts along the ν-axis

The first approach employs vertical cuts along the ν-axis through the FFC spectrum. As an example, we analyze diagonals with positive slope. In order to avoid spectral overlap with diagonals of negative slope, we restrict the analysis to detunings Δ which are larger in magnitude than the outermost crossing point of the diagonals with the $\nu = 0$ axis, as indicated by the red diagonal lines in Fig. 3.3(a). For each such Δ, we analyze a vertical cut through the diagonal structure in the FFC spectrum, as exemplified by the yellow line in Fig. 3.3(a). The section corresponding to the yellow line in (a) is shown in (b), which shows that the maxima of the different diagonals are clearly resolved. The respective lines formed by these maxima across different detunings are then linearly fitted with a fixed slope of 1 and offset b. The detuning range considered for the linear fits is indicated by the red lines in Fig.3.3(a), which represent the result of the linear fits. The fit parameters then allow one to determine the transition frequencies $\omega_{\mathrm{hf}}^{(j)}$ relative to the resonance frequency ω_a of the analyzer via Eq. (3.21).

The results of this analysis for the three positive-valued hyperfine splittings $\Delta\omega$ together with the corresponding fit errors are given in Table 3.1 in the column "Off-resonant". In order to check for residual effects of resonant contributions on the diagonal structure at small detunings, we further repeated the above analysis for different Δ fit ranges. To this end, we evaluated 20 fits $j \in \{1, 2, \ldots, 20\}$ in which the first $5j$ datapoints (stepsize $\delta\Delta = 0.5\gamma$) with the lowest detunings Δ were excluded. Out of those 20 fits, we then chose the one with the lowest fit error as the optimized result. The results of this procedure are shown in column "Off-resonant (opt.)" in Table 3.1. The comparison of the unoptimized and optimized off-resonant fit results with the corresponding theory reference values shows a good agreement within a 2% margin of the relative error which demonstrates the feasibility of spectral parameter determination from the diagonal structure. Further, the optimized result yields lower fit errors and more accurate results indicating that there indeed is a residual effect of resonant (e.g., radiative coupling) effects or the negative-slope diagonal branches on the positive-slope diagonal structure close to $\Delta = 0$.

Horizontal cuts along the Δ-axis

Alternatively, an analogous second approach based on horizontal cuts along the Δ-axis is possible. This approach can be advantageous in case of finite measurement time range for the time-dependent intensity imposed by experimental constraints such as the pulse structure of the x-ray source. The reason is that this time range determines the frequency resolution along the ν axis in the FFC spectrum. If this resolution becomes too coarse due to the experimental limitations, then an accurate determination of the maxima along the vertical sections may be challenging. An example for this will be discussed in Sec. 3.3.4. In contrast, the resolution along the horizontal Δ-axis is determined by the Mössbauer drive, and can be chosen independent of the pulsed x-ray source characteristics. For an analysis along the Δ-axis, smaller detunings Δ should be avoided since they may be perturbed by resonant effects such as the radiative coupling of analyzer and target. Further, also the tails of the negative-slope diagonal structure branch may lead to a slight asymmetry of the positive-slope branch and vice versa at low Δ. In practice, it is possible to perform both the horizontal and the vertical cut analysis on the same data set, and to compare the results for a consistency check.

Summarizing this part on extracting spectral parameters, we conclude that the results of the analysis underpin the theoretical explanation of the diagonal structure given in Sec. 3.2.2 and provide us with an intuitive and simple way of determining the spectral structure of nuclear targets from FFC spectra.

3.3.3 Extracting the resonant target response function via sections through the diagonal structure

In this Subsection, we consider the second method to extract information from the diagonal structure in the FFC spectrum, by making use of the fact that horizontal or vertical cuts through the diagonals in the limit of large analyzer-target detuning provide access to the complex-valued resonant target response function. In the large analyzer-target detuning and thin-analyzer limit, this follows from Eq. (3.18), which states that the FFC spectrum is expected to be essentially proportional to the desired nuclear resonant part of the target response. For thicker analyzers, this result generalizes to Eq. (3.15), which shows that then the FFC spectrum is determined by the cross-correlation between nuclear resonant part of the target response and analyzer response.

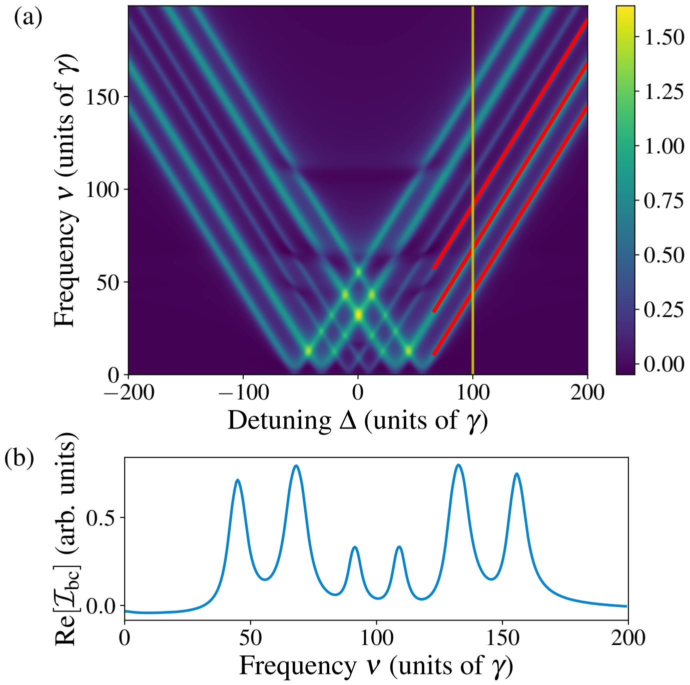

Figure 3.3: Extraction of spectral parameters via linear fits to the diagonal structure. (a) shows the real part of the FFC spectrum for a 2μm thick α-iron enriched in ^{57}Fe probed in Nuclear Forward Scattering (see main text for details). The analyzer is a stainless steel foil as described in the main text. The diagonal structure is clearly visible. The line fits used to extract the resonance positions are marked in red. (b) shows a vertical cut through (a) at a detuning $\Delta = 100\gamma$. This detuning is indicated by the yellow vertical line in (a). The six resonances of the magnetically split α-Fe spectrum can clearly be distinguished.

Extraction of the complex-valued resonant target response function in nuclear forward scattering

As a first example, we consider the same target and analyzer configuration as in Sec. 3.3.2. To this end, as the reference, we calculate the nuclear resonant target response $\hat{S}_t(\Delta)$ alone using Pynuss. Figure 3.4(a) shows the desired energy spectrum $|\hat{S}_t(\Delta)|^2$ obtained with this calculation.

Our goal then is to determine the complex-valued nuclear target response $\hat{S}_t(\Delta)$ itself from the experimentally accessible FFC spectrum which, in turn, is complex-valued as the Fourier transform of the time- and frequency-resolved intensity. Following Eq. (3.15), in the large target-analyzer detuning case, the complex-valued FFC spectrum corresponds to $\hat{S}_t(\Delta)$, cross-correlated with the analyzer response $\hat{S}_a(\Delta)$. In order to verify this prediction, we show the absolute value of a vertical cut through the FFC spectrum at $\Delta = 100\gamma$ as the dashed blue line in Fig. 3.4(b). The black solid line shows the absolute value of the cross-correlated nuclear target response $\hat{S}_t(\Delta)$, according to Eq. (3.15), obtained from the reference calculation using Pynuss. It can be seen that the two curves agree very well.

The corresponding results for the phase of the cross-correlated $\hat{S}_t(\Delta)$ are shown in Fig. 3.4(c). Again, the two curves agree well, except for lower frequencies ν, where the phase of the FFC spectrum deviates from the reference calculation. This deviation can be attributed to resonant couplings between target and analyzer which lead to a low-frequency background at lower ν. It shows that resonant effects do also affect the spectral shape of vertical sections through the FFC spectrum and suggests that small values of ν should be avoided as well. The influence of this defect can be reduced by choosing larger detunings Δ for the vertical cut, such that the relevant part of the target spectrum moves away from lower ν values.

The effect of the cross-correlation of the desired target response with the analyzer response in the FFC spectrum can be seen in the comparison of Fig. 3.4(a) and (b). The resonances in the spectrum in Fig. 3.4(a) exhibit so-called double-hump profiles, which is a well-known effect in thicker targets (see, e.g., [Smi99]). In contrast, these effects are not visible in (b) due to the cross-correlation with the analyzer response, which broadens the observed spectrum.

Overall, we find that the FFC spectrum indeed provides access to the complex-valued nuclear

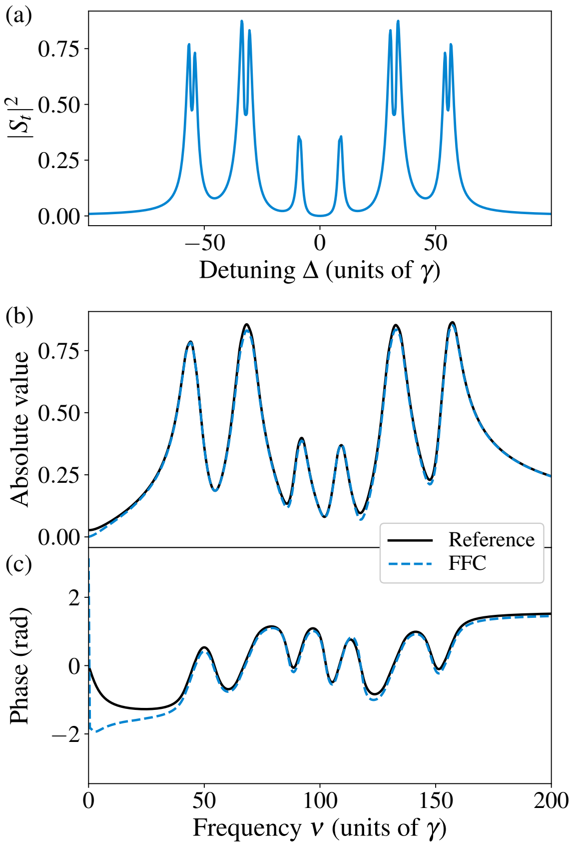

Figure 3.4: Extraction of the target response function. Results are shown for a target and analyzer configuration as in Fig. 3.3. (a) shows the true nuclear resonant target spectrum without analyzer as a reference, evaluated using the extsc pynuss software package. (b) depicts the absolute value of a vertical cut at $\Delta = 100\gamma$ through the FFC spectrum (dashed blue line). For comparison, the absolute value of the reference nuclear resonant target response correlated with the analyzer response according to eq.(3.15) is shown as solid black line. (c) shows the corresponding phase of the two quantities in (b).

resonant target response function. The broadening due to the cross-correlation with the analyzer response again highlights the usefulness of thin analyzers, which allow one to resolve target spectra with higher spectral resolution.

Extraction of the complex-valued resonant target response function in reflection from x-ray cavities

As a second example, we discuss the recovery of the complex-valued resonant target response function for Mössbauer nuclei embedded in x-ray cavities. Similar to the forward-scattering case in the previous section, the nuclear energy spectra observed in reflection and evaluated by standard methods like the late-time integration are modified by an interference with the electronic response of the cavity structure [Röh04]. This interference is particularly prominent in the cavity case, since it depends on the x-ray incidence angle around the cavity resonance, and may lead to a full response with an asymmetric Fano profile [Hee+15a]. For this reason, the extraction of the nuclear response, unperturbed by the electronic cavity response, from the FFC spectrum is of particular relevance for the field of nuclear quantum optics, as discussed below.

For the cavity settings, all calculations are performed using the software package Pynuss [Hee19], which uses the layer formalism [Röh04] to calculate the full (resonant and nonresonant) response, see Sec. 3.3.1. As our model system, we use a thin-film cavity with layer structure 2.2nm Pt/10nm C/0.6nm ^{57}Fe/10nm C/ Pt from top to bottom probed by near-resonant x-rays in grazing incidence (cf. Fig. 3.1). Here, the last Pt layer is assumed to be sufficiently thick to prevent any transmission through this layer. Due to the low thickness of the Fe layer, magnetic long-range order is absent, and the nuclei do not experience a magnetic hyperfine field. As a result, no magnetic splitting appears in the spectra. Fig. 3.5 shows the background-corrected FFC spectrum of such a cavity at incidence

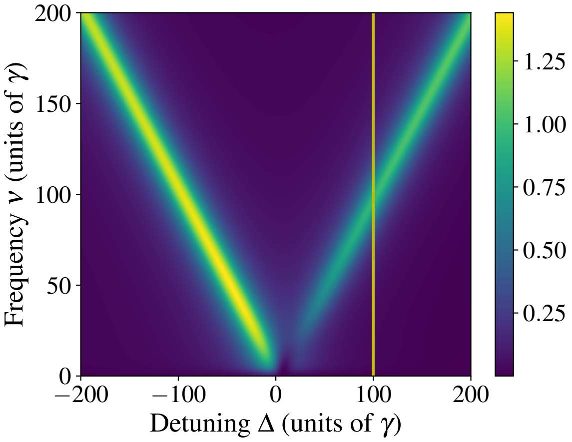

Figure 3.5: Extraction of the complex-valued target response function in reflection for Mössbauer nuclei embedded in a thin-film cavity. The Figure shows the absolute value squared of the background-corrected FFC spectrum as given in Eq. (3.20) with the intensity at time zero set to zero. The cavity structure is 2.2nm Pt/10nm C/0.6nm ^{57}Fe/10nm C/ Pt (layer structure from the top to the bottom), and the probing x-rays impinge at a fixed incidence angle $\theta = 2.8$mrad. In comparison to Fig. 3.3(a), the single-line nature of the nuclear response is clearly visible, as well as an asymmetry of the spectrum around $\Delta = 0$. The yellow vertical line indicates the cut at $\Delta = 100\gamma$ used in the further analysis.

angle $\theta = 2.8$mrad, specifically, the absolute value squared of the quantity given in Eq. (3.20) with the intensity at time zero set to zero.

In contrast to forward scattering, the electronic response of the cavity is different in that it also has a resonance structure, due to the different modes of the cavity. As a result, the magnitude of the off-resonant electronic background observed in reflection varies with the x-rays incidence angle around the cavity resonance, as the variation in the angle effectively scans the incident light frequency across the cavity resonance. On the other hand, a variation of the incidence angle also leads to a relative phase between the electronic and the nuclear response, such that the Lorentzian response of the nuclei appears as Fano line shapes in the total cavity response [Hee+15a] (for details, see Appendix A.2). Both effects are clearly visible in Fig. 3.6(a), which shows reference cavity spectra evaluated using pynuss for different incidence angles. The nuclear response corresponds to the spectral Fano structures around $\Delta = 0$. The off-resonant electronic background becomes visible at large detunings $|\Delta| \gg \gamma$ away from the nuclear resonance.

In Fig. 3.6(b), we show the corresponding nuclear target responses reconstructed via vertical cuts through the FFC spectrum, as illustrated in Fig. 3.5 for one particular incidence angle. In contrast to the reference spectra in (a), in all cases, the reconstructed resonances are of Lorentzian shape, and the off-resonant background is low. In the following, we will show that this difference to Fig. 3.6(a) is due to the fact that the recovery via the FFC spectrum determines the target response function independent of the electronic scattering contribution. As a result, no off-resonant background contributes, and the nuclear line shape is observed in its original Lorentzian form. We note that this is a qualitative difference to the standard late-time integration method for measuring energy spectra of cavity targets, which does not provide access to the nuclear response alone.

As a first approach to verifying the recovery of the nuclear target response alone, we exploit that the resonances for the various incidence angles in Fig. 3.6(b) differ in line-width and center frequency. The variations of the line-width with the incidence angle in Fig. 3.6(b) are known in the literature as superradiance γ_s [Dic54; GH82; Gar11; Röh+10; Chu+18; HT99a; LHH60a; KAK79; GRK17] and the variations in the resonance position are related to the collective Lamb shift Δ_{CLS} [Röh+10; LKE16a; SS89a; FHM73; Scu09b; RJ16; Kea+12; Pey+18; Roo+16; Bro+16]. They are of particular relevance, since the manipulation of the resonance properties via these collective effects forms the basis for the implementation of more advanced quantum optical level schemes with nuclei [Röh+12; HE13; Hee+13; Hee+15c; Hab+16; Hab+17; Len+20; KCP20a; DLE22b; DLE22a; RE21b].

In the ideal two-level case, the nuclear response comprises a single Lorentzian [HE13; Len+20; KCP20a] which can be characterized by the parameters γ_s and Δ_{CLS} only. In the following, we therefore show that these nuclear parameters can be determined from FFC spectra, and thereby the nuclear response. To this end, we employ a fit model to extract γ_s and Δ_{CLS} from cuts through the

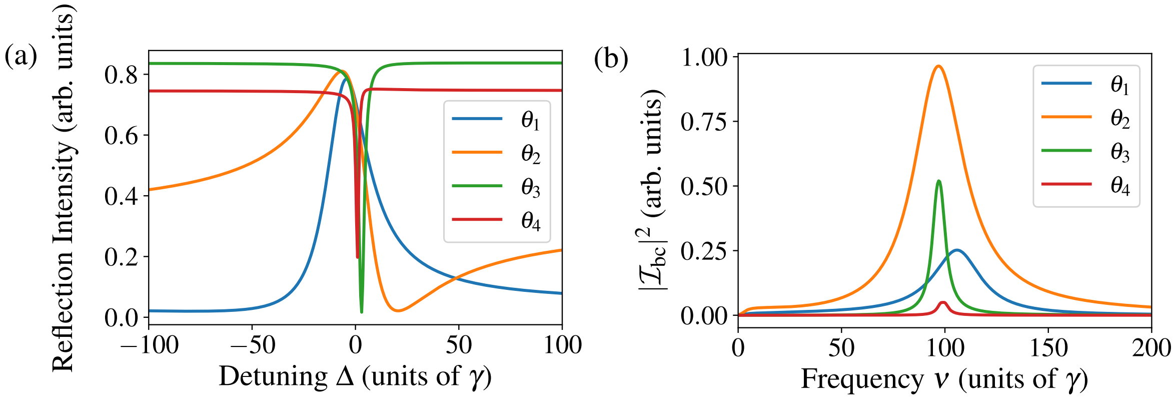

Figure 3.6: Cavity spectra for different x-ray incidence angles $\theta_1 = 2.75$mrad, $\theta_2 = 2.8$mrad, $\theta_3 = 3.0$mrad and $\theta_4 = 3.3$mrad. (a) shows full reference cavity reflection spectra calculated using the software package Pynuss. The effect of the electronic scattering on the cavity structure is clearly visible in the off-resonant background varying with the incidence angle, and in the modification of the Lorentzian nuclear response into a Fano line profile. (b) shows the nuclear target response recovered from the FFC spectrum by vertical sections at $\Delta = 100\gamma$ (cf. yellow line in Fig. 3.5). These spectra are not affected by the electronic scattering on the cavity, and therefore remain of Lorentzian shape for all incidence angles. Therefore, the dependence of the superradiant line broadening and the resonance energy shift on the incidence angle become clearly visible.

FFC spectra (details on the fit model are provided in Appendix A.2). For Δ_{CLS}, we alternatively use a simple determination of the maxima of the cuts through the FFC spectrum, similar to the resonance determination in Sec. 3.3.3.

The results are shown in Fig. 3.7. Panel (a) shows the shift Δ_{CLS} of the resonance energy as function of the incidence angle θ. The red dashed line depicts the parameters extracted via the fit to the cut through the FFC spectrum. Results from the simple maxima determination are shown as the green dashed line. In comparison, the black solid line shows the corresponding values obtained via Fano line fits to the reference cavity spectra in Fig. 3.6(a) calculated using Pynuss. It can be seen that the overall agreement of all curves is good across the entire angular range. At two incidence angles, around $\theta \approx 2.5$mrad and $\theta \approx 3.1$mrad, the simple maxima determination method suffers slightly larger deviations from the other two curves. This deviation can be traced back to uncertainties in the maxima determination because of the residual double-hump spectrum of the analyzer, which becomes relevant since the line-width of the cavity falls below the effective analyzer width at off-resonant angles and thus the shape of the analyzer response dominates the cross-correlation of both response functions.

Fig. 3.7(b) shows corresponding results for the collectively-enhanced total decay rate $\Gamma_c = (\gamma + \gamma_s)/2$ as function of the incidence angle θ. As expected [HT99a; SS89a; Röh+10; LKE16a], the superradiance is highest close to the cavity resonance. Again, the agreement between results extracted from the FFC spectrum to the reference calculations is good. Towards off-resonant incidence angles, the line-width extracted from the FFC spectrum saturates to a value slightly larger than that of the reference spectra. The reason for this is the convolution with the analyzer response, which sets a lower limit to the line-width in the FFC spectrum. In contrast, the resonance position in Fig. 3.7(a) is not affected by the broadening due to the cross-correlation with the analyzer response.

Determination of the complex-valued nuclear response of an EIT cavity

Next, we demonstrate that the FFC spectrum also provides direct access to the complex-valued nuclear response of a more complex cavity structure, using the relevant example of a cavity featuring electromagnetically-induced transparency (EIT) [FIM05; Röh+12; Len+20]. More specifically, we consider a layer structure Pd(1.5nm)/ B_4C(49.8nm)/ ^{57}Fe(0.57nm)/ B_4C(97.1nm)/ ^{57}Fe(0.57nm)/ B_4C(35.4nm)/ Pd(43.7nm)/ Si at incidence angle $\theta = 2.28$mrad, as it was discussed in [DLE22a].

To recover the nuclear resonant target response from the diagonal structure, we consider vertical cuts through the FFC spectrum at $\Delta = -200\gamma$, and show the corresponding real and imaginary parts in Fig. 3.8. As a reference, the figure further shows the cross-correlation between the resonant target and analyzer responses calculated using Pynuss, i.e., it does not contain contributions from the electronic response of the cavity. As in the forward scattering case, the spectral shape of both

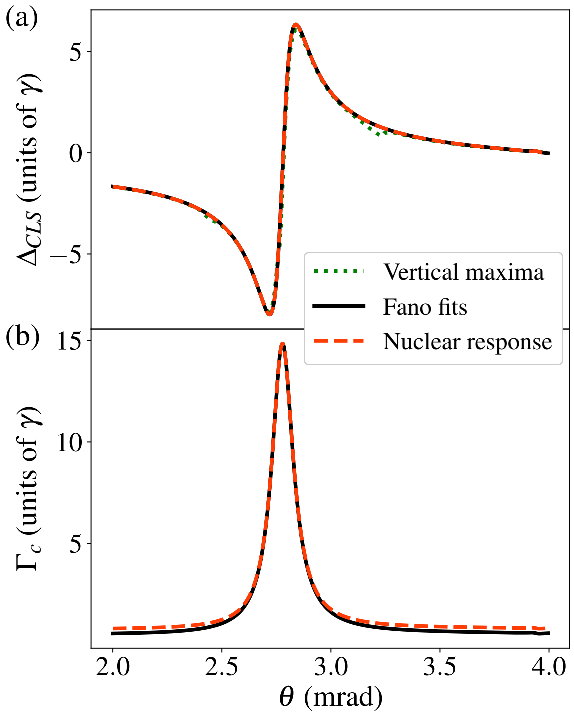

Figure 3.7: Collective nuclear parameters of the two-level system realized by the cavity structure in Fig. 3.5. (a) shows the energy shift of the nuclear resonance related to the collective Lamb shift as function of the x-ray incidence angle, and (b) the corresponding superradiantly enhanced decay rate. The red dashed lines are the recovery results obtained from fitting a model to the FFC spectrum (see main text for details). The green dashed line in (a) is obtained using a simple maximum determination. As a reference, the solid black line shows the parameters obtained via a Fano line fit to the reference cavity spectrum calculated using Pynuss.

real and imaginary part is reproduced well by the FFC spectrum, and we again find that the FFC spectrum calculated from the diagonal spectra provides direct access to the complex-valued nuclear target response. Note, that evaluation of the FFC spectrum at larger detunings Δ compared to the discussion in Sec. 3.3.3 reduces the low-frequency background that impedes the full response reconstruction in the forward scattering case Fig. 3.4.

To summarize the results of Sec. 3.3.3, we showed that the complex-valued target response function can be recovered from the FFC spectrum in the case of nuclear forward scattering as well as in the case of reflection from a cavity. In the latter case, it is important to note that the method presented here indeed provides access to the complex-valued nuclear target spectrum, independent of the background of and interference with possible electronic scattering channels usually present in the cavity reflection spectra. This is a key difference to other spectroscopy techniques such as the late-time integration, which retrieve the absolute value of the total cavity reflection spectrum. The possibility to access the complex-valued nuclear response alone is of considerable interest for the further development of nuclear cavity QED, as discussed in [DLE22a], since the spectra corresponding to the nuclear response relate to the quantum optical level scheme governing the nuclear dynamics inside the cavity. Furthermore, from the recovered spectra, also the collectively-modified quantum optical level scheme parameters can be extracted. Therefore, the techniques presented here are expected to fuel further developments in nuclear quantum optics.

3.3.4 Finite Gating Times

Both, the theoretical discussion and the numerical results presented so far have assumed the ideal case of all times from arrival of the prompt pulse at $t_1 = 0$ at the detector until a time $t_2 \gg 1/\gamma$, where practically all primary and secondary radiation has decayed, being available for data analysis. However, under realistic experimental conditions the first nanoseconds after pulse arrival can not be used for reliable data evaluation due to detector overload caused by the large intensities of the prompt radiation produced by accelerator-based light sources (cf.[R.C+00]). On the other hand, repetition rates of these light sources set an upper limit to recording time after pulse arrival before the next

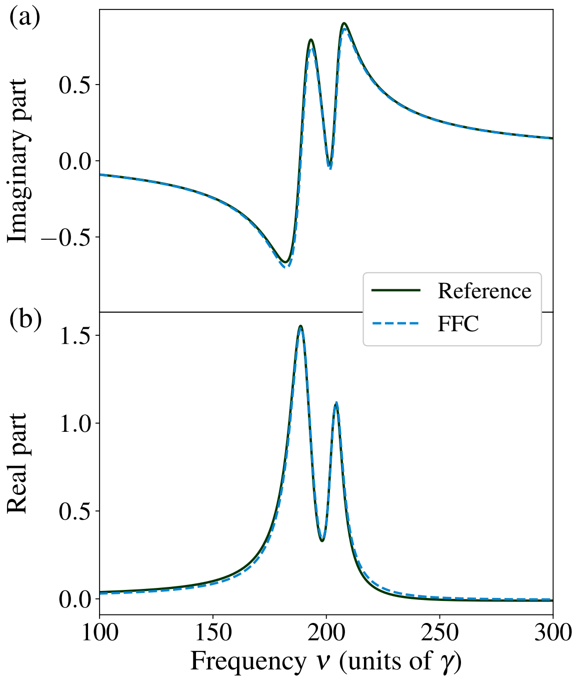

Figure 3.8: Extraction of the nuclear response of a cavity-target probed in reflection. The figure shows the (a) real (b) imaginary parts of a cut through the diagonal structure in the FFC spectrum along the ν axis at detuning $\Delta = -200\gamma$ (dashed blue curves). The solid black lines show the corresponding cross-correlation of the nuclear resonant responses of cavity and analyzer as given by Eq. (3.15) as a reference. The dip in the spectra is an electromagnetically induced transparency feature. The cavity layer structure is Pd(1.5nm)/ B_4C(49.8nm)/ ^{57}Fe(0.57nm)/ B_4C(97.1nm)/ ^{57}Fe(0.57nm)/ B_4C(35.4nm)/ Pd(43.7nm)/ Si, and the x-ray incidence angle is $\theta = 2.28$mrad.

bunch hits the target and detector (cf. [Röh04]). To understand the effect of these restrictions on the FFC spectra, we first reconsider the theoretical derivation of the Fourier-transformed time- and frequency-resolved intensity given in section 3.2.2 by introducing finite integration boundaries and, subsequently, discuss the applicability of diagonal analysis of magnetic hyperfine splitting in ^{57}Fe under these circumstances.

Theoretical analysis

For the theoretical discussion, we formally introduce Heaviside Θ-functions excluding the interval $[-t_1, t_1]$ and times above t_2 as well as below $-t_2$ to ensure proper symmetry in the Fourier domain. The usual lower cutoff of the integral boundaries in the time-domain necessary for causality reasons is part of the target response, i.e. $T_t(t) \sim \Theta(t)$ (cf. Appendix A.3), and gives us this freedom in choosing the form of the gating function at negative times in order to simplify the theoretical analysis. In this case, the Fourier-transformed intensity reads

$$\begin{aligned}\mathcal{I}_{t_1,t_2}(\nu,\Delta) =& E_0^2 \int_{-\infty}^{\infty} dt e^{i\nu t} T^*(t) T(t) \Theta(|t|-t_1)\Theta(t_2-|t|)\\ =& \frac{E_0^2}{4\pi^2}\Big\{\mathcal{F}\left[\Theta(|t|-t_1)\Theta(t_2-|t|)\right] * \mathcal{F}\left[T^*T\right]\Big\}(\nu)\\ =& \frac{E_0^2}{2\pi^2}\left(\delta_{t_1,t_2} * (\hat{T}\star\hat{T})\right)(\nu) \qquad (3.22)\end{aligned}$$

where the operator $\mathcal{F}$ denotes the Fourier transform and the $(*)$ and $(\star)$ operators the convolution and cross-correlation as defined in Eqs. (3.3) and (3.4), respectively. Further, we introduced

$$\delta_{t_1,t_2}(\nu) = \frac{1}{2}\mathcal{F}\left[\Theta(|t|-t_1)\Theta(t_2-|t|)\right](\nu)$$

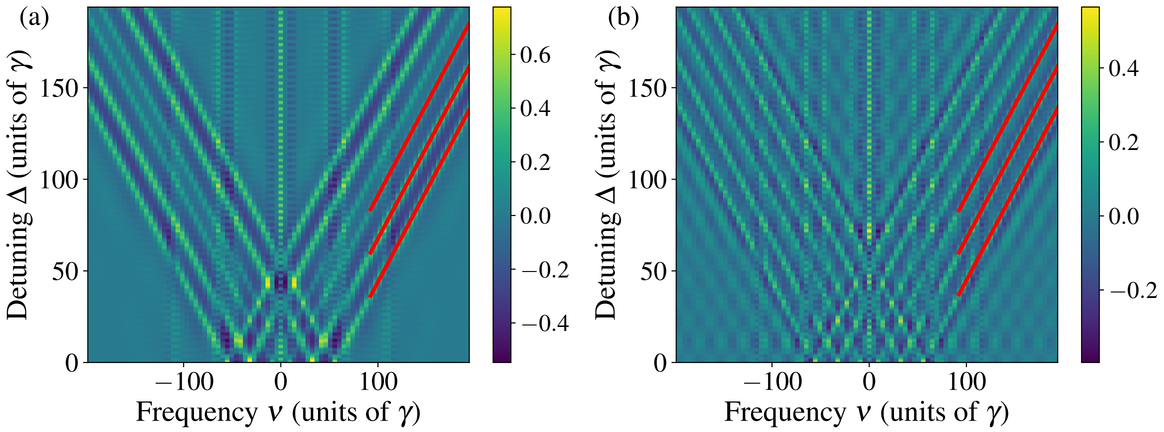

Figure 3.9: Effect of time gating on the extraction of target parameters from the diagonals in the FFC spectra. The two panels show FFC spectra as in Fig. 3.3, but with initial time vetos of (a) 20 ns and (b) 40 ns. In both cases, only times up to an upper limit of 192 ns are considered. Although the Fourier effects due to the time windows are clearly visible, the data can still be reliably fitted with lines of slope one, as indicated by the red lines.

$$= \int_{t_1}^{t_2} dt \cos(\nu t) = \frac{\sin(\nu t_2) - \sin(\nu t_1)}{\nu} \, .$$

The δ_{t_1,t_2}-function acts as a convolutional filter on the autocorrelation of the response $\hat{T}$ of the complete setup, reduces frequency resolution by virtue of the upper integration boundary t_2 and leads to additional oscillations in the final spectrum characteristic of the chosen time-window $[t_1, t_2]$ (cf. [R.C+00; HE20]). In principle, these oscillations can be reduced by different means, e.g., experimentally by using crossed polarizer-analyzer setups (cf. [Toe+95]), by choosing sufficiently late lower cutoff times t_1 (late-time integration) [Röh+10; Hee+15a] (see also Appendix A.1), by smoothing the time window of the lower cutoff during data evaluation [Cal+05], or by stroboscopic detection techniques [Cal+02; Cal+03]. Furthermore, event-based data acquisition providing access to time- and frequency-resolved two-dimensional datasets allow one to choose and optimize the integration limits after the experiment throughout the data analysis [Hee+17; Hee+21]. There are also established deconvolution techniques which, however, face the challenge that the filter function δ_{t_1,t_2} is zero outside the time range $[t_1, t_2]$.

Finally, we note that the time-gated expression Eq. (3.22) is consistent with the previous results without time-gating, since

$$\delta_{t_1,t_2}(\nu) \xrightarrow[t_2\to\infty]{t_1\to 0} \pi\delta(\nu) \tag{3.23}$$

in the limit of vanishing time gating, where $\delta(\nu)$ is the Dirac delta distribution. Then, Eq. (3.22) reduces to Eq. (3.10).

Effect of temporal gating on the analysis of diagonal spectra

After having derived the expression for the FFC spectrum in the presence of gating, we now consider the effect of the gating on the diagonal spectra analysis. For this, we again analyze our example of the magnetic hyperfine splitting in ^{57}Fe as described in Section 3.3.2, using spectra calculated according to Eq. (3.20) with lower gating times $t_1 = 20$ns, 40ns and upper integration time $t_2 = 192$ns. The latter upper integration limit corresponds to a typical time windows in experiments performed in the 40-bunch mode at the P01 High Resolution Dynamics Beamline [Wil+10] at the synchrotron-radiation facility PETRA III [Pet]. The results are shown in Fig. 3.9 and Table 3.1. It can be seen that the resolution in Fourier space along the ν axis is decreased by lowering the upper boundary t_2. In addition to the lower resolution introduced via t_2, well-known periodic structures distort the spectra, an effect that is stronger in the case of the higher lower integration boundary $t_1 = 40$ns due to the stronger truncation of the Fourier transform along the time axis. Further, the visibility of the diagonal structures reduces with increasing t_1 such that the spectra become difficult to analyze for gating times larger than $t_1 = 40$ns.

To overcome these limitations due to the gating, we applied the analysis procedure introduced in Sec. 3.3.2 to cuts through the diagonal structure along the Δ axis, which does not suffer from the reduced resolution, as discussed in Sec. 3.3.2. For this reason, the $\Delta-$ and ν-axes are interchanged in Fig. 3.9 as compared to Fig. 3.3(a). We found that the line fits marked as red lines in Fig. 3.9 still could be performed reliably, and the hyperfine splittings obtained from the crossing points with the ν-axis given in Table I under "Gating (20ns)" and "Gating (40ns)" are accurate up to relative errors in the few percent range.

We therefore conclude that the peak analysis of the background-corrected FFC spectra involving vertical or horizontal cuts through the diagonal structure combined with line fits through the series of found peaks allows one to recover the nuclear target parameters via time- and frequency-resolved Nuclear Resonant Scattering spectra even in the presence of considerable time gatings constraining the measurement. Furthermore, a direct analysis of single cuts allows one to recover the complex-valued nuclear part of the target response, although cross-correlated with the analyzer response. This is particularly interesting for target nuclei embedded in thin-film cavities as the nuclear response provides direct access to the underlying quantum optical level scheme, independent of the usual interference with nonresonant electronic scattering off of the cavity structure. In this sense, our method is complementary to existing analysis methods which provide access to the complete (resonant and nonresonant) cavity response, thereby rendering the retrieval of the pure nuclear response more difficult.

3.4 Analysis of the FFC spectrum beyond the large target-analyzer detuning limit using phase control

In Sec. 3.2.2 we exploited that some of the different scattering pathways contributing to the total detection signal (see Fig. 3.1) can be approximately isolated from the others in the large-detuning limit between target and analyzer. This formed the basis for the off-resonant spectral analysis methods discussed in the present work and the previous literature (cf. Sec. 3.2.4). However, this approach faces several drawbacks. On the one hand, it fails in spectral regions where resonant and off-resonant contributions to the signal overlap, thereby excluding the possibility to study resonant effects such as radiative couplings between targets and related target-analyzer correlation effects. On the other hand, only a restricted Δ range of the diagonal spectra can be used for the off-resonant analysis, since these overlapping parts cannot be disentangled close to resonance using the previously described recording and analysis scheme. Motivated by this, in this Section, we discuss a more sophisticated method to separate the total detection signal into its various contributions, which is based on a phase control of the analyzer response. We demonstrate that this method can selectively remove undesired signal contributions and thus allows access to a larger amount of data, thereby improving the stability of the diagonal line fit analysis against residual resonant effects and the reconstruction of the phase-resolved nuclear target response. In the future, it may further be employed to study resonant effects that currently are discarded in the off-resonant analysis.

The basic idea of this approach is to conduct a series of measurements, systematically varying parameters that change the different scattering contributions in a controlled and unique way. Combining the different data sets then allows one to separate the different scattering contributions. For example, in the infrared to ultraviolet regime, coherent phase control of laser pulses is exploited to remove undesired scattering contributions in collinear geometry by so-called phase cycling [HZ11; Tan08; Cho08; Wit+20]. This raises the question, if similar methods could be applied in nuclear forward scattering as well. While the phase between subsequent pulses at state-of-the-art accelerator-based x-ray light sources can not be controlled, the control of the relative phase between the exciting x-ray pulse and the light scattered off of the nuclei has been demonstrated using various approaches. Examples include the rotation of the hyperfine field quantization axis [Shv+94; Shv94; Shv+96; PKE09; LPK12; WL18], mechanical displacements of the sample after the excitation [Hel+91; Vag+14; SVK13; Hee+17; Hee+21], or transient changes in the magnetic field strength [Boc+21]. In all cases, a rapid manipulation is applied to the nuclei after the initial excitation has passed the sample, such that it only affects the scattered light. Note that the latter two approaches in principle provide access to arbitrary relative phases between incident and scattered light.

In the following, we show that such phase control allows one to separate different scattering contributions without having to impose the large detuning limit or to conduct reference measurements of target and analyzer alone. To this end, we denote the controllable relative phase between incident and scattered light in the analyzer as ϕ. We consider the ideal case in which the phase is applied near-instantaneously after the initial excitation. Then, the analyzer response can be written as (cf. Appendix A.4),

$$T_a(t,\Delta,\phi) = \alpha_a \left[\delta(t) + e^{i\phi} S_a(t,\Delta)\right] \ . \tag{3.24}$$

It is well-known that the scattering off of two targets in general is not commutative [Smi+05]. In the present case, the outgoing field behind both targets takes a different form depending on whether the analyzer is placed before (subscript 1) or behind (subscript 2) the target in the beam propagation direction (for details, see Appendix A.4):

$$E_1(t,\Delta,\phi) = E_0\alpha_a\alpha_t \left[\delta(t) + e^{i\phi}S_a(t,\Delta) + S_t(t) + e^{i\phi}S_{a,t}(t,\Delta)\right] \ , \tag{3.25}$$

$$E_2(t,\Delta,\phi) = E_0\alpha_a\alpha_t \left[\delta(t) + e^{i\phi}S_a(t,\Delta) + S_t(t) + S_{a,t}(t,\Delta)\right] \ . \tag{3.26}$$

In these expressions,

$$S_{a,t}(t,\Delta) = \int_{-\infty}^{\infty} d\omega e^{-i\omega t} S_a(\omega,\Delta) S_t(\omega) \tag{3.27}$$

describes the radiative coupling between analyzer and target in the time domain. In particular, the radiative coupling contribution to the outgoing field depends on the ordering of analyzer and target, since the controllable phase only affects the coupling term if the analyzer is placed in front of the target (case 1). The reason is that in the reverse ordering (case 2), the analyzer phase change is already completed before the scattered light from the upstream target reaches the analyzer, such that no relative phases appear in the coupling term.

The time- and frequency-resolved intensity for the two orderings then evaluate to

$$I_1(t,\Delta,\phi) = I_b + 2I_0^{\mathrm{NR}}\mathrm{Re}\left[e^{i\phi}S_t^*S_a + e^{i\phi}S_t^*S_{a,t} + S_a^*S_{a,t}\right] \ , \tag{3.28a}$$

$$I_2(t,\Delta,\phi) = I_b + 2I_0^{\mathrm{NR}}\mathrm{Re}\left[e^{i\phi}S_t^*S_a + S_t^*S_{a,t} + e^{i\phi}S_a^*S_{a,t}\right] \ . \tag{3.28b}$$

Here, $I_0^{\mathrm{NR}} = E_0^2|\alpha_a\alpha_t|^2$ as introduced in Sec. 3.2.2. Further, the background intensity is given by

$$I_b = I_p + I_0^{\mathrm{NR}}\left(|S_t|^2 + |S_a|^2 + |S_{a,t}|^2\right) \ . \tag{3.29}$$

I_p comprises the terms containing the $\delta(t)$ function characteristic of the prompt unscattered contributions, describing the incoming radiation as well as interference between the prompt pulse and resonantly scattered radiation at $t = 0$. Like the other contributions in I_b, it is phase-independent if the prompt radiation has passed before the phase imprint onto the analyzer response has taken place.

The intensities in Eqs. (3.28) comprise the four contributions I_b, $S_t^*S_a$, $S_a^*S_{a,t}$ and $S_t^*S_{a,t}$. By forming suitable sums or differences of two intensities recorded with appropriate phases, any two combinations of the above contributions can be isolated, by suppressing the respective other two.

In the present context, the term $S_a^*S_t$ is of primary interest, as it is the time-domain version of the scattering paths in Eq. (3.15) which gives rise to the diagonal structure. Therefore, we focus on the combinations

$$\mathcal{D}_1(t,\chi) = I_1(\phi=\chi) - I_1(\phi=\chi+\pi) = 4I_0^{\mathrm{NR}}\mathrm{Re}\left[e^{i\chi}\left(S_t^*S_a + S_t^*S_{a,t}\right)\right] \ , \tag{3.30a}$$

$$\mathcal{D}_2(t,\chi) = I_2(\phi=\chi) - I_2(\phi=\chi+\pi) = 4I_0^{\mathrm{NR}}\mathrm{Re}\left[e^{i\chi}\left(S_t^*S_a + S_a^*S_{a,t}\right)\right] \ , \tag{3.30b}$$

$$\begin{aligned}\mathcal{S}(t,\chi) &= I_1(\phi=\chi+\pi) + I_2(\phi=\chi+\pi) \\ &= 2I_b + 2I_0^{\mathrm{NR}}\mathrm{Re}\left[-2e^{i\chi}S_t^*S_a + \left(1-e^{i\chi}\right)\left(S_a^* + S_t^*\right)S_{a,t}\right] \ .\end{aligned} \tag{3.30c}$$

which each isolate $S_a^*S_t$ with one of the three other terms $S_a^*S_{a,t}$, $S_t^*S_{a,t}$ and I_b, respectively, if $\chi = 0$ is chosen in $\mathcal{S}$. Note that $\mathcal{D}_1$ and $\mathcal{D}_2$ each involve one particular ordering of target and analyzer along the beam propagation direction, while $\mathcal{S}$ is a combination of both orderings. Further, the terms $S_a^*S_t$ in Eqs. (3.30) feature a prefactor of two as compared to the individual spectra Eqs. (3.28). Corresponding to doubled statistics for the desired scattering contribution, this compensates for the larger measurement time required to record two spectra for the sum- and difference evaluations. The additional degree of freedom χ can be used to perform a tomography by scanning the phase of the

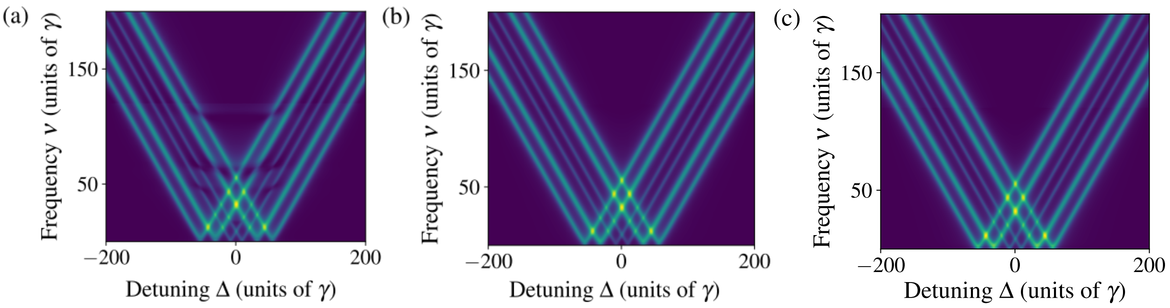

Figure 3.10: FFC spectra obtained with phase-control of the resonant analyzer response. Each panel shows a combination of two FFC spectra recorded with different phase settings: (a) shows the phase-combined spectrum $\mathcal{I}_{S_a}$ with analyzer placed in front of the target. (b) shows the corresponding result $\mathcal{I}_{S_t}$ with analyzer behind the target. (c) shows $\mathcal{I}_{inv}$ after removing the off-resonant background.

Table 3.2: Magnetic hyperfine splittings of ^{57}Fe extracted from spectra using analyzer phase control. As in Tab. 3.1, line fits to the off-resonant diagonal structures of the FFC spectrum are used. The different columns compare results for the three phase-combined quantites in Eqs. (3.31), both, with and without optimization of the fit range. The first column indicates reference values obtained from a calculation using pynuss. All results are given in units of the single-nucleus line-width γ.

PYNUSS Ref.	$\mathcal{I}_{S_a}$	$\mathcal{I}_{S_a}$ (opt.)	$\mathcal{I}_{S_t}$	$\mathcal{I}_{S_t}$ (opt.)	$\mathcal{I}_{inv}$	$\mathcal{I}_{inv}$ (opt.)
8.7596	8.689(23)	8.748(10)	8.819(2)	8.824(2)	8.854(9)	8.852(1)
32.0605	32.032(20)	32.104(12)	32.169(7)	32.193(5)	32.247(8)	32.241(4)
55.3406	55.245(24)	55.310(10)	55.336(13)	55.374(5)	55.416(6)	55.416(6)

desired scattering contribution. Such an analysis, however, is beyond the scope of this paper and a value of $\chi = 0$ is chosen as it recovers the form of the diagonal term $S_t^* S_a$ as discussed in previous sections (cf. e.g. Eq.(3.16)).

In the following, we perform the FFC analysis developed in Sec. 3.3 on the detection signals in Eqs. (3.30a-3.30c).

3.4.1 Extracting spectral parameters from spectra with phase control

We start with the extraction of spectral parameters as in Sec. 3.3.2, by applying line fits of slope one to diagonals formed by the peak maxima of sections along the ν-axis. To allow for a comparison of the different approaches, we again determine the hyperfine splittings of the 2μm thick α-iron target with magnetic hyperfine field $B = 33.3$T. As in Sec. 3.3.2, the sample is irradiated with linearly polarized light while the hyperfine field is oriented perpendicularly to the beam propagation direction and tilted by 45 degrees with respect to the beam polarization axis, in order to observe all six transition lines in the spectrum. For the spectral analysis then the real part of the FFC sum- and difference spectra

$$\mathcal{I}_{S_a}(\nu, \Delta) = \mathcal{F}\left[\mathcal{D}_1(t, \chi = 0)\right] , \tag{3.31a}$$

$$\mathcal{I}_{S_t}(\nu, \Delta) = \mathcal{F}\left[\mathcal{D}_2(t, \chi = 0)\right] , \tag{3.31b}$$

$$\mathcal{I}_{inv}(\nu, \Delta) = -\mathcal{F}\left[\mathcal{S}(t, \chi = 0)\Theta(t - t_1)\right] - \mathcal{I}_b(\nu_0) \tag{3.31c}$$

are considered. The first spectra do not require additional corrections, since the background contributions are automatically removed by taking the difference of two spectra with phase control in Eqs. (3.30a, 3.30b). The third spectrum Eq. (3.31c) contains two background corrections. First, the contribution of the initial prompt pulse is suppressed by the step function $\Theta(t - t_1)$. Second, the single-target contributions $\mathcal{I}_b(\nu_0)$ are removed. However, in contrast to the procedure in Eq. (3.20) involving the subtraction of single-target spectra, here, we follow another approach, directly based on the FFC spectra measured with both targets. For this, we make use of the fact that the FFC spectra approximately reduce to the background in regions away from the diagonal structure. Specifically, we determine the background correction from the FFC contribution at the largest recorded detuning-value Δ for ν values up to an upper limit ν_0 well below the diagonal structure. For ν values above this threshold, we instead approximate the background by the FFC contribution at $\Delta = 0$. This way, the background correction $\mathcal{I}_b(\nu_0)$ is obtained directly from the FFC spectra, in regions away from the diagonals for the entire ν range.

For the numerical analysis, we again calculate all spectra using PYNUSS, including a time-dependent phase shift for the analyzer response which is zero at $t = 0$ and ϕ for times $t > 0$. The FFC sum- and difference spectra Eqs. (3.31a)-(3.31c) considered for the analysis are shown in Fig. 3.10. A comparison of plots (a) and (b) shows that the ordering of analyzer and target indeed has an influence: While the diagonal structure is perturbed by residual effects if the analyzer is placed first, corresponding to $\mathcal{I}_{S_a}(\nu, \Delta)$, shown in plot (a), no such perturbations are visible in plot (b) showing the opposite order, corresponding to $\mathcal{I}_{S_t}(\nu, \Delta)$. Like in the case with the target placed first (plot (b)), the background-corrected case $I_{inv}(\nu, \Delta)$ in plot (c) does not show these perturbations.

The retrieved transition frequencies obtained by the diagonal analysis of the phase-combined FFC spectra Eqs. (3.31a)-(3.31c), corresponding to spectra recorded with the analyzer first, the target first and upon reversing target order, respectively, are summarized in Table 3.2 in the columns $\mathcal{I}_{S_a}$, $\mathcal{I}_{S_t}$ and $\mathcal{I}_{inv}$ for comparison with the results obtained in Sec. 3.3.2 displayed in Table 3.1 without phase control. For the three columns containing the additional "(opt.)", again the optimization procedure involving multiple fits with different ranges of detuning data were performed by subsequently excluding low-detuning data points. From the different fit results, the one with the least fit error is chosen. Overall, all results agree well with the respective theoretical reference values within a 2% margin. We find that the optimization is most effective if the analyzer is placed first ($\mathcal{I}_{S_a}$), which likely is due to the residual perturbations visible in Fig. 3.10(a), while the other two results do not change significantly upon optimization. Together with the undistorted appearance of the diagonal structures in these cases in Fig. 3.10 this implies a larger range of detuning values that can reliably be employed for linear fit analysis compared to the off-resonant case in Sec. 3.3.2 and Tab. 3.1, since the result with the least fit error is reached very close to resonance already.

3.4.2 Effects of the target thickness on the parameter extraction

For a more systematic comparison of phase-combined and off-resonant FFC spectra, we analyze the influence of thickness effects on the diagonal structure of a single-line ^{57}Fe target (i.e., in the absence of hyperfine splitting). Fig. 3.11(a) shows the line shape as function of target thickness. It can be seen that for thicker targets, the single line splits into a double-hump profile [Smi99], which impedes the simple determination of a single maximum. Therefore, next to the simple fit of a line through the maxima in the FFC spectra, we further consider a model to fit the line shape of the single-line target, analogous to the approach in Sec. 3.3.3. We use the model function (for a derivation, see Appendix A.3)

$$f_{\text{fit}}(\nu) = A\left[\exp\left(\frac{b_t}{i(\nu - x) - S_\Gamma}\right) - 1\right] + h \tag{3.32}$$

with amplitude $A \sim b_a I_0^{\text{NR}}$ accounting for electronic absorption and dispersion via I_0^{NR} as well as the resonant coupling of the radiation to the analyzer nuclei via b_a, $x = \Delta - \omega_t + \omega_a$ denoting the center frequency of each vertical spectrum and $S_\Gamma = (\gamma_t + \gamma_a + b_a)/2$ the decay rate of the target broadened by the effective analyzer decay width. The thickness parameters b_a, b_t for both analyzer and target are defined in Appendix A.3. Note that, in deriving this formula, we distinguish between analyzer and target line-width γ_a and γ_t to gain better insight into the functional dependence on both quantities though the analyzed numerical data will continue to use $\gamma_a = \gamma_t = \gamma$.

The exponential form of the fit model Eq. (3.32) is a consequence of multiple scattering of photons propagating through the target, also causing the double-hump profile. An additional offset h was added to account for background in the Fourier spectrum due to residual resonant effects. Knowing that the spectral shape of vertical or horizontal sections through the diagonal structure corresponds to a double-hump profile, the simple maxima determination can also be adapted to include the two most prominent maxima of such sections followed by an average over the lines formed by both sets of maxima.

Results of this analysis are shown in Fig. 3.11(b). It depicts the recovered target-analyzer detuning $\Delta_0 = \omega_t - \omega_a$ if no Doppler shift is applied as function of target thickness. Since for a ^{57}Fe target

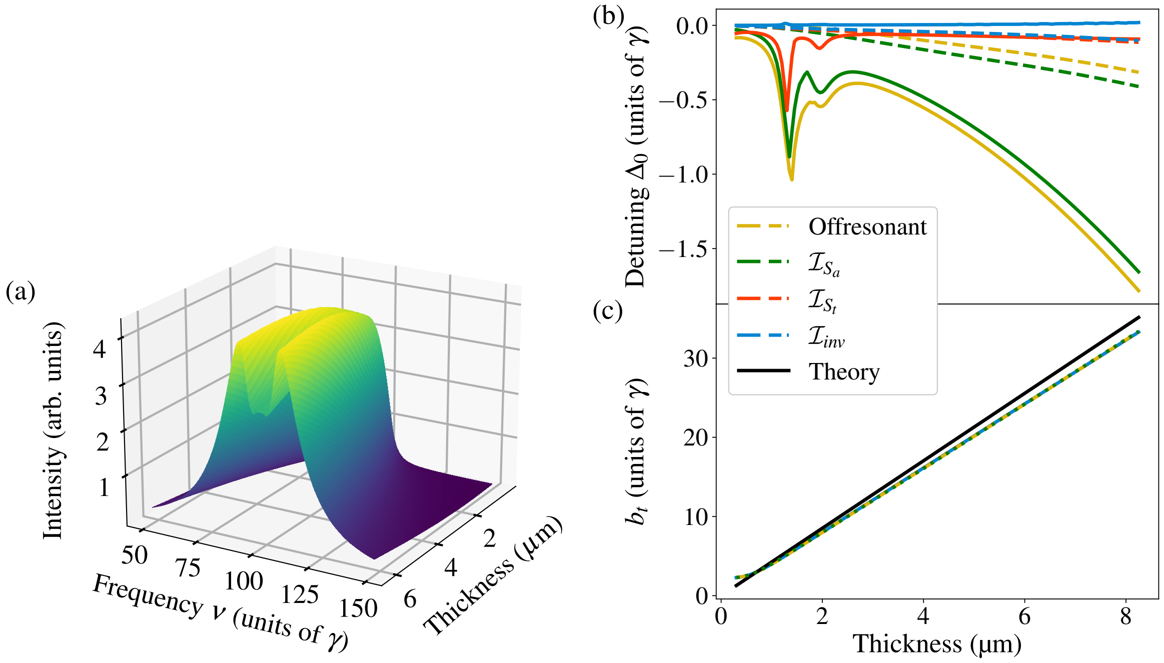

Figure 3.11: Extraction of target parameters as function of target thickness. Panel (a) illustrates how the diagonal structure along the ν-axis at $\Delta = 100\gamma$ varies with target thickness. For thicker targets, a characteristic "double-hump" profile appears. (b) compares the deviations between the reference transition frequency and the corresponding transition frequencies obtained by linear fits to the diagonals using different methods: The off-resonant method (yellow line), and the phase-difference methods based on $\mathcal{I}_{S_a}$ (green), $\mathcal{I}_{S_t}$ (red) and $\mathcal{I}_{inv}$ (blue). In all cases, the solid lines correspond to results obtained by simple maxima determination while the dashed lines are based on model fits to vertical sections through the diagonal structure, as explained in the main text. (c) compares the thickness parameters extracted from the different methods with the theoretical reference value (black).

without hyperfine splitting and a stainless steel analyzer without isomeric shift both transition frequencies are identical ($\omega_t = \omega_a$), the plotted quantity also describes the deviation between the real detuning and the value recovered via diagonal analysis.

Eight curves falling into two categories of diagonal analysis methods are compared: The solid curves represent the method introduced in Section 3.3.2 which determines simple maxima of each section along the ν-direction and subsequent linear fits to the resulting diagonals to give an estimate of the target-analyzer detuning Δ_0. The dashed curves use the same linear fit approach to retrieve the target-analyzer detuning but the peak position of each section along the ν-axis is determined using the fit model Eq. (3.32) via the parameter x. Both of these diagonal analysis methods are applied to four types of FFC spectra: The yellow curves evaluate the off-resonant spectra discussed in Section 3.3 while the other curves result from evaluation of spectra including phase-control, specifically, difference spectra Eq. (3.31a)-(3.31b) with analyzer (green) and target (orange) placed first in the beam path and the sum spectrum $\mathcal{I}_{inv}$ after background removal (blue). In obtaining these results, the detuning fit range was kept constant as $[25\gamma, 175\gamma)$.

From Fig. 3.11(b) we find that all four simple-maxima evaluations exhibit a maximum deviation from the reference value at around 1.5γ which can be attributed to the appearance of the double-hump profile for this target thickness. In contrast, the sum spectrum ($\mathcal{I}_{inv}$, blue curve) is hardly affected. Apart from this, the sum spectrum and the difference spectrum with target placed first ($\mathcal{I}_{S_t}$, orange curve) reproduce the reference value $\Delta_0 = 0$ much better than the other two curves across the entire thickness range, and become almost constant towards larger thicknesses. This feature can be explained by noting that in the corresponding Eqs. (3.31b) and (3.31c), the target spectrum is absent except for the desired diagonal contribution. In contrast, Eq. (3.31a) contains further contributions of the target response which distort the diagonal spectrum with increasing target thickness. Hence, to retrieve reliable spectral information for targets thick compared to the analyzer width it appears to be favourable to choose phase-combinations eliminating the term $S_t^* S_{a,t}$ the influence of which becomes significant towards higher target thicknesses.

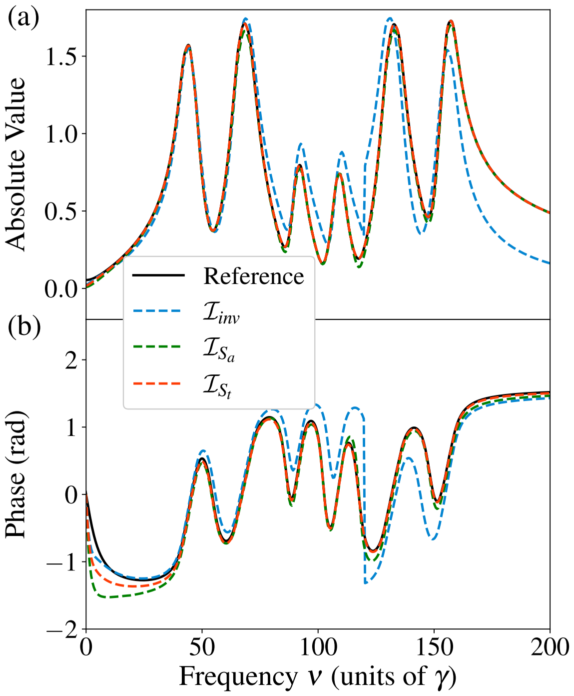

Figure 3.12: Reconstruction of the nuclear resonant target response from phase-combined FFC spectra: (a) depicts the absolute value of a vertical cut through the FFC spectra at $\Delta = 100\gamma$ (dashed lines). For comparison, the absolute value of the reference nuclear resonant response correlated with the analyzer response according to eq.(3.15) is shown as solid black line. (b) shows the corresponding phase of the quantities shown in (a). The blue line corresponds to the background-corrected sum spectrum $\mathcal{I}_{inv}$ while the green and orange line correspond to the cases with the analyzer ($\mathcal{I}_{S_a}$) and the target ($\mathcal{I}_{S_t}$) placed first in the beam path, respectively.

The results using the model fit approach (dashed lines) all agree well with the expected result of zero throughout the entire thickness range, without perturbation by the double hump at around 1.5γ, since the shape of this double-hump profile is included in the fit model Eq. (3.32). However, towards larger target thicknesses, these curves start to deviate more from the reference values than the two better-performing simple-maxima results. We attribute this to the fact that at higher target thickness, both the positive and negative ν diagonal structures become spectrally broader and overlap stronger with the each other leading to deviations from the fit model Eq.(3.32). This effect can be reduced by excluding low-frequency data points in the vertical spectra.

Figure 3.11(c) shows corresponding results for the thickness parameter extracted from the four evaluated spectra as function of the target thickness. In all cases, the retrieved thickness parameter are almost identical and agree well with the calculated values for intermediate thicknesses, even though the deviation increases with the target thickness. Also, in the limit of thin targets, a plateau in the recovered thickness parameter develops as the width of the diagonal spectra is bounded from below by the analyzer spectral width.

In summary, we found that the linear fit analysis of spectra obtained using phase control not only allows one to use larger parts of the recorded data than the corresponding off-resonant methods, but also may provide better target parameter recovery results. As a function of target thickness, a comparison between different phase control approaches revealed that it appears most favorable to eliminate the scattering channels containing the term $S_t^* S_{a,t}$. Then, the phase control methods provide a better recovery than the corresponding approaches based on the off-resonant part of the spectrum only. Finally, a more reliable recovery of the spectra as function of target thickness could be achieved using fit models incorporating the known double-hump profile.

3.4.3 Extracting the target response function using phase control

We conclude our comparison of FFC spectra obtained using phase-control with the off-resonant regime by reconstructing the complex-valued target response from sections along the ν-axis as described in

Section 3.3.3.
Fig. 3.12 compares absolute value and phase of a vertical cut through the FFC spectrum at $\Delta = 100\gamma$ for the three phase combinations Eq. (3.31a)-(3.31c) with the reference spectrum obtained by cross-correlating nuclear resonant target and analyzer response explicitly (solid black line). It can be seen that the results based on the difference spectra $\mathcal{I}_{S_a}$ (orange line) and $\mathcal{I}_{S_t}$ (green line) agree very well with the theoretical reference. In particular for the case with the target placed first in the beam path (orange line), the phase at lower frequencies ν is recovered even better than in the analysis based on the off-resonant regions of the FFC spectrum in Fig. 3.4(b). Interestingly, the analysis based on the sum spectrum $\mathcal{I}_{inv}$ performs much worse, in particular towards higher frequencies. We attribute this to the background removal, which distorts the final result if resonant effects still contribute at the detuning values used to determine the background contributions (cf. discussion after Eq. (3.31c)).
Overall, we therefore conclude that additional control of the relative phase between the resonant and non-resonant radiation in Nuclear Resonant Scattering experiments can improve spectral analysis and target response reconstruction, as it allows one to selectively separate otherwise overlapping scattering channels across the entire detuning range. This improvement is manifest in a higher amount of data close to resonance that can be evaluated during the line fit analysis as well as a better recovery of the phase of the nuclear response in the lower Fourier frequency range compared to the off-resonant approach without phase control. Further, thickness effects impeding a reliable recovery of the spectral target structure via the diagonal lines can be suppressed by selecting appropriate scattering contributions thus allowing the study of thick targets that are not accessible to the off-resonant approach without phase control.

3.5 Discussion and summary

In this Chapter, we introduced frequency-frequency correlation (FFC) spectra as a promising tool for spectral analysis and phase-retrieval of arbitrary Mössbauer targets. These FFC spectra are obtained as Fourier transforms of experimentally accessible time- and frequency-resolved Nuclear Resonant Scattering spectra along the time-axis. Our approach is motivated by the observation that FFC spectra exhibit a simple structure comprising horizontal and diagonal features which relate to different physical processes contributing to the scattered light, and which can conveniently be analyzed.

We showed that this approach translates interference between different scattering channels into frequency-frequency correlations revealing the spectral structure of the underlying scattering system. Specifically, the cross-correlation between nuclear resonant part of analyzer and target response appeared as a diagonal structure in these frequency-frequency correlation spectra that allowed access to target properties in two ways.

First, using linear fits to these diagonals, we were able to extract the resonance frequencies of the target, as well as spectral line features such as collective energy shifts and line broadenings, thereby establishing an intuitive and straightforward analysis tool for the FFC spectra.

Second, we found that sections through the diagonal structure provide access to amplitude and phase of the nuclear resonant part of the target response, cross-correlated with the analyzer response. In particular, they are not affected by the off-resonant electronic scattering in the target. This is of immediate interest for characterizing collective nuclear level schemes in x-ray cavities, which so far have been associated to cavity reflection spectra [RE21b]. However, these spectra also depend on the in- and out-coupling of the x-rays into the cavity and the interference of the nuclear response with the non-resonant empty-cavity scattering, and therefore the associated level schemes may not represent the actual nuclear dynamics inside the cavity [DLE22a]. Then it may be favorable to instead associate a level scheme to the nuclear dynamics inside the cavity alone, and the approach presented here allows one to experimentally access the corresponding nuclear response unperturbed by the electronic scattering contribution. In this sense, the analysis approach presented here has a qualitative advantage over the established late-time integration method. We note that time-domain off-resonant methods, as discussed in Sec. 3.2.4, share this advantage, although so far they have primarily been discussed in the forward scattering case [Cal+05; Goe+19]. This again highlights the advantage of time- and frequency-resolved measurements over time-resolved or frequency-resolved approaches, since they not only allow one to choose the late-time integration range in the data analysis after the actual experiment, but also provide the basis for both off-resonant analysis methods in the time- and energy-domain. In other words, a single dataset can be evaluated using three different methods, thereby also allowing for consistency checks.

To demonstrate the practical feasibility of both FFC analysis approaches in relevant settings, we employed them to determine magnetic hyperfine splittings of α-iron in forward scattering geometry as well as the collective Lamb shift of thin-film x-ray cavities as function of incidence angle θ from simulated data. In all cases, good agreement was achieved with corresponding reference calculations. Further, the superradiant enhancement of the nuclear decay in the cavity could successfully be retrieved using an appropriate fit model. We also considered experimental resolution limitations along the Fourier frequency ν in FFC spectra, which may arise due to measurement constraints in the time domain, e.g., due to the x-ray pulse repetition rate determined by the radiation source. This can be mitigated by employing our approach based on the relative detuning Δ between analyzer and target rather than on ν, since the former has an experimentally controllable resolution independent of the x-ray pulse structure. An example analysis of the hyperfine splitting of α-iron including time gating effects indeed showed that this way, results with reasonable accuracy could be obtained.

In a second part, we considered the possibility of further extending the FFC approach based on a control of the relative phase between the resonant and off-resonant analyzer response. In the presence of such phase-control, the overall response becomes dependent on the ordering of target and analyzer. We showed that sums or differences of FFC spectra recorded with suitable phase shifts or analyzer-target orderings allow one to disentangle different scattering pathways across the entire FFC spectrum. In contrast, most previous approaches separated the pathways by restricting the analysis to particular parameter regions such as the large target-analyzer detuning case. This way, spectral backgrounds can be removed, or scattering paths be excluded which prevent an accurate FFC analysis, especially close to the resonances. In the present work, we employed this technique to isolate the interference contribution between the individual resonant target and analyzer scatterings. We could thereby improve the recovery of phase and spectral target structure as compared to the off-resonant case without phase control and reliably retrieve the target's resonance structure even for thick targets where the off-resonant limit is difficult to reach. In addition, we expect that the approach will also facilitate the study of transition-specific dynamics and resonant couplings [Sch+02b; Smi+05; Hee+21] by suppressing non-resonant contributions to time- and frequency-resolved spectra.

Chapter 4

Time-dependent density matrix perturbation theory

Abbreviations used in this Chapter:

- LER: low-excitation regime
- NRS: nuclear resonant scattering
- XFEL : x-ray free electron laser
- XFELO : x-ray free electron laser oscillator

In this Chapter two types of perturbative density matrix expansions are developed, which form the basis the theoretical descriptions of the dynamics of effective nuclear few-level schemes (Chapter 6, 7 and 5) and the dynamics of interacting nuclear ensembles (Chapter 5). Perturbation theory is a corner stone of the understanding of quantum mechanics [SC95] and quantum field theory [PS95] and entire branches of physical phenomena could not be explained or studied theoretically without perturbative treatments of otherwise unsolvable physical problems. The success of perturbation theory dates back to the first days of quantum mechanics, which can explain such effects in atomic physics and scattering theory such as the Stark effect, Fermi's golden rule [BJ89] or spontaneous emission [SZ97; MS07], and is still in use nowadays, for example, to study physics within and beyond the standard model [PS95]. Time-dependent density matrix perturbation theory is a widely employed tool to interpret and devise coherent multi-pulse experiments in nonlinear optics [Muk95; BP08] and multidimensional spectroscopy [HZ11; Cho19], where (nonlinear) dynamics of complex molecular and atomic systems under the action of time-dependent coherent light fields is studied. With the advent of coherent control techniques and x-ray pulse shaping suitable to design coherent multi-pulse experiments in nuclear resonant scattering, such methods are of great interest also to the Mössbauer community. Moreover, while experiments so far have been mostly conducted in the regime of linear x-ray-nucleus interactions, novel light sources such as XFELOs [Ada+19a] and XFELs including techniques including hard x-ray self-seeding [Ama+12], promise to surpass this regime in the near future. Therefore, perturbative treatments of nuclear dynamics as a function of the nucleus-field interaction seem a logical next step from a theoretical point of view.

The Chapter is structured as follows: In the first part, self-consistent equations for the excited-state population and coherence of quantum optical two-level systems are derived as a formal solution to the optical Bloch equations. In the second part, a more general perturbative density matrix expansion is developed that is based on similar approaches in multidimensional spectroscopy. Finally, the relevance of the results presented here is briefly summarized.

This Chapter is mainly dedicated to technical derivations of the expressions used in the following three Chapters. Readers more interested in the application of the density matrix expansions developed here, are referred to Chapters 5, 6 and 7.

4.1 Self-consistent solution of the optical Bloch equations for two-level systems

In this Section self-consistent solutions for the (time-dependent) population $\rho_{ee}(t)$ and coherence $\rho_{ge}(t)$ of quantum optical two-level systems are derived from the optical Bloch equations (cf. Sec. 2.2.1):

$$\dot{\rho}_{ee} = -\gamma\rho_{ee} + \frac{i}{2}\left[\Omega(t)\rho_{ge} - \Omega^*(t)\rho_{eg}\right] \,, \tag{4.1a}$$

$$\dot{\rho}_{ge} = \left(i\omega_0 - \frac{\gamma}{2}\right)\rho_{ge} + \frac{i\Omega^*(t)}{2}\left(2\rho_{ee} - 1\right) \,, \tag{4.1b}$$

$$\rho_{eg} = \rho_{ge}^* \,, \qquad \rho_{gg} = 1 - \rho_{ee} \,. \tag{4.1c}$$

Recall that, in case of nuclear transitions, γ is the single-nucleus linewidth, ω_0 its resonance frequency and

$$\Omega(t) = \frac{\mathbf{dE}(t)}{\hbar} \tag{4.2}$$

the time-dependent x-ray-nucleus coupling or Rabi frequency. For later discussions we note that, even though these are the equations of motion for a single nucleus, effective collective two-level systems arising, e.g., in thin-film cavities in the LER (cf. Sec. 2.2.2) are governed by the same equations of motion, however, with collectively modified parameters ω_0, γ and $\Omega(t)$.

A similar Ansatz as presented here, has been used in Ref. [HZ11] for multi-level density matrices and in Ref. [MS07] to study few-level operator dynamics in the Heisenberg-Langevin approach.

The optical Bloch equations Eqs. (4.1) can be solved self-consistently in two steps: First, the equations can be integrated formally and, second, the result of both integrations can be inserted into the other density matrix element to decouple the dynamics of the excited-state population and the coherence. By introducing the new variables

$$\tilde{\rho}_{ge}(t) = e^{(-i\omega+\frac{\gamma}{2})t}\rho_{ge}(t) \,, \quad \tilde{\rho}_{ee}(t) = e^{\gamma t}\rho_{ee}(t) \tag{4.3}$$

the time evolution is governed by

$$\dot{\tilde{\rho}}_{ge}(t) = \frac{i}{2}e^{-i\omega t+\frac{\gamma}{2}t}\Omega^*(t)(2\rho_{ee}(t) - 1) \tag{4.4}$$

$$\dot{\tilde{\rho}}_{ee}(t) = -\, e^{\gamma t}\mathrm{Im}\left[\Omega(t)\rho_{ge}(t)\right] \tag{4.5}$$

which we solve by formal integration from an initial time t_0 until observation time t yielding

$$\tilde{\rho}_{ge}(t) - \tilde{\rho}_{ge}(t_0) = \frac{i}{2}\int_{t_0}^{t} dt' e^{-i\omega t'+\frac{\gamma}{2}t'}\Omega^*(t')(2\rho_{ee}(t') - 1) \tag{4.6}$$

$$\tilde{\rho}_{ee}(t) - \tilde{\rho}_{ee}(t_0) = -\int_{t_0}^{t} dt' e^{\gamma t'}\mathrm{Im}\left[\Omega(t')\rho_{ge}(t')\right] \tag{4.7}$$

Rearranging these equations and reinserting the untransformed density matrix elements leads to the following formal coupled integral equations for the density matrix elements:

$$\rho_{ee}(t,t_0) = e^{-\gamma(t-t_0)}\rho_{ee}(t_0) - \int_{t_0}^{t} dt' e^{\gamma(t'-t)}\mathrm{Im}\big[\Omega(t')\rho_{ge}(t',t_0)\big] \tag{4.8}$$

$$\begin{aligned}\rho_{ge}(t,t_0) =& e^{i\omega(t-t_0)}e^{-\frac{\gamma}{2}(t-t_0)}\rho_{ge}(t_0)\\ &+ \frac{i}{2}\int_{t_0}^{t} dt' e^{-i\omega(t'-t)}e^{\frac{\gamma}{2}(t'-t)}\Omega^*(t')[2\rho_{ee}(t',t_0) - 1]\end{aligned} \tag{4.9}$$

where the initial density matrix element is defined as $\rho_{ij}(t_0) := \rho_{ij}(t_0, t_0)$. Inserting the second equation into the first one and vice versa yields:

$$\begin{aligned}\rho_{ee}(t,t_0) =& e^{-\gamma t}\Big\{e^{\gamma t_0}\rho_{ee}(t_0) + e^{\frac{\gamma}{2}t_0}\int_{t_0}^{t} dt' e^{\frac{\gamma}{2}t'}\mathrm{Re}(ie^{i\omega(t'-t_0)}\Omega(t')\rho_{ge}(t_0)) \\ &- \mathrm{Re}\Big[\int_{t_0}^{t} dt' e^{\gamma t'}\Omega^*(t')\int_{t_0}^{t'} dt'' e^{i\omega(t''-t')}e^{\frac{\gamma}{2}(t''-t')}\Omega(t'')\big(\rho_{ee}(t'',t_0)-\frac{1}{2}\big)\Big]\Big\}\end{aligned} \tag{4.10a}$$

$$\begin{aligned}\rho_{ge}(t,t_0) =& e^{i\omega t}e^{-\frac{\gamma}{2}t}\Big\{e^{-i\omega t_0}e^{\frac{\gamma}{2}t_0}\rho_{ge}(t_0) + i\int_{t_0}^{t} dt' e^{-i\omega t'}\Omega^*(t')\big(e^{\gamma(t_0-\frac{t'}{2})}\rho_{ee}(t_0) - \frac{e^{\frac{\gamma}{2}t'}}{2}\big) \\ &- i\int_{t_0}^{t} dt' e^{-i\omega t'}e^{-\frac{\gamma}{2}t'}\Omega^*(t')\int_{t_0}^{t'} dt'' e^{\gamma t''}\mathrm{Im}\big(\Omega(t'')\rho_{ge}(t'',t_0)\big)\Big\}\end{aligned} \tag{4.10b}$$

These equations can systematically be expanded in orders of the semiclassical driving field $\Omega(t)$. Note that the coherence $\rho_{ge}(t)$ only features contributions from odd orders in the x-ray-nucleus interaction $\Omega(t)$, while $\Omega(t)$ contributes only in even orders to the population $\rho_{ee}(t)$. This has important consequences for the low-excitation behaviour of nuclear many-body dynamics as studied in Chapter 5. The power of these equations is that they incorporate the intrinsic two-level dynamics, i.e. nuclear decay and oscillation with the resonance frequency ω_0 to all orders and that, in principle, arbitrary (time-dependent) pulse shapes and sequences including pulse phases and detunings between pulse carrier frequency and nuclear resonance frequency can be studied. This is in contrast to some established analytical approaches such as the pulse area theorem (cf. Appendix A.9), which requires zero detuning between pulse and two-level system, or exact solutions of the two-level dynamics for constant pulse envelopes $|\Omega(t)| = \text{const.}$, that can not incorporat nuclear decay [SZ97].
Within the scope of this thesis, Eqs. (4.10) will be employed to calculate and compare the dynamics of incoherent and coherent radiation emitted by two-level nuclei, associated with the population $\rho_{ee}(t)$ and coherence $\rho_{ge}(t)$, respectively, in the LER (for details, see Chapter 5). In Chapters 5 and 6, where only single-pulse results are studied and the nuclear system is assumed to be in its ground state at the beginning of the interaction with the x-rays, such that initially, at time t_0, $\rho_{ee}(t_0) = 0 = \rho_{ge}(t_0)$ and these equations reduce to

$$\begin{aligned}\rho_{ee}(t,t_0) =& \frac{1}{2}e^{-\gamma t}\mathrm{Re}\Big[\int_{t_0}^{t} dt' e^{\frac{\gamma}{2}t'}e^{-i\omega t'}\Omega^*(t')\int_{t_0}^{t'} dt'' e^{i\omega t''}e^{\frac{\gamma}{2}t''}\Omega(t'')\Big] \\ &- e^{-\gamma t}\mathrm{Re}\Big[\int_{t_0}^{t} dt' e^{\frac{\gamma}{2}t'}e^{-i\omega t'}\Omega^*(t')\int_{t_0}^{t'} dt'' e^{i\omega t''}e^{\frac{\gamma}{2}t''}\Omega(t'')\rho_{ee}(t'',t_0)\Big]\Big\}\end{aligned} \tag{4.11a}$$

$$\begin{aligned}\rho_{ge}(t,t_0) =& -\frac{i}{2}e^{i\omega t}e^{-\frac{\gamma}{2}t}\int_{t_0}^{t} dt' e^{-i\omega t'}\Omega^*(t')e^{\frac{\gamma}{2}t'} \\ &- ie^{i\omega t}e^{-\frac{\gamma}{2}t}\int_{t_0}^{t} dt' e^{-i\omega t'}e^{-\frac{\gamma}{2}t'}\Omega^*(t')\int_{t_0}^{t'} dt'' e^{\gamma t''}\mathrm{Im}\big[\Omega(t'')\rho_{ge}(t'',t_0)\big]\end{aligned} \tag{4.11b}$$

For a study of the convergence behaviour of the self-consistent Eqs. (4.11) to the numerical solution of the optical Bloch Eqs. (4.1), the reader is referred to Appendix A.5.

4.2 Perturbative expansion of the density matrix

Even though the self-consistent Eqs. (4.11) are a powerful tool for studying the dynamics of single collective two-level systems upon very general time-dependent driving fields and pulse sequences, a more general approach is needed to include many interacting two-level systems or to investigate more complex level schemes as studied in Chapters 5 and 6, respectively. These systems are of particular interest for different reasons: While effective few-level descriptions of nuclear ensembles are valid in the LER (cf. Sec. 2.2.2), these are likely to break down at higher excitations conditions as can be reached at XFELs or XFELOs. In this case, a full description of the interacting many-body dynamics of the nuclear ensemble may become necessary. Apart from this, effective few-level schemes involving more than two-levels realized in thin-film cavities (cf. 2.2.2) offer some of the most intriguing phenomena in nuclear quantum optics such as EIT [Röh+12] and couplings between nuclear ensembles [Hab+17]. Therefore, the development of a density matrix perturbation theory applicable to these types of systems is of immediate interest for near-future experiments and applications in nuclear quantum optics.

The time-dependent density matrix perturbation theory derived in this Section is based on similar approaches in nonlinear optics [BP08] and multidimensional spectroscopy [Cho19; HZ11] and was developed especially by Shaul Mukamel [Muk95]. In contrast to many comparable derivations in textbooks, we aim to explicitely include many-body effects and retain nonunitary dynamics in our derivation as these effects can play a significant role in nuclear resonant scattering experiments as argued above.

After a derivation of a general form self-consistent form of the density matrix, the two cases of multi-level and many-body dynamics and the involved approximations are discussed separately.

4.2.1 Many-body nuclear dynamics

In the most general setting, we perturbatively solve the master equation

$$\frac{d}{dt}\hat{\rho} = \frac{1}{i\hbar}\left[\hat{H}, \hat{\rho}\right] + \mathcal{L}[\hat{\rho}]\,. \tag{4.12}$$

We consider Hamiltonians that can be separated into a system part $\hat{H}_{nuc}$ and a nucleus-field coupling part $\hat{W}(t)$ such that

$$\hat{H} = \hat{H}_{nuc} + \hat{W}(t) \tag{4.13}$$

with the nuclear part incorporating the transition energies and potentially coherent couplings between different levels or nuclear few-level systems, i.e. [Len+20]

$$\hat{H}_{nuc} = \hbar\sum_{nl}\omega_{nl}\hat{\sigma}^{+}_{nl}\hat{\sigma}^{-}_{nl} - \hbar\sum_{nn'll'} J_{nn'll'}\hat{\sigma}^{+}_{nl}\hat{\sigma}^{-}_{n'l'} \tag{4.14}$$

the form of which requires coupling constants of the form $J^{*}_{n'nll'} = J_{nn'l'l}$ such that $\hat{H}_{nuc}$ is hermitian. The (coherent) dipole-dipole couplings $J_{nn'll'}$ between the nuclei are radiation-induced and are mediated by surrounding reservoir modes [FS05]. They can be calculated for a specific nuclear environment such as a thin-film cavity or waveguide, e.g. by using the ab initio Green's function approach (for details, see, [Len+20] or Sec. 2.2.2). The diagonal terms J_{nnll} are known as intensity-dependent Stark shifts or Lamb shifts leading to a renormalization of the bare nuclear transition frequencies ω_{nl} [FS05]. The operators $\hat{\sigma}^{+}_{nl} = |l_n\rangle\langle g_n|$, $\hat{\sigma}^{-}_{nl} = |g_n\rangle\langle l_n|$ are the raising/lowering operators creating or destroying excitation in transition l at the nuclear system n. The l labelling may include magnetic Zeeman splittings of the magnetic hyperfine states or different levels arising in effective collective nuclear level schemes in nuclear cavity QED [Len+20]. Here, it is chosen such that each dipole-allowed transition has its own unique label l [FS05][1]. The nucleus-field coupling is modelled as a semiclassical field-dipole coupling allowing for different coupling strengths for each nuclear transition, i.e.

$$\hat{W} = -\frac{\hbar}{2}\sum_{nl}\left(\Omega_{nl}(t)\hat{\sigma}^{+}_{nl} + h.c.\right) \tag{4.15}$$

Here, $\Omega_{nl}(t)$ is the (time-dependent) nucleus-field coupling, which will also be referred to as time-dependent Rabi frequency, acting on nuclear system n and transition l given by

$$\Omega_{nl}(t) = \frac{\mathbf{d}_{nl}\mathbf{E}_{nl}(t)}{\hbar} \tag{4.16}$$

The electric field $E_{nl}(t)$ we allow to be position- and time-dependent and different for each nuclear system n and level l. The effective nuclear dipole moments can vary for different transitions l if

---

[1] For a discussion of effective dipole Hamiltonians for higher order multipole moments see, e.g.,Ref. [Len21] or Sec. 2.2.1.

Zeeman or quadrupole splittings occur, for instance [Len21].

The non-unitary part of the time-evolution is described by the Lindbladian

$$\mathcal{L}[\hat{\rho}] = \sum_{n,l} \sum_{n',l'} \left(\Gamma_{nn'll'} + \delta_{nn'}\delta_{ll'}\Gamma^{\mathrm{IC}}_{nl}\right) \left(2\hat{\sigma}^{-}_{n'l'}\hat{\rho}\hat{\sigma}^{+}_{nl} - \left\{\hat{\sigma}^{+}_{nl}\hat{\sigma}^{-}_{n'l'}, \hat{\rho}\right\}\right) \tag{4.17}$$

Here, the off-diagonal elements correspond to cross-damping terms, also referred to as incoherent couplings, arising from the system-reservoir interaction with background radiation modes, like the coherent coupling constants $J_{nn'll'}$ [FS05]. Similarly, they can be calculated within the ab initio Green's function approach [Len+20] (cf. also Sec. 2.2.2). The diagonal terms contain contributions from two-different processes: First, Γ_{nnll} describes losses of the individual nuclear transitions due to radiative processes related to interactions with the background radiation field while the second part $\Gamma^{\mathrm{IC}}_{nl}$ has its origin in non-radiative losses of nuclear excitation due to internal conversion and related secondary emission processes (cf. 2.1.4). The total line-width γ_{nl} of each nuclear transition combines both loss processes $\gamma_{nl} = 2\left(\Gamma_{nnll} + \Gamma^{\mathrm{IC}}_{nl}\right)$.

4.2.2 Expansion in the nucleus-field coupling

As discussed, nuclear excitations at present day synchrotron and XFEL sources are typically in the low-excitation regime or at the boundary to the observation of nonlinear effects. For this reason, it is reasonable to expand the density matrix in orders of the field-nucleus coupling Hamiltonian

$$\hat{\rho}(t) = \sum_{j=0}^{\infty} \hat{\rho}^{(j)}(t) \tag{4.18}$$

where the jth order of the expansion is characterized by the semiclassical nucleus-field coupling acting j times on the initial density matrix. At the same time we want to include the nuclear Hamiltonian and the nonunitary dynamics nonperturbatively to all orders. To this end, we write the Lindbladian in the form

$$\mathcal{L}\left[\hat{\rho}\right] = \mathcal{L}'\left[\hat{\rho}\right] - \left\{\hat{\Gamma}, \hat{\rho}\right\} \tag{4.19}$$

with

$$\hat{\Gamma} = \sum_{nn'll'} \left(\Gamma_{nn'll'} + \Gamma^{\mathrm{IC}}_{nl}\delta_{nn'}\delta_{ll'}\right) \hat{\sigma}^{+}_{nl}\hat{\sigma}^{-}_{n'l'} \tag{4.20}$$

$$\mathcal{L}'\left[\hat{\rho}\right] = 2\sum_{nl}\sum_{n'l'} \left(\Gamma_{nn'll'} + \Gamma^{\mathrm{IC}}_{nl}\delta_{nn'}\delta_{ll'}\right) \hat{\sigma}^{-}_{n'l'}\hat{\rho}\hat{\sigma}^{+}_{nl} \tag{4.21}$$

In analogy to the interaction picture used extensively in time-dependent perturbation theory in quantum mechanics and quantum field theory [Joa75; SC95; PS95], we introduce the operators

$$\hat{T}_t = \exp\left(-\hat{\Gamma}t + \frac{i}{\hbar}\hat{H}_{nuc}t\right), \quad \hat{T}_t^{-1} = \exp\left(\hat{\Gamma}t - \frac{i}{\hbar}\hat{H}_{nuc}t\right) = \hat{T}_{-t} \tag{4.22}$$

$$\hat{\rho}_I(t) = \left(\hat{T}_t^{-1}\right)^{\dagger} \hat{\rho}(t)\hat{T}_t^{-1} \tag{4.23}$$

Note, that though the transformation $\hat{T}_t$ is not unitary, $\hat{\rho}_I$ is still hermitian.

For reference in Sec. 5.3.3, we note that $\hat{T}_t$ can be expressed as

$$\hat{T}_t = \exp\left(\sum_{n,n',l,l'} \kappa_{nn'll'}\, \sigma^{+}_{nl}\sigma^{-}_{n'l'}\, t\right), \tag{4.24a}$$

$$\kappa_{nn'll'} = -(\Gamma_{nn'll'} + i\, J_{nn'll'}) - (\Gamma^{\mathrm{IC}}_{nl} - i\omega_{nl})\delta_{nn'}\delta_{ll'}\,. \tag{4.24b}$$

With this, the master equation Eq.(4.12) can be written as

$$\dot{\hat{\rho}}(t) = \frac{1}{i\hbar}\left[\hat{H}(t), \hat{\rho}(t)\right] - \left\{\hat{\Gamma}, \hat{\rho}(t)\right\} + \mathcal{L}'[\hat{\rho}(t)] \tag{4.25}$$

$$= \frac{d}{dt}\left[\hat{T}_t^\dagger \hat{\rho}_I(t)\hat{T}_t\right] \tag{4.26}$$

$$= \frac{1}{i\hbar}\left[\hat{H}_0, \hat{\rho}(t)\right] - \left\{\hat{\Gamma}, \hat{\rho}(t)\right\} + \hat{T}_t^\dagger \dot{\hat{\rho}}_I(t)\hat{T}_t \tag{4.27}$$

Comparison and rearrangement of the last and first line leads to the time evolution of the operator $\hat{\rho}_I$ (note that $\hat{T}_t^{-1} = \hat{T}_{-t}$ which we will use to simplify notation further):

$$\dot{\hat{\rho}}_I(t) = \frac{1}{i\hbar}\left[\hat{W}_I(t)\hat{\rho}_I(t) - \hat{\rho}_I(t)\hat{W}_I^\dagger(t)\right] + \hat{T}_{-t}^\dagger \mathcal{L}'[\hat{\rho}(t)]\hat{T}_{-t} \tag{4.28}$$

where we introduced the (non-hermitian!) perturbation operator

$$\hat{W}_I(t) = \hat{T}_{-t}^\dagger \hat{W}(t)\hat{T}_t^\dagger \tag{4.29}$$

that governs the perturbative dynamics of $\hat{\rho}_I(t)$ in the same way as the corresponding interaction picture Hamiltonian does in the unitary case. As we are interested in an expansion of $\hat{\rho}(t)$ in orders of the (weak) driving fields $\Omega_{nl}(t)$, we formally integrate Eq.(4.28) and rewrite the resulting expression for $\hat{\rho}_I(t)$ with Eq.(4.23) to obtain a self-consistent equation for $\hat{\rho}(t)$:

$$\hat{\rho}_I(t) = \hat{\rho}_I(t_0) - \frac{i}{\hbar}\int_{t_0}^{t} dt' \left[\hat{W}_I(t')\rho_I(t') - \hat{\rho}_I(t')\hat{W}_I^\dagger(t')\right] + \int_{t_0}^{t} dt' \hat{T}_{-t'}^\dagger \mathcal{L}'[\hat{\rho}(t')]\hat{T}_{-t'}\,, \tag{4.30}$$

$$\hat{\rho}(t) = \hat{T}_t^\dagger \hat{\rho}(t_0)\hat{T}_t - \frac{i}{\hbar}\int_{t_0}^{t} dt' \hat{T}_{t-t'}^\dagger \left[\hat{W}(t'), \hat{\rho}(t')\right]\hat{T}_{t-t'} + \int_{t_0}^{t} dt' \hat{T}_{t-t'}^\dagger \mathcal{L}'[\hat{\rho}(t')]\hat{T}_{t-t'}\,. \tag{4.31}$$

The first line of Eq. (4.31) is similar to perturbative density matrix expansions presented in many nonlinear and multi-dimensional optics textbooks [BP08; Muk95; HZ11]. However, here we explicitely include many-body and incoherent effects which are often not taken into account explicitely in these types of approaches.

A particular problem for the perturbative density matrix expansion including non-unitary dynamics presented here, in contrast to above-mentioned textbook examples, is the last term in Eq. (4.31). It prevents a straightforward iterative solution of Eq.(4.31) in a Dyson series [SC95]. Therefore, in this thesis we discuss two cases of interest that allow us to neglect this term for the relevant part of our calculations:

i) Only excitations up to second order are considered which is the defining feature of the low-excitation regime. In the following, we refer to this case, studied in Sec. 4.2.3, as LER case

ii) There are no cross-damping terms but only radiative decay, i.e. $\Gamma_{nn'll'} = \Gamma_{nl}\delta_{nn'}\delta_{ll'}$ and the system has a common ground state $|g_n\rangle = |g\rangle$, which is approximately the case, e.g. if an effective single-particle few-level scheme is considered as is the case in the low-excitation regime in x-ray waveguides [Len+20]. This case, studied in Sec. 4.2.4, is referred to as few-level case[2].

4.2.3 The LER case

The LER case is studied in great detail in Chapter 5. In this case, the last term of Eq. (4.31) only contributes to the total ground state of the many-body system up to second order as will be shown by explicite calculation of this term up to second order in the driving field Hamiltonian part $\hat{W}(t)$. Assuming the nuclear system to be in the many-body ground state

---

[2] Regarding the negligibility of the cross-damping terms it is an interesting but still unanswered question whether the general case including cross-damping terms can be reduced to the specific case studied here and in Chapter 6.

$$\hat{\rho}(t_0) = |G\rangle \langle G| = \bigotimes_{n=1}^{N} |g_n\rangle \langle g_n| \tag{4.32}$$

initially, the zero order contribution to the last term Eq. (4.31) becomes

$$\hat{\sigma}^-_{n'l'} |G\rangle \langle G| \hat{\sigma}^+_{nl} = 0 \;\Rightarrow\; \mathcal{L}'[\hat{\rho}^{(0)}] = 0 \tag{4.33}$$

such that this term does not contribute to the zeroth order density matrix. Note that the action of the time evolution operators $\hat{T}_t$ does not change this result since it conserves the total number of nuclei (or, equivalently, the total population including ground and excited states) in the system and thus, if the system is in the many-body ground state at time t_0 it will remain so at all times. Consequently, the zeroth order density matrix contribution is given by

$$\hat{\rho}^{(0)}(t) = \hat{T}^\dagger_t \hat{\rho}(t_0) \hat{T}_t = \hat{\rho}(t_0) \tag{4.34}$$

and remains constant in time. For calculating the contribution of the $\mathcal{L}'[\hat{\rho}]$ to the first order density matrix contribution we again use that the time evolution operators do not change the number of nuclei such that we obtain after a first order excitation by the driving field at time τ_1

$$\begin{aligned} &\hat{\sigma}^-_{m'k'} \left[\hat{W}(\tau_1), \hat{\rho}^{(0)}(\tau_1)\right] \hat{\sigma}^+_{mk} \\ =& -\frac{\hbar}{2} \sum_{nl} \hat{\sigma}^-_{m'k'} \left(\Omega_{nl}(\tau_1) \hat{\sigma}^+_{nl} |G\rangle \langle G| - h.c.\right) \hat{\sigma}^+_{mk} \\ =& 0 \;\Rightarrow\; \mathcal{L}'[\hat{\rho}^{(1)}] = 0 \end{aligned} \tag{4.35}$$

We conclude that, in first order, the problematic term does not contribute to the dynamics of the nuclear system either such that the first order density matrix can be written as

$$\hat{\rho}^{(1)}(t) = -\frac{i}{\hbar} \int_{t_0}^{t} d\tau \, \hat{T}^\dagger_{t-\tau} \left[\hat{W}(\tau), \hat{\rho}^{(0)}(\tau)\right] \hat{T}_{t-\tau} \, . \tag{4.36}$$

Finally, the second order contribution to the density matrix can be calculating by reinserting the first order contribution into Eq. (4.31). The excitation state of the many body system is thus determined by the double commutator with the driving field part $\hat{W}(t)$ at time τ_2 and the contribution to $\mathcal{L}'[\hat{\rho}^{(2)}(\tau_2)]$ is

$$\begin{aligned} &\hat{\sigma}^-_{m'k'} \left[\hat{W}(\tau_2), \left[\hat{W}(\tau_1), \hat{\rho}^{(0)}(\tau_1)\right]\right] \hat{\sigma}^+_{mk} \\ =& \frac{\hbar^2}{4} \hat{\sigma}^-_{m'k'} \sum_{nl} \sum_{n'l'} \left(\Omega^*_{nl}(\tau_2) \Omega_{n'l'}(\tau_1) \hat{\sigma}^-_{nl} \hat{\sigma}^+_{n'l'} |G\rangle \langle G| + h.c. - \Omega_{nl}(\tau_2) \Omega^*_{nl}(\tau_1) \hat{\sigma}^+_{nl} |G\rangle \langle G| \hat{\sigma}^-_{n'l'} + h.c.\right) \hat{\sigma}^+_{mk} \\ =& -\frac{\hbar}{4} \left(\Omega_{m'k'}(\tau_2) \Omega^*_{mk}(\tau_1) + \Omega_{mk}(\tau_2) \Omega^*_{m'k'}(\tau_1)\right) |G\rangle \langle G| \, . \end{aligned} \tag{4.37}$$

We find that, in second order in the driving field, the problematic term Eq. (4.31) contributes to the ground state dynamics only and, thus, can be neglected if only the excited state sector is of interest. The second order contribution to this sector of the density matrix can then be calculated via another iteration in the self-consistent solution Eq. (4.31):

$$\hat{\rho}^{(2)}_{\mathrm{ES}}(t) = -\frac{i}{\hbar} \int_{t_0}^{t} d\tau \, \hat{T}^\dagger_{t-\tau} \left[\hat{W}(\tau), \hat{\rho}^{(1)}(\tau)\right] \hat{T}_{t-\tau} \, , \tag{4.38}$$

where the subscript ES(= excited state sector) denotes that the ground state dynamics is not taken into account by Eq.(4.38).
The effect of $\mathcal{L}'[\hat{\rho}]$ up to second order is consistent with the observation that this term is usually responsible for refilling of the ground state which, if the system is initially in its ground state, can only occur in second order of the driving field in which excited state population is first created during the excitation as can be seen, e.g. from the self-consistent Eqs. (4.11). Therefore, the problematic term can contribute to the excited state coherences and populations beginning from third order excitations. In this case, which is beyond the scope of this thesis, calculation of the excited state density matrix elements in general becomes much more involved.

4.2.4 The few-level case

In the few-level case of negligible cross-damping terms and a single ground state relevant for effective nuclear few-level schemes in x-ray waveguides, the integrand in the last line of Eq. (4.31) simplifies to

$$
\begin{aligned}
&2\hat{T}^{\dagger}_{t-t'}\sum_{nl}\sum_{n'l'}(\Gamma_{nn'll'}+\Gamma^{\mathrm{IC}}_{nl}\delta_{nn'}\delta_{ll'})\hat{\sigma}^{-}_{n'l'}\hat{\rho}(t')\hat{\sigma}^{+}_{nl}\hat{T}_{t-t'} && (4.39)\\
=&\hat{T}^{\dagger}_{t-t'}\sum_{nl}\gamma_{nl}\hat{\rho}_{l_n l_n}(t')\hat{P}_{g_n}\hat{T}_{t-t'} && (4.40)\\
=&\hat{T}^{\dagger}_{t-t'}\sum_{nl}\gamma_{nl}\hat{\rho}_{l_n l_n}(t')\hat{T}_{t-t'}\hat{P}_{g} && (4.41)
\end{aligned}
$$

where we assumed $\Gamma_{nn'll'}=\Gamma_{nl}\delta_{nn'}\delta_{ll'}$ in the first and $\hat{P}_{g_n}=\hat{P}_{g}$ in the second step, consistent with the initial assumptions. It is crucial for this representation that the nonperturbative dynamics of the excited state sector described by $\hat{T}_t$ decouple from the ground state dynamics in this specific case such that $\left[\hat{P}_g,\hat{T}_{-t}\right]=0$. If the ground states of the nuclear few-level systems are different, the coherent couplings between the systems can scramble excitation between different few-level systems which can effectively couple the ground and excited state sector of individual nuclei by transferring excitation from one system to another. In contrast, in the few-level case considered here, this scrambling of excitation does not occur since only a single multi-level system is involved.
Hence, we can neglect the last term of Eq. (4.31) in the few-level case and the dynamics of the excited state sector in each nuclei-field excitation order can just be calculated iteratively inserting the left-hand side into the right hand side of the first line of Eq. (4.31) yielding the desired density matrix expansion Eq. (4.18) with expansion orders

$$
\hat{\rho}^{(0)}(t)=\hat{T}^{\dagger}_{t-t_0}\hat{\rho}(t_0)\hat{T}_{t-t_0} \qquad (4.42)
$$

$$
\begin{aligned}
\hat{\rho}^{(j>0)}_{\mathrm{ES}}(t)=&\left(\frac{-i}{\hbar}\right)^{j}\int_{t_0}^{t}d\tau_j\cdots\int_{t_0}^{\tau_3}d\tau_2\int_{t_0}^{\tau_2}d\tau_1\times \qquad (4.43)\\
&\times\hat{T}^{\dagger}_{t-\tau_j}\left[\hat{W}(\tau_j),\ldots\hat{T}^{\dagger}_{\tau_2-\tau_1}\left[\hat{W}(\tau_1),\hat{T}^{\dagger}_{\tau_1-t_0}\hat{\rho}(t_0)\hat{T}_{\tau_1-t_0}\right]\hat{T}_{\tau_2-\tau_1}\ldots\right]\hat{T}_{t-\tau_j}
\end{aligned}
$$

It is important to note, however, that the ground state state dynamics has to be calculated separately in this case in each order using unitarity of the density operator $\mathrm{Tr}\left[\hat{\rho}\right]=1$ such that

$$
1=\sum_{l}\rho^{(0)}_{ll}\ ,\quad 0=\sum_{l}\rho^{(j)}_{ll}\ ,\quad j\geq 1 \qquad (4.44)
$$

where we dropped the index n referring to the index of each nucleus instead considering the system with the single ground state as a single multi-level system with ground state $|G\rangle$ and excited states $|l\rangle$. We emphasize that the expression Eq. (4.43) is only true for the excited state sector and if the ground state populations are correctly calculated using the Eq. (4.44).

We conclude this Chapter with a brief summary of the results: In the first part, we derived self-consistent equations for the population and coherence of two-level systems that allows for the calculation of the nuclear dynamics, including decay to all orders, for a wide range of pulse shapes and sequences. These equations will be used in Chapter 5 to compare the incoherent and coherent dynamics of effective two-level systems in the LER and beyond and in Chapter 7 to compare the dynamics of two-level systems excited by different double pulse sequences. In the second part of this Chapter, a more general density matrix expansion was presented, that allows to include multiple excited states and many-body dynamics. Two cases of special interest and the necessary approximations to derive explicit perturbative expansions were discussed: First, the case of low excitations, for which explicit expressions for zeroth to second density matrix could be derived. Second, for the few-level case an explicit expression for all orders of the excited state sector could be derived for specific cases of interest. The low-excitation case will be discussed further in Chapter 5 while the few-level case is treated in Chapter 6.

Chapter 5

Detecting and characterizing x-ray excitation of Mössbauer nuclei beyond the low-excitation regime

This chapter is based on the following publication:

A characterization and detection method for x-ray excitation of Mössbauer nuclei in the low-excitation regime
L. Wolff and J. Evers
Accepted by *Physical Review A*
A preprint version can be found on arxiv:
https://arxiv.org/abs/2308.07644

The author of this thesis is the main author of this publication. The main content has been reproduced in many cases verbatim with permission of the journal (© 2023 American Physical Society) and coauthors. A part on the low-excitation emission properties of noninteracting many-body systems was added in Sec. 5.3.2 as an intermediate instructive step to the full interacting case, an alternative derivation of the population-coherence correspondence in a nuclear exciton basis is presented in Appendix A.6, complementing the product basis approach chosen in the publication and main text. Further, the definition of the pulse area $\mathcal{A}$ has been changed by a factor of 1/2 such that it can be interpreted as the polar angle on the Bloch sphere. The plots and calculations have been adapted accordingly. The main physics content has not changed. Finally, two Sections discussing the Autler-Townes splitting of the nuclear resonance at higher excitations (Sec. 5.5.5) and the effect of decaying pulses and nuclear two-level decay have been added to elaborate on corresponding discussions in the publication. To integrate the publication into this thesis some minor changes in the introduction have been undertaken, to avoid repeating content, and the derivation of the density matrix expansions was moved Chapter 4, since it is also used in other Chapters and is seen by the author as an integral part of this thesis.

List of abbreviations used in this Chapter:

- LER: low-excitation regime
- NRS: nuclear resonant scattering
- XFEL : x-ray free electron laser
- XFELO : x-ray free electron laser oscillator
- FFC spectrum : frequency-frequency correlation spectrum

5.1 Introduction

In Chapter 3 we studied and evaluated NRS spectra using linear response theory. This is valid since experiments on Mössbauer nuclei have been restricted to the low-excitation regime (LER) so far, because of their narrow spectral linewidth (cf. 2.1.1), which is orders of magnitude smaller than the bandwidth of x-ray pulses by state-of-the-art accelerator-based x-ray sources. This can be a severe

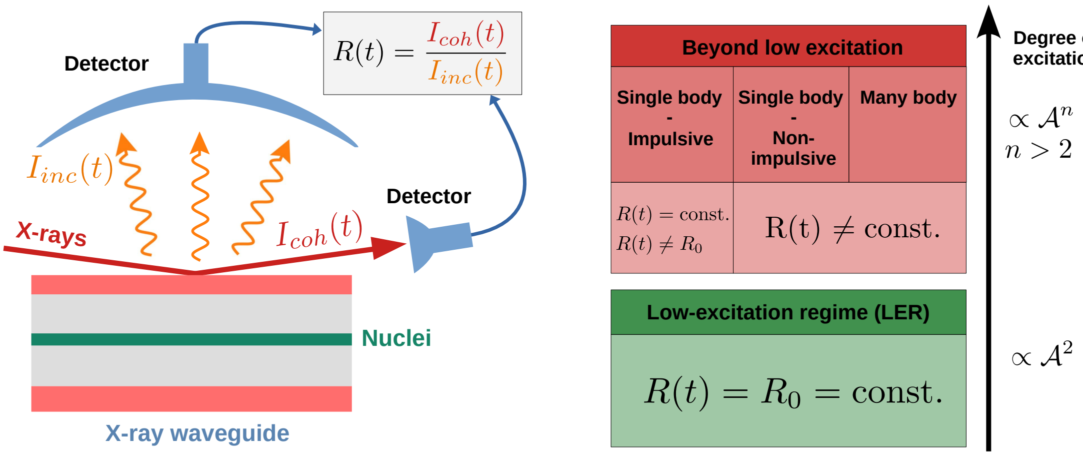

Figure 5.1: Schematic setup and summary of the main results. The central goal of this work is to identify experimentally relevant signatures which enable one to verify the excitation of an ensemble of Mössbauer nuclei beyond the low-excitation regime (LER) explored up to now. For this, we consider an ensemble of two-level nuclei embedded in an x-ray waveguide, probed by near-resonant x-rays in grazing incidence. To detect the non-linear excitation, the coherently and the incoherently (e.g., following internal conversion) scattered intensities are recorded. Our theoretical analysis shows that in the LER, the ratio $R(t) = R_0$ of the two intensities is constant, even though both intensities individually depend on time. We show this by analytically calculating the relevant dynamics of the excited-state populations and the x-ray-induced coherences of the general interacting N-body system in second order of the x-ray pulse area $\mathcal{A}$. Upon excitation beyond the LER, the ratio R changes its properties in a characteristic way. In case of near-instantaneous impulsive excitation of an effective single-particle system or a sufficiently weakly-coupled many-body system, the ratio R remains constant, but changes its value from R_0 depending on the degree of excitation. For a strongly-interacting impulsively-driven many-body system, the ratio becomes time-dependent upon excitation beyond the LER. In case of non-impulsive x-ray excitation with duration of the order of the nuclear lifetime, the ratio is also time-dependent at higher excitation. Based on these results, a variety of different experimental signatures or data analysis approaches is developed which allow one to verify excitations beyond the LER.

restriction, as for many applications in quantum optics and spectroscopy, nonlinear light-matter interactions are essential.
The situation is expected to change with the recent availability of (seeded) x-ray-free electron lasers [Emm+10; Ama+12; Ish+12; Ino+19; Dec+20; Nam+21; Liu+], which can provide a large number of nuclear-resonant photons per pulse. Further progress is anticipated with x-ray free-electron laser oscillators (XFELO) [KSR08; Ada+19b]. Theoretical studies suggest that this may allow one to excite nuclear ensembles even up to the point of inversion [HKE16a; Che+22; BS97; Len21]. However, a first experiment on multi-photon excitation still found data consistent with linear excitation conditions [Chu+18], and initially, future experiments are likely to only slightly surpass the LER. While experiments to verify high excitation and inversion in nuclear resonant scattering have been suggested [HKE16a], experimentally relevant signatures at the onset of non-linear excitation of the nuclear ensemble are still largely lacking.

To fill this gap, here, we develop and explore a method to verify the excitation of nuclear ensembles by intense x-ray light beyond the LER. To this end, we propose to correlate two observables that are readily accessible in nuclear resonant scattering experiments, namely the highly directional coherently scattered intensity on the one hand and incoherent scattering products such as fluorescence emission and conversion electrons that are scattered into the entire solid angle on the other hand, see Fig. 5.1. Our results show that in the LER, i.e. up to second order in the x-ray-nuclei interaction, these two observables become essentially equivalent. In particular, we prove that the ratio of both observables becomes constant, a result that is largely independent of the details of the nuclear system and the temporal and spectral shape of the x-ray-nuclei interaction. Conversely, we demonstrate that already in leading nonlinear excitation order, this ratio changes with the strength of the interaction and in a number of important cases becomes time-dependent. In particular, we study the case of impulsive excitation of nuclear ensembles with weak and strong nucleus-nucleus interactions corresponding to standard pulse conditions at accelerator-based light sources. Further, we identify clear experimental signatures of excitations beyond the LER for near-monochromatic pulses, e.g., from synchrotron-

Mössbauer-like sources [Ger+85b; Smi+97b; Set+09; Mas+08; Pot+12] generalized to operation at x-ray free-electron lasers [Chu+18]. The correlation of coherently and incoherently scattered intensities also allows one to rigorously benchmark theoretical models of nonlinear excitations against experimental data and helps to characterize deviations from effective low-excitation descriptions of nuclear ensembles.

This Chapter is structured as follows: In Sec. 5.2 the theoretical model for the nuclear ensemble is introduced, the two relevant observables are presented and the cases of impulsive and non-impulsive x-ray excitation are defined. Sec. 5.3 outlines the basic principle of the distinction between the LER and excitations beyond that regime. Subsequently the proof of the equivalence between coherent and incoherent dynamics up to second order in the x-ray-nuclei coupling is given first for effective two-level schemes, second for non-interacting many-body systems and finally for interacting many-body systems. The last two sections focus on signatures of excitation beyond the LER for different pulse structures. Sec. 5.4 compares analytical results for weakly-coupled nuclear ensembles with numerical studies of strongly coupled nuclei upon impulsive excitations. Section 5.5 identifies different signatures for nonlinear excitation of effective two-level systems upon near-resonant and exponentially-decaying x-ray fields. Finally, Sec. 5.6 discusses and summarizes the results.

5.2 Theoretical background

In this Section, the theoretical model used to describe the nuclear ensemble dynamics is presented. Subsequently, the two observables relevant for the characterization of nonlinear excitation and the different types of x-ray excitation considered in our analysis are introduced.

5.2.1 Theoretical model for the nuclear ensemble

In the following, for definiteness, we focus our discussion on the case of nuclei embedded in planar thin-film waveguides, probed by the x-rays in grazing incidence on the waveguide structure [HT99b; RE21a; Röh04]. Such photonic environments allow one to tailor the nuclear dynamics, and the possibility to enhance the nuclear excitation for a given x-ray pulse using a suitable design of the nuclear environment has been suggested [HKE16a; Che+22; DLE22b; DLE22c]. Interestingly, the lossy nature of the x-ray waveguides leads to an interplay of multiple cavity modes [Len+23] which may affect the nuclear dynamics favorably. Furthermore, one may expect that waveguides probed in reflection can be more stable under the action of intense x-ray light, as compared to thicker sample foils probed in forward direction. Finally, a detailed quantum optical description has been developed for the waveguide setting [HE13; HE15b; Len+20; KCP20b], which serves as the starting point for our present analysis.

In general, the interaction of x-rays with nuclei gives rise to a large variety of processes, e.g., based on recoil-less interaction or interaction with recoil, or on radiative or non-radiative de-excitation channels. A detailed discussion of these contributions in the LER regime can be found, e.g., in [Smi+07; HT99b]. In the following, we aim at a description of the nuclear dynamics beyond the LER, focusing on coherent scattering in propagation direction of the driving x-ray pulse and incoherent emission following internal conversion as the main observables. To this end, we employ the model of N identical interacting nuclei introduced in Sec. 4.2.1. Here, we consider the specific case of two-level systems such that the indices l, l' labelling different excited states in Eqs. (4.14), (4.15) and (4.17) can be dropped. We further assume the identical transition frequencies ω_0 and radiative and non-radiative decay rates Γ_{nn} and Γ_{IC} which is reasonable in the absence of local perturbations of the nuclear ensemble. In this case, the Hamiltonian of the nuclear ensemble [Aga74; FS05; Kif+10; Len+20; KCP20b; LKE16b; LE14a; LE14b; AG+17] can be written as

$$\hat{H} = \hbar \sum_{n=1}^{N} \omega_0 \, \hat{\sigma}_n^+ \hat{\sigma}_n^- - \frac{\hbar}{2} \sum_{n=1}^{N} \left[\Omega(\mathbf{r}_n, t) \, \hat{\sigma}_n^+ + h.c. \right] - \hbar \sum_{n,n'=1}^{N} J_{nn'} \, \hat{\sigma}_n^+ \hat{\sigma}_{n'}^- \, . \tag{5.1}$$

Here, n and n' label the individual two-level systems and $\hat{\sigma}_n^\pm$ are the raising and lowering operators of nucleus n in its two-level Hilbert space. Further,

$$\Omega(\mathbf{r}_n, t) = \frac{\mathbf{d} \, \mathbf{E}(\mathbf{r}_n, t)}{\hbar} \tag{5.2}$$

denotes the semi-classical light-matter coupling in the form of the time-dependent Rabi frequency with $\mathbf{E}(\mathbf{r}_n, t)$ describing the electric field amplitude at the position $\mathbf{r}_n$ of nucleus n, and $\mathbf{d}$ the transition dipole moment [1]. Note that, compared to Sec. 4.2.1, the dependence of the Rabi frequency on the nuclear index n is assumed to depend on the value of the x-ray field $\mathbf{E}$ at positions $\mathbf{r}_n$ only as the nuclear dipole moments are identical. Finally, possible interactions between the nuclei are included via the dipole-dipole coupling parameters $J_{nn'}$ which satisfy the symmetry property $J_{nn'} = J^*_{n'n}$.

The nuclear many-body dynamics is then characterized by a density operator $\hat{\rho}^{\mathrm{NB}}$ governed by the master equation [Aga74; FS05; Kif+10; Len+20; KCP20b; LKE16b; LE14a; LE14b; AG+17]

$$\frac{d}{dt}\hat{\rho}^{\mathrm{NB}} = \frac{1}{i\hbar}\left[\hat{H}, \hat{\rho}^{\mathrm{NB}}\right] + \mathcal{L}[\hat{\rho}^{\mathrm{NB}}]\,, \tag{5.3}$$

where “NB” stands for N-body, and the Lindblad term is given by

$$\mathcal{L}[\hat{\rho}^{\mathrm{NB}}] = \sum_{n,n'=1}^{N} \Gamma_{nn'}\left(2\hat{\sigma}^-_{n'}\hat{\rho}^{\mathrm{NB}}\hat{\sigma}^+_n - \left\{\hat{\sigma}^+_n\hat{\sigma}^-_{n'}, \hat{\rho}^{\mathrm{NB}}\right\}\right) + \sum_{n=1}^{N}\Gamma_{\mathrm{IC}}\left(2\hat{\sigma}^-_n\hat{\rho}^{\mathrm{NB}}\hat{\sigma}^+_n - \left\{\hat{\sigma}^+_n\hat{\sigma}^-_n, \hat{\rho}^{\mathrm{NB}}\right\}\right)\,. \tag{5.4}$$

It incorporates both, single-particle decay as diagonal elements with $n = n'$, and incoherent dipole-dipole couplings between the nuclei with $n \neq n'$. Note that the total natural line width γ of the nuclei comprises radiative decay contributions ($\propto \Gamma_{nn}$), and non-radiative internal conversion contributions ($\propto \Gamma_{\mathrm{IC}}$),

$$\gamma = 2\left(\Gamma_{nn} + \Gamma_{\mathrm{IC}}\right)\,. \tag{5.5}$$

The coupling constants entering the master equation Eq. (5.3) can conveniently be calculated ab-initio using the classical Green’s function [GW96; DKW02; SB08; AG+17; NH06; BW07] characterizing the nuclear environment [Len+20], which is analytically known [Tom95; BW07; AG+17]. In turn, a suitable optimization of the environment can be used to reverse engineer desired couplings [BB20; DLE22b; DLE22c].

The many-body problem Eq. (5.3) in general is challenging to solve. However, in the LER, enforced in the equations of motion by neglecting possible populations of the nuclear excited states by setting $\langle\hat{\sigma}^+_n\hat{\sigma}^-_n\rangle = 0$, the problem allows for a substantial reduction of the relevant Hilbert space. In this case, by rewriting the system in Fourier space in terms of a spin-wave basis, the problem of many interacting nuclei embedded in the cavity environment can equivalently be rewritten in terms of an effective single-particle level scheme [Röh+10; Röh+12; HE13; HE15b; Len+20; RES20b; RE21a; KCP20b; DLE22c; DLE22b]. Interestingly, the effective level scheme may differ from the original level scheme of the individual nuclei. The number of relevant energy eigenstates can be engineered, and it may also comprise additional couplings between levels induced by the cavity environment which can simulate otherwise unavailable control laser fields. As a result, level schemes can be realized which otherwise are not available with Mössbauer nuclei. This feature forms the basis of most experiments on nuclear quantum optics with nuclei in waveguides reported so far [RES20b; RE21a; Röh+10; Röh+12; Hee+13; Hee+15c; Hab+16; Hab+17; Hee+15b; Ma+22]. A more detailed discussion of the dynamics of effective few-level schemes in the LER can be found in Chapter 6.

It is expected that this equivalent description in terms of a single few-level system breaks down towards higher excitation of the nuclear ensemble [Len+20; LE14a; LE14b]. Nevertheless, the single-particle description provides a good starting point for the following analysis of experimental signatures at the onset of effects beyond the LER. Afterwards, in Sec. 5.3.3, we will also consider the full many-body dynamics in leading and next-to-leading order of the interaction between x-rays and nuclei accompanied by numerical simulations of higher excitation orders to explore possible deviations from the single-particle results in the excitation beyond the linear regime.

Note that a similar treatment in principle can also be applied to nuclear forward scattering (for an introduction, see e.g. [HT99b; Röh04]), by employing the corresponding free-space Green’s function to calculate the parameters entering the master equation. However, in this geometry, the incident x-rays typically excite multiple eigenmodes of the many-body Hamiltonian, and propagational effects arising due to multiple interactions in the thicker samples lead to further modifications of the scattered light signatures [LHH60b; HT99b]. Therefore, for simplicity, we focus on reflection geometries in the following analysis.

---

[1] Note that the Mössbauer transitions in some isotopes such as ^{57}Fe may instead feature other dominant multipole moments, such as M1 magnetic dipole moments. In this case, the expression for the Rabi frequency should be modified accordingly. For details, see also Sec. 2.2.1.

5.2.2 Observables

In the following discussion, we will consider two standard observables in nuclear resonant scattering, see Fig. 5.1. First, the time-dependent intensity $I_{coh}(t)$ of the coherently scattered x-rays. This quantity is highly directional: In forward scattering geometry, this signature is emitted in forward direction, due to interference between the scattering contributions of the different nuclei [Smi86; HT99b; Röh04]. In reflection geometry, it is emitted in a direction essentially given by Bragg's law. Second, the time-dependent intensity $I_{inc}(t)$ of the incoherent signatures, e.g., fluorescence photons or conversion electrons of the nonradiative de-excitation of the nuclei via internal conversion [Stu+96; BHS94; Bar+96; Ser+06; Smi+07]. The relative contribution of the nonradiative to the radiative channel to the total nuclear decay is described by the internal conversion coefficient α [HT99b; Röh04]. Note that the two observables can be measured concurrently [Smi+07]. In the following, we will show that the comparison of these two observables allows one to identify excitations of the nuclei beyond the LER.

In incoherent scattering, the nuclei decay independently, such that the observed signal intensity is proportional to the sum of excited-state populations of the nuclei [Aga74; FS05],

$$I_{inc}(t) \propto \sum_{n=1}^{N} \langle \hat{\sigma}_n^+ \hat{\sigma}_n^- \rangle \,. \tag{5.6}$$

Note that the pre-factors will not be of relevance in the following analysis. This has the additional advantage that experimental details such as the detection geometry, or attenuation within the sample or between sample and detector do not have to be characterized quantitatively for our analysis.

In contrast, the radiatively emitted scattered light can be evaluated by relating the positive- and negative-frequency components of the electric field operators $\hat{E}^{(\pm)}$ to the transition operators $\hat{\sigma}_n^{\mp}$ [Aga74; FS05], which act as source operators for the emitted radiation. The total coherently emitted intensity in direction $\mathbf{k}_{out}$ can then be written as [Aga74; FS05],

$$I_{rad}(t, \mathbf{k}_{out}) \propto \sum_{n,m=1}^{N} \langle \hat{\sigma}_n^+ \hat{\sigma}_m^- \rangle \, e^{i\mathbf{k}_{out}(\mathbf{r}_n - \mathbf{r}_m)} \,, \tag{5.7}$$

where $\mathbf{k}_{out}$ is the wave vector of the emitted radiation, and we again have omitted the pre-factors. Using a decomposition of the transition operators into their expectation values and a fluctuation part $\hat{\sigma}_n^{\pm} = \langle \hat{\sigma}_n^{\pm} \rangle + \delta\hat{\sigma}_n^{\pm}$ [CT77], we can extract the coherently scattered contribution as

$$\begin{aligned} I_{coh}(t, \mathbf{k}_{out}) &\propto \sum_{n,m=1}^{N} \langle \hat{\sigma}_n^+ \rangle \, \langle \hat{\sigma}_m^- \rangle \, e^{i\mathbf{k}_{out}(\mathbf{r}_n - \mathbf{r}_m)} \\ &= \left| \sum_{n=1}^{N} e^{i\mathbf{k}_{out}\mathbf{r}_n} \langle \hat{\sigma}_n^+ \rangle \right|^2 \,. \end{aligned} \tag{5.8}$$

The last expression clearly exhibits the interference between the contributions scattered by the individual two-level nuclei. If the incident x-rays with wave vector $\mathbf{k}_{in}$ imprint a position-dependent phase pattern on the two-level nuclei, the additional phase accumulated due to $\mathbf{k}_{out}$ together with the sum over all two-level atoms leads to the directional emission described at the beginning of this section.

Note that the incoherently and coherently scattered intensities Eqs. (5.6), (5.8) can be expressed in terms of single-particle reduced density matrix elements,

$$\langle \hat{\sigma}_n^+ \hat{\sigma}_n^- \rangle = \mathrm{Tr}\left[\hat{\rho}^{\mathrm{NB}} \hat{\sigma}_n^+ \hat{\sigma}_n^- \right] = \rho_{e_n e_n} \,, \tag{5.9}$$

$$\langle \hat{\sigma}_n^+ \rangle = \mathrm{Tr}\left[\hat{\rho}^{\mathrm{NB}} \hat{\sigma}_n^+ \right] = \rho_{g_n e_n} \,. \tag{5.10}$$

Here, $|g_n\rangle$ [$|e_n\rangle$] denote the ground [excited] state of nucleus n, $\hat{\rho}^{\mathrm{NB}}$ is the N-body density matrix the dynamics of which is governed by the master equation Eq. (5.3), and Tr $[\cdot]$ denotes the trace over the many-body Hilbert space. Analogous relations hold for effective single-particle level schemes as introduced below in Sec. 5.2.1.

Throughout this Chapter, we will consider ratios of these two observables

$$R(t) = \frac{I_{coh}(t)}{I_{inc}(t)} \tag{5.11}$$

and show that this ratio becomes time-independent in the LER, essentially independent of the specific properties of the nuclear ensemble and the time- and frequency structure of the exciting x-ray pulses. Further, we will argue that a time-dependent ratio $R(t)$ or a change of its value as a function of the incident pulse energy signifies excitation beyond the LER.

5.2.3 Impulsive and non-impulsive x-ray excitation

Throughout this work, we consider two qualitatively different x-ray excitation approaches for the nuclei. Accelerator-based x-ray sources typically deliver x-ray pulses with durations on the ∼ps (synchrotron) or ∼fs (x-ray free electron laser) scale. In contrast, typical lifetimes of standard Mössbauer isotopes are orders of magnitude longer (for example, the natural lifetime of the most commonly used Mössbauer resonance in ^{57}Fe is 141 ns [Röh04]). As a result, the x-ray excitation is *impulsive* in the sense that it is near-instantaneous as compared to all natural time scales of decay and coupling dynamics of the nuclei. Therefore, collective effects such as couplings between the nuclei or their decay processes can be completely neglected throughout the x-ray excitation, and the nuclear excitation dynamics can be evaluated simply by considering the x-ray induced dynamics on the single-nucleus level. After initial excitation, the nuclei then evolve on their natural time scales in the absence of the exciting x-ray pulse. This temporal separation of excitation and subsequent nuclear ensemble dynamics considerably simplifies the analysis. [Len21]

Next to this impulsive excitation, we further consider the case in which the duration of the incident x-ray field is not restricted to very short times. We denote this more general case as *non-impulsive* excitation, and will in particular consider the case in which the duration of the driving x-ray field is comparable to the other evolution time scales of the nuclei. This situation becomes of relevance if x-ray pulses are used which are monochromatic on the nuclear energy scales, e.g., delivered by a synchrotron (or analogously extended free-electron laser) Mössbauer source [Ger+85b; Smi+97b; Set+09; Mas+08; Pot+12; Chu+18], or in setups employing additional reference absorbers to shape the incoming x-ray pulse like the recently demonstrated coherent control schemes for nuclear dynamics [Hee+21]. In the non-impulsive case, the complete dynamics involving x-ray excitation, couplings and decay processes must be considered at the same time.

In Sections 5.4 and 5.5, the two cases will be analyzed separately.

5.3 Characterization and detection of dynamics beyond the low-excitation regime

In this Section, we present and analyze the main idea of our approach to detect and characterize nuclear dynamics beyond the low-excitation regime. We start with the simplest possible example involving the coherent dynamics of a two-level system, to illustrate the main idea of identifying dynamics beyond the LER based on a comparison of the coherently scattered intensity and the incoherently scattered intensity. Next, we generalize the idea to the full dissipative dynamics of a single effective two-level system, which is of relevance, e.g., in the context of a nuclear ensemble in a cavity environment. Finally, we establish our approach in the general case of an interacting nuclear many-body system. The main purpose of this Section is to prove the equivalence of coherently and incoherently scattered intensity in the LER, largely independent of the specific details of the nuclear ensemble and the x-ray driving fields, and establish deviations from this equivalence as a means to characterize excitation beyond that regime.

5.3.1 Example illustrating the approach to detect excitation beyond the low-excitation regime

As discussed in Sec. 5.2.1, effective single-particle models for nuclei in waveguides provide a good starting point for the analysis of experimental signatures at the onset of effects beyond the LER. Here, we start with the simplest possible case, and consider the excitation dynamics of a single two-level system resonantly driven by an impulsive x-ray pulse.

We denote the ground and excited states of the two-level system as $|g\rangle$ and $|e\rangle$, respectively, and characterize its state via a density operator with matrix elements $\rho_{ij}(t)$ ($i, j \in \{e, g\}$; see Sec. A.10 for the equations of motion). Assuming the system to be initially in its ground state, i.e.

$$\begin{aligned} \rho_{ee}(t=0) &= 0\,, \qquad & \rho_{ge}(t=0) &= 0\,, \\ \rho_{eg}(t=0) &= 0\,, \qquad & \rho_{gg}(t=0) &= 1\,, \end{aligned}$$

the time-dependent density matrix elements describing the excited-state population and the x-ray induced coherence in a suitable interaction picture can be evaluated using the area theorem (for a derivation, see Sec. A.9 or Refs. [AE75; MS07]) to give

$$\rho_{ee}(t) = \sin^2\left[\frac{1}{2}\mathcal{A}(t)\right]\,, \tag{5.12a}$$

$$\rho_{ge}(t) = -\frac{i}{2}e^{i\phi}\sin\left[\mathcal{A}(t)\right]\,, \tag{5.12b}$$

where t denotes the time after the impulsive x-ray pulse has passed the system, which is much shorter than the lifetime of the resonance such that the decay can be neglected. The x-ray pulse area $\mathcal{A}$ is given by

$$\mathcal{A}(t) = \int_{t_0}^{t} \Omega(t')dt'\,, \tag{5.13}$$

where $\Omega(\phi, t) = \Omega(t)\exp(-i\phi)$ is the Rabi frequency in the interaction picture (cf. Sec. A.9) proportional to the time-dependent x-ray field amplitude, with constant phase ϕ which accounts, e.g., for the spatial dependence of the incident x-ray field. Note that the pulse area enters the diagonal density matrix element corresponding to the nuclear excited-state population with a pre-factor of 1/2. As a result, the two quantities $\rho_{ee}(t)$ and $|\rho_{ge}(t)|^2$ related to the incoherent and coherent x-ray emission from the nuclei are not equivalent in general.

To explore the relation of the two observables in more detail, we expand Eqs. (5.12) for the case of low pulse area,

$$\rho_{ee}(t) = \frac{1}{4}\mathcal{A}(t)^2 - \frac{\mathcal{A}(t)^4}{48} + \frac{\mathcal{A}(t)^6}{1440} + \dots\,, \tag{5.14a}$$

$$|\rho_{ge}(t)|^2 = \frac{1}{4}\mathcal{A}(t)^2 - \frac{\mathcal{A}(t)^4}{12} + \frac{\mathcal{A}(t)^6}{90} + \dots\,. \tag{5.14b}$$

We find that, in leading order, the coherently and incoherently scattered light proportional to the coherence squared and the population are equivalent,

$$\rho_{ee}^{(0-2)}(t) = \frac{1}{4}\mathcal{A}^2(t) = |\rho_{ge}^{(0-2)}(t)|^2\,, \tag{5.15}$$

where the superscript $(0-2)$ indicates the Taylor expansion including all contributions up to second order of the indexed quantities.

In contrast, if the nuclei are excited beyond the leading low-excitation order, we find that the two observables differ,

$$\rho_{ee}^{(4)}(t) \neq \left(|\rho_{ge}(t)|^2\right)^{(4)} = 2\mathrm{Re}\left[\rho_{ge}^{*(1)}(t)\rho_{ge}^{(3)}(t)\right]\,, \tag{5.16}$$

where the superscript (i) denotes the ith-order contribution of the series expansion only. As a result, we conclude that suitably analyzed deviations in the two observables provide a direct signature for the excitation of the nuclear ensemble beyond the LER.

Equation (5.16) also shows how the expansion of the off-diagonal density matrix element itself enters the expansion of its magnitude squared. As expected, the leading order violating the equivalence of the coherent and incoherent scattering comprises contributions from the third order of the off-diagonal density matrix elements, which illustrates the significance of the x-ray-nuclei interaction beyond the linear regime for this contribution.

In analyzing experimental data, it may be favorable to consider ratios of coherently and incoherently scattered light, corresponding to suitable ratios of squared coherences and populations such as

$|\rho_{ge}|^2/\rho_{ee}$ as experimentally-accessible quantities to characterize excitation beyond the leading low-excitation order. The reason is that then, experimental aspects such as pre-factors related to the detection geometry or efficiency become largely irrelevant in analyzing the data. The ratio expands in orders of the pulse area as

$$\begin{aligned}\frac{|\rho_{ge}(t)|^2}{\rho_{ee}(t)} &= \frac{\mathcal{A}(t)^2 - \frac{\mathcal{A}(t)^4}{3} + \frac{2\mathcal{A}(t)^6}{45} + \dots}{\mathcal{A}(t)^2 - \frac{\mathcal{A}(t)^4}{12} + \frac{\mathcal{A}(t)^6}{360} + \dots} \\ &= 1 - \frac{1}{4}\mathcal{A}^2(t) + \frac{\mathcal{A}^4(t)}{48} + \dots . \end{aligned} \tag{5.17}$$

Thus, it deviates from unity already in second order of the pulse area. However, it is important to note that this is due to cancellations in the expansion order of the numerator and the denominator of the ratio. Corrections of order $\mathcal{A}^2(t)$ in the ratio may only occur if the off-diagonal density matrix elements ρ_{eg} and ρ_{ge} have contributions of order $\mathcal{A}^3(t)$ or higher, and/or the populations ρ_{ee} of order $\mathcal{A}^4(t)$ or higher. Therefore, we can attribute deviations in the ratio from unity to excitations of the system beyond the LER.

In the following Sections, we will extend the characterization of excitation beyond the LER based on the relation between coherently and incoherently scattered radiation to more complex settings and to non-impulsive nucleus-field interactions, and will develop various approaches to analyze the two observables for this purpose.

5.3.2 Effective two-level system excited by non-impulsive x-ray fields

In Sec. 5.3.1 we have used the simplest case of the excitation dynamics of a single effective two-level system driven by an impulsive x-ray field to illustrate the main idea of comparing the coherent and the incoherent light scattering off of the nuclei to identify excitation beyond the LER. Next, we develop this argument further by deriving a self-consistent solution to the dynamics of the two-level system driven by x-ray fields with arbitrary time-dependence and including decay dynamics. This will allow us to also study the non-impulsive x-ray excitation case. Note that the effective level scheme may have decay rates or transition frequencies which differ from the bare nuclear properties [Röh+10; HE13; Len+20; DLE22b]. Nevertheless, for notational simplicity, in the following, we will continue to use the symbols γ and ω_0 introduced above as the single-nucleus properties also in the effective two-level case.

Self-consistent solution for the effective two-level system

As discussed in Sec. 5.2.1, the nuclear many-body system in a waveguide can be modeled using an effective single-particle description in the LER. For the simplest case of an effective two-level scheme, self-consistent solutions to the equations of motion for the excited-state population and the x-ray-induced coherence can be derived, which are given by (see Sec. 4.1 for the derivation)

$$\begin{aligned}\rho_{ee}(t,t_0) &= \frac{1}{2}e^{-\gamma t}\mathrm{Re}\Big[\int_{t_0}^{t} dt' e^{\frac{\gamma}{2}t'} e^{-i\omega_0 t'}\Omega^*(t')\int_{t_0}^{t'} dt'' e^{i\omega_0 t''} e^{\frac{\gamma}{2}t''}\Omega(t'')\Big] \\ &\quad - e^{-\gamma t}\mathrm{Re}\Big[\int_{t_0}^{t} dt' e^{\frac{\gamma}{2}t'} e^{-i\omega_0 t'}\Omega^*(t')\int_{t_0}^{t'} dt'' e^{i\omega_0 t''} e^{\frac{\gamma}{2}t''}\Omega(t'')\rho_{ee}(t'',t_0)\Big] ,\end{aligned} \tag{5.18a}$$

$$\begin{aligned}\rho_{ge}(t,t_0) &= -\frac{i}{2}e^{i\omega_0 t}e^{-\frac{\gamma}{2}t}\int_{t_0}^{t} dt' e^{-i\omega_0 t'}\Omega^*(t')e^{\frac{\gamma}{2}t'} \\ &\quad - ie^{i\omega_0 t}e^{-\frac{\gamma}{2}t}\int_{t_0}^{t} dt' e^{-i\omega_0 t'}e^{-\frac{\gamma}{2}t'}\Omega^*(t')\int_{t_0}^{t'} dt'' e^{\gamma t''}\mathrm{Im}\big[\Omega(t'')\rho_{ge}(t'',t_0)\big] .\end{aligned} \tag{5.18b}$$

Here, we have assumed that the effective nucleus is initially in the ground state at time t_0. Note that as expected, the population only comprises terms of even orders in the nucleus-field coupling $\Omega(t)$ while the coherence only comprises odd orders.

In the next Subsection 5.3.2, we will systematically expand this solution in orders of the driving x-ray field amplitude, in order to establish the relations between the excited-state population and the x-ray induced coherences which will allow us to identify signatures for excitation beyond the LER.

Coherence-population correspondence in second-order of the driving x-ray field

As illustrated in Sec. 5.3.1, our approach to identify x-ray excitations of the nuclear ensemble beyond the LER relies on a comparison of the coherently and incoherently scattered light, which relate to the nuclear excited-state population and the x-ray-induced coherence squared. It is based on the result that the population and the absolute value of the coherence squared are identical up to second order in the exciting x-ray field. Any deviation from this equality therefore indicates excitation beyond the LER.

Next, we derive the correspondence between the population and coherence for effective nuclear two-level systems driven by general time-dependent x-ray fields. To this end, we expand Eqs. (5.18) in powers of the driving x-ray field amplitude.

In the absence of the x-ray field, the nuclei are in their ground state,

$$\begin{aligned}\rho_{ee}^{(0)}(t=t_0) &= 0\,, \qquad & \rho_{ge}^{(0)}(t=t_0) &= 0\,,\\ \rho_{eg}^{(0)}(t=t_0) &= 0\,, \qquad & \rho_{gg}^{(0)}(t=t_0) &= 1\,.\end{aligned}$$

Iteratively solving the self-consistent equations in a perturbative expansion, we find in first order in the driving x-ray field that

$$\rho_{ge}^{(1)}(t) = \int_{t_0}^{t} d\tau\, f(t,\tau)\,, \tag{5.19a}$$

$$\rho_{ee}^{(1)}(t) = 0\,, \tag{5.19b}$$

where we defined the function $f(t,\tau)$ as the integrand in Eq. (5.19a) as

$$f(t,\tau) = -\frac{i}{2} e^{-\frac{\gamma}{2}(t-\tau)} e^{i\omega_0(t-\tau)}\, \Omega^*(\tau)\,, \tag{5.20}$$

for reasons which will become clear in the next step. Note that Eq. (5.19a) bears similarity to the lowest-order result in Sec. 5.3.1 involving the pulse area in Eq. (5.13) in that the off-diagonal density matrix element depends on an integral over the coupling Rabi frequency over time. However, the more complete analysis here allows us to incorporate more degrees of freedom in our analysis such as detunings between exciting x-ray pulse and two-level system or decay processes.

Going further in the perturbative expansion, we find that the second-order contributions can be written as,

$$\rho_{ge}^{(2)}(t) = 0\,, \tag{5.21a}$$

$$\begin{aligned}\rho_{ee}^{(2)}(t) &= 2\,\mathrm{Re}\left[\int_{t_0}^{t} dt'\, f(t,t') \int_{t_0}^{t'} dt''\, f^*(t,t'')\right]\\ &= \left|\int_{t_0}^{t} f(t,\tau)\, d\tau\right|^2 = \left|\rho_{ge}^{(1)}(t)\right|^2\,. \end{aligned}\tag{5.21b}$$

The first relation in Eq. (5.21b) follows from a simple re-arrangement of the different terms in the self-consistent Eq. (5.18a). In the second step, we have used a general relation for complex-valued functions, derivable directly using integration by parts. Note that $\rho_{ge}^{(2)}(t, t_0)$ in our notation is the second-order correction, and not the result up to second order.

Hence, we find that the excited-state population and the coherence-squared are identical up to second order in the driving x-ray field also in this more general case,

$$\rho_{ee}^{(0-2)}(t) = \left|\rho_{ge}^{(0-2)}(t)\right|^2\,, \tag{5.22}$$

where the superscript $(0-2)$ indicates that all contributions up to second order are included.

As a result, we have shown for general two-level systems including decay and driven by weak time-dependent x-ray pulses that the coherently emitted intensity is equivalent to the intensity of the incoherent emission in second order of the x-ray-nucleus coupling. Note that this result is independent of the temporal shape of the x-ray field, such that it also holds for pulse sequences.

In terms of experimentally-accessible quantities, this implies that the ratio of the coherently and incoherently scattered intensities Eqs. (5.6),(5.8) is constant as function of time in the LER, i.e., if both observables are expanded up to second order in the driving x-ray field. Conversely, deviations from this time-independence therefore imply dynamics beyond the LER. In particular, as discussed in Sec. 5.3.1, the ratio is expected to change quadratically with the integrated Rabi frequency in leading higher-excitation order. In Secs. 5.4 and 5.5, we will explore particular x-ray pulse examples of experimental relevance for such dynamics beyond the LER, which will also allow for analytical solutions of the nuclear dynamics to higher order.

Incoherent and coherent radiation emitted by non-interacting two-level systems

In this section, we investigate the coherently and incoherently scattered intensity of identical non-interacting two-level nuclei in the LER. This case introduces the basic assumptions of ensemble-scattering and serves as a reference for studies of interacting nuclear systems.

The case of a non-interacting nuclear ensemble is characterized by vanishing coherent couplings $J_{nn'}$ and cross-decay rates $\Gamma_{nn'}$. The Hamiltonian Eq. (5.1) and Lindbladian Eq. (5.4) separate into independent contributions for each nucleus

$$\hat{H} = \sum_n \hat{h}_n \,, \quad \mathcal{L}[\hat{\rho}^{\mathrm{NB}}] = \sum_n \mathcal{L}_n^{1\mathrm{B}}[\hat{\rho}^{1\mathrm{B}}] \tag{5.23}$$

with

$$\hat{h}_n = \hbar\omega_0 \hat{\sigma}_n^+ \hat{\sigma}_n^- - \frac{\hbar}{2}\left(\Omega_n(t)\hat{\sigma}_n^+ + h.c.\right) \tag{5.24a}$$

$$\mathcal{L}_n^{1\mathrm{B}}[\hat{\rho}^{1\mathrm{B}}] = \frac{\gamma}{2}\left(2\hat{\sigma}_n^-\hat{\rho}^{1\mathrm{B}}\hat{\sigma}_n^+ - \left\{\hat{\sigma}_n^+\hat{\sigma}_n^-, \hat{\rho}^{1\mathrm{B}}\right\}\right) \tag{5.24b}$$

In this case, the solution to the N-body problem becomes the product of the solutions to the one-body problem, i.e.

$$\rho^{\mathrm{NB}} = \bigotimes_n \rho_n^{1\mathrm{B}} \tag{5.25}$$

Then, the expectation value of any one-body operator $\hat{\mathcal{O}}^{\mathrm{NB}} = \sum_n \hat{\mathcal{O}}_n^{1\mathrm{B}}$ becomes

$$\langle \hat{\mathcal{O}}^{\mathrm{NB}} \rangle(t) = \mathrm{Tr}\left(\hat{\mathcal{O}}^{\mathrm{NB}}\hat{\rho}^{\mathrm{NB}}(t)\right) = \sum_n \mathrm{Tr}\left(\hat{\mathcal{O}}_n^{1\mathrm{B}}\hat{\rho}^{\mathrm{NB}}\right) \tag{5.26}$$

$$= \sum_n \left[\mathrm{Tr}\left(\hat{\mathcal{O}}_n^{1\mathrm{B}}\hat{\rho}_n^{1\mathrm{B}}\right) \cdot \prod_{l' \neq l} \mathrm{Tr}\left(\hat{\rho}_{n'}^{1\mathrm{B}}\right)\right] \tag{5.27}$$

$$= \sum_n \mathrm{Tr}\left(\hat{\mathcal{O}}_n^{1\mathrm{B}}\hat{\rho}_n^{1\mathrm{B}}\right) = \sum_n \langle \hat{\mathcal{O}}^{1\mathrm{B}} \rangle \tag{5.28}$$

which means that the N-body expectation value of $\hat{\mathcal{O}}$ is just reduced to the sum of the expectation values of the one-body operators $\hat{\mathcal{O}}_n$ acting on each individual nucleus since the dynamics of the different nuclei are not coupled by the Hamiltonian nor the Lindbladian.

For identical nuclei and assuming a plane wave driving field of the form

$$\Omega(\mathbf{r}_n, t) = \Omega(t)\, e^{i\mathbf{k}_{\mathrm{in}}\mathbf{r}_n} \,, \tag{5.29}$$

that excites all nuclear dipoles with the same amplitude, this implies that the coherences of the individual nuclei are only distiguished by their positional phase imprinted via the external driving field, i.e.

$$\rho_{g_n e_n}(t) = e^{-i\mathbf{k}_{in}\cdot\mathbf{r}_n}\rho_{ge}(t)\,. \tag{5.30}$$

This phase-dependence can be obtained from the self-consistent solution Eq. (5.18b) which always, regardless of the expansion order, acquires the phase of the outermost x-ray-nucleus interaction amplitude $\Omega^*(\mathbf{r}_n, t)$ while the phase contribution from the inner integrals cancels. Hence, the coherently scattered intensity Eq. (5.8) under the assumptions of identical non-interacting nuclei and an equal-amplitude excitation by an plane-wave driving field reads

$$I_{coh}(t) = \left|\sum_{n=1}^{N} e^{i(\mathbf{k}_{out}-\mathbf{k}_{in})\mathbf{r}_n}\right|^2 \cdot |\rho_{ge}(t)|^2 \tag{5.31}$$

In contrast to the coherent emission, the incoherent radiation is produced by independently-decaying nuclei without a specific directionality of the released radiation as described by Eq. (5.6). In addition, the plane wave driving field does not imprint a phase on the excited-state populations as can be seen from the self-consistent solution Eq. (5.18a): Here, the positional phase factors of the driving fields $\Omega(\mathbf{r}_n, t)$ as these always appear in pairs. This is related to the fact that only even scattering orders contribute to the population. Note that, like for the coherence, this latter fact is independent of the perturbative expansion order. For these reasons the incoherently scattered intensity Eq. (5.6) becomes

$$I_{inc}(t) = \sum_n \rho_{e_n e_n}(t) = N\rho_{ee}(t)\,. \tag{5.32}$$

With these results, the ratio of both observables up to second order in the x-ray nuclei interaction can be written as

$$R^{\mathrm{NB}}(t) = \frac{I_{coh}(t)}{I_{inc}(t)} = \frac{\left|\sum_n e^{i(\mathbf{k}_{out}-\mathbf{k}_{in})\cdot\mathbf{r}_n}\right|^2}{N}\,\frac{|\rho_{ge}(t)|^2}{\rho_{ee}(t)} \tag{5.33}$$

which is the ratio of the single-nucleus quantities multiplied by a prefactor which is constant in time. This means that the many-body observables are directly related to the corresponding single-body quantities if interactions are neglected. In particular, if the single-nucleus ratio is constant, this is also true for the non-interacting many-body quantity $R^{\mathrm{NB}}(t)$, however, with a prefactor including the directionality of the released coherent radiation. Note, that two assumptions were crucial for the derivation of this result: First, we assumed a plane-wave driving field that excites all nuclei with equal amplitude and, second, all nuclei were required to be identical. In the following sections we will generalize this result to *interacting* nuclear ensembles.

5.3.3 Perturbative solution of the interacting many-body nuclear ensemble

Having established the equivalence of coherent and incoherent radiation in the LER for effective single-particle cases, we now turn to interacting nuclear ensembles. As mentioned, this is of relevance for studies of nuclear ensembles embedded in x-ray waveguides displaying radiation-induced couplings and cooperative effects even in the LER. We establish this equivalence by deriving the population-coherence correspondence in a single-particle basis under the assumptions of homogeneity of the nuclear ensemble and equal-amplitude plane-wave driving fields. This approach requires less assumptions about the geometry of the sample compared to a derivation in a nuclear exciton or spinwave basis, in which the time evolution operator $\hat{T}_t$ becomes diagonal [Len+20; AG+17]. This basis is characteristic for the low-excitation dynamics of nuclear ensembles in x-ray waveguides (cf. Sec. 2.2.2). The homogeneity assumption in this approach is rephrased in terms of translational invariance. A derivation in this basis is shown in Appendix A.6 to complement the analysis given in the main text.

Solution of the N-body system in the single-particle basis

We start by deriving the equivalence between incoherently and coherently scattered radiation in the single-particle basis using the perturbative expressions Eq. (4.34), (4.36) and (4.38) in Sec. 4.2. Using these expressions for the density operator, the relevant density matrix elements for each nuclear two-level system can be obtained as

$$\rho^{(1)}_{g_x,e_x}(t) = \mathrm{Tr}\left[\hat{\sigma}^+_x\,\hat{\rho}^{(1)}(t)\right] , \tag{5.34a}$$

$$\rho^{(2)}_{e_x,e_x}(t) = \mathrm{Tr}\left[\hat{\sigma}^+_x\,\hat{\sigma}^-_x\,\hat{\rho}^{(2)}(t)\right] . \tag{5.34b}$$

These expressions can be obtained from a calculation in a single-particle or nuclear exciton basis. The latter is done in Sec. A.6. Here, we instead proceed with a direct calculation in the single-particle basis.

We start with the coherence, assuming that all nuclei initially are in their ground states, $\hat{\rho}^{(0)}(t) = |G\rangle\langle G|$ (cf. Eq. (4.34)),

$$\rho^{(1)}_{g_x,e_x}(t) = -\frac{i}{\hbar}\int_{t_0}^{t} d\tau\;\mathrm{Tr}\left[\hat{\sigma}^+_x\hat{T}^\dagger_{t-\tau}\left[\hat{W}(\tau),\hat{\rho}^{(0)}(\tau)\right]\hat{T}_{t-\tau}\right] , \tag{5.35}$$

with time evolution operators $\hat{T}_t$ defined in Eq. (4.24) and the nucleus-field interaction Hamiltonian in Eq. (4.15), again specialized to the case of a single excited states and therefore dropping the indices l, l'.

The trace in the integral of Eq. (5.35) is evaluated to

$$\begin{aligned}
&\mathrm{Tr}\left[\hat{\sigma}^+_x\hat{T}^\dagger_{t-\tau}\left[\hat{W}(\tau),\hat{\rho}^{(0)}(\tau)\right]\hat{T}_{t-\tau}\right]\\
&\quad= \langle G|\hat{T}_{t-\tau}\hat{\sigma}^+_x\hat{T}^\dagger_{t-\tau}\hat{W}(t)|G\rangle - \langle G|\hat{W}(\tau)\hat{T}_{t-\tau}\hat{\sigma}^+_x\hat{T}^\dagger_{t-\tau}|G\rangle\\
&\quad= -\langle G|\hat{W}(\tau)\hat{T}_{t-\tau}\hat{\sigma}^+_x|G\rangle
\end{aligned} \tag{5.36}$$

where we have used the cyclic permutation property $\mathrm{Tr}(AB) = \mathrm{Tr}(BA)$ in the first step, and

$$\hat{T}^\dagger_t|G\rangle = |G\rangle = \hat{T}_t|G\rangle , \tag{5.37}$$

$$\langle G|\hat{T}_t = \langle G| = \langle G|\hat{T}^\dagger_t , \tag{5.38}$$

as well as

$$\langle G|\hat{\sigma}^+_x = 0 \tag{5.39}$$

in the second step. We further evaluate Eq. (5.36) by inserting the explicit form of the interaction part $\hat{W}$ which yields

$$\begin{aligned}
-\langle G|\hat{W}(\tau)\hat{T}_{t-\tau}\hat{\sigma}^+_x|G\rangle &= \frac{\hbar}{2}\sum_{n=1}^{N}\Omega^*(\mathbf{r}_n,\tau)\langle G|\hat{\sigma}^-_n\hat{T}_{t-\tau}\hat{\sigma}^+_x|G\rangle\\
&= \frac{\hbar}{2}\sum_{n=1}^{N}\Omega^*(\mathbf{r}_n,\tau)\big[\delta_{nx} + \kappa_{nx}(t-\tau) + \sum_j \kappa_{nj}\kappa_{jx}(t-\tau)^2/2 + \ldots\big]\\
&= \frac{\hbar}{2}\sum_{n=1}^{N}\Omega^*(\mathbf{r}_n,\tau)\left[e^{\mathcal{K}(t-\tau)}\right]_{nx} .
\end{aligned} \tag{5.40}$$

In the second step, we perform a series expansion of the time evolution operator and calculate the expectation values. In the last step, we re-sum the result. For this, we introduce the matrix exponential of the coefficient matrix $\mathcal{K} = (\kappa_{nm})$ with entries κ_{nm} defined by

$$\kappa_{nm} = -(\Gamma_{nm} + i\,J_{nm}) - (\Gamma_{\mathrm{IC}} - i\omega_0)\delta_{nm} , \tag{5.41}$$

in the single-excited state case and $[A]_{xy}$ is the x, y-element of the matrix A. Using Eq. (5.40) in Eq. (5.35), we obtain

$$\rho^{(1)}_{g_x,e_x}(t) = \sum_{n=1}^{N} \int_{t_0}^{t} d\tau \, g_{nx}(\tau) \,, \tag{5.42a}$$

$$g_{nx}(\tau) = -\frac{i}{2}\Omega^*(\mathbf{r}_n, \tau) \left[e^{\mathcal{K}(t-\tau)}\right]_{nx} \,. \tag{5.42b}$$

Analogously, the excited-state population evaluates to

$$\rho^{(2)}_{e_x,e_x}(t) = \mathrm{Tr}\left[\hat{\sigma}_x^+ \, \hat{\sigma}_x^- \, \hat{\rho}^{(2)}(t)\right] = \frac{2}{\hbar^2}\,\mathrm{Re}\left\{\int_{t_0}^{t} d\tau_2 \int_{t_0}^{\tau_2} d\tau_1 \, \mathcal{M}\right\} \,, \tag{5.43}$$

with the matrix element

$$\begin{aligned}
\mathcal{M} &= \langle G|\hat{W}(\tau_2)\hat{T}_{t-\tau_2}\hat{\sigma}_x^+\hat{\sigma}_x^-\hat{T}^\dagger_{t-\tau_1}\hat{W}(\tau_1)|G\rangle \\
&= \frac{\hbar^2}{4}\sum_{nm}\Omega^*(\mathbf{r}_n,\tau_2)\Omega(\mathbf{r}_m,\tau_1)\langle G|\hat{\sigma}_n^-\hat{T}_{t-\tau_2}\hat{\sigma}_x^+\hat{\sigma}_x^-\hat{T}^\dagger_{t-\tau_1}\hat{\sigma}_m^+|G\rangle \\
&= \frac{\hbar^2}{4}\sum_{nm}\Omega^*(\mathbf{r}_n,\tau_2)\Omega(\mathbf{r}_m,\tau_1)\sum_{\mathcal{N}}\langle G|\hat{\sigma}_n^-\hat{T}_{t-\tau_2}\hat{\sigma}_x^+\,|\mathcal{N}\rangle\langle\mathcal{N}|\,\hat{\sigma}_x^-\hat{T}^\dagger_{t-\tau_1}\hat{\sigma}_m^+|G\rangle \\
&= \frac{\hbar^2}{4}\sum_{nm}\Omega^*(\mathbf{r}_n,\tau_2)\Omega(\mathbf{r}_m,\tau_1)\langle G|\hat{\sigma}_n^-\hat{T}_{t-\tau_2}\hat{\sigma}_x^+|G\rangle\langle G|\hat{\sigma}_m^-\hat{T}_{t-\tau_1}\hat{\sigma}_x^+|G\rangle^* \\
&= \frac{\hbar^2}{4}\sum_{nm}\Omega^*(\mathbf{r}_n,\tau_2)\Omega(\mathbf{r}_m,\tau_1)\left[e^{\mathcal{K}(t-\tau_2)}\right]_{nx}\left[e^{\mathcal{K}(t-\tau_1)}\right]^*_{mx} \,.
\end{aligned} \tag{5.44}$$

In this derivation, the crucial step is the insertion of an identity operator $\hat{1} = \sum_{\mathcal{N}} |\mathcal{N}\rangle\langle\mathcal{N}|$ in the center of the matrix element where the $|\mathcal{N}\rangle$ form a basis of the many-body Hilbert space. Of this sum, only the ground state projector $|G\rangle\langle G|$ contributes for the following reason: $\hat{\sigma}_m^+$ creates a single excitation in the state it is acting on, while the time evolution operator $\hat{T}^\dagger_{t-\tau_1}$ conserves the total number of excitations. Then, $\hat{\sigma}_x^-$ annihilates a single excitation such that only initial and final states with the same number of excitations can contribute to $\mathcal{M}$ which means that only the ground state projector remains in the center of the matrix element.

By inserting Eq. (5.44) into Eq. (5.43), we obtain

$$\begin{aligned}
\rho^{(2)}_{e_x,e_x}(t) &= \frac{1}{2}\,\mathrm{Re}\left\{\int_{t_0}^{t} d\tau_2 \int_{t_0}^{\tau_2} d\tau_1 \sum_{nm}\Omega^*(\mathbf{r}_n,\tau_2)\Omega(\mathbf{r}_m,\tau_1)\left[e^{\mathcal{K}(t-\tau_2)}\right]_{nx}\left[e^{\mathcal{K}(t-\tau_1)}\right]^*_{mx}\right\} \\
&= 2\,\mathrm{Re}\left\{\int_{t_0}^{t} d\tau_2 \sum_{n} g_{nx}(\tau_2) \int_{t_0}^{\tau_2} d\tau_1 \sum_{m} g^*_{mx}(\tau_1)\right\} \\
&= \left|\int_{t_0}^{t} d\tau_2 \sum_{n} g_{nx}(\tau_2)\right|^2 = \left|\rho^{(1)}_{g_x,e_x}(t)\right|^2 \,,
\end{aligned} \tag{5.45}$$

where we have used Eqs. (5.42) and the general relation for complex-valued functions already employed in the derivation of Eq. (5.21b).

In summary, from Eqs. (5.42) and (5.45) we thus obtain

$$\rho^{(1)}_{g_x,e_x}(t) = \sum_{n=1}^{N} \int_{t_0}^{t} d\tau \, g_{nx}(\tau) \,, \tag{5.46a}$$

$$\rho^{(2)}_{e_x,e_x}(t) = \left|\rho^{(1)}_{g_x,e_x}(t)\right|^2 \,, \tag{5.46b}$$

$$g_{nx}(\tau) = -\frac{i}{2}\Omega^*(\mathbf{r}_n, \tau) \left[e^{\mathcal{K}(t-\tau)}\right]_{nx} \,, \tag{5.46c}$$

as the desired solution of the N-body dynamics.

As a consistency check, we can reduce the expression Eqs. (5.46a) to the single-particle case. Then, the matrix exponential reduces to a scalar exponential with

$$\kappa_{xx} = -\Gamma_{xx} - \Gamma_{\mathrm{IC}} + i\omega_x = -\frac{\gamma}{2} + i\omega_0\,, \tag{5.47}$$

such that

$$\rho^{(1)}_{g_x,e_x}(t) = -\frac{i}{2}\int_{t_0}^{t} d\tau\, \Omega^*(\tau)\, e^{-\frac{\gamma}{2}(t-\tau)}\, e^{i\omega_0(t-\tau)}\,, \tag{5.48}$$

which agrees with the single-particle result Eqs. (5.19a). Note, that up to this point, we did not use the assumption of a homogeneous nuclear ensemble or equal-amplitude driving field as used in Sec. 5.3.2. For this reason, the derivation can in principle be extended to also account for site-dependent nuclear transition frequencies ω_n and decay rates γ_n. However, we retain these assumptions for the following ensemble derivation and the fact that these assumptions are usually justified.

Coherently and incoherently scattered intensity of homogeneous nuclear ensembles

Now, with the results Eqs. (5.46) at hand, we can proceed by showing the equivalence between the population-based observables and the coherence-based observables also in the many-body case.

The solutions Eqs. (5.46) directly prove the equivalence on the single-particle level,

$$|\rho^{(1)}_{g_x e_x}(t)|^2 = \rho^{(2)}_{e_x e_x}(t)\,, \tag{5.49a}$$

$$\Rightarrow |\rho^{(0-2)}_{g_x e_x}(t)|^2 = \rho^{(0-2)}_{e_x e_x}(t)\,. \tag{5.49b}$$

However, this result on the single-particle level is not sufficient for the experimentally accessible ensemble-based observables, given by Eqs. (5.6) and (5.8) as

$$I_{inc}(t) \propto \sum_{n=1}^{N} \langle \hat{\sigma}_n^+ \hat{\sigma}_n^- \rangle\,, \tag{5.50}$$

$$I_{coh}(t, \mathbf{k}_{out}) \propto \left| \sum_n e^{i\mathbf{k}_{out}\mathbf{r}_n} \langle \hat{\sigma}_n^+ \rangle \right|^2 . \tag{5.51}$$

To evaluate the sums in these expressions, we again make the two assumptions already employed in the non-interacting case Sec. 5.3.2: First, we assume that all nuclei are excited with the same amplitude using a plane-wave field with wave vector $\mathbf{k}_{\mathrm{in}}$ Eq.(5.29). Second, we make the assumption of a homogeneous ensemble of nuclei, i.e.,

$$\begin{aligned}
\rho^{(1)}_{g_x,e_x}(t) &= -\frac{i}{2}\sum_{n=1}^{N}\int_{t_0}^{t} d\tau\, \Omega^*(\mathbf{r}_n,\tau)\, \left[e^{\mathcal{K}(t-\tau)}\right]_{nx} \\
&= -\frac{i}{2} e^{-i\mathbf{k}_{\mathrm{in}}\,\mathbf{r}_x} \sum_{n=1}^{N}\int_{t_0}^{t} d\tau\, \Omega^*(\tau) e^{i\mathbf{k}_{in}(\mathbf{r}_x-\mathbf{r}_n)} \left[e^{\mathcal{K}(t-\tau)}\right]_{nx} \\
&= -\frac{i}{2} e^{-i\mathbf{k}_{\mathrm{in}}\,\mathbf{r}_x} \sum_{n=1}^{N}\int_{t_0}^{t} d\tau\, \Omega^*(\tau) e^{i\mathbf{k}_{in}(\mathbf{r}_{n_0}-\mathbf{r}_n)} \left[e^{\mathcal{K}(t-\tau)}\right]_{nn_0} \\
&= \rho^{(1)}_{ge}(t)\, e^{-i\mathbf{k}_{\mathrm{in}}\,\mathbf{r}_x}\,.
\end{aligned} \tag{5.52}$$

Here, in the second step, we have replaced the index x in the integrand with an (arbitrary) fixed index n_0. This homogeneity assumption requires that the coupling environment of all two-level systems is equivalent and that the nuclei themselves are identical. Note that even in a regular arrangement, nuclei at the boundary of the medium experience different couplings to other nuclei than those in the center of the ensemble. But in macroscopically large ensembles, these boundary effects can be neglected to a good approximation. Within the same assumptions, we also find

$$\rho^{(2)}_{e_x e_x}(t) = \rho^{(2)}_{ee}(t)\,, \tag{5.53}$$

i.e., the nuclear populations evolve independent of the atom index x.

As a result, the result up to second order in the light-matter coupling is

$$I^{(0-2)}_{inc}(t) \propto N\,\rho^{(2)}_{ee}(t)\,, \tag{5.54a}$$

$$I^{(0-2)}_{coh}(t,\mathbf{k}_{out}) \propto \left|\rho^{(1)}_{ge}(t)\right|^2 \cdot \left|\sum_{n=1}^{N} e^{i(\mathbf{k}_{out}-\mathbf{k}_{in})\mathbf{r}_n}\right|^2\,. \tag{5.54b}$$

Together with Eq. (5.49), we thus again find that in second order of the x-ray-nucleus coupling, the ratio of the coherently scattered x-rays to those incoherently scattered is constant in time,

$$\frac{I^{(0-2)}_{coh}(t,\mathbf{k}_{out})}{I^{(0-2)}_{inc}(t)} = \frac{I^{(0-2)}_{coh}(t_0,\mathbf{k}_{out})}{I^{(0-2)}_{inc}(t_0)}\,. \tag{5.55}$$

Note that, as in the non-interacting case, the geometrical factor in Eq. (5.54b) characterizes the directionality of the coherently scattered light.

5.4 Impulsive x-ray excitation beyond the low-excitation regime

In the previous Section, we have analytically established the dynamical equivalence of the coherently and the incoherently scattered x-ray intensities up to second order in the x-ray-nucleus interaction. Deviations from this equivalence in higher excitation orders form the basis of our approach to detect dynamics beyond the LER. Therefore, in this Section, we consider the impulsive excitation case beyond second-order perturbation theory, in order to show that the equivalence is indeed broken once higher-order dynamics sets in. While this is easily possible in analytical form for the case of a single effective two-level system, numerical calculations are required to study the dynamics of an interacting nuclear ensemble.

5.4.1 Two-level analysis

In the impulsive excitation case, the x-ray excitation and the subsequent decay dynamics in the absence of a driving x-ray field can be considered separately. For a single particle, the initial state after the x-ray excitation is given by Eqs. (5.12) as

$$\rho_{ee}(t=0) = \sin^2\left[\frac{1}{2}\mathcal{A}\right]\,, \tag{5.56a}$$

$$\rho_{ge}(t=0) = -\frac{i}{2}\,e^{i\phi}\,\sin\left[\mathcal{A}\right]\,. \tag{5.56b}$$

Here, for simplicity, we denote the time after the exciting x-rays have passed the nuclei as $t=0$, and $\mathcal{A}$ is the total pulse area of the exciting x-ray pulse. Subsequently, the decay is governed by [SZ97]

$$\rho_{ee}(t) = \rho_{ee}(0)\,e^{-\gamma t}\,, \tag{5.57a}$$

$$\rho_{ge}(t) = \rho_{ge}(0)\,e^{-\frac{\gamma}{2}t}\,. \tag{5.57b}$$

As a result, we find that the ratio of the coherent and incoherent intensities Eqs. (5.8) and (5.6) evaluates to

$$\frac{I_{coh}(t)}{I_{inc}(t)} \propto \frac{|\rho_{ge}(t)|^2}{\rho_{ee}(t)} = \frac{|\rho_{ge}(0)|^2}{\rho_{ee}(0)} = \cos^2\left[\frac{1}{2}\mathcal{A}\right]\,. \tag{5.58}$$

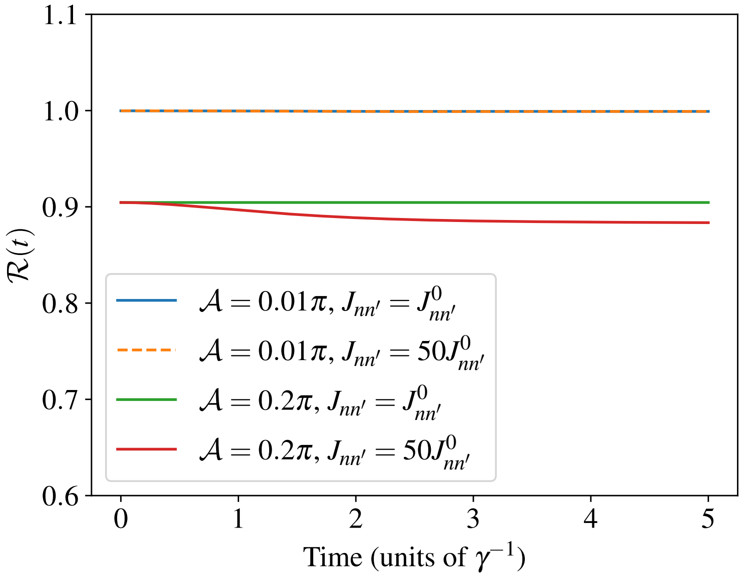

Figure 5.2: Ratio $\mathcal{R}(t)$ of the coherently and incoherently scattered intensity for a regular chain of $N = 8$ nuclei with periodic boundary conditions, scaled by N [see Eq. (5.59)]. The lattice constant $r_0 = 286$ pm and the resonant wavelength $\lambda_0 = 86$ pm are chosen for the case of α-iron enriched in ^{57}Fe to determine the coherent dipole-dipole coupling constants $J^0_{nn'}$. Results are compared for the LER ($\mathcal{A} = 0.01\pi$) and stronger excitation ($\mathcal{A} = 0.2\pi$), as well as for free-space coupling ($J^0_{nn'}$) and cavity-enhanced coupling ($50\,J^0_{nn'}$). Note that the two curves in the LER case coincide, as expected.

Hence, the ratio remains constant over time, but depends on the degree of excitation (cf. Fig. 5.2). Measuring it as a function of the resonant intensity of the exciting x-rays then allows one to search for deviations in this ratio from its value at low x-ray intensities, which indicate excitations beyond the LER. One possibility for this measurement is to exploit the typically large pulse-to-pulse fluctuations in resonant intensity at x-ray free electron lasers, and to sort the intensity data according to the incident (resonant) pulse energy.

5.4.2 Dynamics of a coupled nuclear ensemble after impulsive excitation

If the interactions between the nuclei are weak enough such that the dynamics of the individual nuclei is essentially independent of each other on nuclear decay timescales, then the results of the single two-level nucleus case are recovered for each nucleus separately.

A more interesting situation arises in case of stronger couplings. For example, a suitably designed [Hab+16; Hab+17; DLE22c; DLE22b] waveguide structure may allow one to realize regimes of stronger interactions between the nuclei.

In Sec. 5.3.3 we showed that in this regime, the coherence-population correspondence Eq. (5.22) is still valid up to second order in the nucleus-field interaction. This holds for each nucleus separately and, more importantly, also the scaled ratio of the total incoherently and coherently scattered intensity

$$\mathcal{R}(t) = \frac{1}{N}\frac{|\sum_n e^{i\mathbf{k}_{out}\mathbf{r}_n}\rho_{g_n e_n}(t)|^2}{\sum_{n=1}^{N}\rho_{e_n e_n}(t)} \tag{5.59}$$

is constant in time and equal to one if the two assumptions of excitation by a plane wave field and a homogeneous nuclear ensemble are satisfied (see Sec. 5.3.3). Note that $\mathcal{R}(t)$ is proportional to the intensity ratio $R(t)$ (see Fig. 5.1), and scaled by the number of nuclei N. The scaling factor is introduced since for larger ensembles, the coherently scattered intensity dominates, due to the collective emission with intensity proportional to N^2[VB86; Smi86; SS92; HT99b]. In contrast, the incoherent scattering channels do not exhibit this collective enhancement, and therefore feature an intensity proportional to N. This difference is compensated by the prefactor in order to ensure that $\mathcal{R}(t)$ is independent of N under the aforementioned conditions.

Next, we analyze the dynamics beyond the LER, also in the presence of stronger couplings between the nuclei, using a numerical integration of the full master equation for a limited number of nuclei.

The calculations are performed using the PYTHON library QuTiP [JNN12; JNN13]. In particular, we consider the dynamics of a linear chain of $N = 8$ regularly arranged nuclei with periodic boundary conditions after impulsive x-ray excitation. The coherent dipole-dipole coupling parameters $J_{nn'}$ are chosen assuming nuclear dipole moments $\hat{\mathbf{d}}$ oriented perpendicularly to the relative positions $\mathbf{r}_n - \mathbf{r}_{n'}$ of the nuclei in the chain. Their free space values can then be calculated via [Aga74; FS05]

$$J^0_{nn'} = \frac{3}{2}\Gamma\left(\frac{\cos(\eta_{nn'})}{\eta_{nn'}} - \frac{\sin(\eta_{nn'})}{\eta^2_{nn'}} - \frac{\cos(\eta_{nn'})}{\eta^3_{nn'}}\right), \tag{5.60}$$

where $\Gamma = \Gamma_{nn} = \gamma/[2(1+\alpha)]$ denotes the radiative decay rate of the nuclei. Here, $\alpha = 8.56$ is chosen as the internal conversion coefficient of the archetype Mössbauer isotope ^{57}Fe with the Mössbauer resonance at 14.4 keV transition energy [Röh04]. We further defined $\eta_{nn'} = k_0\, r_{nn'}$. The resonant wave number $k_0 = 2\pi/\lambda_0$ and the distances $r_{nn'} = |n - n'|\, r_0$ between the nuclei are chosen corresponding to the resonant wavelength $\lambda_0 = 86$ pm and the lattice constant $r_0 = 286$ pm for α-iron enriched in ^{57}Fe. Note that for a small ensemble with periodic boundary conditions, the homogeneity criterion for the initial phases imprinted on the nuclei by the x-ray excitation can only be satisfied for particular incidence angles. To satisfy this criterion, we chose the incidence angle such that a relative phase of $k_0\, r_{n,n+1} = 2\pi/N$ is imprinted onto the coherence of neighbouring nuclei. For the same reason the decay rates Γ and nuclear transition frequencies ω_0 are considered to be the same for all nuclei in the chain. Further, incoherent couplings $\Gamma_{nn'}$ were neglected in the numerical simulation.

Figure 5.2 shows the simulation results for different dipole-dipole coupling parameters $J_{nn'}$ and pulse areas $\mathcal{A}$. The chosen parameters correspond to the LER case ($\mathcal{A} = 0.01\pi$) or excitation beyond the LER ($\mathcal{A} = 0.2\pi$), as well as weak dipole-dipole coupling ($J_{nn'} = J^0_{nn'}$) and coupling enhanced by a factor of 50 relative to the free-space coupling ($J_{nn'} = 50\, J^0_{nn'}$).

In the LER case (blue and orange-dashed lines), we find that the ratio $\mathcal{R}(t) = 1$, independent of the dipole-dipole coupling, consistent with our analytical results in Sec. 5.3.3. For excitation beyond the LER case in the presence of weak coupling (green curve), we find a constant ratio $\mathcal{R}$, however, with a value below 1. This agrees with our results in Sec. 5.4.1. In contrast, for excitations beyond the LER with stronger dipole-dipole couplings (red curve), the ratio $\mathcal{R}(t)$ becomes time-dependent and evolves to lower values, initially starting from the ratio for the low-coupling case. This is due to a faster transient decay of the coherences entering the expression for the coherently scattered intensity in the interacting system.

As a result, we conclude that the time-dependent ratio of the coherently- and incoherently scattered x-rays does not only serve as a criterion for the excitation beyond the LER, but may further also reveal the presence of stronger dipole-dipole couplings between the nuclei.

5.5 Non-impulsive x-ray excitation beyond the low-excitation regime

For the case of impulsive excitation, we found that a comparison of the coherently and incoherently scattered intensity provides a handle to identify excitation of the nuclear ensemble beyond the LER. In case of effective single-particle dynamics, the ratio between these two intensities remains constant throughout the decay while it becomes time-dependent at higher excitations in sufficiently-strongly interacting nuclear ensembles. In the following, we extend this discussion to the non-impulsive regime. The calculation of the complete dynamics of a large ensemble of coupled nuclei under the action of time-dependent driving fields and dissipation so far is an unsolved problem, and remains beyond the scope of this work. Instead, we analyze the non-impulsive dynamics in the (effective) single-particle case. It is expected that the single-particle description, which is valid in the LER [Len+20], remains a good approximation at the onset of dynamics beyond the LER but likely breaks down at higher excitation. Nevertheless, in the following, we also explore the dynamics at stronger excitation using the single-particle description, with the motivation of identifying possible experimental signatures for dynamics beyond the LER. Using this approach, the results presented in this Section are then obtained by numerically integrating the optical Bloch equations Eqs. (A.146).

To analyze the non-impulsive case, we consider nucleus-field couplings of the form

$$\Omega(t) = \Gamma_a\, \mathcal{A}\, e^{-i(\omega_0+\Delta)t}\, e^{-\Gamma_a t}\,, \tag{5.61}$$

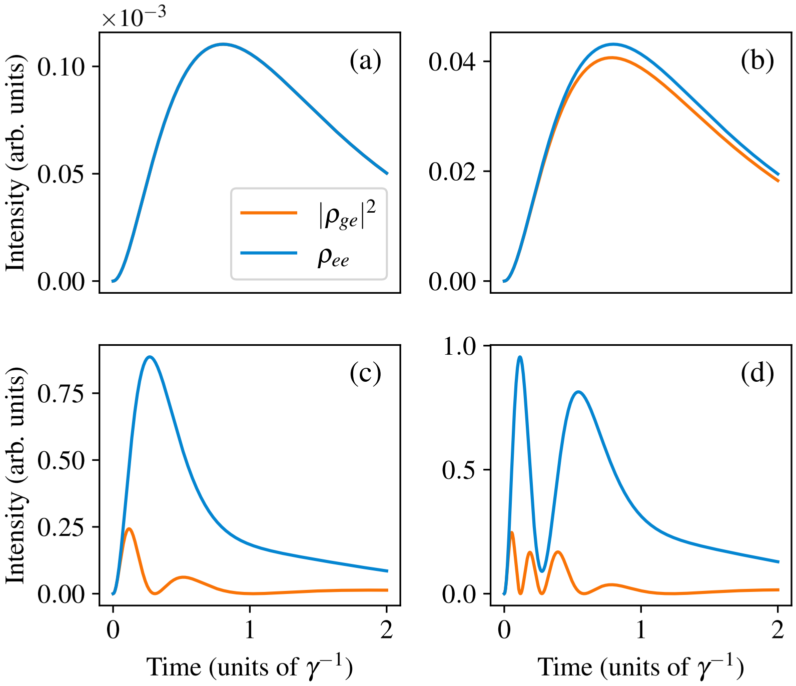

Figure 5.3: Temporal dynamics of the excited-state population ρ_{ee} and the coherence squared $|\rho_{ge}|^2$ of an effective two-level system for different degrees of excitation. The population and the coherence squared relate to the observable incoherently and coherently scattered light intensities. The different panels correspond to driving x-ray pulse areas of (a) $\mathcal{A} = 0.01\pi$, (b) $\mathcal{A} = 0.2\pi$, (c) $\mathcal{A} = 2\pi$, and (d) $\mathcal{A} = 4\pi$. In the LER [panel (a)], population and coherence squared agree, consistent with our analytical results. Upon excitation beyond the LER, the two quantities start to deviate (b), and eventually Rabi oscillations appear (c,d). Note that in (d), the oscillation frequencies of the coherence squared and of the population differ approximately by a factor of 2.

which characterizes an x-ray pulse exponentially decaying with rate Γ_a and center frequency detuned by Δ from the nuclear resonance frequency ω_0. Its total pulse area according to Eq. (5.13) is given by $\mathcal{A}$.

This choice for the driving x-ray field is motivated by the availability of synchrotron Mössbauer sources (SMS) [Ger+85b; Smi+97b; Set+09; Mas+08; Pot+12] which employ pure nuclear reflexes to produce x-ray pulses which are spectrally narrow on nuclear line-width scales from the incident broadband synchrotron pulses. In the future, these sources could be generalized for operation at x-ray free electron lasers [Chu+18]. Another source providing spectrally narrow pulse contributions is the field scattered in forward direction by thin nuclear targets in the LER, which is approximately exponentially-decaying [Smi86; HT99b]. By moving the thin nuclear target before or throughout its decay, the properties of the scattered light relative to those of the incident synchrotron pulse can be tuned [Hel+91; Tit+93; Sch+02a; Vag+14; Hee+17; Hee+21; SS22; Hee+22; Zha+19; LP17; CE19]. In particular, using suitably tailored x-ray pulses, the quantum dynamics of a nuclear target could be controlled [Hee+21]. A possible generalization of such schemes to higher excitation at x-ray free electron lasers again requires further analysis of nuclear dynamics under exponentially-decaying x-ray pulses such as in Eq. (5.61).

As expected, we will find that the non-instantaneous driving field gives rise to a much richer dynamics than in the impulsive case, since the x-ray-induced dynamics and the decay dynamics are not temporally separated in the former case. In particular, this will affect the time-dependence of the ratio of the coherently and incoherently scattered intensities.

Note that this time-dependence of the effective single-particle observables will also be reflected in the corresponding many-body observables as can be seen from Eqs. (5.54) such that their ratio will become time-dependent as soon as the single-particle quantities are.

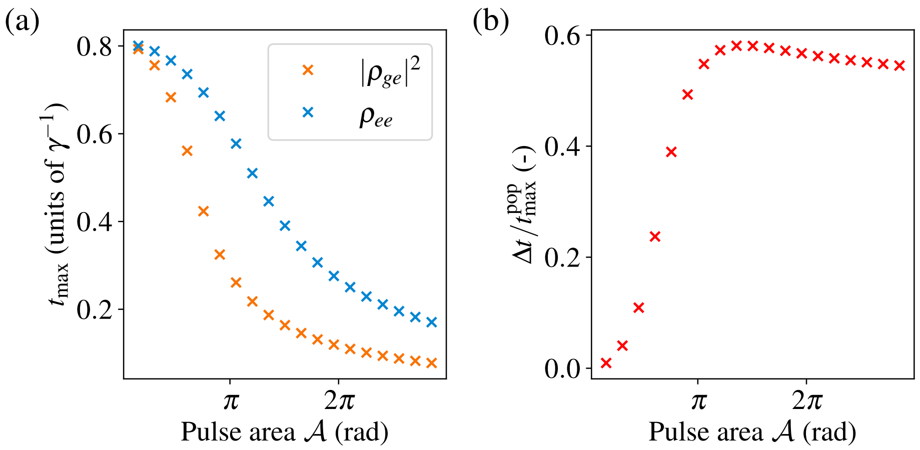

Figure 5.4: Analysis of the times with maximum intensities in the coherence squared and the populations. (a) shows the times defined in Eqs. (5.62) as function of the total pulse area $\mathcal{A}$. The other parameters are as in Fig. 5.3. While the maxima in the population and the coherence squared coincide in the LER, deviations appear towards stronger excitation. (b) shows the peak deviation defined in Eq. (5.63) against $\mathcal{A}$. Starting from zero value in the LER, the deviation steeply increases at the onset of non-linear excitation of the nuclear ensemble.

5.5.1 Resonant case $\Delta = 0$

We start by analyzing the case of a resonant x-ray pulse Eq. (5.61) with detuning $\Delta = 0$ and decay constant $\Gamma_a = 2.5\gamma$, where γ denotes the total line-width of the effective single nucleus. Results for different pulse areas $\mathcal{A} \in \{0.01\pi, 0.2\pi, 2\pi, 4\pi\}$ are shown in Fig. 5.3.

Consistent with the analytical results in Sec. 5.3.2, the coherence squared and the population characterizing the coherently and incoherently scattered intensity, respectively, agree in the low-excitation case [panel (a), $\mathcal{A} = 0.01\pi$]. With increasing excitation, deviations between the two observables start to appear [see panel (b)]. If the driving field becomes strong enough to induce Rabi oscillations [panels (c) and (d)], the different oscillation periods of coherence quared and population become visible. As a result, time-dependent ratios of the coherently and incoherently scattered light intensities can be expected in the non-impulsive driving case beyond the LER.

From these results we find that a first signature for dynamics slightly beyond the LER is a relative shift in the peak maxima of the two time-dependent intensities. This relative shift arises from the competition of the coherent excitation dynamics and the incoherent decay dynamics. To analyze this shift more quantitatively, we define the two corresponding times $t_{\max}^{\text{coh}}$ and $t_{\max}^{\text{pop}}$ with maximum intensities via the conditions

$$|\rho_{ge}(t_{\max}^{\text{coh}})|^2 = \max_{t\in[0,\infty)} \left(|\rho_{ge}(t)|^2\right), \tag{5.62a}$$

$$\rho_{ee}(t_{\max}^{\text{pop}}) = \max_{t\in[0,\infty)} \left(\rho_{ee}(t)\right). \tag{5.62b}$$

We further consider a peak deviation defined as

$$\Delta t / t_{\max}^{\text{pop}} = \frac{|t_{\max}^{\text{coh}} - t_{\max}^{\text{pop}}|}{t_{\max}^{\text{pop}}}. \tag{5.63}$$

Note that multiple maxima may appear due to Rabi oscillations at stronger x-ray driving. In this case, we consider the respective maxima appearing first after the onset of excitation.

Figure 5.4 shows the times $t_{\max}^{\text{coh}}$ and $t_{\max}^{\text{pop}}$ [panel (a)] and the corresponding peak deviation [panel (b)] as a function of the total pulse area $\mathcal{A}$. The deviations in case of dynamics beyond the LER are clearly visible. In particular, the steep increase of the peak deviation at small pulse areas renders it a promising signature for characterizing dynamics at the onset of the nonlinear excitation regime.

5.5.2 Non-resonant case $\Delta \neq 0$

Next, we generalize to the non-resonant case $\Delta \neq 0$. To this end, we analyze the coherence squared $|\rho_{ge}|^2$ and the population ρ_{ee} as a function of time and detuning Δ. This correlated analysis of

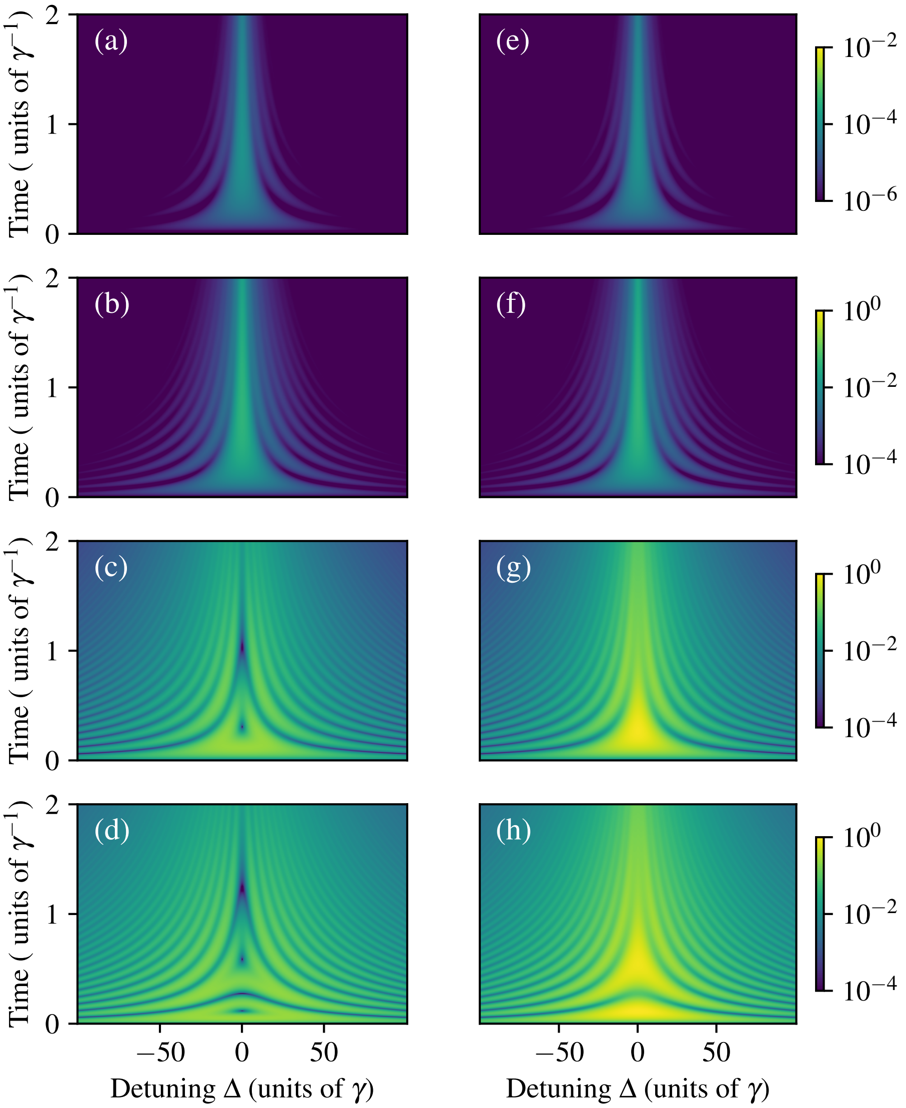

Figure 5.5: Time- and frequency-resolved coherence squared (left panels (a) - (d)) and populations (right panels (e) - (h)) for the case of non-impulsive excitation with an exponentially decaying pulse Eq. (5.61). The pulse envelope decays with $\Gamma_a = 2.5\gamma$. The rows from top to bottom are calculated for pulse areas of $\mathcal{A} \in \{0.01\pi, 0.2\pi, 2\pi, 4\pi\}$.

temporal- and spectral properties has proven to be a powerful tool in analyzing nuclear resonant scattering [Hee+17; Hee+21; WE23a]. However, it is important to note that the experimental setup underlying the theoretical analysis of this manuscript is different from previous approaches to record such time- and frequency-resolved spectra. Previous studies considered an *impulsive* x-ray excitation of the nuclear ensemble. The frequency resolution in these setups is achieved via an additional frequency-tunable reference absorber with an approximately exponential temporal decay. As a result, the time-frequency spectra are dominated by the interference of the light scattered by the reference absorber and the target, respectively [WE23a].

In contrast, here, we consider time-frequency spectra for the target driven by a *non-impulsive* frequency-tunable driving pulse of the form Eq. (5.61), in the absence of additional reference absorbers. This setup could be realized, e.g., using a synchrotron-Mössbauer-source, by correlating the detuning Δ of the source with the time-dependence of the scattered photons.

Figure 5.5 compares the time-frequency spectra for different pulse areas $\mathcal{A}$. Again, a pulse decay rate of $\Gamma_a = 2.5\gamma$ is chosen in the calculation. The left panels (a-d) show the coherence squared, whereas the right panels (e-h) depict the population. In the LER, the two signatures agree, as expected [top row, panels (a,e)]. Differences between the spectra appearing at larger pulse areas

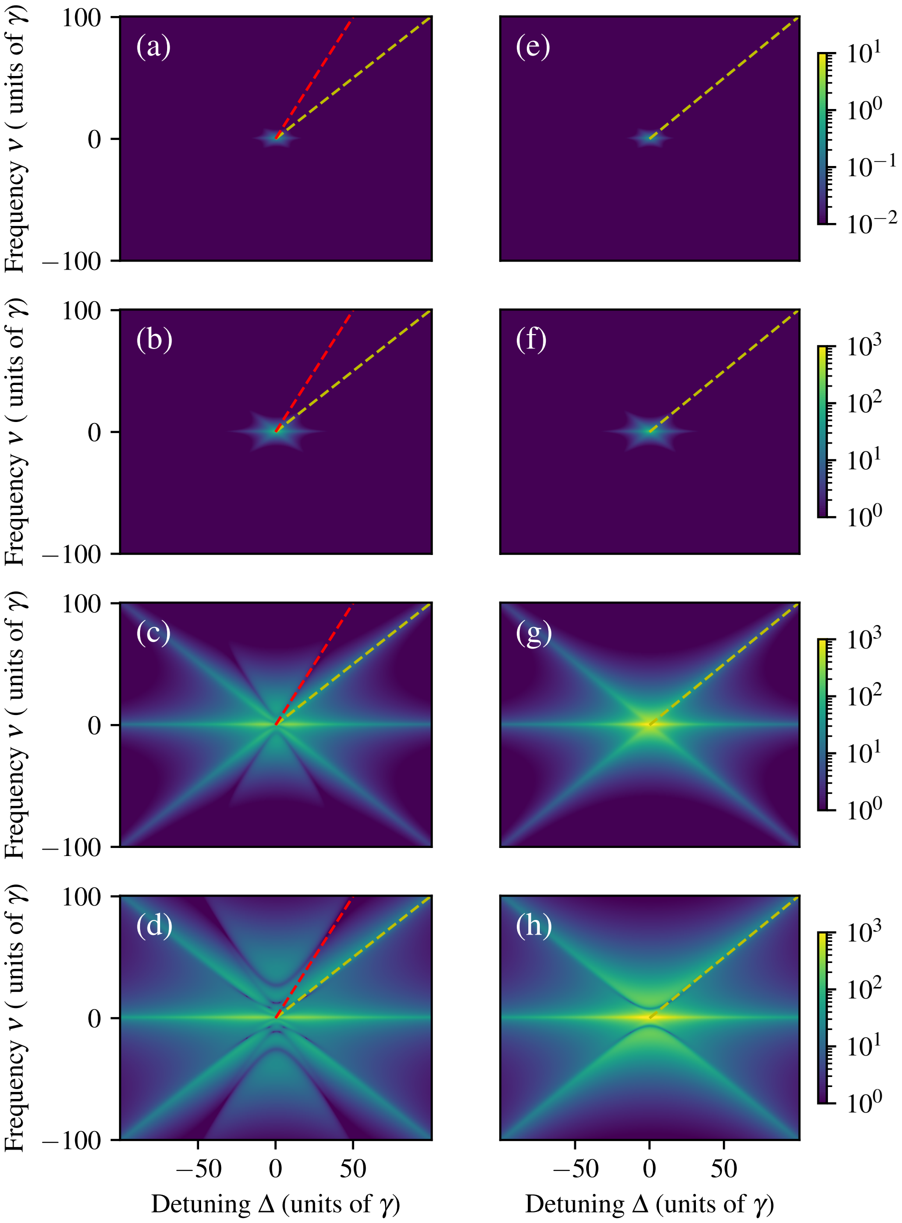

Figure 5.6: Frequency-frequency correlation spectra. The results are obtained via Fourier transforms along the time axes of the time-frequency spectra in Fig. 5.5. Data is shown in color-coded logarithmic scale for the coherence squared [left panels, (a)-(d)] and for the populations [right panels, (e)-(h)]. As in Fig. 5.5, the rows from top to bottom refer to different pulse areas of $\mathcal{A} \in \{0.01\pi, 0.2\pi, 2\pi, 4\pi\}$. The yellow [red] lines indicate slope one [two] as guide to the eye to facilitate the interpretation.

[panels (c,g) or (d,h)] are most pronounced at small detunings, which can be understood by noting that the excitation of the nuclei for a given pulse area is highest towards resonance, such that the deviations from the LER are more pronounced while higher excitation orders are suppressed further off-resonance. The visible deviations are a consequence of the Rabi oscillations discussed in the previous Section (cf. Fig. 5.3). Therefore, we conclude that also the energy-time correlation spectra may be used to identify the presence of excitation beyond the LER. However, it turns out that these spectra contain additional signatures for a non-linear excitation, which can be revealed using a Fourier transform along the time axis, as discussed next.

5.5.3 Frequency-frequency correlation-spectra analysis of the non-resonant case $\Delta \neq 0$

The interpretation of the time- and frequency-resolved spectra in Fig. 5.5 is facilitated by a Fourier transform along the time axis, which yields a frequency-frequency correlation (FFC) spectrum [WE23a]. In particular, the hyperbolic structures in the time-frequency spectra convert into diagonal lines in the FFC spectra, which greatly assists their analysis. However, we stress again that the present manuscript considers *non-impulsive* x-ray driving pulses without additional reference absorbers, such that the results cannot directly be compared to previous studies (see the discussion in Sec. 5.5.2).

Results for the FFC spectra are shown in Fig. 5.6. For lower pulse areas, the diagonal structures in the FFC spectra are suppressed as compared to the impulsive case [WE23a], since the nuclear excitation at off-resonant energies is negligible, which is in contrast to the impulsive case, where resonant contributions from the reference absorber give rise to visible contributions at all detunings. Towards higher pulse areas and stronger excitation, we recognize two distinct features. First, on resonance $\Delta = 0$, the population and the coherence squared show qualitatively different behavior, because of their different Rabi oscillation frequencies in the time domain (cf. Sec. 5.3.1). The appearance of these differences again serves as a signature for dynamics beyond the LER. Second, off-resonance ($\Delta \neq 0$), diagonal structures start to appear. Interestingly, the population only exhibit diagonals of slope one (yellow lines), corresponding to a dependence of its dynamics on the detuning [WE23a]. In contrast, the coherence squared exhibits diagonals with slope one (yellow lines) and two (red lines), corresponding to contributions oscillating with frequencies Δ and 2Δ. The additional pair of diagonals with slope two arises from a frequency-mixing of different scattering orders in squaring the coherence. In Sec. 5.5.4, we analyze this feature further, and show that in the LER, only the diagonals of slope one appear in the coherence squared. Starting from the next higher order, diagonals of both slopes become visible. Therefore, the appearance of diagonals with slope two are a clear qualitative signature for excitation beyond the LER. At even higher pulse areas, the Rabi oscillations dominate, and the diagonals in the FFC spectra develop an anti-crossing-like feature towards their center, which can be attributed to the onset of an Autler-Townes splitting of the resonance.

5.5.4 Nonresonant excitation of two-level systems beyond the low-excitation regime

In Fig. 5.6 we found that the FFC spectra of the population exhibit diagonal structures with slope one, while the corresponding coherence squared may feature diagonals of slope one and two. In this Section, we explain this difference, based on the exact solution to a two-level system near-resonantly driven by a continuous light field with constant Rabi frequency Ω_0 [SZ97].

The population and the coherence squared for this system can be written in terms of the generalized Rabi frequency $\Omega_\Delta = \sqrt{\Omega_0^2 + \Delta^2}$ as

$$\begin{aligned} \rho_{ee}(t) =& \frac{\Omega_0^2}{4\Omega_\Delta^2}\left(2 - e^{i\Omega_\Delta t} - e^{-i\Omega_\Delta t}\right)\,, \\ |\rho_{ge}(t)|^2 =& \frac{\Omega_0^2}{16\Omega_\Delta^4}\left[6\Delta^2 + 2\Omega_\Delta^2 - \Omega_0^2\left(e^{2i\Omega_\Delta t} + e^{-2i\Omega_\Delta t}\right) - 4\Delta^2(e^{i\Omega_\Delta t} + e^{-i\Omega_\Delta t})\right]\,. \end{aligned} \tag{5.64}$$

Here, we have rewritten the usual form of the expressions [SZ97] in terms of exponential functions, since they directly reveal the different contributing frequency components. We find that the population features oscillations with the generalized Rabi frequency $\pm\Omega_\Delta$ only. In contrast, the absolute square of the coherence evolves with frequency $\pm\Omega_\Delta$ and $\pm 2\Omega_\Delta$. Note that the coherence $\rho_{ge}(t)$ itself does not comprise components oscillating at $\pm 2\Omega_\Delta$. This suggests that the origin of the oscillation with double frequency in the coherence squared is a frequency-mixing between the negative and positive frequency component of the dipole oscillation.

In the limit $\Delta \gg \Omega_0$ of large detunings, $\Omega_\Delta \approx \Delta$, and thus oscillations with $\pm\Delta$ and $\pm 2\Delta$ appear that convert into the diagonal lines in the FFC spectra in Fig. 5.6 upon Fourier transformation along the time axis (cf. [WE23a]).

To demonstrate that the second pair of diagonal lines with slope two is a consequence of an excitation beyond the LER, we use the self-consistent Eqs. (5.18) to derive the lowest and next-to-leading order results for the coherence squared. In order to focus on detuning-dependent effects, we again

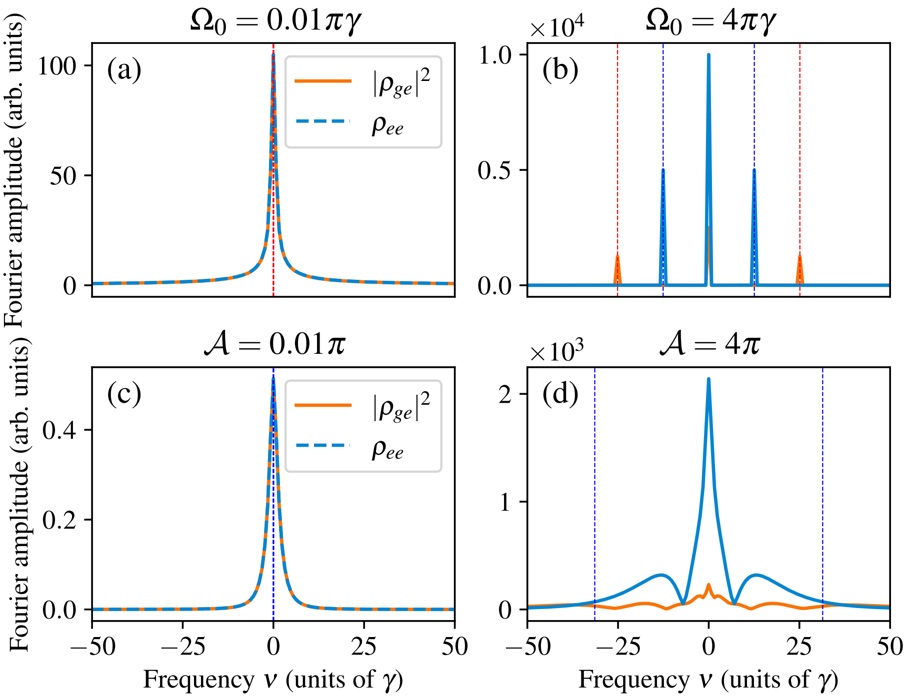

Figure 5.7: Fourier-transformed 1D time-spectra at low and high excitations: The upper panels show the constant envelope case without nuclear decay, while the lower panels show the exponentially-decaying case including level decay. In the LER no splitting of the resonance line occurs (left panels), while at higher excitations an Autler-Townes-splitting of the resonance becomes visible in the constant-envelope case (panel (b)). This is modified by a broadening and shifting of the resonance position in the exponentially-decaying case (panel (d)).

assume a pulse with constant envelope Ω_0. The results read:

$$\left(|\rho_{ge}(t)|^2\right)^{(0-2)} = \frac{\Omega_0^2}{4\Delta^2}\left(2 - e^{i\Delta t} - e^{-i\Delta t}\right) , \tag{5.65}$$

$$\left(|\rho_{ge}(t)|^2\right)^{(4)} = 2\mathrm{Re}\left[\rho_{ge}^{*(1)}(t)\rho_{ge}^{(3)}(t)\right] \tag{5.66}$$

$$= -\frac{7}{8}\frac{\Omega_0^4}{\Delta^4} + \left(\frac{\Omega_0^4}{16\Delta^4} - i\frac{\Omega_0^4\, t}{8\Delta^3}\right)e^{i\Delta t} + \left(\frac{\Omega_0^4}{16\Delta^4} + i\frac{\Omega_0^4\, t}{8\Delta^3}\right)e^{-i\Delta t} - \frac{\Omega_0^4}{16\Delta^4}\left(e^{2i\Delta t} + e^{-2i\Delta t}\right) . \tag{5.67}$$

As expected from the general proof of the equivalence of population and coherence squared in second order of the x-ray-nucleus interaction, the lowest order contribution to the coherence squared features oscillations with $\pm\Delta$ only, like the population. In contrast, already in fourth order the coherence squared oscillates with both frequencies $\pm\Delta$ and $\pm 2\Delta$. Therefore, we conclude that the diagonals with slope two only appear in the FFC in case of excitation beyond the LER. This suggests to use the appearance of the diagonal lines of slope two in the coherently scattered intensity as a feature to characterize dynamics beyond the LER.

5.5.5 Autler-Townes-splitting on resonance

The Autler-Townes splitting visible in the FFC spectra Fig. 5.6 is further evaluated by plotting a section through these spectra at $\Delta = 0$ along the axis of the Fourier frequency ν. This corresponds to Fourier transforms of the resonant spectra discussed in Sec. 5.5.1. Fig. 5.7 shows the Fourier amplitude of coherence squared (orange curve) and population (blue curve) on resonance. The constant-envelope case excluding decay of the nuclear transition is displayed in panel (a) and (b) at low ($\Omega_0 = 0.01\pi\gamma$) and high excitations ($\Omega_0 = 2\pi\gamma$), respectively. Here, γ is the single-nucleus linewidth, which is introduced even in the case without nuclear decay as a reference frequency to compare to the results including nuclear decay. The lower panels (c) and (d) show the non-impulsive case as treated in Sec. 5.5 for corresponding small ($\mathcal{A} = 0.01\pi$) and large ($\mathcal{A} = 4\pi$) pulse areas. To compare the two results, we note that the Rabi frequency in the constant-envelope case can be interpreted as the total pulse area per unit time.

In the ideal Rabi case a splitting of the resonance line at higher excitations becomes visible (panels (a) and (b)). Note that the splitting in the population appears at frequencies $\nu = \pm\Omega_0$ while the coherence squared shows peaks at both once and twice the Rabi frequency as indicated with the orange and blue dashed lines. This is in agreement with the analytical results of Sec. 5.5.4 and with the interpretation of the bending of the diagonal structures as an Autler-Townes splitting [SZ97; MS07]. In comparison, the experimentally relevant non-impulsive case also developes a splitting of the resonance line toward higher excitations (panels (c) and (d)). However, these peaks are much reduced in amplitude and significantly broadened. Further, the peaks seem shifted from the pulse amplitude at time zero $\nu = \pm\Gamma_a\mathcal{A}$ which we indicated as a frequency reference as blue dashed lines in the plot. The decrease in peak height we mainly attribute to damping of the resonance due to decay of the nuclear transition. The broadening and shifting of the peak can be explained by spreading of the driving pulse's frequency distribution due to its exponential decay, which is discussed in more detail in the next Section. We conclude that the bending of the diagonal structures in the lower panels of Fig. 5.6 can indeed be related to Autler-Townes-splitting of the nuclear resonance. However, in the non-impulsive case the zero detuning splittings can not directly be related to the driving pulse amplitude due to the more complex frequency structure of exponentially-decaying pulses. This reveals the impact that the pulse structure of non-impulsive x-ray excitations can have also on spectral properties of the scattered radiation beyond the LER.

5.5.6 Interplay of pulse and resonance decay for non-impulsive excitation

In Sec. 5.5.5 the influence of the pulse envelope on the Autler-Townes splitting in the FFC spectra and Fourier-transformed time spectra was studied. Here, we briefly discuss the effect the time-dependence of non-impulsive x-ray-nuclei interaction can have on the measured intensity in the LER and beyond. Specifically, we show that the interplay between nuclear resonance decay and duration of exponentially-decaying pulses is directly reflected in the time-dependence of the coherently and incoherently scattered light. This is of importance for future research in nuclear quantum optics for two reasons: First, for specific quantum optical applications decay rates γ of effective level schemes in x-ray wave guides have to be designed properly [DLE22a] and, second, in case of single-line reference absorbers producing near-monochromatic x-ray fields [Hee+21] the thickness of these absorbers defines the effective decay rate of the driving field. This, however, has to be optimized for specific experimental needs as the thickness also leads to a different absorption and temporal shape of the emitted x-ray light. For these reasons, in the following we study features of the temporal dynamics of coherently and incoherently scattered light as a function of resonance and pulse decay.

Fig. 5.8 compares the time response of coherence squared and population of an exponentially-decaying pulse envelope with rate $\Gamma_a = 2.5\gamma$ excluding resonance decay (panels (a) and (b)) with the one of an excitation with constant pulse envelope but including resonance decay (panels (c) and (d)). Again, both cases are compared at low pulse areas or Rabi frequencies (left panel) and large pulse areas or Rabi frequencies (right panel) for the same parameter sets as in Sec. 5.5.5. By considering only one decay parameter at a time, it becomes clear that resonance decay leads to a damping of the Rabi oscillations (panel (d)), as expected, while pulse decay leads to a stretching (panel (b)). The latter effect is caused by the amplitude of the x-ray-nuclei interaction reducing in time for the exponentially-decaying pulse which causes the oscillation to slow down. This change in the oscillation frequency is also the reason for the broadening and shift in the Autler-Townes splitting frequencies discussed in Sec. 5.5.5 and for the peak deviation of the local intensity being different from the constant-envelope case in Fig. 5.4 (b).

Another feature which distinguishes these two cases from the non-impulsive excitation discussed in Sec. 5.5 is the non-existence of local maxima in the LER (left panels) compared to Fig. 5.3 (a). Indeed, an analytical evaluation of the self-consistent Eqs. 5.18 in the the lowest excitation order for exponentially decaying pulse of the form Eq. (5.61) yields

$$\rho_{ee}^{(2)}(t) = = |\rho^{(1)}(t)|^2 = \frac{1}{4}e^{-\gamma t}\left|\int_0^t dt' e^{\frac{\gamma}{2}t'}e^{i\omega_0 t'}\Omega(t')\right|^2 \tag{5.68}$$

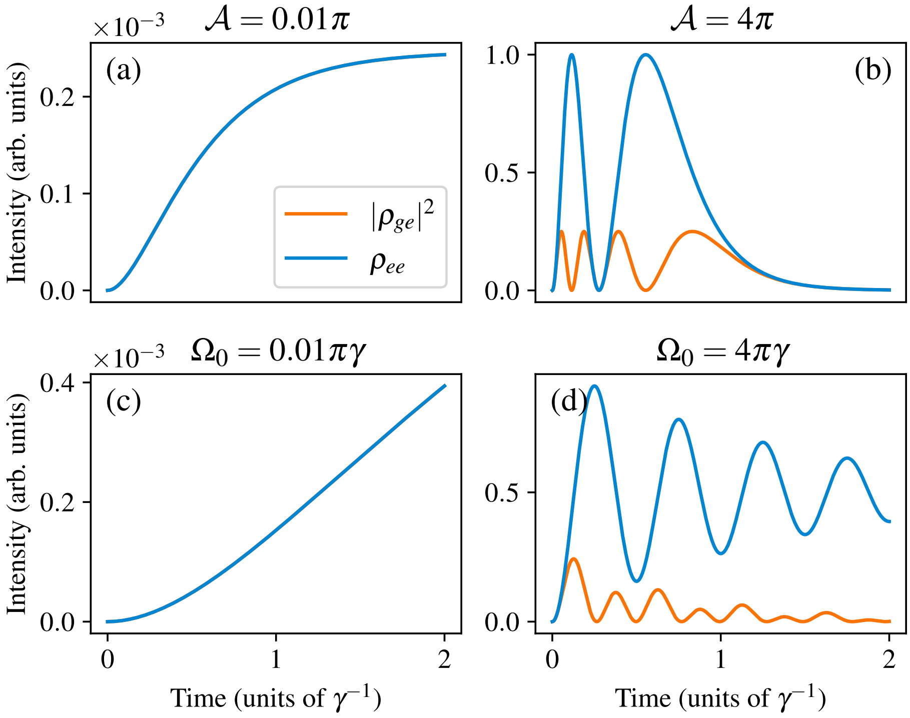

Figure 5.8: Effects of resonance and pulse decay on coherently and incoherently scattered light: The upper panels show the case without nuclear decay but an exponentially-decaying driving pulse. No local maximum appears in the LER case (panel (a)) and a stretching of the Rabi oscillations can be seen at higher excitations (panel (b)). The lower panels show the case including nuclear decay but feature a driving pulse with a constant envelope. As in the previous case, no local maximum appears in the LER (panel (c)), while at higher excitations the Rabi oscillations are damped, as expected (panel (d)).

$$= \frac{(\Gamma_a \mathcal{A})^2}{4(\Delta^2 + (\Delta\Gamma)^2)} \left[e^{-\gamma t} + e^{-2\Gamma_a t} - 2e^{-\Gamma_{tot} t} \cos(\Delta t) \right] \tag{5.69}$$

with $\Gamma_{tot} = \Gamma_a + \frac{\gamma}{2}$, $\Delta\Gamma = \Gamma_a - \frac{\gamma}{2}$. On resonance, the local maxima of this expression can be found as

$$t_{max} = 2 \frac{\log\left(\frac{2\Gamma_a}{\gamma}\right)}{2\Gamma_a - \gamma} , \tag{5.70}$$

which shows that only an interplay between resonance and pulse decay causes the time-dependent coherently and incoherently scattered intensity to develop a local maximum in the LER as $t_{max} \to \infty$ if one of the two decay rates tends to zero. The existence of these local maxima in lowest excitation order is also responsible for the steep increase of the peak deviation Fig. 5.4 (b) starting at zero pulse area since the maxima of the two observables change smoothly as a function of the pulse area.
Our findings demonstrate the importance of both nuclear decay dynamics and the temporal shape of non-impulsive driving fields for time spectra measured upon non-impulsive x-ray excitation.

5.6 Discussion and summary

In this Chapter we have developed methods to verify the excitation of an ensemble of Mössbauer nuclei beyond the low-excitation regime (LER). This is motivated by the recent availability of x-ray free-electron lasers which are capable of delivering many resonant photons per pulse, such that the as-yet unexplored regime of stronger excitation of the nuclei comes within reach. Since source limitations will likely persist at least in the near future, we focused our analysis on practically relevant and experimentally robust approaches which are applicable already in a regime where the linear x-ray-nuclei interaction is only slightly surpassed.

Our approach is based on the comparison of two observables, which can be measured concurrently in an experiment: the coherently scattered light, which features a directional emission in a narrow angular range, and the incoherently emitted internal conversion signatures (photons or electrons) which are emitted essentially into the full solid angle. The latter signature is proportional to the sum of the excited-state populations of the nuclei, while the former is related to the absolute value squared of the coherent sum of the induced dipole moments augmented by phase factors related to the excitation and de-excitation of the nuclei.

As a key step, we established that the time-dependent intensities emitted into the coherent and the incoherent channels are equivalent up to second-order in the driving x-ray field for a wide range of systems, such that their ratio is constant in time. To this end, we first proved the corresponding equivalence between the populations and coherences for an effective single-particle system describing a nuclear ensemble embedded in a waveguide environment. Subsequently, we extended the proof to a general homogeneous N-body system of interacting nuclei. As a result, we found that any deviations in the ratio between the x-rays coherently and incoherently scattered off of the nuclei can directly be traced back to an excitation beyond the LER.

Throughout our analysis, we considered two relevant cases: First, a near-instantaneous impulsive excitation, e.g., via an XFEL. Second, a more general non-impulsive excitation, such as an exponentially decaying pulse from a synchrotron-Mössbauer-like source. The general results for the coherence-population equivalence in second-order of the driving x-ray field hold in both cases. We further focused on the case of nuclei embedded in waveguides, for which the observables are largely unaffected by propagational effects. It remains an interesting open question whether a generalized equivalence between coherently- and incoherently scattered intensity can also be established in the presence of propagational effects.

We found that the various considered settings feature different dynamics in case of excitation beyond the LER. For an impulsively excited single effective level scheme, the ratio between coherently and incoherently scattered intensity changes with the degree of excitation, but it remains constant over time. Analogously, the ratio also depends on the degree of initial impulsive excitation in the interacting many-body system. However, the many-body system further exhibits a time-dependence of the intensity ratio if the excitation exceeds the LER and if simultaneously the inter-particle coupling is sufficiently enhanced beyond the free-space value, e.g., via a suitable waveguide environment.

In case of non-impulsive excitation, we found that the time-dependence of the intensity ratio becomes much richer. To this end, we numerically studied the temporal dynamics of a single effective level scheme driven by an exponentially-decaying x-ray pulse. Based on the results, we proposed several signatures which can be used to identify excitation beyond the LER. In the case of a resonant driving field, the first indication are the respective times at which the two intensities become maximal. These times agree in case of low excitation, but characteristic deviations appear for stronger excitation. At even higher excitation Rabi oscillations typical for the strongly nonlinear regime dominate the dynamics of both scattering observables, however, with different respective oscillation frequencies. We further studied off-resonant excitation, using time-frequency correlated and frequency-frequency correlated spectra. In the time-frequency spectra, near resonance again resonant Rabi oscillations appear as the strongest indicator of excitation beyond the LER, while the off-resonant regime strongly resembles the LER even at higher excitations. In the frequency-frequency correlation spectra, characteristic diagonal structures appear. We could show that the incoherent intensity only exhibits a single pair of diagonals, with slope one. In contrast, at excitation beyond the LER, the coherently-scattered intensity shows two pairs of diagonals at slopes one and two. Thus, the characteristic diagonal structure may also serve as a signature for stronger excitation of the nuclear ensemble.

Overall, we therefore conclude that the ratio of the coherently and incoherently scattered intensities serves as a strong indicator for excitation of a nuclear ensemble beyond the LER. Its time structure can further reveal the presence of dipole couplings between nuclei.

In general, our approach has the advantage that both observables, the coherently and the incoherently scattered light, are well-established in experiments with Mössbauer nuclei. Most related experiments at accelerator-based x-ray sources have focused on the coherently scattered intensity, but the incoherently scattered intensity typically could be measured in addition without changing the original setup significantly. This suggests the usefulness of our approach even for experiments in which the degree of excitation is not the primary research goal. A comparable situation existed in the traditional distinction between Mössbauer experiments measuring either in the time or in the energy domain. It was recently shown [Hee+17; Hee+21; WE23a] that combined spectra correlating temporal and spectral information of the coherently scattered x-rays provide significant advantages over the individual time or frequency spectra, in particular also related to the comparison between theory and experiment. Also in that case, the original experimental setup could remain largely unchanged, and only had to be augmented by an event-based detection electronics. We envision that similar progress will be achieved in future experiments by the additional correlation of the coherently and incoherently scattered radiation proposed in the present work.

Chapter 6

Coupling dynamics of effective few-level systems

List of abbreviations used in this Chapter:

- LER: low-excitation regime
- EIT : electromagnetically-induced transparency
- FFC spectrum : frequency-frequency correlation spectrum
- XFEL : x-ray free electron laser
- XFELO : x-ray free electron laser oscillator
- SMS : synchrotron Mössbauer source
- CEMS : conversion electron Mössbauer spectroscopy

6.1 Introduction

In Ch. 5 we studied the dynamics of coupled two-level nuclei upon impulsive x-ray excitation in the LER and beyond in the full many-body basis. For the non-impulsive case we switched to an effective two-level description, which is a valid description of the collective behaviour of single layers of Mössbauer nuclei embedded in thin-film x-ray cavities (cf. Sec. 2.2.2). This prompts the question whether our findings for two-level systems can be generalized to more complex level schemes. These can arise, e.g., if more than one nuclear layer is embedded in the wave guide structure [HE15a; DLE22a; Hab+17; Röh+12] or if the resonances of nuclear layers experience Zeeman splitting through magnetic hyperfine fields [HE13; Hee+13]. Some of the most intriguing phenomena in nuclear quantum optics have been realized with such multilevel schemes including spontaneously-generated coherences [Hee+13], electromagnetically-induced transparency (EIT) [Röh+12; DLE22a] and Rabi oscillations between nuclear ensembles [Hab+17].

Rigorous theoretical descriptions of these systems at low excitations in the framework of cavity quantum electrodynamics (QED) are now available, e.g. using the ab initio Green's function approach [Len+20] (see also Sec. 2.2.2) and both the calculation of quantum optical parameters from the known cavity structure [Len+20] as well as inverse design of cavities to realize particular level schemes [DLE22a; DLE22b] are possible. However, it was shown that an interpretation of frequency-resolved transmission or reflection spectra in terms of collective level schemes may not be unique [DLE22a]. One possibility to resolve this issue is to measure more complex spectra with additional degrees of freedom or correlate different observables. Chapter 3 presented one such approach, that analyzed time- and frequency-resolved spectra via Fourier transformation and additionally employed phase control of the incident x-ray light to selectively enhance specific features of the measured spectra and suppress others. With this, in Sec. 3.3.3 it was possible to retrieve the complex-valued nuclear resonant response of a thin-film cavity featuring EIT including phase information. Another approach to obtain additional information about the dynamics of nuclear ensembles correlated the measurement of incoherent and coherent radiation emitted by these ensembles. This approach was presented in Chapter 5 and was used to study excitation beyond the LER.

In this Chapter, we build on these approaches to study the dynamics of effective three-level systems realized in thin-film cavities with two resonant layers including coupling between the excited states associated with this cavity structure in the LER. Such a cavity and the corresponding three-level scheme are shown in Fig. 6.1. Regardless of a specific realization of such a collective level scheme, the retrieval of couplings between nuclear excited states is of general interest. It is known from the longer wavelength regime that such couplings critically determine the dynamics and reaction properties of molecular and atomic systems and entire branches of spectroscopy deal specifically with the

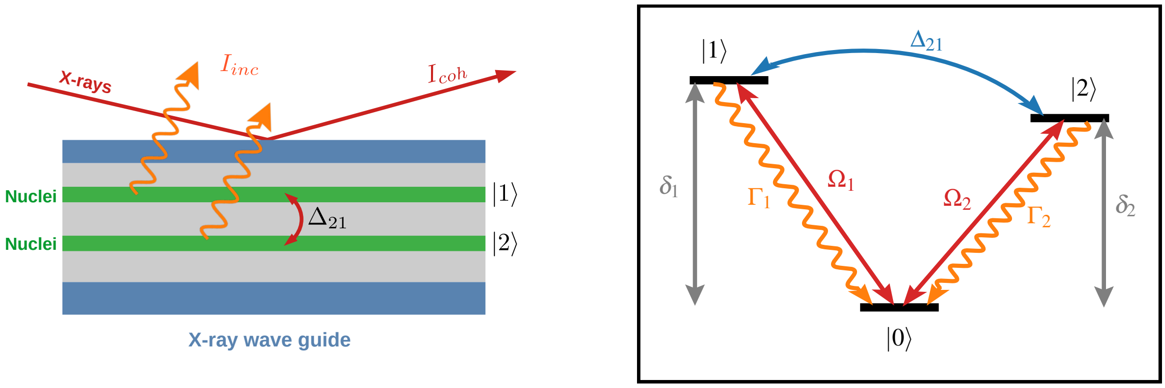

Figure 6.1: Cavity structure with two resonant layers (left panel) and corresponding effective three-level scheme (right panel) as studied in Ch. 6. Γ_l denote the effective decay rates of the two transitions, δ_l the (renormalized) detunings between ground and excited state l, Ω_l are the amplitudes of the time-dependent Rabi frequencies and Δ_{21} denotes the coherent coupling between the excited states.

determination and characterization of such couplings [Cho19; HZ11]. Therefore, it is the aim of this Chapter to discuss how such excited state couplings can be measured using different data acquisition and evaluation approaches. To this end, methods developed in the previous Chapters are employed: Time- and frequency-resolved spectra and their analysis as FFC spectra are discussed upon impulsive and non-impulsive excitation pulses. Further, the coherently and incoherently scattered intensity are compared. To interpret the data obtained in such measurments, the density matrix perturbation theory developed in Chapter 4 is used.

This Chapter is structured as follows: For the interpretation of measured spectra in the LER, we first derive the up-to-second order coherences and populations of effective three-level systems, related to the coherently and incoherently scattered intensity (cf. Sec. 5.2.2), including excited-state couplings. This is done with the help of the perturbative density matrix expansion developed in Sec. 4.2. We present a graphical interpretation of the different contributions to these quantities and discuss specific limits. In the second part numerical simulations of incoherently and coherently scattered intensities off of these effective three-level systems upon impulsive and non-impulsive excitations in the LER are compared. Various signatures of the presence of an excited-state coupling are discussed, including diagonal structures similar to those studied in Chapter 3 and oscillations of the single-layer coherences that can be retrieved using depth-sensitive measurement methods. Finally, the results are summarized.

6.2 Density matrix expansions of effective few-level systems

To study the dynamics of collective few-level systems at low excitations, we employ the perturbative density matrix expansion developed in Sec. 4.2 specialized to the case of a single few-level system arising in x-ray cavities under low-excitation conditions. In this case, the indices n, n' indexing different nuclei in a many-body description can be dropped in the Hamiltonian and Lindbladian presented in Sec. 4.2. For convenience, we briefly revisit the import equations and parameters: The dynamics of the nuclear few-level density matrix can be described by the master equation

$$\frac{d}{dt}\hat{\rho} = \frac{1}{i\hbar}\left[\hat{H},\hat{\rho}\right] + \mathcal{L}[\hat{\rho}]\,. \tag{6.1}$$

with the Hamiltonian

$$\hat{H} = \hat{H}_{\text{nuc}} + \hat{W}(t)\,. \tag{6.2}$$

In a few-level description the nuclear system part of the Hamiltonian can be written as

$$\hat{H}_{\text{nuc}} = \hbar\sum_{l}\omega_l\,|l\rangle\,\langle l| - \hbar\sum_{ll'}\Delta_{ll'}\hat{\sigma}_l^{+}\hat{\sigma}_{l'}^{-} \tag{6.3}$$

where ω_l denotes the transition frequency of the effective collective transition l and $|l\rangle\langle l|$ the projector on the corresponding excited state. The parameters $\Delta_{ll'}$ are coherent couplings between different excited states for $l \neq l'$ and account for renormalization of the transition frequencies known as collective Lamb shift [FS05; Röh+10] if $l = l'$. These quantities are related to the cavity's Fourier-transformed Green's tensor via [Len21] (see also Sec. 2.2.2)

$$\Delta_{ll'} = \frac{N}{A_{\parallel}} \frac{\mu_0 \omega_l^2}{\hbar} \mathbf{d}_l^* \cdot \mathrm{Re}\left[\mathbf{G}(z_l, z_{l'}, \mathbf{k}_{\parallel}, \omega_l)\right] \cdot \mathbf{d}_{l'} \tag{6.4}$$

where N denotes the number of resonant nuclei per layer, $A_{\parallel}$ the area covered by the nuclei in the planar cavity and μ_0 the vacuum permeability. The Green's tensor $\mathbf{G}$ depends on the depth of the two layers z_l, $z_{l'}$ and the cavity in-plane wave vector component $\mathbf{k}_{\parallel}$. The collective raising and lowering operators $\hat{\sigma}_l^{\pm}(\mathbf{k}_{\parallel})$ for a given parallel wave vector $\mathbf{k}_{\parallel}$, in contrast to the single-particle operators $\hat{\sigma}_n^{\pm}$ introduced in Sec. 5.2.1, create and annihilate exciton states in layer l if acting on the collective ground state $|0\rangle$ with all nuclei in the cavity in their respective ground states $|g_n\rangle$, i.e.

$$\sigma_l^+(\mathbf{k}_{\parallel})\,|0\rangle = \frac{1}{\sqrt{N}} \sum_n e^{i\mathbf{k}_{\parallel}\mathbf{r}_n} \,|g_1 \dots l_n \dots g_n\rangle \,, \tag{6.5}$$

where $|l_n\rangle$ refers to the excited state of the nucleus n in layer l.
In the following, we suppress the dependence of the raising and lowering operators on the parallel wave vector $\mathbf{k}_{\parallel}$ for notational simplicity.
The nucleus-field interaction part of the Hamiltonian in the few-level description reads

$$\hat{W}(t) = -\frac{\hbar}{2} \sum_{nl} \left(\Omega_l(t)\hat{\sigma}_l^+ + h.c.\right) \tag{6.6}$$

with time-dependent Rabi frequency

$$\Omega_l(t) = \frac{\mathbf{d}_l \mathbf{E}(z_l, \mathbf{k}_{\parallel}, t)}{\hbar}\,. \tag{6.7}$$

Here, the electric driving field is given by the Fourier transform of the incident field in the cavity layer plane, i.e. [Len+20]

$$\mathbf{E}(z_l, \mathbf{k}_{\parallel}, t) = \int d^2\mathbf{r}_{\parallel,n} \mathbf{E}(\mathbf{r}_{ln}, t) e^{-i\mathbf{k}_{\parallel}\cdot\mathbf{r}_{\parallel,n}} \tag{6.8}$$

Finally, the Lindbladian in this effective description becomes

$$\mathcal{L}\left[\hat{\rho}\right] = \sum_{ll'} \Gamma_{ll'} \left[2\hat{\sigma}_{l'}^- \hat{\rho} \hat{\sigma}_l^+ - \left\{\hat{\sigma}_l^+ \hat{\sigma}_{l'}^-, \hat{\rho}\right\}\right] \tag{6.9}$$

Like the coherent couplings $\Delta_{ll'}$, the cross-damping terms are related to the cavity Green's function $\mathbf{G}$ via [Len21]

$$\Gamma_{ll'} = \frac{N}{A_{\parallel}} \frac{\mu_0 \omega_l^2}{\hbar} \mathbf{d}_l^* \cdot \mathrm{Im}\left[\mathbf{G}(z_l, z_{l'}, \mathbf{k}_{\parallel}, \omega_l)\right] \cdot \mathbf{d}_{l'} \tag{6.10}$$

Note, that the diagonal damping terms $\Gamma_l = \Gamma_{ll}$ here include all radiative and non-radiative decay processes, for notational convenience. Noting that the system has only a single ground state, the perturbative expansion described in Sec. 4.2.4 can directly be applied to calculate the LER coherences and populations of the few-level system if the cross-damping terms $\Gamma_{ll'} = 0$ are neglected for $l \neq l'$.

The density matrix elements in zeroth, first and second order can be calculated via the expressions Eqs.(4.34), (4.36) and (4.38), respectively, from an initial state $\hat{\rho}(t_0)$ which we restate here:

$$\hat{\rho}^{(0)}(t) = \hat{T}_t^{\dagger}\hat{\rho}(t_0)\hat{T}_t = \hat{\rho}(t_0) \tag{6.11a}$$

$$\hat{\rho}^{(1)}(t) = -\frac{i}{\hbar}\int_{t_0}^{t} d\tau\, \hat{T}_{t-\tau}^{\dagger}\left[\hat{W}(\tau), \hat{\rho}^{(0)}(\tau)\right]\hat{T}_{t-\tau}\,, \tag{6.11b}$$

$$\hat{\rho}^{(2)}(t) = -\frac{i}{\hbar}\int_{t_0}^{t} d\tau\, \hat{T}_{t-\tau}^{\dagger}\left[\hat{W}(\tau), \hat{\rho}^{(1)}(\tau)\right]\hat{T}_{t-\tau}\,. \tag{6.11c}$$

where $\hat{T}_t$ given by Eq. (4.22), the explicit form of which will be given in the following Section.

6.3 Evaluation of the perturbative expansion

6.3.1 Explicit matrix form of the time evolution operator

Specializing to the case of a three-level system including a coherent excited state coupling Δ_{21} as depicted in Fig. 6.1, the solutions to the first and second order density matrix can be obtained by casting the problem into a matrix form, i.e.

$$\hat{H}_{\text{nuc}} = \hbar\begin{pmatrix} \delta_2 & -\Delta_{21} & 0 \\ -\Delta_{12} & \delta_1 & 0 \\ 0 & 0 & 0 \end{pmatrix}\,, \quad \hat{\Gamma} = \begin{pmatrix} \Gamma_2 & 0 & 0 \\ 0 & \Gamma_1 & 0 \\ 0 & 0 & 0 \end{pmatrix} \tag{6.12}$$

where, without loss of generality, we subtracted the ground state energy from the Hamiltonian such that $\delta_i = \omega_i - \omega_0$ and we absorbed the collective Lamb shifts Δ_{ii} into the respective transition frequencies. Now, the matrix form of the time evolution operator $\hat{T}_{t-t_0}$ can be obtained via diagonalization of the excited state sector which, since the nucleus-field coupling $\hat{W}(t)$ is treated perturbatively, separates from the ground state dynamics. A more detailed account of one possible diagonalization approach of the time evolution operator is given in Appendix A.7. Here, we just state the final matrix form of this operator:

$$\hat{T}_t = \exp\left(-\hat{\Gamma}t + \frac{i}{\hbar}\hat{H}_{nuc}t\right) = \begin{pmatrix} T_t^{22} & T_t^{21} & 0 \\ T_t^{12} & T_t^{11} & 0 \\ 0 & 0 & T_t^{00} \end{pmatrix} \tag{6.13}$$

with entries

$$T_t^{22} = \frac{e^{i\bar{\delta}t}e^{-\bar{\Gamma}t}}{\Delta_R}\left[\Delta_R\cos\left(\frac{\Delta_R t}{2}\right) + (i\Delta\delta - \Delta\Gamma)\sin\left(\frac{\Delta_R t}{2}\right)\right]\,, \tag{6.14a}$$

$$T_t^{11} = \frac{e^{i\bar{\delta}t}e^{-\bar{\Gamma}t}}{\Delta_R}\left[\Delta_R\cos\left(\frac{\Delta_R t}{2}\right) - (i\Delta\delta - \Delta\Gamma)\sin\left(\frac{\Delta_R t}{2}\right)\right]\,, \tag{6.14b}$$

$$T_t^{12} = -2i\frac{\Delta_{12}}{\Delta_R}e^{i\bar{\delta}t}e^{-\bar{\Gamma}t}\sin\left(\frac{\Delta_R t}{2}\right)\,, \tag{6.14c}$$

$$T_t^{21} = -2i\frac{\Delta_{21}}{\Delta_R}e^{i\bar{\delta}t}e^{-\bar{\Gamma}t}\sin\left(\frac{\Delta_R t}{2}\right)\,, \tag{6.14d}$$

$$T_t^{00} = 1\,, \tag{6.14e}$$

where

$$\Delta_R = \sqrt{(\Delta\delta + i\Delta\Gamma)^2 + 4|\Delta_{21}|^2}\,, \tag{6.15}$$

$$\bar{\delta} = \frac{\delta_2 + \delta_1}{2}\,, \quad \bar{\Gamma} = \frac{\Gamma_1 + \Gamma_2}{2}\,, \tag{6.16}$$

$$\Delta\delta = \delta_2 - \delta_1\,, \quad \Delta\Gamma = \Gamma_2 - \Gamma_1\,. \tag{6.17}$$

Note that the cross-terms $T_t^{ll'}$, $l \neq l'$ become identical up to a phase ϕ_{21} defined by

$$e^{i\phi_{21}} = \frac{\Delta_{21}}{|\Delta_{21}|} \tag{6.18}$$

which means that transfer between the excited states via the coupling is symmetric except for the case of a complex-valued coupling Δ_{21}. In contrast, the generalized coupling Δ_R becomes complex-valued, if and only if the two decay rates are different, i.e. $\Gamma_1 \neq \Gamma_2$, independent of the phase ϕ_{21} of the coupling Δ_{21}.

6.3.2 Evaluation of density matrix elements

This said, the density matrix in jth order can be obtained by explicit calculation of each term in Eq. (4.43) in matrix representation starting with the initial ground state density matrix

$$\hat{\rho}(t_0) = |0\rangle\langle 0| = \begin{pmatrix} 0 & 0 & 0 \\ 0 & 0 & 0 \\ 0 & 0 & 1 \end{pmatrix} . \tag{6.19}$$

Up to second order $j \in \{0, 1, 2\}$, an explicit calculation of the first three terms given by Eqs. (6.11) yields

$$\hat{\rho}^{(j)}(t) = \begin{pmatrix} \rho_{22}^{(j)}(t) & \rho_{21}^{(j)}(t) & \rho_{20}^{(j)}(t) \\ \rho_{12}^{(j)}(t) & \rho_{11}^{(j)}(t) & \rho_{10}^{(j)}(t) \\ \rho_{02}^{(j)}(t) & \rho_{01}^{(j)}(t) & \rho_{00}^{(j)}(t) \end{pmatrix} \tag{6.20}$$

with all nonzero entries up to second order given by

$$\rho_{02}^{(1)}(t) = -\frac{i}{2}\int_{t_0}^{t} d\tau (T_{t-\tau}^{00})^* \left[T_{t-\tau}^{22}\Omega_2^*(\tau) + T_{t-\tau}^{12}\Omega_1^*(\tau)\right] , \tag{6.21a}$$

$$\rho_{01}^{(1)}(t) = -\frac{i}{2}\int_{t_0}^{t} d\tau (T_{t-\tau}^{00})^* \left[T_{t-\tau}^{21}\Omega_2^*(\tau) + T_{t-\tau}^{11}\Omega_1^*(\tau)\right] \tag{6.21b}$$

$$\begin{aligned} \rho_{22}^{(2)}(t) = \int_{t_0}^{t} d\tau \Big\{ &-|T_{t-\tau}^{22}|^2 \mathrm{Im}\left[\Omega_2(\tau)\rho_{02}^{(1)}(\tau)\right] - |T_{t-\tau}^{12}|^2 \mathrm{Im}\left[\Omega_1(\tau)\rho_{01}^{(1)}(\tau)\right] \\ &-\mathrm{Im}\left[T_{t-\tau}^{22}(T_{t-\tau}^{12})^* \left(\Omega_1(\tau)\rho_{02}^{(1)}(\tau) - \Omega_2^*(\tau)\rho_{10}^{(1)}(\tau)\right)\right]\Big\} , \end{aligned} \tag{6.21c}$$

$$\begin{aligned} \rho_{11}^{(2)}(t) = \int_{t_0}^{t} d\tau \Big\{ &-|T_{t-\tau}^{11}|^2 \mathrm{Im}\left[\Omega_1(\tau)\rho_{01}^{(1)}(\tau)\right] - |T_{t-\tau}^{21}|^2 \mathrm{Im}\left[\Omega_2(\tau)\rho_{02}^{(1)}(\tau)\right] \\ &-\mathrm{Im}\left[T_{t-\tau}^{11}(T_{t-\tau}^{21})^* \left(\Omega_2(\tau)\rho_{01}^{(1)}(\tau) - \Omega_1^*(\tau)\rho_{20}^{(1)}(\tau)\right)\right]\Big\} , \end{aligned} \tag{6.21d}$$

$$\rho_{00}^{(0)}(t) = 1 \quad , \quad \rho_{00}^{(2)}(t) = -\rho_{22}^{(2)}(t) - \rho_{11}^{(2)}(t) . \tag{6.21e}$$

Note that, like in the two-level single- and many-body cases Sec. 5.3.2 and 5.3.3, the excited-state populations contribute in second order only and the coherences in first order only. From these equations it becomes clear immediately that excitation from one level is transferred to the coherence and population of the second level and vice versa via the off-diagonal time-evolution matrix elements $T_{t-\tau}^{ll'}$, $l \neq l'$. According to Eqs. (6.14), these are proportional to the excited-state coupling Δ_{21} and thus correspond to population and coherence transfer via the coupling of the excited states.

A more detailed graphical interpretation of the different contributions to the first and second order density matrix elements Eqs. (6.21) is given in Fig. 6.2 for the coherence $\rho_{01}^{(1)}(t)$ and in Fig. 6.3 for the population $\rho_{11}^{(2)}(t)$ of state $|1\rangle$. The contributions to state $|2\rangle$ can be interpreted analogously. Contributions to the coherences are indicated as large dashed gray ellipses involving the ground state

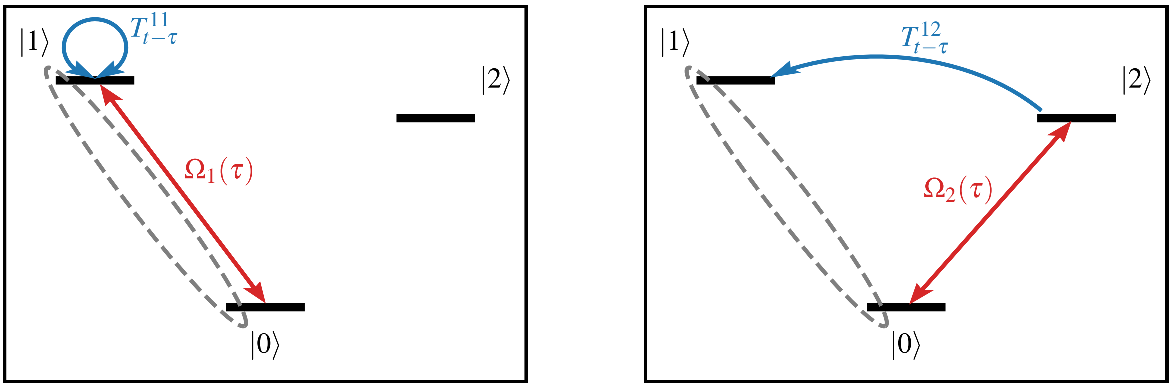

(a) Depiction of the direct coherence contribution to $\rho^{(1)}_{01}$.

(b) Depiction of the cross coherence contribution to $\rho^{(1)}_{01}$.

Figure 6.2: Graphical interpretation of contributions to the ground state coherence ρ_{01} of a three-level system as depicted in Fig. 6.1. The dashed gray ellipses indicate a contribution to the coherence between the states that are encircled.

and excited state between which the coherence is calculated. Contributions to the population are indicated as small solid gray circles in the corresponding level. Blue arrows indicate propagation via the time-evolution matrix elements $\hat{T}^{ll'}_t$.

A first-order coherence $\rho^{(1)}_{01}$ can be created in two ways, according to Eq. (6.21b):

a) The transition $|1\rangle$ is driven directly with Rabi frequency $\Omega_1(\tau)$ at time τ and evolves with diagonal contribution $T^{11}_{t-\tau}$ of the time evolution operator until measurement time t (Fig. 6.2a).

b) First, transition $|2\rangle$ is driven with Rabi frequency $\Omega_2(\tau)$ at time τ and the coherence $\rho^{(1)}_{01}(t)$ is created by transfer of the excitation to state $|1\rangle$ via the cross-coupling term $T^{12}_{t-\tau}$ (Fig. 6.2b). This second contribution is nonzero only in the presence of an excited-state coupling while the first one persists even in case of uncoupled transitions.

In comparison, the population $\rho^{(2)}_{11}(t)$ can be created via four excitation paths, according to Eq. (6.21d):

a) The coherence $\rho^{(1)}_{01}(\tau)$ is translated into a population with an additional excitation by the Rabi drive $\Omega(\tau)$ and is propagated until time t by the diagonal time evolution matrix element $|T^{11}_{t-\tau}|^2$.

b) The second order excitation of state $|2\rangle$ from the coherence $\rho^{(1)}_{02}(\tau)$ and the Rabi frequency $\Omega_2(\tau)$ is transformed into a population $\rho^{(2)}_{11}(t)$ via the cross-coupling term $|T^{12}_{t-\tau}|^2$.

c) + d) a coherence $\rho^{(1)}_{0l}(\tau)$ of one of the states l is combined with an x-ray excitation $\Omega_{l'}(\tau)$ to create a population in state $|1\rangle$ via the cross coupling $T^{12}_{t-\tau}$ and a time evolution with the diagonal term $T^{11}_{t-\tau}$.

Of these contributions, the latter three only contribute in presence of an excited state coupling Δ_{21} while the first one remains even in its absence.

Despite this graphical interpretation, Eqs. (6.21) remain relatively complex and the integrals cannot be evaluated for arbitrary pulse shapes $\Omega_l(\tau)$. However, they can be solved in a number of important cases: Under δ-like near-instantaneous Eqs. (6.21) simplify greatly, a case discussed in Sec. 6.4.1. The integrals can be solved for exponentially-decaying pulses, which will be discussed in Sec. 6.4.2. Further, in the limit of large coupling or in the absence of coupling the entries of the time evolution operator Eqs. (6.14) can be simplified which assists the evaluation of Eqs. (6.21) and subsequent interpretation of time- and frequency-resolved nuclear resonant scattering spectra studied in Sec. 6.4. In the following, we give a brief overview of the two coupling limits.

6.3.3 The large coupling limit

We start by deriving simplified expressions for the matrix elements of the time evolution operator in the large coupling limit. We define the large coupling limit by

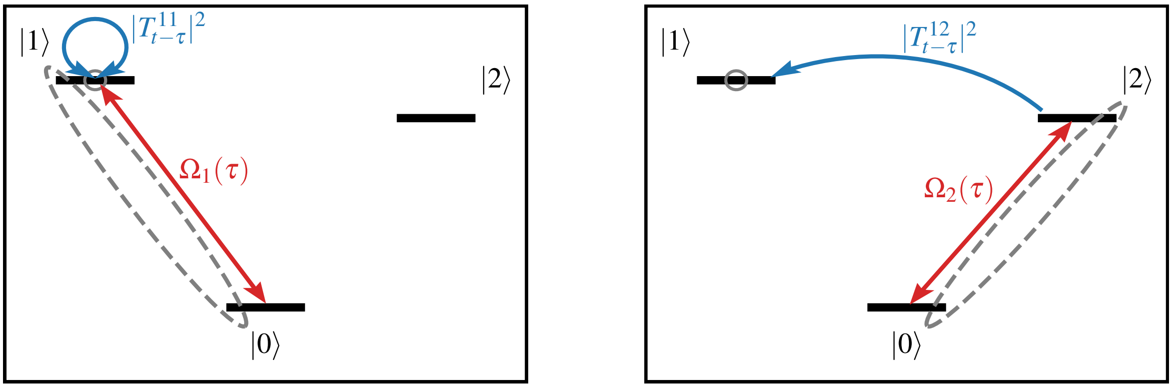

(a) Depiction of the direct population contribution to $\rho^{(2)}_{11}$.

(b) Depiction of the cross population contribution to $\rho^{(2)}_{11}$.

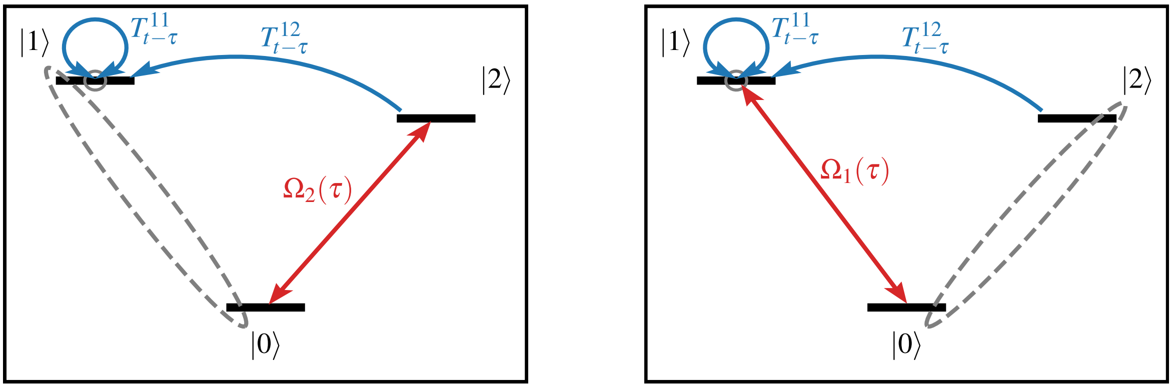

(c) Depiction of the direct coherence contribution to $\rho^{(2)}_{11}$.

(d) Depiction of the cross coherence contribution to $\rho^{(2)}_{11}$.

Figure 6.3: Graphical interpretation of contributions to the excited-state population ρ_{11} of a three-level system as depicted in Fig. 6.1. Again, dashed gray ellipses indicate coherence contributions between the encircled states created in first order, while small solid gray circles indicate a finite second-order contribution in the respective excited state.

$$\Delta_R \approx 2|\Delta_{21}|\,, \tag{6.22}$$

i.e. when the coupling dynamics is dominated by the excited state coupling Δ_{21} instead of the separate transition frequencies δ_l and decay constants Γ_l of the two transitions. Note, that apart from increasing the coupling Δ_{21} between the collectively excited states, this limit can also be realized by tuning the (effective) decay constants and (renormalized) transition frequencies of the two levels in the cavity such that they become approximately equal to each other. In this case, Eq. (6.22) is approximately satisfied since the differences of these parameters enter the generalized coupling Δ_{21}. Numerical methods that can calculate cavity structures that are needed to realize certain effective level structures have recently been established for thin-film cavities [DLE22b; DLE22a].
In the large coupling limit, the entries in the time evolution operator Eqs. (6.14) reduce to

$$T^{22}_t = e^{-\bar{\Gamma}t} e^{i\bar{\delta}t} \cos(|\Delta_{21}|t) = T^{11}_t \tag{6.23a}$$

$$T^{12}_t = -\, i e^{-i\phi_{21}} e^{-\bar{\Gamma}t} e^{i\bar{\delta}t} \sin(|\Delta_{21}|t) \tag{6.23b}$$

$$T^{21}_t = -\, i e^{i\phi_{21}} e^{-\bar{\Gamma}t} e^{i\bar{\delta}t} \sin(|\Delta_{21}|t) \tag{6.23c}$$

Remarkably, the intrinsic dynamics of the two excited states becomes identical up to the phase ϕ_{21} of the the cross-coupling terms $T^{ll'}_t$, $l \neq l'$, which is indicated by the fact that the diagonal terms T^{11}_t and T^{22}_t become identical in this limit.

6.3.4 No coupling

In the limit that no coupling is present, i.e. $\Delta_{21} = 0$, the two levels are expected to evolve in time independently. Indeed, the cross-coupling terms become zero and the diagonal entries simplify to

$$T_t^{ll} = e^{i\delta_l t} e^{-\Gamma_l t} \tag{6.24}$$

$$T_t^{ll'} = 0\,, \quad l \neq l' \tag{6.25}$$

such that the intrinsic dynamics of two independent two-level systems is recovered. Note, that the generalized coupling Eq. (6.15) that governs the dynamics of the effective three-level system is not zero but reduces to

$$\Delta_R \approx \Delta\delta + i\Delta\Gamma \tag{6.26}$$

in the limit of vanishing couplings $\Delta_{21} = 0$.

6.3.5 Population-coherence correspondence for effective three-level systems

In Sec. 5.3, we proved that the (time-dependent) coherence squared and the population of nuclear two-level systems become identical in the LER even in the case of interactions between the nuclei. Further, under the conditions of homogeneity of the nuclear ensemble and equivalent plane-wave x-ray-nucleus couplings for all nuclei, this could be extended to an equivalence of coherently scattered and incoherently scattered intensity of the entire nuclear ensemble associated with the coherent sum over the x-ray induced coherences and the nuclear excited state populations, respectively. In this Section, we aim to establish this correspondence of coherent and incoherent emission for effective three-level systems for each transition separately. Within the scope of this thesis, this result will mainly be used in Sec. 6.4 to simplify analytical evaluations of the second-order nuclear dynamics described by Eqs. (6.21). However, we envision that the methods used to establish this correspondence in the context of effective three-level systems can also be extended to more general multi-level systems and help to interpret NRS data obtained from such systems, e.g. via an interpretation in terms of dressed-states. Here we only state the final result

$$\rho_{ll}^{(0-2)}(t) = |\rho_{0l}^{(0-2)}(t)|^2, \tag{6.27}$$

while for a derivation of this result using a diagonalization approach of the time evolution operator $\hat{T}_t$ Eq. (6.13) the reader is referred to Appendix A.7.

6.4 Evaluation and interpretation of time and frequency spectra

In this Section, the dynamics of effective three-level systems upon different driving fields in the LER is studied numerically. The results are interpreted using explicit analytical evaluations of the density matrix expressions Eqs. (6.21) in the large and no coupling limits. The time and frequency spectra discussed below are obtained by numerical evaluation of the optical Bloch equations of the three level system Fig. 6.1 using the ODEINT function of the SCIPY package [Vir+20] in PYTHON [VRD09]. The three-level Bloch equations read

$$\dot{\rho}_{22}(t) = -\operatorname{Im}[\Omega_2\rho_{20}^*] - 2\operatorname{Im}[\Delta_{21}\rho_{21}^*] - 2\Gamma_2\rho_{22}\,, \tag{6.28a}$$

$$\dot{\rho}_{11}(t) = -\operatorname{Im}[\Omega_1\rho_{10}^*] + 2\operatorname{Im}[\Delta_{21}\rho_{21}^*] - 2\Gamma_1\rho_{11} \tag{6.28b}$$

$$\dot{\rho}_{20}(t) =(-i\delta_2 - \Gamma_2)\rho_{20} + i\Delta_{21}\rho_{10} - \frac{i}{2}\Omega_1\rho_{21} - i\Omega_2\rho_{22} - \frac{i}{2}\Omega_2\rho_{11} + \frac{i}{2}\Omega_2\,, \tag{6.28c}$$

$$\dot{\rho}_{10}(t) =(-i\delta_1 - \Gamma_1)\rho_{10} + i\Delta_{21}^*\rho_{20} - \frac{i}{2}\Omega_2\rho_{21}^* - i\Omega_1\rho_{11} - \frac{i}{2}\Omega_1\rho_{22} + \frac{i}{2}\Omega_1\,, \tag{6.28d}$$

$$\dot{\rho}_{21}(t) =(-i\Delta\delta - 2\bar{\Gamma})\rho_{21} + \frac{i}{2}\Omega_2\rho_{10}^* - \frac{i}{2}\Omega_1^*\rho_{20} - i\Delta_{21}(\rho_{22} - \rho_{11})\,, \tag{6.28e}$$

$$\dot{\rho}_{02} =\dot{\rho}_{20}^*\,, \quad \dot{\rho}_{01} = \dot{\rho}_{10}^*\,, \quad \dot{\rho}_{12} = \dot{\rho}_{21}^*\,, \quad \dot{\rho}_{00} = -\dot{\rho}_{22} - \dot{\rho}_{11}\,. \tag{6.28f}$$

and are obtained by evaluating the Liouvillian Eq. (6.1) with three-level Hamiltonian Eq. (6.3) and Lindbladian Eq. (6.9) in the three-state basis $\{|0\rangle, |1\rangle, |2\rangle\}$. Similar to the discussion in Chapter 5, we compare two types of excitations: First, impulsive near-instantaneous excitations are considered. Second, non-impulsive x-ray-nuclei interactions are studied that can be produced using a synchrotron Mössbauer source [Smi+97a] or the secondary radiation emitted by single-line reference absorbers (cf. Sec.2.1.5). Both, the incoherently scattered intensities, in form of the time-dependent population (cf. Sec. 5.2.2), and the coherently scattered intensity, in form of the coherence-squared, are investigated. The resulting spectra are interpreted employing methods developed and applied in Chapters. 3 and 5.

6.4.1 Impulsive excitations

In this part, we discuss effective three-level dynamics upon impulsive x-ray excitations. We will see that this gives rise to characteristic oscillations in incoherently scattered intensity I_{inc} from the single excited states associated with the populations $\rho_{ll}(t)$. Such a signal emitted from thin-film cavities could be measured using depth-sensitive detection methods.

For our simulation of near-instantaneous impulsive x-ray excitations, we use temporal Gaussian pulses of the form

$$\Omega_l(t) = \frac{\mathcal{A}_l}{\sqrt{2\pi\tau^2}} e^{-i\omega_p t} \exp\left(-\frac{(t - t_{exc})^2}{2\tau^2}\right) \tag{6.29}$$

where $\mathcal{A}_l$ is the total pulse area of the nucleus-field coupling of transition $|l\rangle$, τ is the duration of the pulse, ω_p its carrier frequency and t_{exc} the time of excitation of the nuclear ensemble. Note, that for short enough interaction periods τ this essentially simulates the effect of a near-instantaneous δ-like excitation with negligible effect of the detuning between the nuclear transitions and the carrier frequency of the driving pulse. The fundamental reason for this is that the spectrum of a Gaussian pulse broadens via Fourier principles if the pulse is made shorter such that a pulse with duration short enough compared to the nuclear decay dynamics has an effectively flat spectrum and excites the nuclear transition like a δ-pulse with the pulse effectively resonant with the nuclear transition essentially independent of the pulse's carrier frequency.

Fig. 6.4 shows the dynamics of the three-level system Fig. 6.1 as a function of the (real-valued) excited state coupling Δ_{21} and time. The parameters are chosen as: $\mathcal{A}_2 = 2\mathcal{A}_1 = 0.02\pi$, $\delta_1 = 5\gamma$, $\delta_2 = 15\gamma$, $\Gamma_1 = 0.5\gamma$ and $\Gamma_2 = 4\Gamma_1$. The excitation occurs at $t_{exc} = 10\tau$ with $\tau = 5 \cdot 10^{-3}\gamma^{-1}$. The pulse duration τ should not be chosen too short such that numerical integration performs reliably on the time scale of excitation. Here, we introduced a reference line-width γ which is not necessarily the single-nucleus linewidth but can be superradiantly broadened. This allows for a comparison of different realizations of the effective three-level schemes. Panel (a) and (b) show the populations ρ_{22} and ρ_{11}, respectively. Oscillations that become faster with increasing excited-state coupling are clearly visible, clear evidence of population transfer due to these couplings. However, these oscillations are strongly suppressed if the sum of both populations is considered (panel (c)), which corresponds to a strong suppression of this signature in the total incoherent radiation captured by a detector measuring in 4π. Indeed, in the limit $\Gamma_1 \to \Gamma_2$ these oscillations disappear completely only leaving an exponential decay of the incoherent intensity. This can be understood by the fact that the total

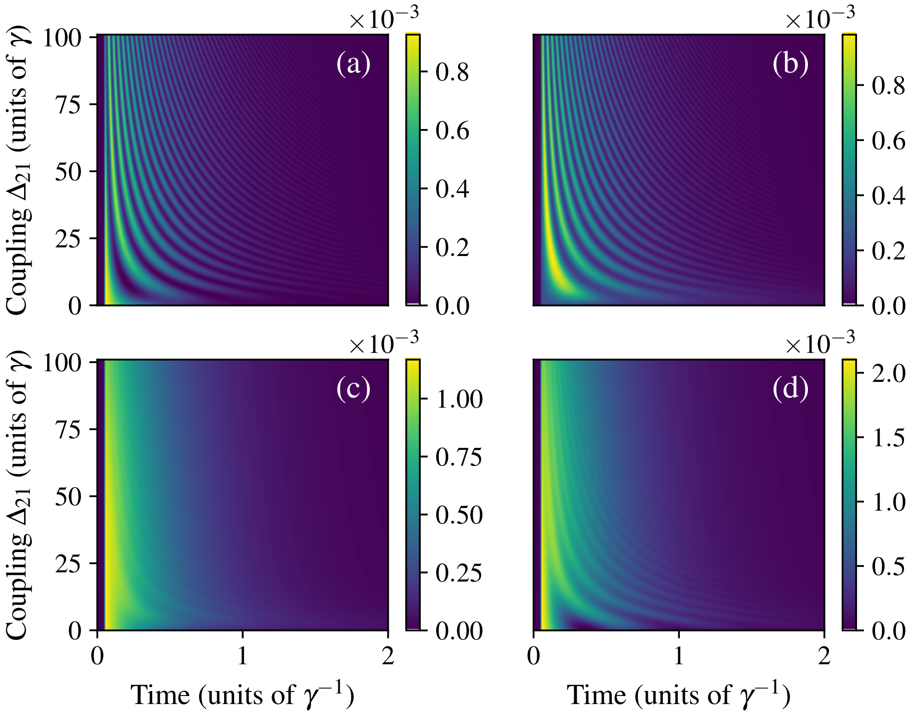

Figure 6.4: Coupling dynamics of the three-level system as a function of time and coupling strength between the two excited states upon a short excitation pulse. Panel (a) shows the population ρ_{22}, panel (b) the population ρ_{11}, panel (c) the sum of both populations $\rho_{11} + \rho_{22}$ and panel (d) the absolute squared of the sum of both coherences $|\rho_{01} + \rho_{02}|^2$. The pulse areas of the driving Rabi frequencies are related by $\mathcal{A}_2 = 2\mathcal{A}_1 = 0.02\pi$.

population in the excited states is not changed by the coherent coupling. In contrast, independent of the choice of the decay rates Γ_l, the absolute squared of the sum of the excited state coherences $|\rho_{01} + \rho_{02}|^2$ oscillate due to interference between the two transitions, as can be seen in panel (d).

In Fig. 6.5 the Fourier transform of the population ρ_{22} (panel (a)), ρ_{11} (panel (b)), $\sum_l \rho_{ll}$ (panel (c)) and $|\rho_{01} + \rho_{02}|^2$ (panel (d)) along the time axis is shown for the case of identical decay rates $\Gamma_2 = \Gamma_1 = 0.5\gamma$. Note, that diagonal structures with slope 1/2 appear at large Fourier frequencies ν that are most pronounced in the single populations panel (a) and (b). These diagonals we identify as the frequency-domain analogue of the oscillations found in the time spectra Fig. 6.4. These oscillations we relate to the generalized coupling Δ_R, as we will argue below in the large and no coupling limits. In particular, in the large coupling limit as introduced in Sec. 6.3.3, the generalized coupling reduces to

$$\Delta_R \approx \pm 2|\Delta_{21}| \tag{6.30}$$

which then explains the diagonals at large Fourier frequencies. The bending of the diagonals towards zero coupling is caused by the interference between the two transitions such that the generalized coupling in this regime is given by

$$\Delta_R \approx \pm(\delta_2 - \delta_1) \tag{6.31}$$

which is indicated by vertical dashed lines as guide to the eye.

To relate the behaviour of the generalized coupling Δ_R in Fig. 6.5 to the Fourier frequency ν, we analytically evaluate the coherences ρ_{02} and ρ_{01} in Eqs. (6.21) in the impulsive case, considering the limit $\tau \to 0$ such that the Gaussian pulse Eq. (6.29) reduces to a Dirac δ. The two coherences can then be written as

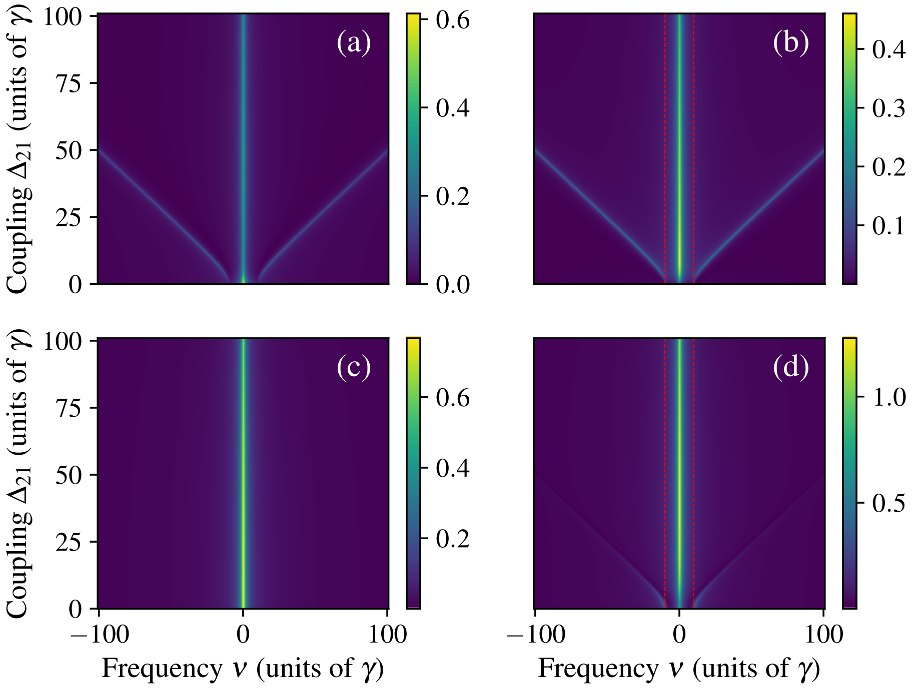

Figure 6.5: Fourier analysis along the time axis of coupling dynamics in the three-level system as a function of the coupling strength Δ_{21}. Panels (a) and (b) show the populations ρ_{22} and ρ_{11}, respectively. In panel (c), the sum of the populations is plotted. Finally, the absolute square of the coherent sum of both coherences is shown in panel (d). The red dashed lines in (b) and (d) mark the condition Eq. (6.31).

$$\begin{aligned}\rho_{02}^{(1)}(t) &= -\frac{i}{2}\left(\mathcal{A}_2 T_t^{22} + \mathcal{A}_1 T_t^{12}\right) \\ &= -\frac{i}{2}e^{-\bar{\Gamma}t}e^{i\bar{\delta}t}\left[\mathcal{A}_2\left(\cos\left(\frac{\Delta_R t}{2}\right) + \frac{(i\Delta\delta - \Delta\Gamma)}{\Delta_R}\sin\left(\frac{\Delta_R t}{2}\right)\right) - 2i\mathcal{A}_1\frac{\Delta_{12}}{\Delta_R}\sin\left(\frac{\Delta_R t}{2}\right)\right] \qquad (6.32)\\ \rho_{01}^{(1)}(t) &= -\frac{i}{2}\left(\mathcal{A}_1 T_t^{11} + \mathcal{A}_2 T_t^{21}\right) \\ &= -\frac{i}{2}e^{-\bar{\Gamma}t}e^{i\bar{\delta}t}\left[\mathcal{A}_1\left(\cos\left(\frac{\Delta_R t}{2}\right) - \frac{(i\Delta\delta - \Delta\Gamma)}{\Delta_R}\sin\left(\frac{\Delta_R t}{2}\right)\right) - 2i\mathcal{A}_2\frac{\Delta_{21}}{\Delta_R}\sin\left(\frac{\Delta_R t}{2}\right)\right] \qquad (6.33)\end{aligned}$$

which contain oscillatory terms with frequency components Δ_R and $\bar{\delta}$.
First, we consider the large coupling limit. In this case, the two coherences simplify to

$$\rho_{02}^{(1)}(t) = -\frac{i}{2}e^{-\bar{\Gamma}t}e^{i\bar{\delta}t}\left[\mathcal{A}_2\cos(|\Delta_{21}|t) - i\mathcal{A}_1 e^{-i\phi_{21}}\sin(|\Delta_{21}|t)\right] \qquad (6.34a)$$

$$\rho_{01}^{(1)}(t) = -\frac{i}{2}e^{-\bar{\Gamma}t}e^{i\bar{\delta}t}\left[\mathcal{A}_1\cos(|\Delta_{21}|t) - i\mathcal{A}_2 e^{i\phi_{21}}\sin(|\Delta_{21}|t)\right]\,. \qquad (6.34b)$$

In case of real-valued couplings $\phi_{21} = 0$, the populations in the LER, that can be calculated as the absolute square of the coherences in Eqs. (6.34) according to the population-coherence correspondence Eq. (6.27), read

$$\rho_{22}(t) = |\rho_{02}(t)|^2 = \frac{1}{4}e^{-2\bar{\Gamma}t}\left[\frac{\mathcal{A}_1^2 + \mathcal{A}_2^2}{2} + \frac{\mathcal{A}_2^2 - \mathcal{A}_1^2}{2}\cos(2|\Delta_{21}|t)\right] \qquad (6.35a)$$

$$\rho_{11}(t) = |\rho_{01}(t)|^2 = \frac{1}{4}e^{-2\bar{\Gamma}t}\left[\frac{\mathcal{A}_1^2 + \mathcal{A}_2^2}{2} - \frac{\mathcal{A}_2^2 - \mathcal{A}_1^2}{2}\cos(2|\Delta_{21}|t)\right] \qquad (6.35b)$$

which corresponds to oscillations at frequencies $\nu = 0$ and $\nu = \pm 2|\Delta_{21}|$ consistent with Fig. 6.5 (a) and (b). Note, that the sum of both populations does not experience oscillations since the two oscillating contributions cancel each other. Similarly, the absolute squared of the summed coherences in the large coupling limit Eq. (6.34) reads

$$|\rho_{02}^{(1)}(t) + \rho_{01}^{(2)}(t)|^2 = \frac{1}{4} e^{-2\bar{\Gamma} t} (\mathcal{A}_1 + \mathcal{A}_2)^2 \tag{6.36}$$

which explains the disappearence of the oscillations in Fig. 6.4 and of the diagonal structures in Fig. 6.5 for large couplings.

In the opposite case of negligible couplings, introduced in Sec. 6.3.4, the dynamics of the two transitions decouples such that

$$\rho_{0l}^{(1)}(t) = -\frac{i}{2} \mathcal{A}_l e^{-\Gamma_l t} e^{i\delta_l t} \tag{6.37}$$

Hence, neither of the populations will show oscillations in this scenario while the absolute squared of the summed coherences oscillates with the difference of both frequencies which explains the bending of the diagonals in Fig. 6.5 (d) towards zero coupling. For intermediate generalized couplings Δ_R between the large and no coupling regime, we expect a frequency behaviour that interpolates between the two regimes. A detailed analytical description of this regime, however, is beyond the scope of this thesis.

We note, that the oscillations with the coupling strength $\pm\Delta_R$ and with it the diagonal structures are most prominent in the single populations. They completely disappear if no coupling is present as can be seen from Eqs. (6.35) and Eq. (6.37), which provides us with a criterion for distinguishing the presence of an excited-state coupling from its absence. One possibility to access these oscillations in the single populations in experiments on thin-film x-ray cavities, where the two effective excited states correspond to nuclear ensembles placed at different depths in the cavity, can be offered by methods that allow for depth-selectivity of the incoherently detected intensity. One such method used in Mössbauer science is conversion electron Mössbauer spectroscopy (CEMS) [Röh04; Fro+85; Fry+08] which captures conversion electrons and secondary radiation emitted after the process of internal conversion. These electrons experience absorption by the surrounding material whilst travelling through the cavity to the surface where they can be detected. Electrons or secondary radiation emitted from a nuclear ensemble deeper in the cavity thus feature more absorption which leads to a different electron yield from the two ensembles associated with the two effective excited states in the cavity (cf. Fig. 6.1). In this way, the relative weight between the incoherently scattered ratiation from each nuclear ensemble, associated with the excited state population of each collective state, becomes different and oscillations like those shown in Fig. 6.4 (a) and (b) could be detected.

6.4.2 Non-impulsive excitations

The results of the simulations for the impulsive case Sec. 6.4.1 with varying coupling strength Δ_{21} suggest that a frequency-resolved detection scheme may be of advantage in analyzing the coupling dynamics of effective three-level schemes. To this end, we continue our evaluation by employing non-impulsive excitation pulses of the form

$$\Omega(t) = \Gamma_a \, \mathcal{A} \, e^{-i(\omega_0 + \Delta)t} \, e^{-\Gamma_a t} \, , \tag{6.38}$$

which can be realized in experiment using synchrotron Mössbauer sources or single-line nuclear reference absorbers (cf. Sec. 5.5). Recall, that $\mathcal{A}$ denotes the total pulse area of the temporally-extended driving pulse as defined in Eq. (A.126), Γ_a the decay rate of the exponentially-decaying pulse, ω_0 the center frequency of the resonant reference absorber and Δ the detuning imposed by, e.g., a Doppler shift.

Fig. 6.6 shows the time-resolved populations (panel (a) and (b)), the sum of the populations (panel (c)) and the absolute squared of the summed coherences (panel (d)) upon the excitation by a exponentially decaying pulse of the form Eq. (6.38) with a decay rate $\Gamma_a = 2.5\gamma$ and a pulse frequency of $\omega_0 + \Delta = \frac{\delta_2 + \delta_1}{2} + 10\gamma$. The decay rates of the two transitions are chosen identically $\Gamma_2 = \Gamma_1 = 0.5\gamma$. The remaining parameters are identical to those of Fig. 6.4. Apart from weak hyperbolic oscillations

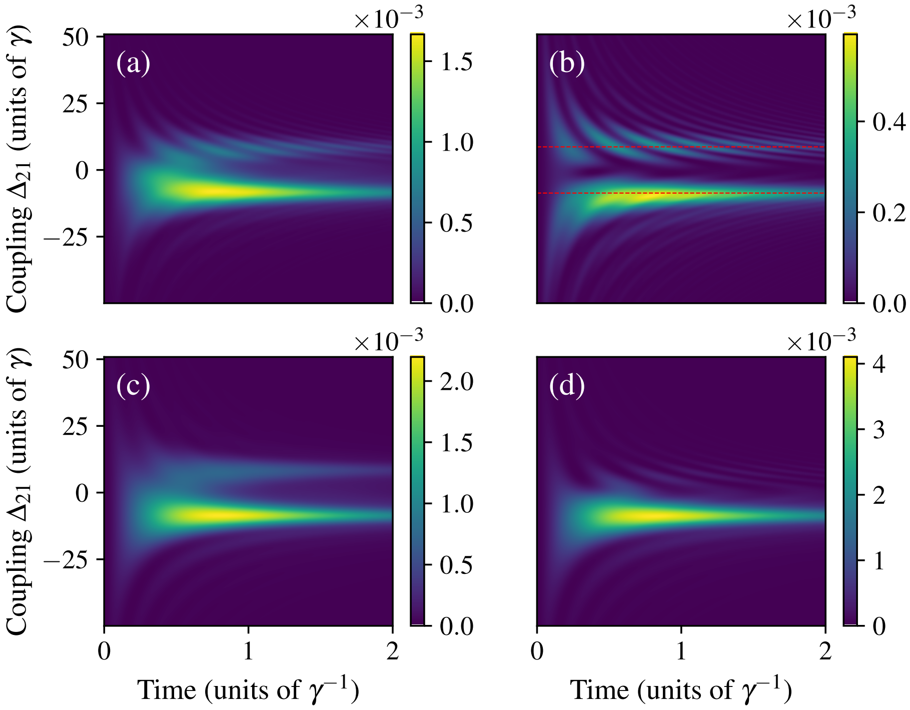

Figure 6.6: Coupling dynamics of the three-level system as a function of time and coupling strength between the two excited states upon an exponentially-decaying excitation pulse. Panel (a) shows the population ρ_{22}, panel (b) the population ρ_{11}, panel (c) the sum of both populations and panel (d) the absolute squared of the sum of both coherences. The total pulse areas of the driving Rabi frequencies are related by $\mathcal{A}_2 = 2\mathcal{A}_1 = 0.02\pi$. Condition Eq. (6.39) is indicated as a red dashed line in panel (b).

reminiscent of those appearing in nuclear time-frequency-spectra (cf. ch. 3), most prominent are peak structures appearing very pronounced in all plotted quantities. They occur at couplings that satisfy the condition

$$\Delta_{21} = \frac{1}{2}\sqrt{|(\omega_0 + \Delta)^2 - (\delta_2 - \delta_1)^2|} \tag{6.39}$$

which are indicated in panel (b) as dashed red lines. This condition corresponds to the driving field being resonant with the generalized coupling Δ_R which suggests to study the coupling dynamics using time-frequency spectra like Sec. 5.5. Note that these resonant features also appear in the incoherently and coherently scattered light off of both transitions as shown in panel (c) and (d), in contrast to the impulsive case where strong oscillations were mainly restricted to the single populations and coherences squared.

Fig. 6.7 compares the sum of the populations $\rho_{11} + \rho_{22}$ (upper panels) and the absolute squared of the summed coherences $|\rho_{01} + \rho_{02}|^2$ (lower panels) in the case without excited state coupling $\Delta_{21} = 0$ (left panels) and with a coupling of $\Delta_{21} = 10\gamma$ (right panels). As a reference frequency for the pulse's center frequency a value between the two transition frequencies is chosen, i.e. $\omega_0 = \frac{\delta_1+\delta_2}{2}$. The remaining parameters are the same as in Fig. 6.6. As in that Figure, pronounced peak structures appear in all plotted quantities that peak at detunings

$$\Delta = \pm\frac{\Delta_R}{2} \tag{6.40}$$

which are indicated as dashed red lines in panel (c) and (d). Note, that there is an asymmetry in the intensity of the two peaks at positive and negative generalized couplings: Without coupling (left panels) the peak at positive detuning $\Delta = \Delta\delta$ is more pronounced, corresponding to the transition from state $|0\rangle$ to state $|2\rangle$. In contrast, in the case of finite coupling (right panels), the negative detuning peak, corresponding to $\Delta = -\frac{\Delta_R}{2}$ has a higher visibility while the positive detuning contribution is barely visible. For a qualitative understanding of this behaviour, we evaluate the first-order

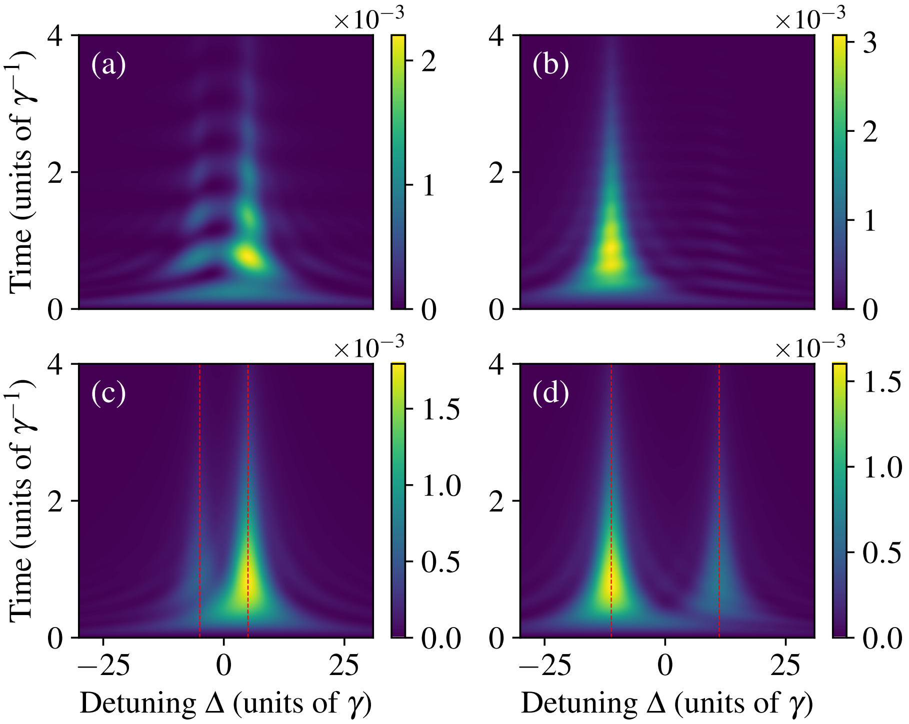

Figure 6.7: Time-frequency spectra with an excited state coupling of Δ_{21} (right panels) and without coupling (left panels) upon an exponentially decaying pulse. The upper panels shows incoherently scattered intensity in form of the summed populations while the lower panels show the coherently and resonantly scattered intensity in form of the absolute square of the superposition of both coherences. The red dashed lines in (c) and (d) indicate the condition Eq. (6.40).

coherence $\rho^{(1)}_{02}(t)$, given in Eq. (6.21), in the limit of large coupling (cf. Sec. 6.3.3) and no coupling (cf. Sec. 6.3.4).
The result for the large coupling case, again assuming the coupling constant Δ_{21} to be real, reads:

$$\begin{aligned}\rho^{(1)}_{02}(t) =& \frac{i}{4}e^{-\Gamma t}\int_0^t d\tau e^{-\Delta\Gamma\tau}\left[\Omega_2\left(e^{i(\bar{\delta}+\Delta_{21})t}e^{i\Delta_-\tau}+e^{i(\bar{\delta}-\Delta_{21})t}e^{i\Delta_+\tau}\right)\right.\\ &\left.+\Omega_1\left(e^{i(\bar{\delta}-\Delta_{21})t}e^{i\Delta_+\tau}-e^{i(\bar{\delta}+\Delta_{21})t}e^{i\Delta_-\tau}\right)\right]\\ =& -\frac{i}{4}\left[(\Omega_2-\Omega_1)\frac{e^{-\Gamma t}e^{i(\bar{\delta}+\Delta_{21})t}-e^{-\Gamma_a t}e^{i(\omega_0+\Delta)t}}{\Delta\Gamma-i\Delta_-}\right.\\ &\left.+(\Omega_2+\Omega_1)\frac{e^{-\Gamma t}e^{i(\bar{\delta}-\Delta_{21})t}-e^{-\Gamma_a t}e^{i(\omega_0+\Delta)t}}{\Delta\Gamma-i\Delta_+}\right]\end{aligned} \tag{6.41}$$

where we introduced the quantities

$$\Delta_\pm = \omega_0+\Delta-\bar{\delta}\pm|\Delta_{21}|\,, \tag{6.42}$$

$$\Omega_l = \Gamma_a\mathcal{A}_l\,. \tag{6.43}$$

This result shows that the first-order coherence, and with it the second order population of state $|2\rangle$ peaks at $\Delta = \pm\Delta_{21}$ in the large coupling limit if $\omega_0 = \bar{\delta}$ is chosen. This becomes evident from the time-independent prefactors $(\Delta\Gamma - i\Delta_-)^{-1}$ and $(\Delta\Gamma - i\Delta_+)^{-1}$. Further, it can be seen that the contribution that reaches its maximum at Δ_- is suppressed by the difference of the two pulse amplitudes $\Omega_2 - \Omega_1$ while the contribution at Δ_+ is enhanced by the sum $\Omega_2 + \Omega_1$. We conclude, that the Δ_- component is suppressed compared to the Δ_+ component, which explains the asymmetry in the peak intensity in the right panels of Fig. 6.7. Recall, that in the large coupling limit, the time-evolution of the two coherences becomes analogous such that $\rho_{01}^{(1)}(t)$ can be obtained from Eq. (6.41) by interchanging Ω_1 and Ω_2. Consequently, the Δ_- component is suppressed for this coherence as well and thus the mentioned asymmetry of the two peak intensities in the right panels of Fig. 6.7 is preserved if we sum over both coherences. Since this asymmetry is a feature of both coherences separately, it can also be found in the two populations (lower panels of Fig. 6.7), which can be calculated as the absolute square of each coherence separately in the LER according to the population-coherence correspondence Eq. (6.27). Further note, that the numerical results further suggest that this asymmetry is still present at intermediate couplings since the right panels of Fig. 6.7 correspond to that intermediate regime. As a final remark, we note that Eq. (6.41) suggests that the Δ_- peak will completely disappear in the limit $\Omega_2 \to \Omega_1$, i.e. if the effective x-ray nucleus couplings at the psitions of the two layers become identical.

In the opposite case without coupling, the dynamics of both transitions becomes independent, such that the first order coherences read

$$\rho_{0l}^{(1)}(t) = -\frac{i}{2}\frac{\Omega_l}{\Delta\Gamma - i\Delta_l}\left[e^{-\Gamma_l t}e^{i\delta_2 t} - e^{-\Gamma_a t}e^{i(\omega_0+\Delta)t}\right] \tag{6.44}$$

where we defined the relative pulse-resonance detuning

$$\Delta_l = \omega_0 + \Delta - \delta_l \tag{6.45}$$

Thus, if $\omega_0 = \bar{\delta}$, the peak intensities of well-separated resonances at δ_l change with the respective excitation strengths Ω_l squared and are found at the positions $\Delta = \pm\Delta\delta$, consistent with the left panels of Fig. 6.7 which featured relative excitation strengths of $\Omega_2 = 2\Omega_1$. Thus, for the same nucleus-field interaction $\Omega_1 = \Omega_2$ of both transitions, the two peaks are of equal intensity. Remarkably, these results suggest that the relative peak strength in presence of an excited state coupling behaves quite differently as a function of the relative nucleus-field interaction compared to the case without coupling: While the asymmetry grows as the excitation interactions differ from each other in the latter case, in the former case the second peak only appears if the two excitation strengths are different which can be used to distinguish the two cases.

For later comparison with the result using pulse sequences as produced by single-line reference absorbers Sec. 7.3.2, Fig. 6.8 shows the corresponding frequency-frequency correlation (FFC) spectra, i.e. the Fourier transform along the time axis of the coherently and incoherently scattered time-frequency-spectra for the same parameters as shown in Fig. 6.7. Building on the previous discussions, the complex structures appearing in these spectra can be interpreted one by one: First, the asymmetric non-oscillating peak structures discussed before that dominated the time-frequency-spectra Fig. 6.7 translate into intense peaks at $\nu = 0$. These peaks are located at detunings satisfying Eq. (6.40), like in the time domain as indicated by vertical red dashed lines in the lower panels of Fig. 6.8. Second, diagonal structures extending from these peaks with slope one are related to weak hyperbolic oscillation patterns barely visible in Fig. 6.7 and reminiscent of similar structures in Sec. 5.5.2 and Ch. 3. Finally, additional horizontal detuning-independent lines appear in the coherently scattered intensities which relate to weak oscillations in the time-domain (cf. Fig. 6.7 panel (b)). These horizontal lines are the frequency-analogue of the oscillations discussed extensively in Sec. 6.4.1, related to the generalized couupling between the excited states. As a validation of this interpretation, red dotted horizontal lines corresponding to the condition

$$\nu = -\Delta_R \tag{6.46}$$

were drawn in panel (a) and (b) of Fig. 6.8 as a guide to the eye which is consistent with the discussion of the oscillatory behaviour of the nuclear dynamics in Sec. 6.4.1. Recall, that these (time-domain) oscillations disappear in the sum of the populations such that the lower panels of Fig. 6.8 do not contain such horizontal structures.

In summary, we first studied the dynamics of collective nuclear three-level systems in the time domain upon impulsive x-ray excitations. Oscillations depending on the strength of the coupling between the excited states were observed that could be measured by accessing the incoherent emission from one of the nuclear layers in an thin-film cavity alone. This could be achieved by employing depth-sensitive

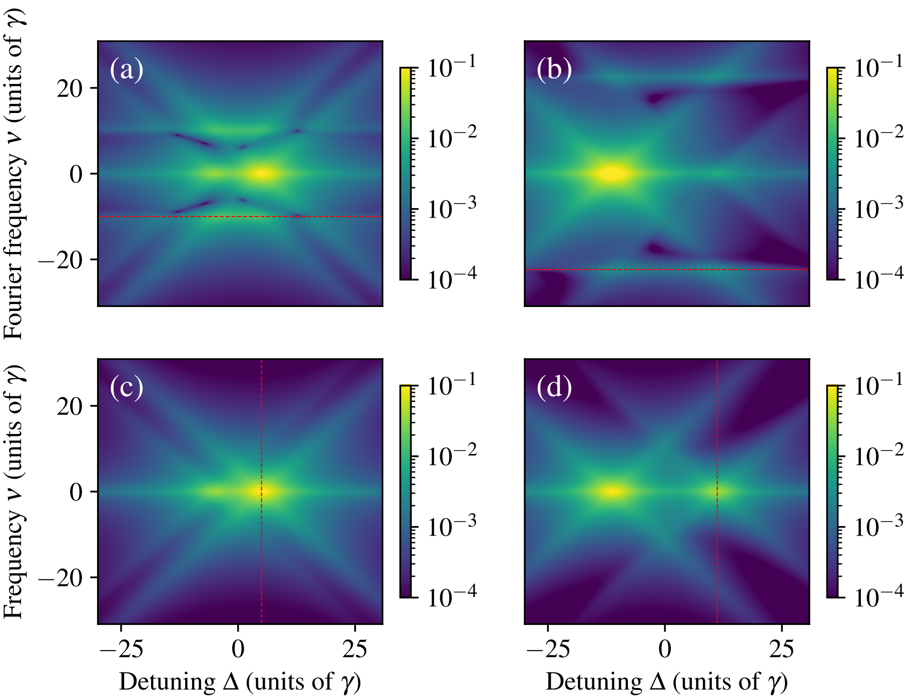

Figure 6.8: FFC spectra of coherently (upper panels) and incoherently (lower panels) scattered intensity upon a non-impulsive excitation without coupling (left panels) and with a coupling of $\Delta_{21} = 10\gamma$. The horizontal dashed lines in panel (a) and (b) correspond to the condition Eq. (6.46) while the vertical dashed lines in panel (c) and (d) are drawn at detunings Eq. (6.40).

detection methods such as CEMS. Next, we studied time- and frequency-resolved spectra measured using narrowband impulsive excitations as provided by SMS or single-line reference nuclear reference absorbers. We discovered intense peak structures in the scattered intensity as a function of the carrier frequency of the narrowband excitation pulse, the position of which depend on the coupling between the excited states.

The main results of this Section are summarized in Table 6.1. It compares the most important signatures of coupling dynamics in effective three-level systems upon impulsive and non-impulsive nuclear excitations. The observables compared are the single populations that can be accessed via depth-sensitive techniques like CEMS, the sum of the populations $\rho_{11} + \rho_{22}$ of both nuclear ensembles that can measured by capturing incoherently emitted radiative contributions and the absolute square of the coherent sum $|\rho_{01} + \rho_{02}|^2$ that is accessed by monitoring the cavity reflection spectrum in propagation direction of the incident radiation (cf. left panel of Fig. 6.1). As the results found in this Chapter are unpublished and preliminary, we comment on the validity of the assertions made in Table 6.1: Upon impulsive excitations, we found strong numerical evidence that the single populations oscillate with the generalized coupling Δ_R in the time domain. Analytical calculations confirmed this in the limit of large and no coupling. Corresponding analytical evaluations for intermediate couplings have not been carried out so far. The analytical results in these regimes suggest that the incoherently and coherently scattered intensities associated with the sum of the populations and the coherent sum of the coherences, respectively, do not show such oscillations. However, the numerical results still show such oscillations in the intermediate coupling regime that are, however, much weaker than in the single populations ρ_{ll}.

In the non-impulsive case we found that, next to the time-domain oscillations also present upon impulsive excitation, peak structures centered around the half the generalized coupling Δ_R appeared as a function of Doppler-shifted frequency Δ of the narrow-band reference pulse if the center frequency of the driving x-ray pulse is placed at the mean transition frequency $\bar{\delta} = \frac{\delta_1+\delta_2}{2}$ of the two nuclear transitions. These peak structures showed a particular asymmetry characteristic for the strength of the coupling Δ_{21} and the form of the x-ray-nucleus coupling of the two-transitions. We saw that these peaks do also convert into diagonal lines in frequency-frequency correlation (FFC) spectra, similar to renormalized nuclear transition frequencies in single-layer cavities discussed in Sec. 3.3.3.

Table 6.1: Signatures of coupling dynamics of three-level systems in the low-excitation regime in relevant observables upon impulsive and non-impulsive excitations.

pulse excitation	ρ_{ll}	$\rho_{11} + \rho_{22}$	$\lvert\rho_{01} + \rho_{02}\rvert^2$
impulsive	$\nu = \pm\Delta_R$	weak oscillations	weak oscillations
non-impulsive	$\Delta = \pm\frac{\Delta_R}{2}$	$\Delta = \pm\frac{\Delta_R}{2}$	$\Delta = \pm\frac{\Delta_R}{2}$

Again, analytical evaluations in the large and no coupling regimes based on Eqs. (6.21) supported our findings.

6.5 Conclusion

In this Chapter, we studied the coupling dynamics of collective nuclear three-level systems as realized in thin-film x-ray cavities with two separate layers of resonant nuclei embedded in its center as shown in Fig. 6.1 to retrieve the coupling between the excited states. To this end, we derived the up-to-second order contributions to the time-resolved coherences and populations associated with this effective few-level system. This allowed us to study and interpret the coupling dynamics of these systems as reflected in time- and frequency-resolved nuclear resonant scattering spectra upon the excitation with different experimentally-relevant x-ray pulse shapes. To compare calculations of the nuclear dynamics based on the numerical integration of the optical Bloch equations with explicit analytical results, we established the correspondence of coherence squared and population in the low-excitation regime for each transition separately. A combined numerical and analytical evaluation of the nuclear dynamics revealed that, in the impulsive case, time-domain oscillations related to the coupling strength between the effective states appear that are strongest in the incoherent emission of the effective nuclear populations of the single nuclear ensembles. We suggested that these can be accessed, e.g., by measuring the electron yield in a cavity setting via depth-selective methods such as conversion electron Mössbauer spectroscopy. In addition to these time-domain oscillations, we found that peak structures related to the coupling strength dominate time- and frequency-resolved spectra measured upon non-impulsive excitation. Both features could also be identified in frequency-frequency correlation spectra of such non-impulsive excitations again demonstrating the potential of this evaluation method of time- and frequency-resolved NRS spectra.

In essence, we could define several experimental signatures for excited-state couplings in nuclear systems that can be accessed using advanced measurement methods such as time- and frequency-resolved detection and by taking into account incoherent emission from thin film cavities in addition to the coherent emission channel. We envision the methods presented here to be of great advantage for the unambiguous interpretation of NRS data to characterize engineered quantum optical level schemes in x-ray cavities and thus advance nuclear quantum optics, a goal that is of great importance given that one-dimensional spectra, at least in certain cases can not provide unambiguous interpretations of such schemes.

Interesting open questions regarding the systems studied in this Chapter regard the generalization to multi-level schemes and to higher excitations beyond the LER as discussed for effective two-level systems in Chapter 5.

Chapter 7

Probing nuclear dynamics using phase-coherent double pulses

List of abbreviations used in this Chapter:

- LER: low-excitation regime
- SCU: split-and-control unit
- NRS: nuclear resonant scattering
- XFEL : x-ray free electron laser
- XFELO : x-ray free electron laser oscillator
- FFC spectrum : frequency-frequency correlation spectrum

7.1 Introduction

7.1.1 Phase-coherent pulse sequences in nuclear resonant scattering

As discussed in Sec. 2.3, the long coherence times of Mössbauer transitions in combination with the strong enhancement of coherently scattered radiation allow for the time-domain control of nuclear resonances using various techniques to shape the temporal and spectral response of the nuclei and to tune the properties of the resonantly scattered light off of the nuclei [Hee+17]. Among these techniques, we highlight the control of the nuclear hyperfine fields via external static [Shv+96; LPK12] and transient [Boc+21] magnetic fields and mechanical control of the nuclear transition frequencies via time-dependent Doppler shifts [KK12; Vag+14; Hee+17; Hee+21]. Recently, x-ray light suitably shaped using fast piezo motion of nuclear absorbers has been used to also control the dynamics of nuclear excitonic states with x-ray light alone [Hee+21] via the precise control of the relative phase between nonresonantly and resonantly scattered light. Moreover, several techniques have been proposed that allow for a controlled suppression or enhancement of the resonantly scattered radiation of Mössbauer-active targets during selected time-intervals [Ger21; Lee23; Shv+96; LPK12] such that the production of phase-coherent double-pulses including time delays at hard x-ray energies for NRS experiments comes into reach. Further, direct implementations of split-and-delay-lines for pump-probe experiments at XFELs are developed [Lu+18]. This raises the question whether suitably shaped x-ray pulses can be used to devise advanced detection schemes and spectroscopy methods built upon coherent control of nuclear resonances and time-gating of the resonantly scattered radiation.

In this context, established methods requiring phase-coherent control fields are Ramsey interferometry [Ram90], pump-probe spectroscopy [Cho19; HZ11] and photon echo experiments [Tan08; Cho19]. Advanced techniques potentially requiring multiple coherent pulses are multidimensional spectroscopy [Ern92; ABE76; Muk95; HZ11; Cho19] which have recently been established up to the XUV regime [Wit+20]. Recently, optical-pump x-ray-probe experiments were performed involving nuclear scattering [Sak+17]. These developments raise the question whether the gating and phase control techniques above, applicable in NRS experiments, can be used to establish similar techniques in the hard x-ray regime. Potential applications involve processes that require time- and frequency-resolution such as studies of couplings between excited nuclear states or the dynamics of nuclear ensembles under x-ray, other electromagnetic or thermal perturbations, e.g. to investigate the dynamics of the nuclear environment by probing nuclear degrees of freedom. Further, such techniques as Ramsey interferometry and photon echo experiments can enhance precision of frequency-resolved measurements due to a reduction field-inhomogeneities and dephasing [Ram50; HZ11]. Many of the mentioned spectroscopic techniques are typically performed under nonlinear excitation conditions which can conveniently be achieved with state-of-the-art laser sources driving atomic or molecular transitions. The ultranarrow linewidth of nuclear transitions, while ideal for coherent scattering, makes strong driving at present-day accelerator-based light sources challenging. Thus, it is of immediate interest for the implementation of advanced spectroscopic techniques based on phase-coherent pulse sequences to understand whether nonlinear excitation conditions are essential for the success of such studies.

7.1.2 Outline of this Chapter

This Chapter is concerned with the question how suitably shaped double pulse sequences and phase control can be exploited to study nuclear few-level dynamics with special focus on the comparison of different shapes of the double-pulse sequence. One of the conceptually simplest cases of the interaction between quantum matter and a pulse sequence with fixed phase-relation is the excitation and de-excitation of a two-level system by a double-pulse sequence consisting of two short pulses with variable time delay. Such a setup forms the basis for the technique known as separated oscillatory field method or Ramsey interferometry [Ram50] that was instrumental in establishing atomic clocks as time-keeping standards [Ram90] and is the starting point for more advanced spectroscopic techniques such as photon echo experiments [HZ11; Cho19; Tan08]. While computationally and conceptionally simple from a theoretical perspective, separated oscillatory x-ray fields with variable time-delay on nuclear dynamics time scales are experimentally challenging due to the lack of coherence-preserving x-ray optics and the high stability requirement of these optics down to fractions of the optical cycle of hard x-rays. Nevertheless, methods for coherent time-gating of coherent radiation emitted by nuclear scatterers have been investigated theoretically [Lee23; LPK12] and even demonstrated experimentally [Ger21; Shv+96]. However, the pulses created with these methods are expected to yield pulses on the nanosecond scale such that their temporal duration and frequency structure may not be completely negligible on the nuclear time and frequency scale. For this reason, here we discuss the influence of pulse shape on the outcome of a Ramsey experiment, specifically comparing the ideal case of a sequence of two short pulses, in following denoted as *standard Ramsey* with a sequence of a short followed by a temporally-extended narrow-band pulse as is typical for the radiation response of single-line nuclear reference absorber (cf. 2.3). This second case is therefore called *nuclear Ramsey* in the following.

A second interesting question is whether the evaluation of double pulse experiments in terms of time- and frequency-resolved spectra offers advantages in the interpretation of the underlying nuclear dynamics. In Chapters 3, 5 and 6 the potential of time- and frequency-resolved spectra their analysis in frequency space has been shown in various contexts. Therefore, the same methods will be employed here to get additional insight into time-dependent perturbations of nuclear systems and couplings between excited states.

A third very important question regarding the realization of advanced multi-pulse schemes in NRS is whether such techniques, usually associated with nonlinear driving of the transitions of interest can also be realized in the LER typical for NRS experiments at synchrotron sources.

A schematic illustrating the pulse creation and measurement approach discussed in this Chapter to adress these three aspects is shown in Fig. 7.1: First, a short pulse delivered by a coherent x-ray source like as synchrotron or XFEL is split into a double pulse sequence using a split-and-control unit (SCU)[1], that splits the initial x-ray pulse and controls the time delay and relative phase of the two pulses. This can be any device like a split-and-delay line [Lu+18] or a combination of nuclear reference absorbers including sample motion and magnetic field control [Hee+21; Ger21; Lee23]. This pulse sequence excites and de-excites a nuclear two-level system, here depicted in the Bloch sphere representation, to probe its dynamics during the experiment. The emitted incoherent or coherent radiation is subsequently detected in a time- and frequency-resolved measurement.

This Chapter is structured as follows: Section 7.1.3 demonstrates the feasibility of Ramsey experiments in the LER by studying the simple example of an two-level system without decay. Building up on this, Section 7.2 employs a more rigorous model including decay of the nuclear two-level system and the relative phase between the two pulses to calculate the low-excitation intensity measured in a nuclear double-pulse experiment. The cases of two short excitation pulses and a pulse sequence of an impulsive excitation followed by a temporally-extended narrow-band excitation are compared. Finally, Section 7.3 investigates two cases of nuclear dynamics using double-pulse sequences: First, time-dependent perturbations of the nuclear resonance frequency are studied with different pulse pat-

---

[1] The name split-and-control unit was taken from Ref. [Hee+21]

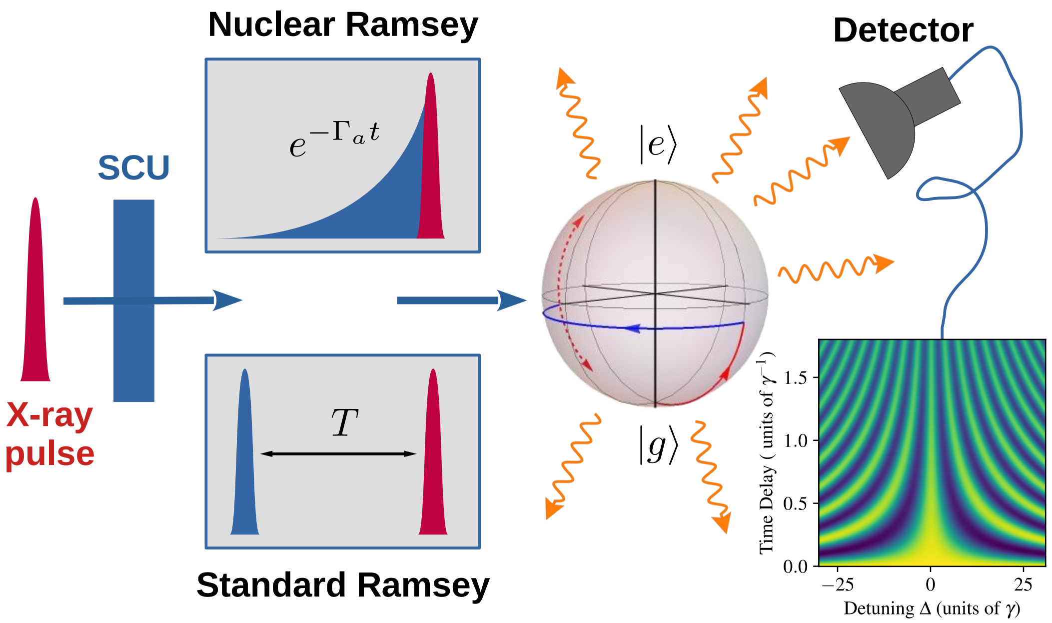

Figure 7.1: Double pulse experiment in nuclear resonant scattering: An incident short x-ray pulse delivered by a coherent x-ray source is split into a double pulse sequence by a split-and-delay unit (SCU) either consisting of two short pulses (standard Ramsey) or a short pulse followed by a temporally-extended narrowband probe pulse (nuclear Ramsey). This sequence is used to excite and deexcite a nuclear two-level system to probe its dynamics during the double pulse experiment. Finally, the radiation emitted by the nuclear two-level system is captured in a time- and frequency-resolved measurement.

terns. Second, coupling dynamics of effective three-level systems are investigated using double-pulse sequences and compared to the corresponding single-pulse results in Chapter 6.

7.1.3 Ramsey interferometry under low-excitation conditions

In this Section, we compare the ideal Ramsey case of two pulses of neglibible duration and variable time delay between the pulses under high-excitation and low-excitation conditions. This serves as a motivation for more rigorous comparisons of this ideal case with pulse sequences that can be realized conveniently in NRS experiments. To compare the results with earlier Chapters, we interpret the intensity measured in a Ramsey experiment in terms of time- and frequency-resolved spectra and motivate the use of the Ramsey method regardless of the degree of excitation of the two-level system, which is crucial for future double pulse experiments at coherent x-ray sources since the number of photons delivered on resonance with the nuclear transitions is typically very small. This is in stark contrast to the nonlinear excitation conditions usually found in Ramsey experiments in the longer wavelength regime.

To obtain the intensity measured in a Ramsey interferometer, we calculate the population of a two-level system initially excited from its ground state by a short near-instantaneous pump pulse of the form

$$\Omega_1(t) = \frac{\mathcal{A}_1}{\sqrt{2\pi}\tau_1} e^{-i\omega_{p_1} t} \exp\left(-\frac{(t - t^1_{exc})^2}{2\tau_1^2} \right), \tag{7.1}$$

followed by a non-interaction period of duration T. Finally, the system interacts with a second pulse of the same form as the first pulse but centered at time $t^2_{exc} = t^1_{exc} + T$ where t^1_{exc} refers to the time of interaction between the two-level system and the first pulse. For our simulation we assumed the ideal case that all other pulse parameters are identical, i.e. the pulse areas $\mathcal{A} \equiv \mathcal{A}_1 = \mathcal{A}_2$, $\omega_p \equiv \omega_{p_1} = \omega_{p_2}$ and $\tau_p \equiv \tau_1 = \tau_2$. The population is calculated by solving the optical Bloch equations Eq. (A.146) numerically, including nuclear decay. This was done by using the ODEINT function from the SCIPY package [Vir+20] of the PYTHON programming language [VRD09]. Recall that the incoherently scattered intensity in an NRS experiment is proportional to the nuclear excited

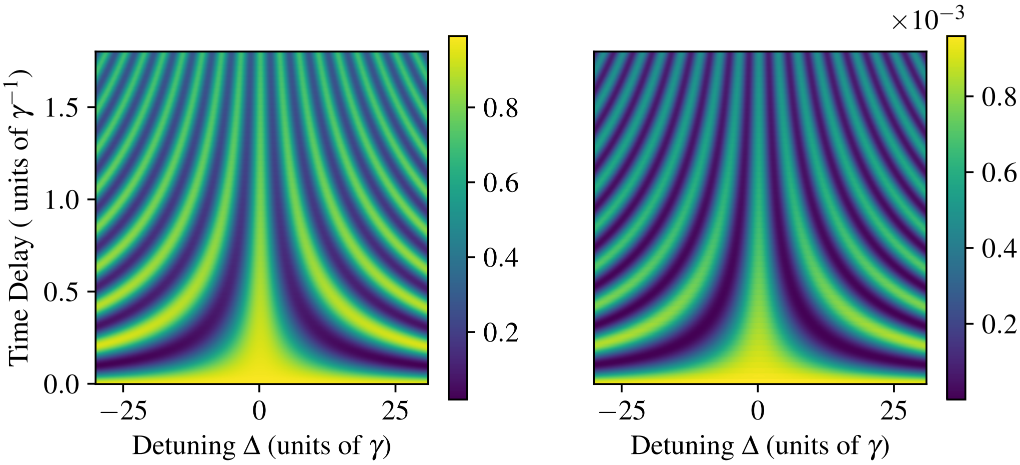

Figure 7.2: Time- and frequency-resolved incoherent intensity upon a double pulse excitation in a Ramsey experiment as a function of time delay T between the pulses and detuning Δ between the resonance frequency and the pulse carrier frequency. The left panel shows the result for a pulse area of $\mathcal{A} = \pi/2$ while the right panel shows the LER result with a pulse area of $\mathcal{A} = 0.01\pi$.

state population as argued in Sec. 5.2.2. The main reason for studying this observable instead of the coherently scattered intensity is the fact that read-out of the incoherent intensity is typically preferred in Ramsey experiments and thus, to compare our analytical results with earlier approaches, we choose the same observable here. As demonstrated in Sec. 5.3.2, however, both observables are equivalent in the LER. Note that, as discussed in more detail in Sec. 2.2.2, the interpretation of ensembles of nuclei in terms of effective few-level systems is valid in the LER such that the few-level excited-state populations and x-ray induced coherences studied here should be thought of as effective nuclear ensemble quantities.

In Fig. 7.2, the population is plotted as a function of the delay T (cf. Fig. 7.3) and the detuning $\Delta = \omega_p - \omega_0$ between the pulse carrier frequencies ω_p and the system's resonance frequency ω_0. Remarkably, the hyperbolic shape of the Ramsey fringe pattern is very similar to the patterns observed in time- and frequency-resolved nuclear resonant scattering spectra as discussed, for instance, in Ch. 3 and Sec. 5.5.2. We further note, that the LER result (right panel) looks very similar to the $\pi/2$-pulse result (left panel). This suggests that Ramsey-type experiments could be performed even in the LER, for instance in NRS with synchrotron radiation if proper coherent pulse patterns are available. To get a better insight into the origin of these hyperbolic structures in Ramsey interferometry, and for later comparison with analytical expressions from the LER, we use the analytical result for the excited state population obtained by Ramsey [Ram50], adapted to the notation of this thesis,

$$\rho_{ee}(\Delta, T) = 4\frac{\Omega_0^2}{\Omega_\delta^2}\sin^2\left(\frac{\Omega_\delta \tau_p}{2}\right)\left[\cos\left(\frac{\Delta T}{2}\right)\cos\left(\frac{\Omega_\delta \tau_p}{2}\right) - \frac{\delta}{\Omega_\delta}\sin\left(\frac{\Delta T}{2}\right)\sin\left(\frac{\Omega_\delta \tau_p}{2}\right)\right]^2 , \tag{7.2}$$

which assumes two short interaction periods of the two-level system with duration τ_p, constant Rabi frequency Ω_0 and a detuning of δ within the interaction periods. During the interaction-free period of duration T in between the two pulses, the detuning between field and nucleus is given by Δ, which includes potential fluctuations of the two-level system's transition frequency in this time interval. Finally, the generalized Rabi frequency of the driving pulse is given by

$$\Omega_\delta = \sqrt{\Omega_0^2 + \delta^2}\,. \tag{7.3}$$

Eq. (7.2) can be used to describe the right panel of Fig. 7.2 if decay processes are neglected. This comparison suggests that the hyperbolic oscillations are described by the sine and cosine terms oscillating with ΔT. To see this more clearly, we consider an impulsive excitation such that the initial detuning can be neglected ($\delta = 0$). In this case Eq. (7.2) reduces to

$$\rho_{ee}(\Delta, T) = \sin^2\left(\Omega_0 \tau_p\right) \cos^2\left(\frac{\Delta T}{2}\right) , \tag{7.4}$$

which clearly connects the hyperbolic structures to the oscillations with ΔT. For the special case of an pulse area of $\mathcal{A} = \Omega_0 \tau_p$ the prefactor is equal to one, which yields the typical cosine squared oscillation known as Ramsey fringes [Bor+84]. The narrowing of the oscillatory structures in Fig. 7.2 towards larger time delays T can then directly be related to the narrowing of the Ramsey fringe pattern and the related high precision of frequency determination in measurements using the Ramsey method.

The numerical and analytical results above suggest that Ramsey fringes are observable even under low-excitation conditions and thus Ramsey-like experiments and even more complex spectroscopy schemes like photon echo could be performed with Mössbauer nuclei at state-of-the-art accelerator-based light sources such as synchrotrons. The crucial assumption here is that pump and probe pulse both are impulsive. This, together with the apparent similarity of the Ramsey fringe pattern with time- and frequency-resolved NRS spectra, invites more rigorous comparisons of time- and frequency-resolved intensities upon different double pulse sequences in the LER.

7.2 Double pulse excitations of two-level systems in the low-excitation regime

In this Section, we provide a detailed comparison of nuclear two-level dynamics upon double-pulse excitations in the LER, including level decay, for different time-dependent pulse envelopes. This allows us to compare the case of a temporally short probe field with the one of a temporally long but narrowband probe field. Our findings are of importance for future implementations of double pulse experiments with Mössbauer nuclei as the compared pulses require different pulse-shaping techniques but on the other hand offer different experimental advantages. Further, the results allow for an interpretation of the time- and frequency-resolved spectra obtained by solving the optical Bloch equations.

Specifically, we study the two-pulse sequences depicted in Fig. 7.3, i.e. the ideal case of two short pulses separated by a variable time-delay of duration T (panel (b)) and a sequence of a short pulse excitation followed by a temporally-extended narrow-band probe pulse (panel (a)). To study the action of such double pulses on nuclear two-level systems in the LER, we employ the self-consistent equations derived in Sec. 4.1. These equations can, in principle, be used to study arbitrary pulse shapes and sequences and, therefore, are the ideal starting point for our discussion. For convenience, we restate these equations here:

$$\begin{aligned}
\rho_{ee}(t, t_0) =& e^{-\gamma t}\Big\{ e^{\gamma t_0}\rho_{ee}(t_0) + e^{\frac{\gamma}{2}t_0}\int_{t_0}^{t} dt' e^{\frac{\gamma}{2}t'} \mathrm{Re}(i e^{i\omega_0 (t'-t_0)}\Omega(t')\rho_{ge}(t_0)) \qquad \text{(7.5a)} \\
& - \mathrm{Re}\Big[\int_{t_0}^{t} dt' e^{\gamma t'}\Omega^*(t') \int_{t_0}^{t'} dt'' e^{i\omega_0 (t''-t')} e^{\frac{\gamma}{2}(t''-t')}\Omega(t'')\big(\rho_{ee}(t'', t_0) - \frac{1}{2}\big)\Big]\Big\} , \\
\rho_{ge}(t, t_0) =& e^{i\omega_0 t} e^{-\frac{\gamma}{2}t}\Big\{ e^{-i\omega_0 t_0} e^{\frac{\gamma}{2}t_0}\rho_{ge}(t_0) + i\int_{t_0}^{t} dt' e^{-i\omega t'}\Omega^*(t')\big(e^{\gamma(t_0 - \frac{t'}{2})}\rho_{ee}(t_0) - \frac{e^{\frac{\gamma}{2}t'}}{2}\big) \\
& - i\int_{t_0}^{t} dt' e^{-i\omega_0 t'} e^{-\frac{\gamma}{2}t'}\Omega^*(t') \int_{t_0}^{t'} dt'' e^{\gamma t''}\mathrm{Im}\big(\Omega(t'')\rho_{ge}(t'', t_0)\big)\Big\} . \qquad \text{(7.5b)}
\end{aligned}$$

Recall that ρ_{ee} denotes the nuclear excited state population associated with incoherent emission (cf. Sec. 5.2.2) and ρ_{ge} the x-ray induced coherence related to coherent emission. Further, γ denotes the total single-nucleus linewidth, ω_0 the transition frequency of the nuclear two-level system, t_0 the initial time and $\Omega(t)$ the time-dependent nucleus-field coupling related to the nuclear dipole moment $\mathbf{d}$ and the driving x-ray field $\mathbf{E}(t)$ by

$$\Omega(t) = \frac{\mathbf{d}\mathbf{E}(t)}{\hbar} . \tag{7.6}$$

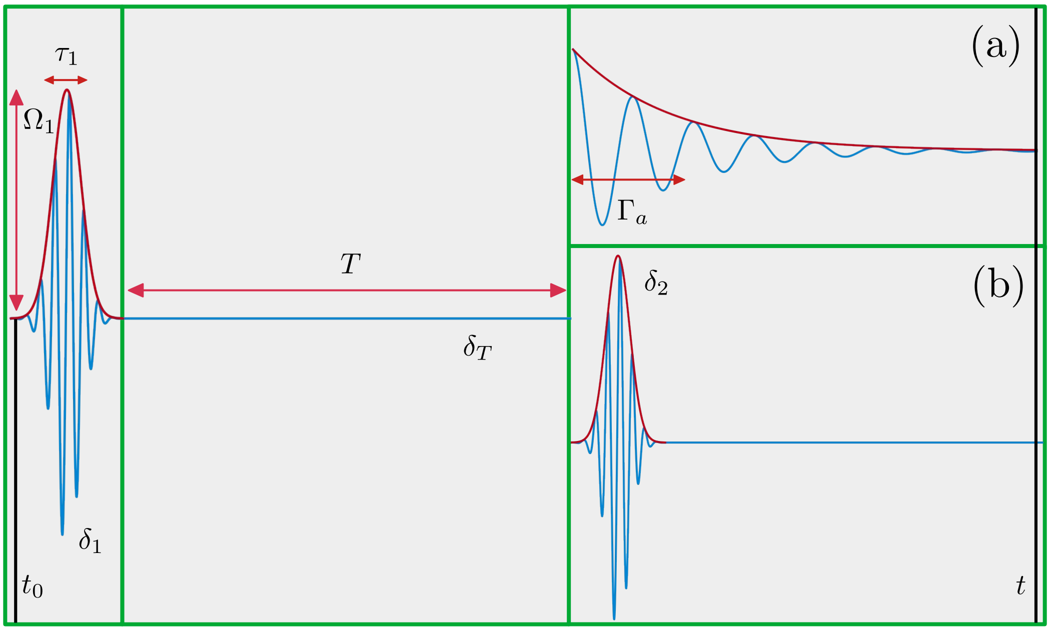

Figure 7.3: Double pulses created in nuclear resonant scattering using split-and-control units. The measurement time t proceeds from left to right: On the left the first short excitation pulse arriving at initial time t_0 with pulse-nucleus detuning δ_1 can be seen, followed by the non-interaction region of duration T with a corresponding detuning δ_T. On the right, the two cases of excitation/deexcitation are shown, both with a pulse nucleus-detuning δ_2: Panel (a) shows the nuclear Ramsey case with an exponentially-decaying probe pulse. In panel (b) the standard Ramsey case with a second short probe pulse is shown.

The time-dependent nuclear excited state population calculated with these equations allows to compare the result for different pulse shapes and sequences. Moreover, it provides a generalization of the result Eq.(7.2) in that it incorporates the nuclear decay at low excitations, where Eqs. (7.5) can be expanded up to second order in the x-ray-nucleus interaction $\Omega(t)$. In this regime, it also allows for more detailed insights into the dependence of the detuning between x-ray pulses and the nuclear resonance compared to the area theorem A.9 that has been demonstrated to provide good results upon impulsive excitations, where detunings can typically be neglected.
To calculate the time-dependent nuclear excited-state population $\rho_{ee}(t)$ we split the double pulse experiments into three parts as depicted in Fig. 7.3: First, the two-level system is excited by a short pump pulse at time t_0. Second, the system evolves freely in time for a duration of T. Finally, two cases are distiguished: Panel(b) shows the standard Ramsey case with a second short pulse probing the system dynamics followed by subsequent free-induction decay. Panel (b) depicts the case of a nuclear reference absorber with an exponentially-decaying probe pulse. Finally the measurement is performed at time t. During the different regions we allow the detuning between pulse carrier frequency ω_p and nuclear resonance frequency ω_0 to vary to account for two aspects: First, possible time-dependent variations in the nuclear environment may change the resonance frequency ω_0. Second, especially in the case of a narrow-band probe pulse (panel (a)), the pulse frequency ω_p can vary in the different regions. To simplify notation we account for these variations by assuming a different nuclear resonance frequency in the three parts since only relative detunings between pulse carrier frequency and nuclear resonance frequency are important for the final result: The initial excitation is characterized by a pulse-nucleus detuning of $\delta_1 = \omega_p \omega_1$, the non-interaction region by a detuning of $\delta_T = \omega_p - \omega_T$ and the second interaction region by a detuning $\delta_2 = \omega_p - \omega_2$. This allows us to distinguish the influence of variations during the different parts of the experiment on the final measurement outcome. In the following, we provide a detailed analysis of the three regions.

7.2.1 Initial excitation and free time evolution

To obtain the time-dependent nuclear populations $\rho_{ee}(t)$ at measurement time t after the double pulse sequence, we start by calculating the initial density matrix elements $\rho_{ee}(t_0)$ and $\rho_{ge}(t_0)$, which can be done in two ways depending on the properties of the first-pulse excitation in the double-pulse sequence:

a) In case of an impulsive initial excitation which is subsequently probed either by a second short pulse or a temporally-extended narrowband pulse, Eqs. (7.5) can be used to include an initial state of the system that can be computed using any analytical method that is suitable to the specific problem, e.g. the area theorem or the exact solution for a short constant-envelope pulse (see below), which can even provide results to all orders with the restriction if nuclear decay during the excitation period is negligible. This approach further allows for an interpretation of the double-pulse setup as a scheme for studies of non-equilibrium dynamics: The system is initially prepared in the state $\hat{\rho}(t_0)$ and the induced dynamics are probed by the second pulse.

b) Regardless of the pulse shapes of the first and second pulse, both pulses can be treated perturbatively starting from an initial ground state, i.e.

$$\rho_{ee}(t_0) = 0 = \rho_{ge}(t_0) \tag{7.7}$$

before the first pulse arrives.

The results obtained within both approaches should provide identical results in the LER. Here, we mainly pursue the first approach using the exact solution of a short constant-envelope pulse to model the initial near-instantaneous excitation as provided by synchrotron or XFEL sources. This can be done as long as the nuclear decay can be neglected during the initial excitation[2] and the spectral and temporal details of the short pump pulse are not relevant on nuclear interaction and decay time scales such that, in the analytical derivation, a short rectangular pulse as introduced below, a narrow Gaussian pulse like Eq. (7.1) or a Dirac δ description may be used equivalently depending on the specific calculation method. This, in principle, allows one to study the influence of the underlying pulse structure on the measured signal, which is of importance, for instance, if the pulses are *not* short compared to nuclear evolution time scales.
Under these assumptions, the initial density matrix after a short rectangular pulse of the form

$$\Omega_1(t) = \Omega_1 e^{-i\omega_p t}\Theta(t)\Theta(\tau_1 - t) \tag{7.8}$$

of duration τ_1, a pulse-level detuning $\delta_1 = \omega_p - \omega_1$ and pulse envelope frequency Ω_1 starting from the system's ground state at time $t_0 = 0$ can be obtained analytically (see, e.g., Ref. [SZ97]) as

$$\rho_{ge}(\tau_1) = -\, e^{i\omega_p \tau_1}\left[\frac{\Omega_1 \delta_1}{\Omega_{\delta_1}^2}\sin^2\left(\frac{\Omega_{\delta_1}\tau_1}{2}\right) + \frac{i\Omega_1}{2\Omega_{\delta_1}}\sin\left(\Omega_{\delta_1}\tau_1\right)\right] \tag{7.9a}$$

$$\rho_{ee}(\tau_1) = \frac{\Omega_1^2}{\Omega_{\delta_1}^2}\sin^2\left(\frac{\Omega_{\delta_1}\tau_1}{2}\right) \tag{7.9b}$$

with the generalized Rabi frequency given by

$$\Omega_{\delta_1} = \sqrt{\Omega_1^2 + \delta_1^2}\,. \tag{7.10}$$

Eqs. (7.9) have been derived neglecting nuclear decay, which is reasonable for accelerator-based pulse durations much shorter than the nuclear decay dynamics (cf. Sec. 5.2.3). However, this decay can not be neglected during the subsequent time evolution. Therefore, we need a refined model including the nuclear decay which is provided by the self-consistent Eqs. (7.5) with initial values $\rho_{ee}(t_0)$ and $\rho_{ge}(t_0)$ obtained from Eq. (7.9). As we mainly focus on synchrotron applications in the present discussion, which typically operate in the LER, we expand Eqs. (7.9) up to second order in the x-ray-nuclei interaction. Note that this simplification is convenient for our purposes but, in principle, a more rigorous treatment of the initial excitation including all scattering orders as given in Eqs. (7.9) is

---

[2] for a more detailed discussion of pulse durations and nuclear dynamics time scales, see also Sec. 5.2.3

possible if initial excitation conditions beyond the LER can be provided in experiment. In the limit of low excitations, the initial density matrix contributions Eqs. (7.9) reduce to

$$\rho_{ge}^{(0-2)}(\tau_1) = -\frac{i}{2} e^{i\omega_1 \tau_1} \Omega_1 \tau_1 \tag{7.11a}$$

$$\rho_{ee}^{(0-2)}(\tau_1) = \frac{1}{4} \Omega_1^2 \tau_1^2 \tag{7.11b}$$

where we used that the detuning between the excitation pulse and the nuclear resonance can be neglected during the time τ_1, i.e. $\delta_1 \tau_1 \approx 0$. Note, that Eqs. (7.11) are in agreement with the population-coherence correspondence in the LER derived in Sec. 5.3.2, Eq. (5.22), i.e. the absolute square of the x-ray-induced coherence $\rho_{ge}^{(0-2)}(\tau_1)$ is identical to the nuclear excited state population $\rho_{ee}^{(0-2)}(\tau_1)$ up to second order in the driving field Ω_1, as expected.

After the initial excitation, the system evolves in time freely, i.e. without interaction with an external driving field. The internal two-level dynamics governing the time evolution during this period is included to all orders in the self-consistent Eqs. (7.5). An evaluation of these equations for the population and coherence after time T of the initial excitation and with a potentially modified but constant transition frequency ω_T of the nuclear system in this interaction period yields:

$$\rho_{ee}^{(0-2)}(T, \tau_1) = e^{-\gamma(T-\tau_1)} \rho_{ee}^{(0-2)}(\tau_1) \approx \frac{1}{4} \Omega_1^2 \tau_1^2 e^{-\gamma T} \tag{7.12a}$$

$$\rho_{ge}^{(0-2)}(T, \tau_1) = e^{i\omega_T T} e^{-i\omega_1 \tau_1} e^{-\frac{\gamma}{2}(T-\tau_1)} \rho_{ge}^{(0-2)}(\tau_1) \approx -\frac{i}{2} \Omega_1 \tau_1 e^{i\omega_T T} e^{-\frac{\gamma}{2} T} \tag{7.12b}$$

where we neglected the exponential terms $e^{-\gamma\tau_1}$, $e^{-\frac{\gamma}{2}\tau_1}$ for consistency as nuclear decay was also neglected during the excitation period of duration τ_1. Again, the two results are consistent with the population-coherence correspondence Sec. 5.3.2.

7.2.2 Probing the system dynamics with a second pulse

After the initial excitation of the two-level system by a short pulse described by Eqs. (7.11) and a subsequent non-interaction period of variable length T leading to Eqs. (7.12), we now discuss two different cases of nuclear and pulse dynamics depicted in Fig. 7.3:

a) First, after the non-interaction period an exponentially-decaying narrow-band probe pulse

$$\Omega_2(t) = \Omega_2 e^{i\phi} e^{-i\omega_p t} e^{-\Gamma_a t} \Theta(t - T) \tag{7.13}$$

with decay rate Γ_a, amplitude Ω_2, phase ϕ and detuning δ_2 probes the nuclear two-level system until observation time t. This exponential decay is typical for the resonant response of thin single-line nuclear reference absorbers (see, e.g., Sec. 2.1.4 or Ref. [Hee+21]) and is therefore referred to as *nuclear Ramsey* in the following. In the following, we will adopt the name split-and-control unit (SCU) for these reference absorbers which was introduced in Ref. [Hee+21]. The name arises from the fact that these absorbers create double pulses from near-instantaneous impulsive single pulse excitations (split) via resonant nuclear and nonresonant electronic scattering while the frequency- and phase-structure of nuclear resonant part of the radiation can be controlled via mechanical motion or other control means (cf. Sec. 2.3). In the present discussion, however, the term SCU refers to any device or method that produced phase-coherent double pulses from a short coherent x-ray pulse.

Note, that in Eq. (7.13) we assumed a pulse with zero-amplitude until time T, i.e. an non-interaction region of duration T, that is switched on at time T. However, we assume that until that time the amplitude has already decayed and evolved in time from time zero on. This is the reason why the exponential factor $e^{-i\omega_p t} e^{-\Gamma_a t}$ instead of $e^{-i\omega_p (t-T)} e^{-\Gamma_a (t-T)}$ appears in Eq. (7.13). The reason for this is that gating schemes realized with Mössbauer nuclei prevent the secondary radiation from reaching the sample stage but the secondary radiation emitted by the reference absorber still evolves in time and decays during the gating period which leads to a loss in probe pulse amplitude over time [Shv+96; Ger21]. Note, that typical SCU responses without an additional phase ϕ are shifted in phase by π with respect to the incident radiation leading to an additional minus sign in front of the secondary pulse contribution $\Omega_2(t)$ leading to destructive interference (absorption) between the two contributions. This sign is absorbed into the amplitude Ω_2 in our analytical calculation but is crucial for the interpretation of numerical and experimental data.

b) Second, a scenario with another short pulse interaction period of duration τ_2, detuning δ_2, amplitude Ω_2 and a pulse phase of ϕ relative to the first pulse described by

$$\Omega_2(t) = \Omega_2 e^{i\phi} e^{-i\omega_p t} \Theta(t - T)\Theta(T + \tau_2 - t) \tag{7.14}$$

is considered. After the interaction of duration τ_2 the system undergoes free induction decay until measurement time t. This scenario closely resembles the assumptions of the Ramsey method in the longer wavelength regime and is therefore referred to as *Standard Ramsey.* Important differences to the calculation leading to Eq.(7.2) [Ram50] are the incorporation of resonance decay and a different pulse-nucleus detuning $\delta_2 = \omega_p - \omega_2$ and amplitude Ω_2 from that one of the first pulse. This choice is made here because current proposals of double-pulse creation in NRS experiments do rely on gating of exponentially-decaying pulses as discussed in case a) such that at time T of the second interaction period the second pulse has a modified amplitude Ω_2 that is related to the decay of the nuclear excitation in the SCU. This amplitude relative to the first pulse amplitude can in principle be modified by employing reference absorbers of different thickness (for a more detailed discussion, see Sec. 2.1.4. Finally, the detuning $\delta_2 = \omega_p - \omega_2$ of this second pulse relative to the resonance frequency ω_2 can be different from the one of the first impulsive excitation to account for frequency control of the narrow-band probe pulse, e.g., via mechanical motion of an SCU absorber (cf. Sec. 2.1.5).

In the following, the two cases are discussed separately.

Standard Ramsey case

We start by evaluating the conceptually and computationally simpler standard Ramsey case where the second pulse takes the form Eq. (7.14). The coherence at time t can be calculated using Eq. (7.5b) up to first order in the driving field $\Omega_2(t)$ using the expression Eq. (7.12b) as initial state $\rho_{ge}(t_0)$. According to the population-coherence correspondence Eq. (5.22), discussed in Sec. 5.3.2, the population up to second order is obtained as the absolute square of the coherence. Recall that the coherence only acquires contributions from the first excitation order while the population only from the second order. The results are:

$$\rho_{ge}^{(0-2)}(t, \tau_2, T, \tau_1) = -\frac{i}{2} e^{i\omega_2(t-T)} e^{-\frac{\gamma}{2}(t-T)} \left(\Omega_1 \tau_1 e^{i\omega_T T} e^{-\frac{\gamma}{2}T} + \Omega_2 \tau_2 e^{-i\phi} e^{i\omega_p T} \right) \tag{7.15}$$

$$\rho_{ee}^{(0-2)}(t, \tau_2, T, \tau_1) = \frac{1}{4} e^{-\gamma(t-T)} \left(\Omega_1^2 \tau_1^2 e^{-\gamma T} + \Omega_2^2 \tau_2^2 + 2e^{-\frac{\gamma}{2}T} \Omega_1 \Omega_2 \tau_1 \tau_2 \cos(\delta_T T - \phi) \right) \tag{7.16}$$

For simplicity, we again omitted exponential terms containing the parameter $\gamma\tau_2$ in the final expression, assuming negligible decay during the pulse duration. The results can be interpreted as follows: The coherence Eq. (7.15) is easily interpreted as a superposition of the two first-order excitation contributions from the two pulses, respectively. The population result is more interesting and consists of three terms: The first term describes excitation by the first pulse with subsequent exponential decay, the second term excitation by the second pulse followed by exponential decay. Finally, the third contribution is the interference between these two excitation contributions the amplitude of which depends, via the cosine term, on the detuning $\delta_T = \omega_p - \omega_T$ between pulse carrier frequency ω_p and nuclear resonance frequency ω_T during the non-interaction period, the time T the system spends in the non-interaction region, i.e. the time delay between the two pulses, and the second pulse's phase ϕ. This result describes the Ramsey fringe interference pattern shown in the right panel of Fig. 7.2. Note, that the result Eq. (7.16) becomes identical to Eq. (7.2), expanded in second order of the pulse area $\mathcal{A} = \Omega_0 \tau_p$, if identical pump and probe pulses are assumed, i.e. $\Omega_0 \equiv \Omega_1 = \Omega_2$, $\tau_p \equiv \tau_1 = \tau_2$ and if nuclear decay and the detuning during the interaction periods can be neglected $\delta\tau \approx 0$.
With Eq. (7.16), we obtained a more general expression for the measured signal in a Ramsey experiment in the LER compared to Eq. (7.4). This allows for the discussion of the influence of nuclear

decay γ and the probe pulse phase ϕ on the measured spectrum. In this context, we first note that the phase ϕ entering the cosine function can be used to shift the fringe pattern, for instance from a symmetric line shape at resonance to an asymmetric one, which is used in atomic clocks to lock onto the resonance [Ram90]. Further, it can be used to change the relative sign between the oscillating and the non-oscillating terms in Eq. (7.16) turning destructive interference into constructive interference and vice versa as demonstrated in Ref. [Hee+17] and further discussed in Sec. 7.3.1. In addition, by varying the time-delay T the decay dynamics described by γ can be studied in a time-resolved manner.

In summary, we conclude that Ramsey fringe patterns are observable even in the LER and if frequencies and amplitudes of the two pulses do not match. The crucial condition is the impulsive type of excitation during the two interaction periods, i.e. the detuning during the interaction periods has to be negligible, a condition which is well satisfied for nuclear resonant excitation at accelerator-based x-ray sources due to the orders-of-magnitude larger bandwidth of synchrotron and XFEL radiation compared to the nuclear resonance width. The only limiting factor is the reduced visibility due to the small pulse area during the interaction periods.

Nuclear Ramsey case

We showed that suitably-shaped x-ray double pulses can be used to measure Ramsey fringe patterns like in Fig. 7.2 even at low-excitation conditions typical for nuclear resonant scattering experiments. Since SCU double pulses produced by nuclear resonance control consist of a short excitation pulse followed by a temporally-extended narrow-band probe pulse, we also discuss such double-pulse sequences as a case of immediate experimental interest. Note, that such pulse sequences were also instrumental in creating the interference patterns in the time-frequency-spectra discussed in Ch. 3. In the latter case, however, the second narrow-band part of the SCU was only used as a reference field heterodyning the nuclear target response and not to steer the dynamics of the nuclear ensemble in the target.

Analogously to the standard Ramsey case, the up-to-second-order coherence and population can be calculated using Eq. (7.5) with initial density matrix elements given by Eqs. (7.12) upon an excitation with an exponentially-decaying pulse of shape Eq. (7.13):

$$\begin{aligned}\rho_{ge}^{(0-2)}(t,T,\tau_1) =& -\frac{i}{2}\Omega_1\tau_1 e^{i\omega_2(t-T)}e^{i\omega_T T}e^{-\frac{\gamma}{2}t} - \frac{i\Omega_2}{2(i\delta_2-\Delta\Gamma)}e^{-i\phi}e^{i\omega_p T}e^{-\Gamma_a T}\times \\ &\times\left(e^{i\omega_p(t-T)}e^{-\Gamma_a(t-T)} - e^{i\omega_2(t-T)}e^{-\frac{\gamma}{2}(t-T)}\right)\,, \end{aligned} \tag{7.17}$$

$$\begin{aligned}\rho_{ee}^{(0-2)}(t,T,\tau_1) =& \frac{1}{4}\left\{\Omega_1^2\tau_1^2 e^{-\gamma t} + \frac{1}{\delta_2^2+(\Delta\Gamma)^2}\left[\Omega_2^2 e^{-2\Gamma_a T}(e^{-2\Gamma_a(t-T)} + e^{-\gamma(t-T)})\right.\right. \\ & +2\Omega_1\tau_1\Omega_2 e^{-\Gamma_{tot}t}\left(\delta_2\sin(\delta_2(t-T)+\delta_T T-\phi)\right. \\ & \left.-\ \Delta\Gamma\cos(\delta_2(t-T)+\delta_T T-\phi)\right) \\ & -2\Omega_1\tau_1\Omega_2 e^{-\gamma t}e^{-2\Gamma_a T}\left(\delta_2\sin(\delta_T T-\phi)-\Delta\Gamma\cos(\delta_T T-\phi)\right) \\ & \left.\left.-\ 2\Omega_2^2 e^{-\Gamma_{tot}(t-T)}e^{-2\Gamma_a T}\cos(\delta_2(t-T))\right]\right\}\,. \end{aligned} \tag{7.18}$$

Here, we defined the relative decay $\Delta\Gamma = \Gamma_a - \gamma/2$ between the pulse decay Γ_a and the nuclear decay $\gamma/2$ and the total decay $\Gamma_{tot} = \Gamma_a + \gamma/2$.

The first line of Eq. (7.18) consists of the single pulse results: The term proportional to Ω_1^2 is the population initially created by the first short pulse subsequently decaying. The term proportional to Ω_2^2, in turn, is the population created by the second long pulse starting to interact at time T until measurement time t. The remaining terms are interference terms between the excitations created by the first and second pulse: The contributions proportional to $\Omega_1\Omega_2$ describes interference between the first pulse and second pulse excitation and contains the Ramsey-like oscillation contribution from the non-interaction region. Finally, the term in the last line proportional to Ω_2^2 describes interference between the two long-pulse contributions oscillating with the driving pulse frequency ω_p and the two-level resonance frequency ω_2 in the long-pulse interaction region (case a) in Fig. 7.3), respectively.

For an interpretation of the result Eq. (7.18), its comparison to the standard Ramsey case Eq. (7.16) and the interpretation of numerical time-frequency-spectra discussed in Sec. 7.3, in the following we specifically focus on three aspects: The oscillatory behaviour of the measured signal, the frequency-dependence of the amplitude of the measured signal and the influence of probe pulse phase ϕ. First, oscillations with the detuning δ_T and the time delay T in the non-interaction region appear in Eq. (7.18) like in the standard Ramsey case Eq. (7.16). However, additional oscillations that also depend on measurement time t occur in Eq. (7.18) that cannot be found in the standard Ramsey case Eq. (7.16). These account for the continuous driving and beating of the two-level response with the narrow-band probe pulse leading to oscillations with the detuning $\delta_2 = \omega_p - \omega_2$ between the nuclear resonance frequency ω_2 and the probe pulse carrier frequency ω_p in the second interaction region. In this respect the nuclear Ramsey case is different as these oscillations are not field-free which leads to an oscillation pattern that does not only depend on the underlying nuclear dynamics but also on the pulse specifics. This can be seen, e.g., by noting that the terms oscillating with δ_2 i.e. the beating terms in the second interaction region decay with the total decay constant $\Gamma_{tot} = \Gamma_a + \gamma/2$ instead of the nuclear decay $\gamma/2$ alone, which makes nuclear decay dynamics more accessible in the standard Ramsey case Eq. (7.16), since it is not perturbed by details of the probe pulse, a feature that is well-known in nonlinear spectroscopy (see, e.g., [HZ11]).

A feature of the nuclear case Eq. (7.18), that does not appear in the standard Ramsey case Eq. (7.16), is the envelope term $\frac{1}{\delta_2^2+(\Delta\Gamma)^2}$ characterizing the contributions to the population involving the second pulse. This envelope leads to a decrease of the Ramsey fringe pattern off-resonance, which is the reason that time- and frequency-resolved NRS spectra feature narrow peak structures as found, e.g., in Sec. 6.4.2, which are further discussed in Sec. 7.3. The specific Lorentzian shape of this envelope is typical for exponentially decaying pulses and leads to a centering of the scattered intensity around the nuclear resonance in the second pulse interaction region. However, such a reduction of the measured signal is typical for narrow-band probe pulses. While this narrowing causes the Ramsey fringe pattern to decrease quickly off-resonance, it provides access to the target resonance structure via the center of the hyperbolic interference pattern as will be discussed in more detail in Sec. 7.3.1.

The last aspect to be discussed is the influence of the probe pulse phase ϕ. It can be seen in Eq. (7.18) that this phase, as in the standard Ramsey case Eq. (7.16), enters the oscillatory terms such that similar applications of phase control can be thought of: The fringe pattern can be shifted to an asymmetric or symmetric line shape on resonance depending on the specific needs of the conducted experiment and the relative sign between background and oscillatory contributions can be changed thus turning destructive interference between pump and probe contributions into constructive interference, a case discussed in Sec. 7.3.1.

In this Section, two cases of double-pulse sequences were compared to study nuclear dynamics in the LER: First, the standard Ramsey case of two short-pulse excitations with an intermediate non-interaction period of variable duration T was discussed. As a main result, it was found that Ramsey-fringe patterns can be observed under low-excitation conditions typical for NRS experiments provided that the pulse excitation is impulsive, i.e. that the detuning between the pulse carrier frequency and the nuclear resonance frequency can be neglected during the interaction period. Next, the case of short-pulse excitations followed by temporally-extended narrow-band excitations was studied, which showed oscillatory structures that are typically found in time-and frequency-resolved NRS experiments, and that are similar to Ramsey fringe patterns. Compared to the case of two short pulses, two additional features were observed: First, the pulse characteristics of probe pulse influence the measured signal and can make the analysis of nuclear decay dynamics more challenging. Second, in the narrow-band probe pulse case a decrease of the visibility of the fringe pattern was found around the resonance, which can be used as an additional indicator of the underlying nuclear resonance structure. Finally, the application of phase control to optimize the measured signal were discussed.

7.3 Studying nuclear dynamics using double-pulse sequences

The previous Section provided analytical expressions for the time-dependent nuclear excited-state population for the two cases of a short-pump short-probe double pulse sequence and a short-pump long probe double pulse sequence. Here, specific dynamics of interest occuring in nuclear few-level systems using such pulse sequences are studied numerically by solving the optical Bloch equations Eqs. (A.146). In particular, two types of effects are investigated: First, in Sec. 7.3.1 time-dependent perturbations of resonance frequencies in nuclear two-level systems are studied using time-frequency-spectra. Second, in Sec. 7.3.2 the coupling dynamics of effective three-level schemes as discussed in

Ch. 6, are investigated using double pulse excitations and compared to the single-pulse results in Sec. 6.4.2. Regarding the pulse sequence of a short pump followed by a narrow-band probe pulse, we restrict ourselves to the case with vanishing time delay T, which can conveniently be provided experimentally, e.g. by mechanical motion of a nuclear reference absorber SCU [Hee+21].

The pulse sequences used in the numerical studies in this Section are described by the nucleus-field interaction

$$\Omega_l^{\mathrm{dp}}(t) = \Omega_1(t) + \Omega_2(t) \tag{7.19}$$

where the superscript 'dp' indicates a double-pulse sequence of an initial impulsive excitation $\Omega_1(t)$ given by Eq. (7.1) followed by either another short pulse of the same form to model the standard Ramsey case or a non-impulsive probe pulse $\Omega_2(t)$ described by Eq. (7.13) with delay $T = 0$. The subscript l refers to the excited state $|l\rangle$ in case a nuclear three-level system with different nucleus-field couplings Ω_l is studied as is the case in Sec. 7.3.2.

7.3.1 Time-dependent perturbations of the nuclear transition frequency in two-level systems

As a simple example of time-dependent external perturbations we study a changing resonance frequency of the nuclear two-level system. This can be caused, e.g., by transient magnetic fields [Boc+21] or by mechanical motion via the Doppler effect (cf. Sec. 2.1.5) and can be used to retrieve the actual time-dependent behaviour of these external perturbations without interfering with their dynamics. As a special and instructive case we investigate linear drifts in the resonance frequency ω_2 during the interaction with an exponentially-decaying probe pulse given by

$$\omega_2(t) = \omega_0(1 + \gamma t) \tag{7.20}$$

Fig. 7.4 shows the excited state population of a nuclear two-level system with such a linear drift in the resonance frequency excited by different pulse sequences: Panel (a) shows the standard Ramsey case of two short pulses and a non-interaction period of time delay T in between. Panel (b) shows the nuclear Ramsey case of a short-long pulse sequence without time delay in between the pulses and no additional relative phase imprinted onto the exponentially-decaying probe pulse. Panel (c) shows the same excitation but now with an additional phase of $\phi = \pi$ imprinted onto the second pulse thus turning the original destructive interference between the nonresonantly scattered short pulse response of the SCU and the resonantly-scattered exponentially-decaying response into constructive interference. The central intensity minimum in the center of the hyperbolic oscillatory structure in panel (b) is thus turned into an intensity maximum in panel (c). Finally, panel (d) shows the corresponding time- and frequency-resolved intensity upon a single-pulse narrow-band excitation like Eq. (7.13), for comparison.

Panel (a) supports the earlier finding in Sec. 7.2.2 that the center of the Ramsey fringe pattern can be used as an indicator of changes in the nuclear resonance frequency since the pattern is leaning towards larger detunings with increasing time and thus with increasing resonance frequency $\omega_2(t)$. A similar drift in the hyperbolic oscillation pattern and the central peak structure is also observed in panels (b) - (d) featuring a narrow-band probe pulse. However, the center of the fringe pattern less shifted towards larger detunings than in the standard Ramsey case panel (a). We attribute this to the fact, that in case of a temporally-extended probe pulse, the population at measurement time t is averaged over the nuclear response up to time t in contrast to the standard Ramsey case that only evaluates the shifted resonance frequency at delay time T. We conclude that effects of temporal shifts of the nuclear resonance frequency can be observed in time-frequency-spectra using both nuclear and standard Ramsey pulse configurations. The extraction of such shifts is potentially simpler in the standard Ramsey case as only the resonance frequency at time delay T contributes while a time-averaged value of the nuclear response describes the time-frequency-spectrum at measurement time t in the nuclear Ramsey case.

We conclude our discussion about studies of time-dependent perturbations of nuclear resonances via double-pulse sequences with some remarks: The comparison between panel (b) and (c) shows the potential of using phase control to specifically study certain features of time- and frequency-resolved NRS spectra, here by increasing the resonant peak structure that follows the dynamics of

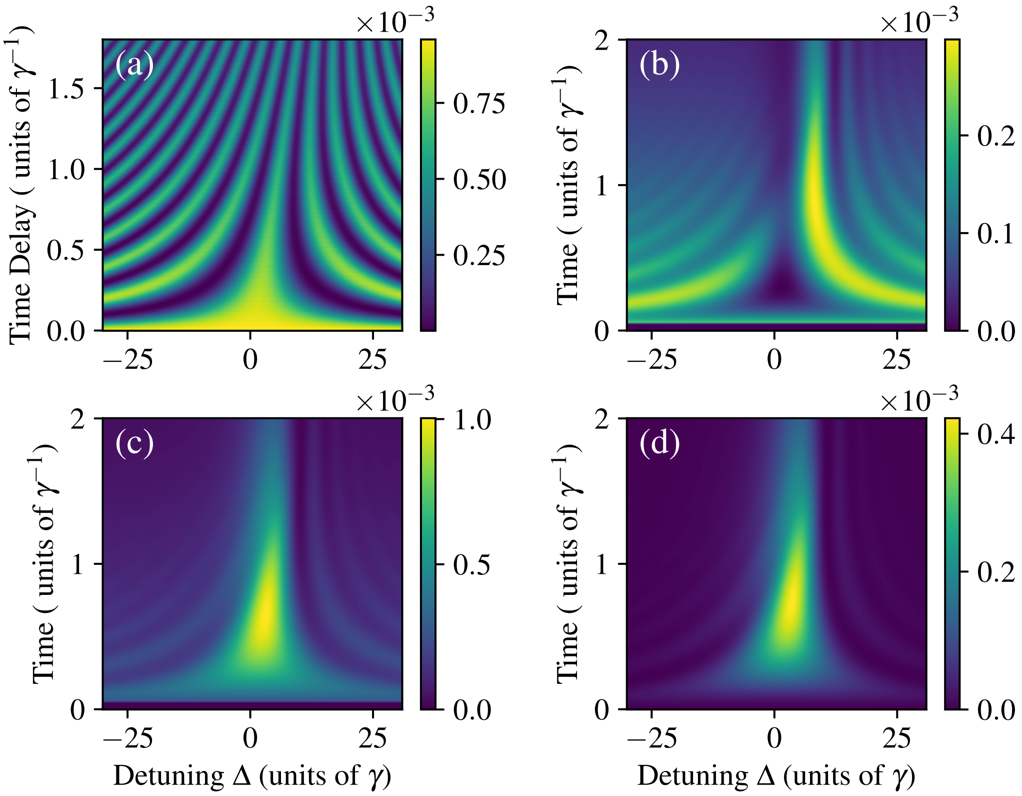

Figure 7.4: Time-frequency spectra of two-level systems with linearly increasing transition frequency: Panel a) shows the Ramsey case as a function of the detuning and the delay between the two pulses, panel (b) the SCU case with zero time delay and without additional relative phase between the pump and probe pulse and panel (c) the SCU case with an additional relative phase of $\phi = \pi$. For comparison, panel (d) shows the excited state population upon a single exponentially-decaying monochromatic pulse.

the nuclear transition in time. While the oscillatory structure is more pronounced in the destructive interference case (b), the central peak is enhanced in the $\phi = \pi$ case in panel (c). A similar feature was also studied experimentally for pure frequency-resolved spectra in Ref. [Hee+17]. Regarding time-dependent phase shifts $\phi(t)$ we also note that similar asymmetric time-frequency-spectra were already studied experimentally in the coherent channel in Ref. [Goe+19]. Finally, a comparison between the single-pulse result panel (d) and the double pulse result panel (c) demonstrates that temporal shifts of the nuclear resonance frequency can also be studied using single narrow-band excitations only, however, with reduction of both the interference pattern visibility as well as the overall visibility. Note that the advantages of phase control in shaping the measured signal as shown in panel (b) and (c) can only be harvested in the double pulse case.

7.3.2 Coupling dynamics in effective three-level systems

In Sec. 6.4.2, signatures of excited-state couplings in effective three-level systems arising in thin-film cavities with two resonant layers of nuclei upon non-impulsive single-pulse excitations were discussed to characterize the dynamics and level structure of effective collective level schemes in these systems. Here, we extend this discussion to nuclear Ramsey double-pulse excitations.

Fig. 7.5 shows time-frequency-spectra of the coherently (upper panels) and incoherently (lower panels) scattered intensity associated with the x-ray induced coherence squared $|\rho_{gl}(t)|^2$ and the nuclear excited state populations ρ_{ll}, respectively, upon an excitation like Eq. (7.19). Here, l labels the excited state associated with nuclear ensembles in a thin-film cavity as depicted in Fig. 6.1. The left panels of Fig. 7.5 show the case of no coupling and the right panels the case of a coupling $\Delta_{21} = 10\gamma$. The remaining pulse and level parameters are chosen as $\mathcal{A}_1 = 0.01\pi$ $\Gamma_a = 2.5\gamma$, $\Gamma_1 = \Gamma_2 = 0.5\gamma$, $\delta_1 = 5\gamma$, $\delta_2 = 15\gamma$, $t^1_{exc} = 10\tau_1$ and $\tau_1 = 5 \cdot 10^{-3}\gamma^{-1}$ with level parameters of the three-level system defined in Fig. 6.1 and the first and second pulse parameters in Eq.(7.1) and Eq.(7.13). In the last equation $\phi = 0$ and $\Omega_2 = \Gamma_a$ was chosen. Compared to the non-impulsive case Fig. 6.7, the peak

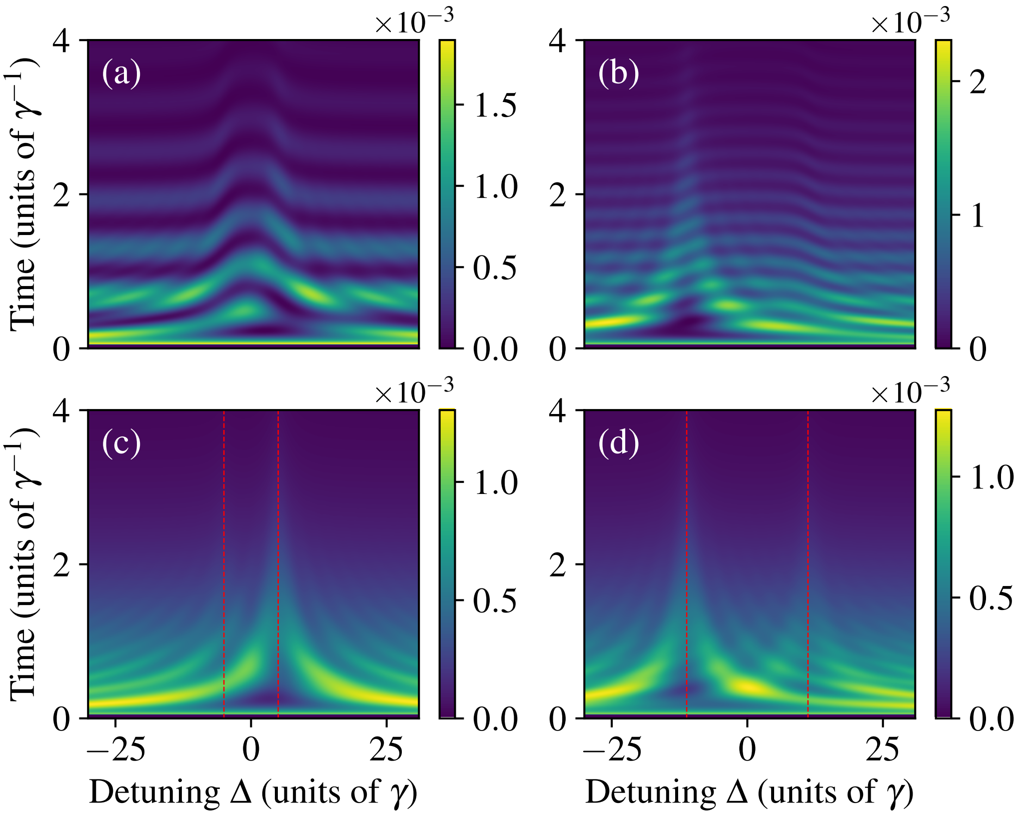

Figure 7.5: Time- and frequency-resolved coherently (upper panels) and incoherently (lower panels) scattered radiation after an initial impulsive pump pulse probed by a non-impulsive second pulse with zero time-delay. Compared are the cases without coupling (left panels) and with a coupling of $\Delta_{21} = 10\gamma$ (right panels)

structures are inverted in intensity due to the destructive interference between short pump pulse and extended probe pulse excitation. Recall that the peak structures in the left panels (no coupling) are only related to the transition frequencies of the two resonances in the three-level scheme but are modified by the coupling between the excited states in the right panels including coupling. In Sec. 6.4.2 we found that they lie at positions

$$\Delta = \pm\frac{\Delta_R}{2} \tag{7.21}$$

with the generalized coupling

$$\Delta_R = \sqrt{(\Delta\delta + i\Delta\Gamma)^2 + 4|\Delta_{21}|^2}\,, \tag{7.22}$$

which is indicated as red dashed lines in the left and right panels as guide to the eye. Further, the hyperbolic oscillations as well as the detuning-independent oscillation along the time axis are much more pronounced owing to the strong initial excitation by the pump pulse. In addition, the observation of the destructive interference in the peak structures in Fig. 7.5 compared to Fig. 6.7 in combination with the finding in the previous Subsection promises enhancements of the resonant peak structures employing phase control in the double-pulse case compared to the single pulse result. This can facilitate the fitting of these peak structures for the characterization of the excited-state couplings Δ_{21}, for instance.

As we are interested in the frequency structure of the three-level system, we also study the frequency-frequency correlation (FFC) spectrum obtained as the Fourier transform of the time-frequency-spectra shown in Fig. 7.5 along the time axis (cf. Chapter 3). Fig. 7.6 shows this FFC spectrum. Compared to the single-pulse result Fig. 6.8 the double-pulse result Fig. 7.6 features the same horizontal and diagonal lines. Again, the diagonal lines point to a crossing with the detuning

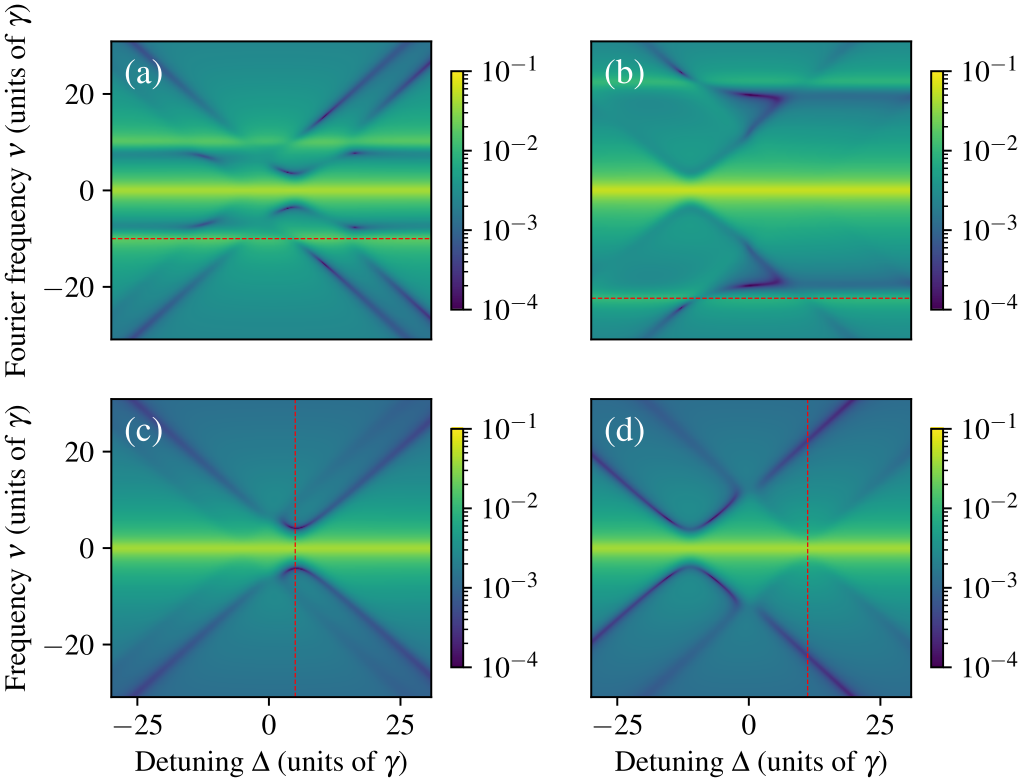

Figure 7.6: FFC spectrum of coherently (upper panels) and incoherently (lower panels) scattered intensity after an initial impulsive pump pulse probed by a non-impulsive second pulse with zero time-delay. Compared are again the cases without coupling (left panels) and with a coupling of $\Delta_{21} = 10\gamma$ (right panels)

axis at detunings satisfying Eq. (7.21) where the peak structures lied in the time-frequency-spectra Fig. 7.5. This condition is indicated via vertical dashed lines. While these crossings are less visible towards zero Fourier frequencies, the horizontal lines in the coherent channel (upper panels) are more pronounced compared to the corresponding single-pulse result Fig. 6.8. This is expected, since the horizontal lines in Fig. 7.6 are the frequency-domain analogue of the strong detuning-independent oscillations in Fig. 7.5 along the time axis, which were also more pronounced in the double pulse case compared to the single pulse result. The horizontal lines are described by the equation

$$\nu = \pm\Delta_R \,, \tag{7.23}$$

which is indicated as red dashed lines in the lower plots of Fig. 7.6. In summary, it was found that time-frequency-spectra and FFC spectra obtained after double-pulse excitation show the same features as the corresponding non-impulsive single-pulse spectra, however, with more pronounced time-domain oscillations induced by the initial short pulse and overall better visibility. One can speculate to use phase control to enhance or remove specific features, such as the horizontal lines or diagonal structures in Fig. 7.6 as was possible in Fig. 7.4 or similar to the methods presented in Sec. 3.4.

7.4 Discussion and outlook

In this Chapter, we studied the dynamics of effective nuclear two-level systems upon different double-pulse sequences in terms of time- and frequency-resolved spectra. Specifically, we discussed the observability of Ramsey-fringe patterns as a particular realization of coherent multi-pulse experiments. A perturbative analysis of the low-excitation incoherently-scattered intensity revealed that such experiments are indeed feasible if the condition of an initial impulsive excitation with negligible detuning during the initial excitation period is satisfied. This result promises the possibility to conduct advanced spectroscopy schemes using phase-coherent double pulses in nuclear resonant scattering at state-of-the-art coherent x-ray sources without further need of nonlinear excitation or even inversion of the nuclear two-level system.

In addition to this promising result two different pulse sequences were compared to study the dependence of the measured signal on the pulse specifics: First, a sequence consisting of two short pulses with variable delay T was studied and, second, a sequence of a short pump followed by a long narrow-band pulse. As a result, we found that the first case can have advantages in determining the nuclear decay dynamics due to the absence of perturbations introduced by the probe field, as expected. Further, the narrow-band probe-pulse case featured a decrease of the fringe pattern off-resonance that could be exploited to determine the nuclear resonance structure. Finally, both pulse sequences have the potential advantage of steering the relative weight of different contributions to the measured signal by controlling the phase of the probe pulse.

In the last part, two specific cases of nuclear dynamics were studied numerically: A time-dependent shift of the nuclear resonance frequency during the double pulse experiment and a coupling between nuclear excited states as can be realized, e.g., in thin-film cavities betwenn nuclear ensembles. In the first case, the shift of the resonance frequency could clearly be observed for the short-pump short-probe sequence, the short-pump narrowband-probe sequence and the single narrowband excitation. Compared to the single pulse, we highlight the higher visibility of the time-dependent peak and fringe structure in the double pulse cases and the possibility of enhancing the signal on resonance using phase control. The second study of excited-state couplings in effective three-level systems revealed the same features as the single pulse result but again with a higher visibility of the relevant features. The case of a short-pump short-probe sequence was not studied here. In this context, we note that this Chapter presents ongoing research that several questions remain open at this point. These include, for instance, the rigorous comparison of both pulse sequences in all considered cases and a comparison to the single pulse results. Further, one could study short pulses with finite pulse duration, which are likely to be created by nuclear SCUs. The full potential of phase control as studied, e.g., in Sec. 3.4 has not been exploited so far. Also, one could aim for the exctraction of decay parameters from the measured signal. These are but a few questions that could be tackled in future investigations using the methods presented here. Nevertheless, we found evidence that at least a certain class of coherent multi-pulse experiments can be performed under low-excitation conditions similarly as in the nonlinear regime, which promises new insights in nuclear many-body decay and coupling dynamics in the near future.

Chapter 8

Summary and conclusion

This thesis started with the goal of bringing together two different branches of current research with Mössbauer nuclei, namely the coherent control of nuclear resoances in the time-domain employed to shape x-ray light, on the one hand, and the design and study of collective quantum optical phenomena in thin-film x-ray cavities on the other. To this end, several advanced measurement and data evaluation techniques were discussed with the goal of retrieving collective nuclear dynamics beyond what is currently possible with widely-used one-dimensional data acquisition techniques using single observables. To interpret the data obtained from such time-, frequency- and phase-resolved measurement methods and to devise future experiments using suitably-shaped x-ray driving pulses for advanced spectroscopy schemes with Mössbauer nuclei, we developed perturbative density matrix expansions to study few-level and many-body dynamics of nuclei in the low-excitation regime (LER) for a wide range of x-ray pulse shapes and sequences. In the following, we briefly review the main methods and results of this thesis:

In Chapter 3, we discussed time- and frequency-resolved spectra measured by employing frequency-tunable single-line nuclear reference absorbers via Fourier transforms along the time axis. This resulted in frequency-frequency correlation (FFC) spectra that could be shown to provide unique access to the underlying resonance structure and the phase-resolved nuclear response of Mössbauer targets. By employing linear response theory we were able to explain the features appearing in time- and frequency-resolved nuclear resonant scattering spectra and FFC spectra one-by-one. This way we could link diagonal structures appearing in these spectra directly to the phase-resolved nuclear resonant target response, that is of immediate interest for the characterization of quantum optical phenomena in thin-film cavities. By selecting certain parts of these spectra, this contribution could be singled out with a high quality of the retrieval of nuclear parameters in this regime. In addition, we could show that the additional control of the phase of the emitted radiation of the reference absorber can be used to selectively suppress certain scattering paths and contributions to these FFC spectra and enhance others that are desirable for a specific experiment. The evaluation of time- and frequency-resolved spectra in terms of FFC spectra proved further useful in the interpretation of phenomena studied in the remaining Chapters of this thesis. Therefore, we envision this technique to be very versatile in evaluating NRS data for different experimental platforms and excitation conditions, i.e. to say for both, cavities or nuclear forward scattering, for both synchrotron and XFEL data and experiments with very different pulse structures.

Next, in Chapter 4, two types of density matrix expansions where presented that were used successfully in the following Chapters to interpret time- and frequency-behaviour of nuclear ensembles embedded in thin-film cavities upon differently-shaped x-ray light pulses. The first of these techniques provided self-consistent equations for the populations and coherences of effective nuclear two-level schemes that could be studied including decay dynamics and detunings between driving pulse and nuclear resonance. Further, with this approach, in principle arbitrary pulse shapes and sequences can be studied. This approach was subsequently be generalized to a perturbative density matrix expansion to also include multi-level and many-body systems, which is crucial for the interpretation of many intriguing phenomena in nuclear quantum optics. We are convinced that these methods can assist the interpretation and development of advanced coherent spectroscopy techniques in nuclear resonant scattering.

Both types of density matrix perturbation theory were employed in Chapter 5 to compare the coherently and incoherently scattered intensity measured in NRS experiments with nuclear two-level ensembles. Using these methods we could show that both observables are essentially equivalent largely-independent of the nuclear ensemble properties in the cavity and the time- and frequency-structure of the x-ray excitation. This lead us to establish the time-independence of the ratio of both observables as a criterion for detecting excitation beyond the LER. This helped to propose various experimental signatures for nonlinear excitation in a regime, which only slightly surpasses the LER, as is expected for near-future experiments at XFEL sources. Thus, we expect this measurement approach to be of high relevance for upcoming XFEL experiments.

In Chapter 6 the coupling dynamics of effective three-level schemes arising in thin-film cavities with two resonant layers containing Mössbauer nuclei were studied with the goal of retrieving couplings between the collective excited states. To this end, we devised various signatures of such couplings in time and time- and frequency-resolved measurements by studying numerical solutions to the equations of motion of the effective three-level system. Using the perturbative density matrix expansions developed in Chapter 4, these signatures could be related to the coupling of the excited states. This way couplings between nuclear excited states can be retrieved to characterize quantum-optical few-level schemes.

Finally, Chapter 7 discusses the feasibility and features of coherent double pulse experiments with Mössbauer nuclei. We could show that, from a theoretical point of view, Ramsey interferometry with effective two-level systems can be achieved even under low-excitation conditions such that coherent double pulse experiments with Mössbauer nuclei seem feasible using impulsive excitations. Further, could present first results comparing narrowband single pulse excitations, short-pump short-probe double pulse sequences and short-pump narrowband probe sequences, which suggested that phenomena requiring time- and frequency resolution can be studied in all three approaches but that additional degrees of freedom like phase- and time-delay control can be advantageous for the study for such phenomena.

In total, we conclude that control of time-, frequency- and phase-variables of x-ray pulses shaped using Mössbauer nuclei or by other means bears a great potential for future studies of quantum optical and dynamical phenomena at both synchrotron and XFEL facilities. Further, due to the availability of gating and pulse-shaping techniques the realization of coherent multi-pulse spectroscopy techniques is not a distant dream but is expected to be feasible in the near future, which could unlock all the methods and phenomena that are studied in the longer wavelength regime for the field of Mössbauer science as a whole. We hope that the theoretical and data evaluation methods presented in this thesis can contribute to this development.

Appendix A

A.1 Spectroscopy via late-time integration

The late-time integration spectroscopy method also employs frequency-tunable reference absorbers and has proven to be particularly successful in quantum optical studies involving thin-film cavities [Röh+10; Röh+12; Hee+13; Hee+15a; Hee+15c; Hab+16; Hab+17]. To gain insight into its main assumptions, we briefly recall the derivation of the late-time method given in Ref. [Röh+10]. The experimentally accessible time- and frequency-resolved intensity $I(t, \Delta)$ as given in Eq. (3.8) is integrated for late photon arrival times $[t_1, t_2]$ yielding the frequency-resolved observable

$$\mathcal{I}_{LTM}(\Delta) = E_0^2|\alpha_a|^2 \int_{t_1}^{t_2} dt|T_t(t) + (T_t * S_a)(t)|^2 \tag{A.1}$$

where the detuning dependence enters via the Doppler-shifted analyzer response $T_a(t) = \alpha_a \left[\delta(t) + S_a(t, \Delta)\right]$. If the nuclear resonant part of the analyzer response S_a is only nonzero in the vicinity of $\omega = \omega_a + \Delta$ and the target response varies slowly over this frequency range, their convolution can be written as

$$(T_t * S_a)(t) = \mathcal{F}^{-1}\left[\hat{T}_t(\omega)\hat{S}_a(\omega, \Delta)\right] \approx \hat{T}_t(\omega_a + \Delta)S_a(t, \Delta)\,. \tag{A.2}$$

This approximation can be extended straightforwardly to include first order derivatives of the phase of $\hat{T}_t$ (cf. [HE20; Hee14a]) but in general requires that the target response is approximately constant across the spectral range of the analyzer. Assuming further that at late times $t_1 \gg 0$ the target response $T_t(t)$ has already decayed, one can further approximate

$$\mathcal{I}_{LTM}(\Delta) \approx E_0^2|\alpha_a|^2\mathcal{C}|\hat{T}_t(\omega_a + \Delta)|^2\,, \tag{A.3}$$

where $\mathcal{C} = \int_{t_1}^{t_2} dt|S_a(t)|^2$. Thus, for sufficiently late integration times the integrated intensity $\mathcal{I}_{LTM}$ becomes proportional to the absolute squared of the frequency-domain target response $|\hat{T}_t(\omega_a + \Delta)|^2$.

The two key approximations performed above require target spectra which are spectrally broad and smooth on scales of the spectral analyzer width. Therefore, the method is particularly useful for thin-film cavities probed in reflection which feature spectrally broad resonances.

The strengths of the late-time method lies in its simple measurement and analysis approach. However, in comparison to the FFC methods discussed here, the late-time integration has several drawbacks. First, it does not allow one to retrieve the complex-valued target response. Second, it relies only on data recorded at late times, such that most of the signal photons cannot be used for the spectrum recovery. Finally, the recovery sensitively depends on the choice of t_1 and t_2, and the obtained spectra may be perturbed by time gating effects. Some of these challenges are illustrated in Fig. A.1, which shows late-time spectra of a thin-film cavity with layer structure as given in Sec. 3.3.3 for the incidence angles considered in Fig.3.6 with integration boundaries of $t_1 = 180$ns, $t_2 = 1600$ns.

At incidence angles θ_1 and θ_2, the target spectra are reproduced well. However, the neglect of the early photons causes a reduction of the usable spectral intensity by about three orders of magnitude, as can be seen in comparison to the reference spectra Fig.3.6, which are drawn using the same scale. Further, the late-time spectra for incidence angles θ_3 and θ_4 are completely distorted, even though only the incidence angle was changed. The reason for this is that at these incidence angles, the cavity resonance line-width is small (cf. Fig. 3.7(b)), such that the approximations underlying the late-time integration method break down. Note that time- and frequency-resolved data acquisition can partially compensate for this downside since it allows for *a posteriori* selection of the integration time window.

A.2 Collective parameters in cavity reflection spectra

In order to retrieve collective nuclear parameters such as the collective Lamb shift Δ_{CLS} and superradiance γ_s from the diagonal structure appearing in FFC spectra, a model function is required to fit the section along the ν-axis through the diagonals shown in Fig. 3.6.

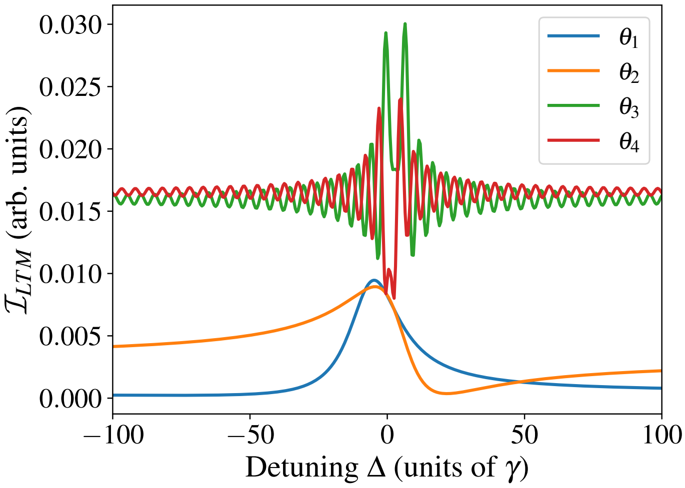

Figure A.1: Recovery of cavity-spectra using late-time integration. The Figure shows spectra obtained by integrating the time- and frequency-resolved spectra over the time interval between $t_1 = 180$ns and $t_2 = 1600$ns. The four curves correspond to incidence angles $\theta_1 = 2.75$mrad, $\theta_2 = 2.8$mrad, $\theta_3 = 3.0$mrad and $\theta_4 = 3.3$mrad. The cavity is the same as the one considered in Sec. 3.3.3, and the intensity scale is as in Fig. 3.6(a). At incidence angles θ_1 and θ_2, the nuclear resonant response is spectrally broad, and the spectra are reproduced well by the late-time integration, though with reduced visibility. In contrast, the late-time spectra at incidence angles θ_3, θ_4 suffer from artefacts of the time integration and do not represent the refrence spectra in Fig. 3.6 well.

To obtain such a fit function, we employ a quantum optical model [HE13] of Mössbauer nuclei embedded in thin-film cavities, which allows one to derive analytical expressions for these parameters. For this, we calculate the time-domain response for grazing-incidence reflection from a thin-film cavity with a single layer of Mössbauer nuclei embedded in its center (cf. Fig.3.1) by Fourier transforming the cavity's frequency-domain response [Hee14a]

$$T_t(\omega) = \alpha_t - i(\alpha_t + 1)\frac{\left(\frac{\gamma_s}{2} + i\Delta_{CLS}\right)}{\omega - (\omega_t + \Delta_{CLS}) + i\Gamma_c} \tag{A.4}$$

where the empty-cavity reflection coefficient is given by

$$\alpha_t = \frac{2\kappa_R}{\kappa + i\Delta_c} - 1\,. \tag{A.5}$$

Here, κ is the total loss rate of the cavity, Δ_c the detuning between the cavity mode and an external driving mode, and κ_R is the in- and outcoupling rate of the cavity [HE13]. $\Gamma_c = (\gamma + \gamma_s)/2$ denotes the total decay rate of the nuclei in the cavity with γ_s the superradiant line-width [Dic54; GH82; Gar11; Röh+10; Chu+18; HT99a; LHH60a; KAK79; GRK17], and Δ_{CLS} a level shift experienced by the nuclear ensemble known as collective Lamb shift [Röh+10; LKE16a; SS89a; FHM73; Scu09b; RJ16; Kea+12; Pey+18; Roo+16; Bro+16]. Though in general frequency-dependent through the cavity-detuning Δ_c, we regard Δ_{CLS}, γ_s and α_t as constants as function of frequency since the cavity resonances are typically orders of magnitude broader than nuclear resonances [Len+20] and thus the empty-cavity part becomes essentially flat in frequency-space. In this case, a Fourier transform of the frequency response yields:

$$T_t(t) = \alpha_t\delta(t) - (\alpha_t + 1)\left(\frac{\gamma_s}{2} + i\Delta_{CLS}\right)e^{-i(\omega_t + \Delta_{CLS})t}e^{-\Gamma_c t}\Theta(t)\,, \tag{A.6}$$

Employing the early-time approximation Eq. (A.12) for the analyzer response, the FFC spectrum in the large analyzer-target detuning limit Eq. (3.15) for a cavity target given by Eq. (A.6) can be calculated in the time domain as

$$\begin{aligned}\mathcal{I}(\nu,\Delta) =&E_0^2\int_0^\infty dte^{i\nu t}e^{-S_\Gamma t}\left[ce^{-ixt}+c^*e^{ixt}\right]\\ =&iE_0^2\left[\frac{c}{\nu-x+iS_\Gamma}+\frac{c^*}{\nu+x+iS_\Gamma}\right]\\ =&4E_0^2\left[\frac{\mathrm{Re}(c)(i\nu-S_\Gamma)-\mathrm{Im}(c)x}{(\nu+iS_\Gamma)^2-x^2}\right].\end{aligned}\tag{A.7}$$

Here, we have introduced the parameters

$$S_\Gamma=\Gamma_c+\frac{\gamma_a+b_a}{2}\,,\tag{A.8a}$$

$$x=\Delta-(\Delta_{CLS}+\omega_t-\omega_a)\,,\tag{A.8b}$$

$$c=\alpha_t(\alpha_t^*+1)\left(\frac{\gamma_s}{2}-i\Delta_{CLS}\right)b_a\,.\tag{A.8c}$$

Note that evaluating the absolute value squared of the complex-valued FFC spectrum Eq. (A.7) yields two Lorentzians in the limit of large detunings,

$$\begin{aligned}|\mathcal{I}(\nu,\Delta)|^2 =&16E_0^4\left(\frac{|c|^2}{(\nu-x)^2+S_\Gamma^2}+\frac{|c|^2}{(\nu+x)^2+S_\Gamma^2}+2\mathrm{Re}\left[\frac{c^2}{(\nu-x+iS_\Gamma)(\nu+x-iS_\Gamma)}\right]\right)\\ \xrightarrow[x\gg S_\Gamma]{}&16E_0^4|c|^2\left(\frac{1}{(\nu-x)^2+S_\Gamma^2}+\frac{1}{(\nu+x)^2+S_\Gamma^2}\right).\end{aligned}$$

This is consistent with our observation of a Lorentzian line shape in diagonal cavity spectra in Sec. 3.3.3, and further supports our key result that the diagonal cavity spectrum indeed yields the nuclear resonant part S_t of the spectrum only. This is most easily seen by the fact that spectra affected by the interference of the nuclear response with the electronic background response in general have Fano line shapes, see Fig.3.6. As in the case of nuclear forward scattering, the response is shifted in the FFC spectrum by the analyzer-target detuning via x, and broadened by the analyzer response width via S_Γ.

In order to retrieve collective nuclear parameters from vertical cuts through the diagonal structure, we define a more general fit function based on the absolute value of Eq. (A.7) as

$$D(\nu)=|\mathcal{I}(\nu,\Delta)|=A\sqrt{\frac{\nu^2+(px)^2}{(\nu^2-x^2+S_\Gamma^2)^2+4x^2S_\Gamma^2}}\tag{A.9}$$

where we assumed that $\frac{S_\Gamma}{x}\ll 1$, which is consistent with the off-resonant approximation used to derive $\mathcal{I}(\nu,\Delta)$. The fit parameters related to Eqs. (A.8) are $A=4E_0^2\mathrm{Re}(c)$ and $p=\mathrm{Im}(c)/\mathrm{Re}(c)$. The position of the maximum of each vertical section is given by x and the lines formed by these maxima can be fitted similarly to the procedure described in Section 3.3.2 to obtain Δ_{CLS} as crossing point with the ν-axis. The total decay rate Γ_c is determined by averaging over the S_Γ retrieved from each vertical section and subsequent subtraction of the effective analyzer width $\frac{\gamma_a+b_a}{2}=1.67\gamma_a$ for a 1μm thick stainless steel analyzer containing 55% of ^{57}Fe.

Since cavity spectra can be considerably broadened by superradiance, we use two optimization strategies to reduce resonant effects: First, we optimize the Δ fit range towards the lowest line fit error as described in Section 3.3.2, however, by evaluating the first 40 fits. This suppresses resonant effects affecting the shape of the diagonal line at small detunings while at the same time taking into account as many data points as possible. The second optimization is related to low-frequency deviations from the Lorentzian line shape also caused by resonant effects: To minimize its influence on the fit outcome, a series of model fits given by eq.(A.9) with adapted ν fit range is performed on each vertical cut taking into account a different number of data points below the peak maximum. Specifically, we first include a frequency range starting right below the expected peak maximum only and evaluate eight fits $j\in\{0,1,\ldots,7\}$ in which $10j$ datapoints are added at the lower end of the vertical cut. Again, the fit with the least fit error is selected. It was found that this approach improves the fit result especially in the vicinity of the superradiance maximum where resonant effects are expected to be strongest.

A.3 Line shapes in nuclear forward scattering

In this Appendix, we briefly discuss the response functions of single-line targets in nuclear forward scattering in the time domain, and employ them to evaluate their line shape in the FFC spectra.

For a single-line target, the scattering part of the generic response function in the time domain Eq. (3.5) evaluates to [LHH60a; KAK79; Smi99; Shv+98; Röh04; HT99a]

$$S_t(t) = -\Theta(t)\,\sqrt{\frac{b_t}{t}}\,J_1(2\sqrt{b_t t})e^{-\frac{\gamma_t}{2}t}\,e^{-i\omega_t t}\,, \tag{A.10}$$

where $\Theta(t)$ is the Heaviside step function, γ_t the decay rate of the individual nuclei, and ω_t the transition frequency. The thickness parameters b_i for target $(i = t)$ and analyzer $(i = a)$ are given by

$$b_i = \frac{\pi\rho_i f_{LM}\gamma_i}{k_i^2(1+\alpha)}d_i \tag{A.11}$$

where ρ_i denotes the number density of resonant nuclei, γ_i its line-width, k_i the wave number of the resonant radiation, d_i the target's thickness, f_{LM} the Lamb-Mössbauer factor and α the internal conversion coefficient (for more details, see e.g. [HT99a; Röh04]). For α-iron the internal conversion coefficient is given by $\alpha = 8.56$ [Röh04] and the Lamb-Mössbauer factor at ambient conditions is of the order $f_{LM} \approx 0.8$ [Stu04].

In the early-time approximation $b_a t \ll 1$, the corresponding response for a thin single-line analyzer evaluates to

$$S_a(t,\Delta) = -\Theta(t)\,b_a\,e^{-\frac{\gamma_a+b_a}{2}t}\,e^{-i(\omega_a+\Delta)t}\,. \tag{A.12}$$

This early-time approximation of the analyzer response is based on

$$\sqrt{\frac{b_a}{t}}J_1(2\sqrt{b_a t}) \approx b_a e^{-\frac{b_a}{2}t} \tag{A.13}$$

which is valid for $b_a t \ll 1$ up to first order.

The two response functions Eq. (A.10) and (A.12) can be used to evaluate the expression for the FFC spectrum in Eq. (3.15) in the time domain. Then, the Fourier transform of the positive branch (also c.f. Eq. (3.16)) is given by

$$\begin{aligned} f(\nu) =& I_0^{\mathrm{NR}} \int_{-\infty}^{\infty} dt\, e^{i\nu t}\, S_t^*(t)\, S_a(t) \\ =& I_0^{\mathrm{NR}}\, b_a \int_0^{\infty} dt\, \sqrt{\frac{b_t}{t}} e^{i(\nu-x)t} e^{-S_\Gamma t} J_1(2\sqrt{b_t t}) \\ =& A\left[\exp\left(\frac{-ib_t}{\nu - x + iS_\Gamma}\right) - 1\right] \end{aligned} \tag{A.14}$$

with

$$x = \Delta - \omega_t + \omega_a\,, \tag{A.15}$$

$$S_\Gamma = \frac{\gamma_t + \gamma_a + b_a}{2}\,, \tag{A.16}$$

$$A = b_a I_0^{\mathrm{NR}}\,. \tag{A.17}$$

Since the line shapes obtained from the FFC spectrum coincide with the target response functions as shown in the main text, Eq. (A.14) also corresponds to the well-known frequency response function in nuclear forward scattering, as expected. However, as compared to the standard expressions [Smi99], Eq. (A.14) contains a spectral broadening entering in S_Γ caused by the convolution with the analyzer, and an additional frequency shift due to the interference with the analyzer radiation leading to the diagonal structure of the FFC spectrum.

In the main text, we employ Eq. (A.14) as the fit model in Eq. (3.32) to extract spectral parameters from the phase-combined and off-resonant spectra.

A.4 Phase-dependence of fields and intensities upon reversing sample order

In this appendix, we derive the x-ray field behind a combination of two nuclear absorbers, both of which acquire sudden relative phase shifts immediately after arrival of the x-ray pulse, either by near-instantaneous displacements or by rapid changes of the magnetic field at the nuclear positions (for details, see Sec. 3.4). In particular, we focus on the effect of the ordering of the two absorbers.

We start by deriving the field behind a single absorber. In order to evaluate the response of the absorber, it is convenient to transform into its rest frame, which refers to the frame where the nuclear resonances are time-independent. Denoting the lab frame incident field $E^L_{in}(t)$, the corresponding incident field in the rest frame is

$$E^R_{in}(t) = e^{-i\phi(t)} E^L_{in}(t)\,, \tag{A.18}$$

where $\phi(t)$ is the time-dependent phase shift. The outgoing field in the rest frame is

$$E^R_{out}(t) = \left(T * E^R_{in}\right)(t) = \int_{-\infty}^{\infty} dt'\, T(t-t')\, e^{-i\phi(t')}\, E^L_{in}(t')\,. \tag{A.19}$$

Finally, transforming back into the lab frame yields

$$E^L_{out}(t) = e^{i\phi(t)} E^R_{out}(t) = \int_{-\infty}^{\infty} dt'\, e^{i[\phi(t)-\phi(t')]}\, T(t-t')\, E^L_{in}(t')\,. \tag{A.20}$$

Next, we calculate the field behind two absorbers, the nuclear resonances of both change with time. We denote the response function of the upstream [downstream] absorber as T_1 [T_2], with phase shifts given by ϕ_1 [ϕ_2]. We obtain

$$E_{out}(t) = \int_{-\infty}^{\infty} dt' \int_{-\infty}^{\infty} dt''\, e^{i[\phi_2(t)-\phi_2(t')]}\, T_2(t-t') e^{i[\phi_1(t')-\phi_1(t'')]}\, T_1(t'-t'')\, E^L_{in}(t'')\,. \tag{A.21}$$

Assuming a near-instantaneous incident field $E^L_{in}(t'') = E_0\delta(t)$, we find

$$\begin{aligned} E_{out}(t) =& E_0 \int_{-\infty}^{\infty} dt'\, e^{i[\phi_2(t)-\phi_2(t')]}\, T_2(t-t') e^{i[\phi_1(t')-\phi_1(0)]}\, T_1(t') \\ =& E_0 \Big[\delta(t) + e^{i[\phi_1(t)-\phi_1(0)]}\, S_1(t) + e^{i[\phi_2(t)-\phi_2(0)]}\, S_2(t) \\ &+ \int_0^t dt' e^{i[\phi_2(t)-\phi_2(t')]}\, e^{i[\phi_1(t')-\phi_1(0)]} S_2(t-t') S_1(t')\Big] \end{aligned} \tag{A.22}$$

Here, we have used $T(t) = \delta(t) + S(t)$, neglected for simplicity the non-resonant electronic absorption, and the integral ranges are constrained since $S(t) \propto \Theta(t)$, where $\Theta(t)$ is the Heaviside unit step function. As expected, the individual resonant responses of the two absorbers are modified by their respective phase shift, as can be seen from the second and third term in in Eq. (A.23). However, the last term, which corresponds to the radiative coupling, is only affected by the motion of the upstream absorber in case of near-instantaneous phase-jumps. This is due to the fact that the effect of the step-like shift of the second absorber can be neglected since $\exp(i[\phi_2(t) - \phi_2(t')])$ in the radiative coupling term contributes only in the negligible interval $t' = 0$. Intuitively, only relative phase shifts between in- and outgoing radiation may modify the outgoing field, and all x-rays scattered by the upstream absorber reaching the second absorber after the incident pulse at $t = 0$ are not affected by its change in phase since it is already finished. For analogous reasons, the contribution of the step-like phase ϕ_1 can be moved out of the integral, since $\phi_1(t') = \phi_1(t'')$ for any $t', t'' > 0$. With this, Eq.(A.22) can be written as

$$E_{out}(t) = E_0 \Big[\delta(t) + e^{i[\phi_1(t)-\phi_1(0)]}\, S_1(t) + e^{i[\phi_2(t)-\phi_2(0)]}\, S_2(t) + e^{i[\phi_1(t)-\phi_1(0)]} S_{1,2}(t)\Big]\,, \tag{A.23}$$

where we have defined the radiative coupling contribution

$$S_{1,2}(t) = \int_{-\infty}^{\infty} dt' S_2(t-t') S_1(t')\,. \tag{A.24}$$

Using Eq. (A.23), adding the absorption and dispersion prefactors α, assuming $\phi_1(0) = 0 = \phi_2(0)$ without loss of generality, and specifying the ordering of analyzer and target, immediately leads to Eqs. (3.25)-(3.26) of the main text.

Finally, the intensity after the two absorbers follows from Eq. (A.23) as

$$I(t) = I_b + 2I_0 \mathrm{Re}\left[e^{i(\phi_2-\phi_1)} S_1^* S_2 + S_1^* S_{1,2} + e^{i(\phi_2-\phi_1)} S_2 S_{1,2}^*\right] , \tag{A.25}$$

where we have again assumed $\phi_1(0) = 0 = \phi_2(0)$ and defined $\phi_i \equiv \phi_i(t > 0)$. From this result, two important conclusions can be drawn. First, phase control of both absorbers does not add an additional degree of freedom beyond the phase control of only one absorber, since only the difference of the two phases enters the expression for the experimentally accessible intensity. Hence, we restrict our discussion to the phase control of the analyzer, since a target phase control may not always be experimentally feasible, i.e., for thin-film cavities. Second, if only one of the absorbers (analyzer) is moved, then the ordering of the two absorbers is crucial. The corresponding intensities for either the first or the second absorber being moved are given in Eqs. (3.28) of the main text.

A.5 Convergence of self-consistent density matrix elements

The self-consistent equations Eqs. 4.11 can be used to calculate each perturbation order separately and study the convergence of the perturbation series of the density matrix elements to the result obtained by numerical integration of the Bloch equations. This can be used to estimate how many orders of x-ray-nucleus interaction are relevant for the interpretation of a specific measurement of the observables $\rho_{ee}(t)$ and $\rho_{ge}(t)$.

Fig. A.2 studies this convergence for both quantities, coherence squared and population, for the two cases of a total pulse area $\Omega_0 = 0.2\pi$ and $\Omega_0 = \pi$, where Ω_0 is defined as

$$\Omega_0 = \int_{t_0}^{\infty} dt' \Omega(t') . \tag{A.26}$$

The result obtained by (exact) integration of the Bloch equations Eq. (A.146) using the ODEINT function of the SCIPY [Vir+20] package in PYTHON [VRD09] is shown as a red solid curve, the lowest order contribution as a blue dashed curve and the perturbative result obtained by iteratively solving Eqs. (4.11a) and (4.11b) including all calculated orders is shown as a black dashed curve. The single-order contributions are shown as dashed lines in different colors in the plots. The lower excitation result (left panel) indicates that the perturbative result describes the true dynamics well in the next-to-leading order already which can be seen from the fact that the highest order included (brown dashed curve) is very close to zero. Including this highest order both, the perturbative and Bloch result, become essentially identical (red solid and black dashed curve). In contrast, for a total pulse area of $\Omega_0 = \pi$ (right panel) convergence can only be assured by including many orders into the expansion. Convergence is achieved at early times first while the blow-up of higher expansion orders slows down convergence at later times.

As a main result of the discussion above, we conclude that the perturbative expansion Eqs. (4.11) indeed provide accurate results for the two-level dynamics if enought orders in the x-ray-nucleus interaction $\Omega(t)$ are included.

A.6 Derivation of the coherence-population correspondence in a nuclear exciton basis

To complement the derivation of the coherence-population correspondence in single-particle space given in the Section 5.3.3, we derive the same result in a nuclear exciton basis. This provides us with new insights into the physics underlying this correspondence in the LER which can also support further research in the direction of nuclear many-body dynamics beyond that regime. The reason for this is that collective nuclear excited states, so-called nuclear excitons (cf., e.g., Sec. 2.2.2), dominate the dynamics of nuclear ensembles in the LER. In particular, the nuclear exciton can be described by the symmetric superposition of all states with a single nucleus excited including the position-dependent phase of the x-ray excitation, i.e.

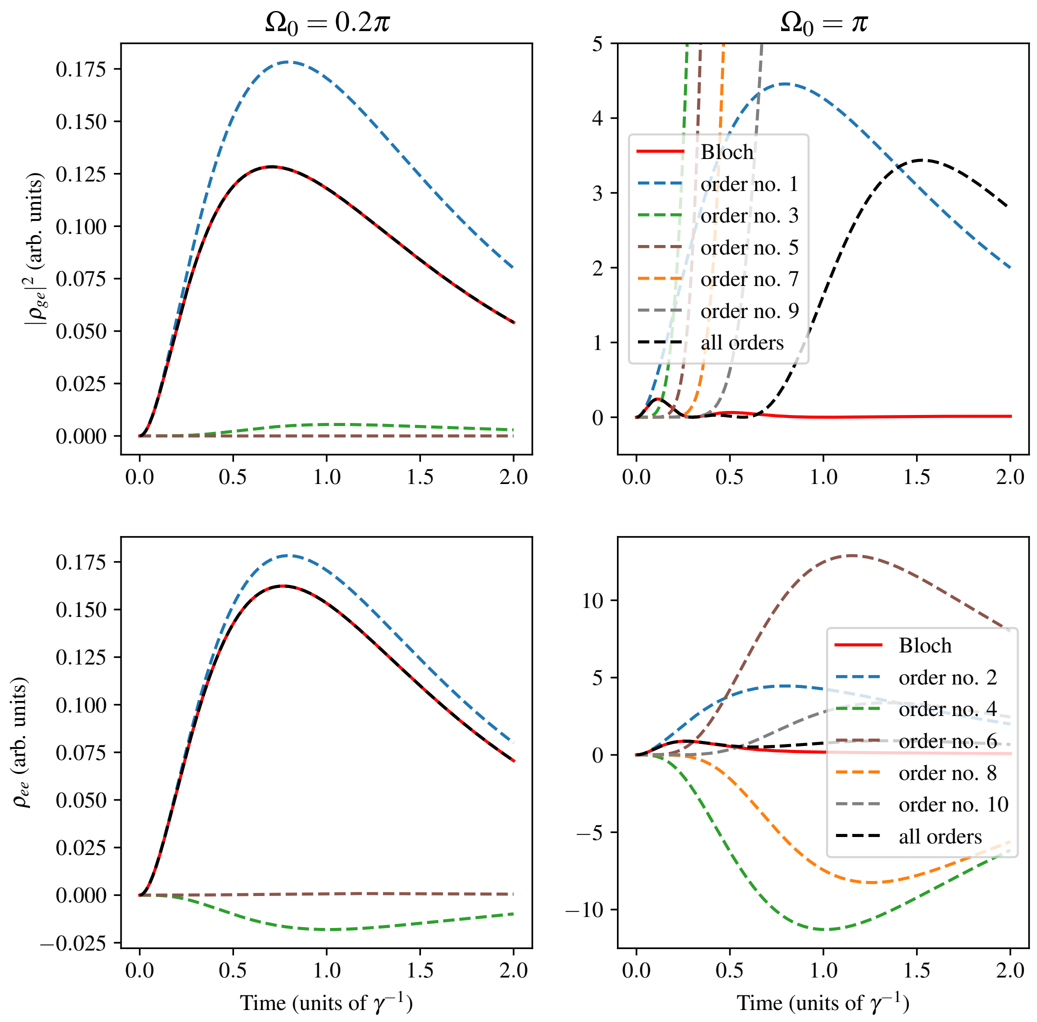

Figure A.2: Convergence behaviour of the self-consistent equations Eqs. (4.11a) and (4.11b) for pulse areas $\Omega_0 = 0.2\pi$ (left panel) and $\Omega_0 = \pi$ (right panel) : At lower excitations the perturbative result approximates the (exact) numerical result (red curve) well already in next-to-leading order and becomes essentially identical to it if one additional order is added (black curve). At higher excitations (right panel) higher order blow up at later times and convergence is ensured only at early times.

$$|E\rangle = \hat{\sigma}^{+}_{\mathbf{k}_{in}} |G\rangle = \frac{1}{\sqrt{N}} \sum_{n=1}^{N} e^{i\mathbf{k}_{in}\mathbf{r}_n} |g_1 \dots e_n \dots g_n\rangle \tag{A.27}$$

known as timed Dicke state [HE13]. The exciton creation and annihilation operators $\hat{\sigma}^{\pm}_{\mathbf{k}}$ are related to the single-particle raising and lowering operators $\hat{\sigma}^{\pm}_{n}$ via the discrete Fourier transform

$$\hat{\sigma}^{\pm}_{\mathbf{k}} = \frac{1}{\sqrt{N}} \sum_{n=1}^{N} e^{\pm i\mathbf{k}\mathbf{r}_n} \hat{\sigma}^{\pm}_{n} \,, \tag{A.28a}$$

$$\hat{\sigma}^{\pm}_{n} = \frac{1}{\sqrt{N}} \sum_{\mathbf{k}} e^{\mp i\mathbf{k}\mathbf{r}_n} \hat{\sigma}^{\pm}_{\mathbf{k}} \,. \tag{A.28b}$$

on a discrete finite lattice with translational invariance. These operators satisfy the canonical anti-commutation relations

$$\left\{\hat{\sigma}^+_{\mathbf{k}},\hat{\sigma}^-_{\mathbf{k}'}\right\} =\delta_{\mathbf{k}\mathbf{k}'} \tag{A.29}$$

$$\left\{\hat{\sigma}^+_{\mathbf{k}},\hat{\sigma}^+_{\mathbf{k}'}\right\} =\left\{\hat{\sigma}^-_{\mathbf{k}},\hat{\sigma}^-_{\mathbf{k}'}\right\} = 0 \tag{A.30}$$

using the analogous anticommutation relations for the single particle operators $\hat{\sigma}^+_n$ and the plane wave orthonormality condition holding on a translationally invariant lattice

$$\sum_{\mathbf{k}} e^{i\mathbf{k}(\mathbf{r}_n-\mathbf{r}_{n'})} = N\delta_{\mathbf{r}_n,\mathbf{r}_{n'}}\ , \qquad \sum_{n=1}^{N} e^{i(\mathbf{k}-\mathbf{k}')\mathbf{r}_n} = N\delta_{\mathbf{k},\mathbf{k}'} \tag{A.31}$$

Having defined the basis transformation into the exciton basis, we proceed as follows to show the single-nucleus identities Eqs. (5.49) as well as the time-independece of the ratio between coherently and incoherently scattered intensity Eq.(5.55): First, it is shown that the exciton transformation Eq. (A.28) diagonalizes the coupling matrix $\mathcal{K}$ defined in Eq. (4.24). Next, an equivalent excitonic basis representation of the identities Eqs. (5.49) is formulated to inform about the quantities to be calculated perturbatively. Finally, the relevant quantities are calculated up to second order in the nucleus-field coupling and the identity Eqs. (5.49) is proven in its excitonic representation.
We start by diagonalizing the time evolution operators $\hat{T}_t$. Again, assuming translational variance, one can diagonalize the interaction Hamiltonian using the excitonic basis as follows

$$\hat{H}^{sw}_{int} =-\hbar\sum_{\mathbf{k},\mathbf{k}'}\hat{\sigma}^+_{\mathbf{k}}\hat{\sigma}^-_{\mathbf{k}'}\sum_{n=1}^{N}\sum_{n'=1}^{N} e^{-i\mathbf{k}\mathbf{r}_n}e^{i\mathbf{k}'\mathbf{r}_{n'}}J_{nn'} \tag{A.32}$$

$$=-\frac{\hbar}{N}\sum_{\mathbf{k},\mathbf{k}'}\hat{\sigma}^+_{\mathbf{k}}\hat{\sigma}^-_{\mathbf{k}'}\sum_{n=1}^{N} e^{-i(\mathbf{k}-\mathbf{k}')\mathbf{r_n}}\sum_{n'=1}^{N} e^{i\mathbf{k}'(\mathbf{r}_{n'}-\mathbf{r}_n)}J_{nn'} \tag{A.33}$$

$$=-\frac{\hbar}{N}\sum_{\mathbf{k},\mathbf{k}'}\hat{\sigma}^+_{\mathbf{k}}\hat{\sigma}^-_{\mathbf{k}'}J_{\mathbf{k}'}\sum_{n=1}^{N} e^{-i(\mathbf{k}-\mathbf{k}')\mathbf{r}_n} \tag{A.34}$$

$$=-\hbar\sum_{\mathbf{k}} J_{\mathbf{k}}\hat{\sigma}^+_{\mathbf{k}}\hat{\sigma}^-_{\mathbf{k}} \tag{A.35}$$

where the excitonic coupling constant

$$J_{\mathbf{k}} = \sum_{n'=1}^{N} J_{n_0n'}e^{-i\mathbf{k}(\mathbf{r}_{n_0}-\mathbf{r}_{n'})} \tag{A.36}$$

was introduced in the third step. This form, as in the single-particle derivation Sec. 5.3.3, assumes a coupling environment of each nucleus independent of the position of that specific nucleus in the ensemble such that its index n can be replaced by any fixed index n_0. Note that $J_{\mathbf{k}}$ is real-valued due to the Hermiticity of the matrix $(J_{nn'})$. Analogously, the remaining parts of the nuclear Hamiltonian $\hat{H}_{nuc}$ and the diagonal and cross-damping terms can be diagonalized under the same assumptions assuming identical internal conversion decay constants $\Gamma^{\mathrm{IC}}_n = \Gamma_{\mathrm{IC}}$ and transition frequencies $\omega_n = \omega_0$, as before, such that the time evolution operator $\hat{T}_t$ defined in Eq. (4.24) can be rewritten as

$$\hat{T}^{exc}_t =\exp\left(\sum_{\mathbf{k}}\kappa_{\mathbf{k}}\hat{\sigma}^+_{\mathbf{k}}\hat{\sigma}^-_{\mathbf{k}}t\right) = \bigotimes_{k}\exp\left(\kappa_{\mathbf{k}}\hat{\sigma}^+_{\mathbf{k}}\hat{\sigma}^-_{\mathbf{k}}t\right) \tag{A.37a}$$

$$\kappa_{\mathbf{k}} =-\left(\Gamma_{\mathbf{k}}+iJ_{\mathbf{k}}\right)-\left(\Gamma_{\mathrm{IC}}-i\omega_0\right) \tag{A.37b}$$

The product form of the time propagation operators is possible since the excitonic state projectors for different **k** modes commute, i.e.

$$\left[\hat{\sigma}^{+}_{\mathbf{k}}\hat{\sigma}^{-}_{\mathbf{k}}, \hat{\sigma}^{+}_{\mathbf{k}'}\hat{\sigma}^{-}_{\mathbf{k}'}\right] = 0 \tag{A.38}$$

Before calculating the zeroth to second order contributions to the exciton space density matrix $\hat{\rho}_{exc}$, we derive relations for the excitonic density matrix elements, that are equivalent to Eq. (5.49), and allow for a complementary interpretation of the population-coherence correspondence in the LER in terms of excitonic modes. This is done by rewriting the single particle raising and lowering operators in terms of their excitonic quantities such that the single-particle density matrix elements can be written as

$$\rho_{g_x e_x}(t) = \langle\hat{\sigma}^{+}_{x}\rangle = \frac{1}{\sqrt{N}}\sum_{\mathbf{k}} e^{-i\mathbf{k}\mathbf{r}_x}\langle\hat{\sigma}^{+}_{\mathbf{k}}\rangle \tag{A.39a}$$

$$\rho_{e_x e_x}(t) = \langle\hat{\sigma}^{+}_{x}\hat{\sigma}^{-}_{x}\rangle = \frac{1}{N}\sum_{\mathbf{k}\mathbf{k}'} e^{-i(\mathbf{k}-\mathbf{k}')\mathbf{r}_x}\langle\hat{\sigma}^{+}_{\mathbf{k}}\hat{\sigma}^{-}_{\mathbf{k}'}\rangle \tag{A.39b}$$

Hence, the identity Eq. (5.49) can be rewritten in the following way:

$$\frac{1}{N}\sum_{\mathbf{k}\mathbf{k}'} e^{-i(\mathbf{k}-\mathbf{k}')\mathbf{r}_x}\langle\hat{\sigma}^{+}_{\mathbf{k}}\rangle_1\langle\sigma^{-}_{\mathbf{k}'}\rangle_1 = \frac{1}{N}\sum_{\mathbf{k}\mathbf{k}'} e^{-i(\mathbf{k}-\mathbf{k}')\mathbf{r}_x}\langle\hat{\sigma}^{+}_{\mathbf{k}}\hat{\sigma}^{-}_{\mathbf{k}'}\rangle_2 \tag{A.40}$$

where we used the fact that $\langle\hat{\sigma}^{-}_{\mathbf{k}}\rangle = \langle\hat{\sigma}^{+}_{\mathbf{k}}\rangle^*$ and introduced subscripts for the expectation values to indicate whether the first or second order density matrix is used to calculate it. This shows that to prove Eq. (5.49) in single-particle space, we need to show the relationship

$$\langle\hat{\sigma}^{+}_{\mathbf{k}}\rangle_{(0-2)}\langle\sigma^{-}_{\mathbf{k}'}\rangle_{(0-2)} = \langle\hat{\sigma}^{+}_{\mathbf{k}}\hat{\sigma}^{-}_{\mathbf{k}'}\rangle_{(0-2)} \tag{A.41}$$

with the subscript referring to the expectation value including the density matrix up to second order. One interpretation of Eq. (A.41) is that the equivalence of coherence squared and population in the LER is equivalent to the fact that up to second order in the nucleus-field coupling the classical correlations or interference between excitonic dipolar emission for different modes $\mathbf{k}$, $\mathbf{k}'$, described by the left hand side, are identical to the first-order quantum correlations between different excitonic dipole modes, represented by the right hand side.

To calculate the expectation values

$$\langle\hat{\sigma}^{+}_{\mathbf{k}}\rangle_j(t) = \mathrm{Tr}\left[\hat{\sigma}^{+}_{\mathbf{k}}\hat{\rho}^{(j)}_{exc}\right], \tag{A.42a}$$

$$\langle\hat{\sigma}^{+}_{\mathbf{k}}\hat{\sigma}^{-}_{\mathbf{k}'}\rangle_j(t) = \mathrm{Tr}\left[\hat{\sigma}^{+}_{\mathbf{k}}\hat{\sigma}^{-}_{\mathbf{k}'}\hat{\rho}^{(j)}_{exc}(t)\right] \tag{A.42b}$$

where the index $j = 0, 1, 2$, we also have to transform the nucleus-field coupling Hamiltonian $\hat{W}(t)$ into excitonic space, in addition to the time evolution operator $\hat{T}^{exc}_t$ Eq. (A.37). This is done by inserting the Fourier representation of $\hat{\sigma}^{\pm}_n$ into Eq. (4.15) for a single layer, yielding

$$\hat{W}^{exc}(t) = -\frac{\hbar}{2}\sum_{\mathbf{k}}\left(\Omega_{\mathbf{k}}(t)\hat{\sigma}^{+}_{\mathbf{k}} + h.c.\right) \tag{A.43}$$

with the Fourier-transformed nucleus field couplings

$$\Omega_{\mathbf{k}}(t) = \frac{1}{\sqrt{N}}\sum_{n} e^{-i\mathbf{k}\mathbf{r}_n}\Omega(\mathbf{r}_n, t) \tag{A.44}$$

With this the zero order density matrix can be written as

$$\hat{\rho}^{(0)}_{exc}(t) = \left(\hat{T}^{exc}_{t-t_0}\right)^{\dagger}\hat{\rho}_{exc}(t_0)\hat{T}^{exc}_{t-t_0} = \hat{\rho}^{\mathrm{NB}}(t_0) = |G\rangle\langle G| \tag{A.45}$$

if the system is initially in its ground state, which is the same in both single particle and excitonic space. Note, that the zeroth order contribution to the excitonic coherence and population of mode **k** becomes zero since the two traces in the Eqs. (A.42) vanish in the collective ground state, i.e.

$$\rho^{(0)}_{g_{\mathbf{k}},e_{\mathbf{k}}}(t) = 0 = \rho^{(0)}_{e_{\mathbf{k}}e_{\mathbf{k}'}}(t) \tag{A.46}$$

The first order density matrix can be calculated using Eq. (4.36) with the corresponding excitonic operators $\hat{T}^{exc}_t$, $\hat{W}^{exc}(t)$ and $\rho^{(0)}_{exc}(t)$ derived above. The action of the operator $\hat{W}^{sw}$ on the ground state $\hat{\rho}^{(0)}_{exc}(t)$ creates a superposition of nuclear exciton states like Eq. (A.27) for each k-mode. The exciton states are eigenstates of the time evolution operators by construction, which can be shown excplicitely by

$$\hat{\sigma}^{+}_{\mathbf{k}'}\hat{\sigma}^{-}_{\mathbf{k}'}\hat{\sigma}^{+}_{\mathbf{k}}\hat{\rho}^{(0)}_{exc}(\tau) = \hat{\sigma}^{+}_{\mathbf{k}'}\left[\{\hat{\sigma}^{-}_{\mathbf{k}'},\hat{\sigma}^{+}_{\mathbf{k}}\} - \hat{\sigma}^{+}_{\mathbf{k}}\hat{\sigma}^{-}_{\mathbf{k}'}\right]\hat{\rho}^{(0)}_{exc}(\tau) \tag{A.47}$$

$$= \delta_{\mathbf{k}\mathbf{k}'}\hat{\sigma}^{+}_{\mathbf{k}}\hat{\rho}^{(0)}_{exc}(\tau) \tag{A.48}$$

where we used the canonical anticommutation relations and the fact that

$$\hat{\sigma}^{-}_{\mathbf{k}}\hat{\rho}^{(0)}_{exc}(\tau) = 0 = \hat{\rho}^{(0)}_{exc}(\tau)\hat{\sigma}^{+}_{\mathbf{k}} \tag{A.49}$$

in the second step. Therefore, the action of the time evolution operator on the single exciton states yields

$$\left(\hat{T}^{exc}_{t-t_0}\right)^{\dagger}\hat{\sigma}^{+}_{\mathbf{k}}\hat{\rho}^{(0)}_{exc}(\tau) = e^{\kappa^{*}_{\mathbf{k}}(t-t_0)}\hat{\sigma}^{+}_{\mathbf{k}}\hat{\rho}^{(0)}_{exc}(\tau) \tag{A.50}$$

With this, the

$$\hat{\rho}^{(1)}_{exc}(t) = \sum_{\mathbf{k}}\left[\frac{i}{2}\int_{t_0}^{t} d\tau\Omega_{\mathbf{k}}(\tau)e^{\kappa^{*}_{\mathbf{k}}(t-\tau)}\hat{\sigma}^{+}_{\mathbf{k}}\hat{\rho}^{(0)}_{exc}(\tau) + h.c.\right] \tag{A.51}$$

The first order contribution to the single exciton expectation value Eq. (A.42a) becomes

$$\langle\hat{\sigma}^{+}_{\mathbf{k}}\rangle_1(t) = -\frac{i}{2}\int_{t_0}^{t} d\tau\sum_{\mathbf{k}'}\Omega^{*}_{\mathbf{k}'}(\tau)e^{\kappa_{\mathbf{k}}(t-\tau)}\mathrm{Tr}\left[\hat{\sigma}^{+}_{\mathbf{k}}\hat{\rho}^{(0)}_{exc}(t)\hat{\sigma}^{-}_{\mathbf{k}'}\right]$$

$$= -\frac{i}{2}\int_{t_0}^{t} d\tau\Omega^{*}_{\mathbf{k}}(\tau)e^{\kappa_{\mathbf{k}}(t-\tau)} \tag{A.52}$$

where we used the cyclic property of the trace and the fact that the trace is only nonzero if both bra and ket are in the ground or excited state, i.e.

$$\mathrm{Tr}\left[\hat{\sigma}^{+}_{\mathbf{k}}\hat{\rho}^{sw,(0)}(t)\hat{\sigma}^{-}_{\mathbf{k}'}\right] = \delta_{\mathbf{k}\mathbf{k}'} \tag{A.53}$$

$$\mathrm{Tr}\left[\hat{\sigma}^{+}_{\mathbf{k}'}\hat{\rho}^{(0)}_{sw}(\tau)\hat{\sigma}^{+}_{\mathbf{k}}\right] = 0 \tag{A.54}$$

since the initial state is the collective ground state. Similarly, the first-order correlation between mode **k** and **k**′ Eq. (A.42b) vanishes since the traces

$$\mathrm{Tr}\left[\hat{\sigma}^{+}_{\mathbf{k}}\hat{\sigma}^{-}_{\mathbf{k}'}\hat{\rho}^{sw,(0)}(t)\hat{\sigma}^{-}_{\mathbf{k}''}\right] = 0 \tag{A.55}$$

$$\mathrm{Tr}\left[\hat{\sigma}^{+}_{\mathbf{k}''}\hat{\rho}^{(0)}_{exc}(\tau)\hat{\sigma}^{+}_{\mathbf{k}}\hat{\sigma}^{-}_{\mathbf{k}'}\right] = 0 \tag{A.56}$$

are zero in the collective ground state $\hat{\rho}^{(0)}_{exc}(\tau)$ and thus

$$\langle \hat{\sigma}^{+}_{\mathbf{k}} \hat{\sigma}^{-}_{\mathbf{k}'} \rangle_1 = 0 \,. \tag{A.57}$$

The second order contribution to the excitonic density matrix can be obtained by evaluation of Eq. (4.38) using again the exciton space quantities $\hat{W}^{exc}(t)$, $\hat{T}^{exc}_{t}$ and the first order density matrix Eq. (A.51). The result reads:

$$\begin{aligned}\hat{\rho}^{(2)}_{exc}(t) = &-\frac{1}{4}\int_{t_0}^{t} d\tau_2 \int_{t_0}^{\tau_2} d\tau_1 \Bigg[\sum_{\mathbf{k}',\mathbf{k}} \Omega_{\mathbf{k}'}(\tau_2)\Omega_{\mathbf{k}}(\tau_1) e^{\kappa^*_{\mathbf{k}}(t-\tau_1)} e^{\kappa^*_{\mathbf{k}}(t-\tau_2)} \hat{\sigma}^{+}_{\mathbf{k}'}\hat{\sigma}^{+}_{\mathbf{k}}\hat{\rho}^{sw,(0)}(\tau_1) \\ &- \Omega_{\mathbf{k}'}(\tau_2)\Omega^*_{\mathbf{k}}(\tau_1) e^{\kappa_{\mathbf{k}}(t-\tau_1)} e^{\kappa^*_{\mathbf{k}'}(t-\tau_2)} \hat{\sigma}^{+}_{\mathbf{k}'}\hat{\rho}^{sw,(0)}(\tau_1)\hat{\sigma}^{-}_{\mathbf{k}} \\ &+ \Omega^*_{\mathbf{k}'}(\tau_2)\Omega_{\mathbf{k}}(\tau_1) e^{\kappa^*_{\mathbf{k}}(t-\tau_1)} e^{\kappa_{\mathbf{k}'}(t-\tau_2)} \hat{\sigma}^{-}_{\mathbf{k}'}\hat{\sigma}^{+}_{\mathbf{k}}\hat{\rho}^{sw,(0)}(\tau_1) + h.c.\Bigg]\end{aligned} \tag{A.58}$$

Upon calculation of the second order correlation of mode $\mathbf{k}$ and $\mathbf{k}'$ Eq. (A.42b) the following traces and their complex-conjugates have to be evaluated:

$$\mathrm{Tr}\left[\hat{\sigma}^{-}_{\mathbf{k}'}\hat{\sigma}^{+}_{\mathbf{k}}\hat{\rho}^{(0)}_{exc}(\tau_1)\hat{\sigma}^{+}_{\mathbf{k}''}\hat{\sigma}^{-}_{\mathbf{k}'''}\right] = 0\,, \tag{A.59}$$

$$\mathrm{Tr}\left[\hat{\sigma}^{+}_{\mathbf{k}'}\hat{\sigma}^{+}_{\mathbf{k}}\hat{\rho}^{(0)}_{exc}(\tau_1)\hat{\sigma}^{+}_{\mathbf{k}''}\hat{\sigma}^{-}_{\mathbf{k}'''}\right] = 0\,, \tag{A.60}$$

$$\mathrm{Tr}\left[\hat{\sigma}^{+}_{\mathbf{k}'}\hat{\rho}^{(0)}_{exc}(\tau_1)\hat{\sigma}^{-}_{\mathbf{k}}\hat{\sigma}^{+}_{\mathbf{k}''}\hat{\sigma}^{-}_{\mathbf{k}'''}\right] = \delta_{\mathbf{k}\mathbf{k}''}\delta_{\mathbf{k}'\mathbf{k}'''}\,. \tag{A.61}$$

Thus, the second order contribution to the $\mathbf{k}$ and $\mathbf{k}'$ mode correlation in the exciton basis reads

$$\begin{aligned}\langle \hat{\sigma}^{+}_{\mathbf{k}} \hat{\sigma}^{-}_{\mathbf{k}'} \rangle_2(t) = &\frac{1}{4}\int_{t_0}^{t} d\tau_2 \int_{t_0}^{\tau_2} d\tau_1 \Big\{\Omega_{\mathbf{k}'}(\tau_2)\Omega^*_{\mathbf{k}}(\tau_1) e^{\kappa_{\mathbf{k}}(t-\tau_1)} e^{\kappa^*_{\mathbf{k}'}(t-\tau_2)} \\ &+ \Omega^*_{\mathbf{k}}(\tau_2)\Omega_{\mathbf{k}'}(\tau_1) e^{\kappa^*_{\mathbf{k}'}(t-\tau_1)} e^{\kappa_{\mathbf{k}}(t-\tau_2)}\Big\}\end{aligned} \tag{A.62}$$

and the second order contribution to the single-exciton expectation value

$$\langle \hat{\sigma}^{+}_{\mathbf{k}} \rangle_2(t) = 0 \tag{A.63}$$

vanishes with the traces

$$\mathrm{Tr}\left[\hat{\sigma}^{-}_{\mathbf{k}'}\hat{\sigma}^{+}_{\mathbf{k}}\hat{\rho}^{(0)}_{exc}(\tau_1)\hat{\sigma}^{+}_{\mathbf{k}''}\right] = 0\,, \tag{A.64}$$

$$\mathrm{Tr}\left[\hat{\sigma}^{+}_{\mathbf{k}'}\hat{\sigma}^{+}_{\mathbf{k}}\hat{\rho}^{(0)}_{exc}(\tau_1)\hat{\sigma}^{+}_{\mathbf{k}''}\right] = 0\,, \tag{A.65}$$

$$\mathrm{Tr}\left[\hat{\sigma}^{+}_{\mathbf{k}'}\hat{\rho}^{(0)}_{exc}(\tau_1)\hat{\sigma}^{-}_{\mathbf{k}}\hat{\sigma}^{+}_{\mathbf{k}''}\right] = 0\,. \tag{A.66}$$

Defining the functions

$$g(\tau) = -\frac{i}{2}\Omega^*_{\mathbf{k}'}(\tau) e^{\kappa_{\mathbf{k}}(t-\tau)} \tag{A.67}$$

$$f(\tau) = -\frac{i}{2}\Omega^*_{k}(\tau) e^{\kappa_{\mathbf{k}'}(t-\tau)} \tag{A.68}$$

and the general relation between complex-valued functions

$$\int_{t_0}^{t} g^*(\tau_2)d\tau_2 \int_{t_0}^{t} f(\tau_1)d\tau_1 = \int_{t_0}^{t} d\tau_2 g^*(\tau_2) \int_{t_0}^{\tau_2} d\tau_1 f(\tau_1) + \int_{t_0}^{t} d\tau f(\tau_2) \int_{t_0}^{\tau_2} d\tau_1 g^*(\tau_1) \tag{A.69}$$

proves Eq. (A.41) since the left-hand side of Eq. (A.69) is identical to $\langle \hat{\sigma}^+_k \rangle_1 \langle \hat{\sigma}^-_{k'} \rangle_1$ while its right-hand side yields the two terms in Eq. (A.62). With this, we have shown that the classical single-exciton correlations are identical to the quantum correlations up to second order. This together with the Eqs. (A.39) and (A.40), also proves the identity Eq. (5.49).
In summary, we have derived the equivalence of single-particle incoherent emission, which is proportional to the single-particle excited state population $\hat{\rho}_{e_x e_x}$, and the single-particle coherent emission proportional to $|\rho_{g_x e_x}|^2$ up to second order in the x-ray-nuclei interaction using a coupling matrix diagonalization approach. It is complementary to the single-particle derivation used in Sec. 5.3.3 and allowed for an interpretation of this equivalence in terms of correlations between nuclear exciton correlations that are crucial for quantum optical interpretations of many-body nuclear dynamics in the LER and beyond.

Incoherent and coherent emission of nuclear ensembles in the exciton basis

To show that the ratio Eq. (5.55) of the incoherently and coherently scattered intensities $I^{(0-2)}_{inc}(t)$ Eq. (5.6) and $I^{(0-2)}_{coh}(t)$ Eq. (5.8) is constant, we need to derive explicitely the single-particle coherences and populations. This can be done using the backtransform of the exciton creation and annihilation operators Eq. (A.29) such that

$$\begin{aligned}
\rho^{(1)}_{g_x,e_x}(t) =& \frac{1}{\sqrt{N}} \sum_{\mathbf{k}} e^{-i\mathbf{k}\mathbf{r}_x} \langle \hat{\sigma}^+_{\mathbf{k}} \rangle_1(t) && \text{(A.70)}\\
=& -\frac{i}{2\sqrt{N}} \int_{t_0}^{t} d\tau \sum_{\mathbf{k}} e^{-i\mathbf{k}\mathbf{r}_x} \Omega^*_{\mathbf{k}}(\tau) e^{\kappa_{\mathbf{k}}(t-\tau)} && \text{(A.71)}\\
\rho^{(2)}_{e_x,e_x}(t) =& \frac{1}{N} \sum_{\mathbf{k},\mathbf{k}'} e^{-i(\mathbf{k}-\mathbf{k}')\mathbf{r}_x} \langle \hat{\sigma}^+_{\mathbf{k}} \hat{\sigma}^-_{\mathbf{k}'} \rangle_2 && \text{(A.72)}\\
=& \frac{1}{4N} \sum_{\mathbf{k},\mathbf{k}'} e^{-i(\mathbf{k}-\mathbf{k}')\mathbf{r}_x} \int_{t_0}^{t} d\tau_2 \int_{t_0}^{\tau_2} d\tau_1 \Big\{ \Omega_{\mathbf{k}'}(\tau_2) \Omega^*_{\mathbf{k}}(\tau_1) e^{\kappa_{\mathbf{k}}(t-\tau_1)} e^{\kappa^*_{\mathbf{k}'}(t-\tau_2)} \\
&+ \Omega^*_{\mathbf{k}}(\tau_2) \Omega_{\mathbf{k}'}(\tau_1) e^{\kappa^*_{\mathbf{k}'}(t-\tau_1)} e^{\kappa_{\mathbf{k}}(t-\tau_2)} \Big\} && \text{(A.73)}
\end{aligned}$$

Now, using the assumption that all nuclei are excited by the same-amplitude of a plane-wave driving field Eq. (5.29), also employed in Sec. 5.3.3, the Fourier transform of the field-nucleus coupling can be written as

$$\Omega_{\mathbf{k}}(t) = \sqrt{N} \Omega(t) \delta_{\mathbf{k},\mathbf{k}_{in}} \tag{A.74}$$

if the plane wave orthonormality relations Eqs. (A.31) are used. Note, that for the incident wave vector to satisfy this orthonormality with one of the exciton modes, full translational invariance or, rephrased a homogeneous nuclear ensemble, is crucial. This is of special importance if finite systems are considered since an incident wave vector $\mathbf{k}_{in}$ not matching an exciton mode creates phase offsets between the nuclei at the boundaries this way breaking translational invariance. Thus, in finite systems, only certain incident wave vectors in agreement with a nuclear exciton mode, satisfy the conditions necessary for the ratio of incoherently and coherently scattered radiation to be constant in time. However, for all practical purposes this restriction can be neglected since boundary effects are usually negligble in macroscopic nuclear ensembles.
This said, the single-particle coherence can be written as

$$\rho^{(1)}_{g_x,e_x}(t) = -\frac{i}{2} e^{-i\mathbf{k}_{in}\mathbf{r}_x} \int_{t_0}^{t} d\tau e^{\kappa_{\mathbf{k}_{in}}(t-\tau)} \Omega^*(\tau) = \rho_{ge}(t) e^{-i\mathbf{k}_{in}\mathbf{r}_x} \tag{A.75}$$

Note that the site-independent coherence $\rho_{ge}(t)$ defined here indeed is identical to the one in Eq. (5.52) since

$$\left[e^{\mathcal{K}(t-\tau)}\right]_{nn_0} = e^{-i\mathbf{k}_{in}(\mathbf{r}_{n_0}-\mathbf{r}_n)}e^{\kappa_{\mathbf{k}_{in}}(t-\tau)} \tag{A.76}$$

which can be shown by explicity applying the diagonlizing transformation Eq. (A.29) to the matrix exponential $e^{\mathcal{K}(t-\tau)}$. Hence, the exciton and single-particle basis approach provide identical results. Analogously, the single-particle population Eq. (A.73) can be shown to be independent of the position of the nucleus in ensemble Eq. (5.53). This finally demonstrates that the exciton basis approach to evaluate the irradiance of nuclear ensembles in the LER is consistent with the single-particle derivation. Further, it provides an alternative method to compute the ensemble scattering observables of coupled many-nuclei systems via the relation Eq. (A.76).

A.7 Derivation of the population-coherence correspondence for effective three-level systems

Here, derive the population-coherence correspondence for effective three-level systems as described in Sec. 6.3.5.

In view of the discussed transfer of population and coherence from one excited state to another as evident in Eq. (6.21) and its graphical interpretation Figs. 6.2 and 6.3, it may seem surprising that a population-coherence correspondence similar to Eq. (5.22) is still valid in the case of effective three-level systems. Indeed, we will show that

$$\rho^{(2)}_{ll}(t) = |\rho^{(1)}_{0l}(t)|^2 \tag{A.77}$$

is true for each transition $l = 1, 2$ separately using a diagonalization approach of the excited-state sector of the three-dimensional state space. This result will help us to compare incoherent and coherent nuclear resonant scattering spectra discussed in Sec. 6.4.

To prove Eq. (6.27), we follow a similar procedure as the one used in Sec. A.6: First, the time evolution operators

$$\hat{T}_t = e^{i\Lambda t} = \exp\left(-\hat{\Gamma}t + \frac{i}{\hbar}\hat{H}_{nuc}t\right) \tag{A.78}$$

are diagonalized using the similarity transformation

$$\hat{A}^{-1}\Lambda\hat{A} = \begin{pmatrix} d_2 & 0 & 0 \\ 0 & d_1 & 0 \\ 0 & 0 & 1 \end{pmatrix} \quad , \quad d_{2,1} = \bar{\delta} + i\bar{\Gamma} \pm \frac{1}{2}\Delta_R \tag{A.79}$$

Next, conditions for the diagonal-basis density matrix elements equivalent to Eq. (6.27) are derived, which will be used to show that this identity is valid even in the presence of coherent couplings between the excited states. This equivalent condition reads:

$$|\rho^{(1)}_{g+}|^2 = \rho^{(2)}_{++} \ , \quad |\rho^{(1)}_{g-}|^2 = \rho^{(2)}_{--} \ , \quad \rho^{(1)}_{g+}\rho^{(1)}_{-g} = \rho^{(2)}_{-+} \tag{A.80}$$

which, like in the exciton case Sec. A.6, can be interpreted as the equality of first-order correlation between dipoles in the diagonal basis and classical interference or correlation between dipole-emitted radiation. In the last two steps, the perturbative expansion of the density matrix Eq. (4.43) is calculated in the diagonal basis to obtain the first and second order density matrix elements, which are used to eventually prove Eq. (A.80) and with it Eq. (6.27).

A.7.1 Diagonalization of the time evolution operator

The density matrix elements in the diagonal basis appearing in Eq. (A.80) are the entries of the transformed density matrix

$$\hat{\rho}_d(t) = \hat{A}^\dagger \hat{\rho}(t) \hat{A} = \begin{pmatrix} \rho_{++}(t) & \rho_{+-}(t) & \rho_{+g}(t) \\ \rho_{-+}(t) & \rho_{--}(t) & \rho_{-g}(t) \\ \rho_{g+}(t) & \rho_{g-}(t) & \rho_{gg}(t) \end{pmatrix} \tag{A.81}$$

where the subscript d refers to the dressed-state picture since the transformation diagonalizing the excited state sector including coupling is analogous to the dressed-atom model in quantum optics [MS07; SZ97; FS05]. Note, that in Eq. (A.81) the adjoint of $\hat{A}$ appears instead of its inverse as in Eq. (A.79). These two quantities, for general non-Hermitian Λ are not identical. Appendix A.8 discusses the conditions an effective three-level system has to satisfy such that $\hat{A}$ can be chosen unitary. Here, however, we accept non-unitary similarity transformations $\hat{A}$ and, in analogy to the dressed-state picture transformation [MS07], we define

$$\hat{A} = \begin{pmatrix} \cos\theta & -e^{i\phi}\sin\theta & 0 \\ e^{-i\phi}\sin\theta & \cos\theta & 0 \\ 0 & 0 & 1 \end{pmatrix} , \quad \hat{A}^{-1} = \begin{pmatrix} \cos\theta & e^{i\phi}\sin\theta & 0 \\ -e^{-i\phi}\sin\theta & \cos\theta & 0 \\ 0 & 0 & 1 \end{pmatrix} \tag{A.82}$$

which transforms the excited-state sector only since the common ground state is not affected by the coupling and evolves trivially in time under the action of $\hat{T}_t$ (cf. Eqs. (6.14)). To ensure diagonalizability of Λ, the phase ϕ in the similarity transformation has to be equal to the coherent coupling phase Eq. (6.18), i.e.

$$\phi = \phi_{21} \, . \tag{A.83}$$

The generalized angle θ can be derived from the off-diagonal elements of the excited state sector in Eq. (A.79) and satisfies

$$\tan(2\theta) = \frac{2|\Delta_{21}|}{\Delta\delta + i\Delta\Gamma} \tag{A.84}$$

Note, that θ in general is complex-valued and thus $\hat{A}$ is not unitary except for the case when $\Gamma_1 = \Gamma_2$ which is the same condition under which the energy-decay matrix Λ (cf. Eq. (A.118) in Appendix A.8) becomes normal. Considering the general case with $\Gamma_1 \neq \Gamma_2$, the time evolution operators in the dressed-state basis become diagonal by construction, i.e.

$$\hat{T}^d_t = \hat{A}^{-1} e^{i\Lambda t} \hat{A} = \begin{pmatrix} e^{id_2 t} & 0 & 0 \\ 0 & e^{id_1 t} & 0 \\ 0 & 0 & 1 \end{pmatrix} \, . \tag{A.85}$$

With this, the first step of the proof, i.e. the diagonalization of the intrinsic (incoherent and coherent) nuclear dynamics, is finished.

A.7.2 Population-coherence correspondence in the dressed-state basis

Before the perturbative density matrix expansion is calculated, the bare-state identity Eq. (6.27) has to be translated into an equivalent form involving the dressed-state density matrix elements Eq. (A.81). To this end, we write down the explicit form of the backtransformation from the dressed-state basis to the bare-state basis to be inserted into Eq. (6.27) which reads

$$\hat{\rho}^{(j)}(t) = (\hat{A}^{-1})^\dagger \hat{\rho}^{(j)}_d(t) \hat{A}^{-1} = \begin{pmatrix} \rho^{(j)}_{22} & \rho^{(j)}_{21} & \rho^{(j)}_{20} \\ \rho^{(j)}_{12} & \rho^{(j)}_{11} & \rho^{(j)}_{10} \\ \rho^{(j)}_{02} & \rho^{(j)}_{01} & \rho^{(j)}_{00} \end{pmatrix} \tag{A.86}$$

with entries

$$\rho_{22}^{(j)} = \rho_{++}^{(j)}|\cos\theta|^2 + \rho_{--}^{(j)}|\sin\theta|^2 - (\rho_{-+}^{(j)} e^{i\phi_{21}} \sin\theta^* \cos\theta + \rho_{+-}^{(j)} e^{-i\phi_{21}} \sin\theta \cos\theta^*) \tag{A.87}$$

$$\rho_{11}^{(j)} = \rho_{--}^{(j)}|\cos\theta|^2 + \rho_{++}^{(j)}|\sin\theta|^2 + (\rho_{-+}^{(j)} e^{i\phi_{21}} \sin\theta \cos\theta^* + \rho_{+-}^{(j)} e^{-i\phi_{21}} \sin\theta^* \cos\theta) \tag{A.88}$$

$$\rho_{20}^{(j)} = \rho_{+g}^{(j)} \cos\theta^* - \rho_{-g}^{(j)} e^{i\phi_{21}} \sin\theta^* \,, \quad \rho_{10}^{(j)} = \rho_{+g}^{(j)} e^{-i\phi_{21}} \sin\theta^* + \rho_{-g}^{(j)} \cos\theta^* \tag{A.89}$$

$$\rho_{21}^{(j)} = \rho_{+-}^{(j)}|\cos\theta|^2 - \rho_{-+}^{(j)} e^{2i\phi_{21}}|\sin\theta|^2 + e^{i\phi_{21}} \left(\rho_{++}^{(j)} \sin\theta \cos\theta^* - \rho_{--}^{(j)} \cos\theta \sin\theta^*\right) \tag{A.90}$$

$$\rho_{12}^{(j)} = \left(\rho_{21}^{(j)}\right)^* \,, \quad \rho_{02}^{(j)} = \left(\rho_{20}^{(j)}\right)^* \,, \quad \rho_{01}^{(j)} = \left(\rho_{10}^{(j)}\right)^* \,, \quad \rho_{00}^{(j)} = \rho_{gg}^{(j)} \tag{A.91}$$

By inserting the matrix elements of transition $|2\rangle$ into Eq. (6.27), one obtains

$$|\rho_{02}^{(1)}(t)|^2 = \rho_{22}^{(2)}(t) \tag{A.92}$$

$$\begin{aligned} \Leftrightarrow & |\rho_{g+}^{(1)}|^2|\cos\theta|^2 + |\rho_{g-}^{(1)}|^2|\sin\theta|^2 - 2\mathrm{Re}\left[\rho_{g+}^{(1)}\rho_{-g}^{(1)} e^{i\phi_{21}} \cos\theta \sin\theta^*\right] \\ = & \rho_{++}^{(2)}|\cos\theta|^2 + \rho_{--}^{(2)}|\sin\theta|^2 - 2\mathrm{Re}\left[\rho_{-+}^{(2)} e^{i\phi_{21}} \cos\theta \sin\theta^*\right] \end{aligned} \tag{A.93}$$

which, for arbitrary times t can be satisfied if and only if Eqs. (A.80) are valid. Note, that the evaluation of the analogous expressions for transition $|1\rangle$ yields identical conditions.

A.7.3 Density matrix expansion in the dressed-state basis

To calculate the dressed state density matrix elements required to prove Eqs. (A.80), the perturbative expansion of the density matrix is performed with the help of Eq. (4.43) or, in the lowest expansion orders, using Eq. (6.11). To this end, note that each perturbation order is transformed separately into the dressed-state picture via Eq. (A.81). By inserting identity operators $\hat{1} = \hat{A}^{-1}\hat{A}$ such that the lower order density matrices and the nucleus-field coupling part $\hat{W}(t)$ are properly transformed into the dressed-state picture, we obtain the zeroth to second order density matrix contributions

$$\hat{\rho}_d^{(0)}(t) = \left(\hat{T}_{t-t_0}^d\right)^\dagger \hat{\rho}^d(t_0)\hat{T}_{t-t_0}^d \tag{A.94}$$

$$\hat{\rho}_d^{(1)}(t) = -\frac{i}{\hbar}\int_{t_0}^t d\tau (\hat{T}_{t-\tau}^d)^\dagger \left[(\hat{W}^d(\tau))^\dagger \hat{\rho}^{d,(0)}(\tau) - \hat{\rho}^{d,(0)}(\tau)\hat{W}^d(\tau)\right] \hat{T}_{t-\tau}^d \tag{A.95}$$

$$\hat{\rho}_d^{(2)}(t) = -\frac{i}{\hbar}\int_{t_0}^t d\tau (\hat{T}_{t-\tau}^d)^\dagger \left[(\hat{W}^d(\tau))^\dagger \hat{\rho}^{d,(1)}(\tau) - \hat{\rho}^{d,(1)}(\tau)\hat{W}^d(\tau)\right] \hat{T}_{t-\tau}^d \tag{A.96}$$

with the dressed state time evolution operators Eq. (A.85) and the non-Hermitian dressed state nucleus-field interaction matrix

$$\hat{W}^d(t) = \hat{A}^{-1}\hat{W}(t)\hat{A} = -\frac{\hbar}{2}\begin{pmatrix} 0 & 0 & \Omega_{+g}(t) \\ 0 & 0 & \Omega_{-g}(t) \\ \Omega_{g+}(t) & \Omega_{g-}(t) & 0 \end{pmatrix} \tag{A.97}$$

Its entries are given by

$$\Omega_{+g}(t) = \Omega_2(t)\cos\theta + \Omega_1(t)e^{i\phi_{21}}\sin\theta \tag{A.98}$$

$$\Omega_{-g}(t) = \Omega_1(t)\cos\theta - \Omega_2(t)e^{-i\phi_{21}}\sin\theta \tag{A.99}$$

$$\Omega_{g+}(t) = \Omega_2^*(t)\cos\theta + \Omega_1^*(t)e^{-i\phi_{21}}\sin\theta \tag{A.100}$$

$$\Omega_{g-}(t) = \Omega_1^*(t)\cos\theta - \Omega_2^*(t)e^{i\phi_{21}}\sin\theta \tag{A.101}$$

With this, the density matrix contributions in zeroth to second order can be evaluated. If the system is initially in its ground state, it remains so in zeroth order and is constant in time, i.e.

$$\rho_d^{(0)}(t) = \rho_d(t_0) = \hat{\rho}(t_0) = \begin{pmatrix} 0 & 0 & 0 \\ 0 & 0 & 0 \\ 0 & 0 & 1 \end{pmatrix} \tag{A.102}$$

Note that we used that the dressed and bare ground state are identical in the second step. We conclude that in zeroth order the dressed-state coherences and excited state populations are zero, i.e.

$$\rho_{g+}^{(0)}(t) = \rho_{g-}^{(0)}(t) = 0 = \rho_{++}^{(0)}(t) = \rho_{--}^{(0)}(t) \tag{A.103}$$

The first order is given by

$$\hat{\rho}_d^{(1)}(t) = \begin{pmatrix} 0 & 0 & \rho_{+g}^{(1)}(t) \\ 0 & 0 & \rho_{-g}^{(1)}(t) \\ \rho_{g+}^{(1)}(t) & \rho_{g-}^{(1)}(t) & 0 \end{pmatrix} \tag{A.104}$$

with entries

$$\rho_{g+}^{(1)}(t) = -\frac{i}{2}\int_{t_0}^{t} d\tau e^{-\bar{\Gamma}(t-\tau)} e^{i\bar{\delta}(t-\tau)} e^{\frac{i}{2}\Delta_R(t-\tau)} \Omega_{g+}(\tau) \tag{A.105a}$$

$$\rho_{g-}^{(1)}(t) = -\frac{i}{2}\int_{t_0}^{t} d\tau e^{-\bar{\Gamma}(t-\tau)} e^{i\bar{\delta}(t-\tau)} e^{-\frac{i}{2}\Delta_R(t-\tau)} \Omega_{g-}(\tau) \tag{A.105b}$$

$$\rho_{+g}^{(1)} =(\rho_{g+}^{(1)})^* \,, \quad \rho_{-g}^{(1)} = (\rho_{g-}^{(1)})^* \tag{A.105c}$$

$$\rho_{++}^{(1)}(t) =0 = \rho_{--}^{(1)}(t) \,, \tag{A.105d}$$

i.e., like in previous nuclear systems considered, only coherences but no populations are created in first order. Finally, the second order reads

$$\hat{\rho}_d^{(2)}(t) = \begin{pmatrix} \rho_{++}^{(2)}(t) & \rho_{+-}^{(2)}(t) & 0 \\ \rho_{-+}^{(2)}(t) & \rho_{--}^{(2)}(t) & 0 \\ 0 & 0 & \rho_{gg}^{(2)}(t) \end{pmatrix} \tag{A.106}$$

with entries

$$\rho_{++}^{(2)}(t) = \int_{t_0}^{t} d\tau e^{-(2\bar{\Gamma}+\mathrm{Im}[\Delta_R])(t-\tau)} \mathrm{Im}\left[\Omega_{g+}(\tau)\rho_{+g}^{(2)}(\tau)\right] \tag{A.107a}$$

$$\rho_{--}^{(2)}(t) = \int_{t_0}^{t} d\tau e^{-(2\bar{\Gamma}-\mathrm{Im}[\Delta_R])(t-\tau)} \mathrm{Im}\left[\Omega_{g-}(\tau)\rho_{-g}^{(2)}(\tau)\right] \tag{A.107b}$$

$$\rho_{+-}^{(2)}(t) =\frac{i}{2}\int_{t_0}^{t} d\tau e^{-2\bar{\Gamma}(t-\tau)} e^{-i\mathrm{Re}[\Delta_R](t-\tau)} \left(\Omega_{g+}^*(\tau)\rho_{g-}^{(1)}(\tau) - \Omega_{g-}(\tau)\rho_{+g}^{(1)}(\tau)\right) \tag{A.107c}$$

$$\rho_{-+}^{(2)}(t) =\frac{i}{2}\int_{t_0}^{t} d\tau e^{-2\bar{\Gamma}(t-\tau)} e^{i\mathrm{Re}[\Delta_R](t-\tau)} \left(\Omega_{g-}^*(\tau)\rho_{g+}^{(1)}(\tau) - \Omega_{g+}(\tau)\rho_{-g}^{(1)}(\tau)\right) \tag{A.107d}$$

$$\rho_{g+}^{(2)}(t) =0 = \rho_{g-}^{(2)}(t) \tag{A.107e}$$

Note, that the second order ground state population can in principle be derived by evaluating the trace condition $\mathrm{Tr}[\hat{\rho}] = 1$ in the dressed state basis. However, as we are interested in the coherences and excited state populations only, an explicit evaluation is not necessary at this point. With this, the density matrix expansion up to second order in the x-ray-nucleus coupling is established and we can proceed to prove the population-coherence correspondences Eq. (A.80) and Eq. (6.27).

A.7.4 Proof of the population-coherence correspondence

The first and second order dressed-state density matrix elements Eqs. (A.105) and (A.107) will now be used to prove Eq. (A.80) Eq. (6.27). To this end, we follow a similar procedure as in the two-level case Sec. 5.3.2 by defining the functions

$$f(t,\tau) = -\frac{i}{2}e^{-\bar{\Gamma}(t-\tau)}e^{i\bar{\delta}(t-\tau)}e^{-\frac{i}{2}\Delta_R(t-\tau)}\Omega_{g-}(\tau) \tag{A.108}$$

$$g(t,\tau) = -\frac{i}{2}e^{-\bar{\Gamma}(t-\tau)}e^{i\bar{\delta}(t-\tau)}e^{\frac{i}{2}\Delta_R(t-\tau)}\Omega_{g+}(\tau) \tag{A.109}$$

such that the dressed state coherences can be expressed as

$$\rho_{g+}^{(1)}(t) = \int_{t_0}^{t} d\tau g(t,\tau) \tag{A.110}$$

$$\rho_{g-}^{(1)}(t) = \int_{t_0}^{t} d\tau f(t,\tau) \tag{A.111}$$

Using the general identities for complex-valued functions already employed in Eqs. (5.21b) and (A.69), one can show

$$\rho_{--}^{(2)}(t) = 2\mathrm{Re}\left[\int_{t_0}^{t} d\tau f^*(\tau)\int_{t_0}^{\tau} d\tau' f(\tau')\right] = \left|\int_{t_0}^{t} d\tau f(\tau)\right|^2 = \left|\rho_{g-}^{(1)}(t)\right|^2 , \tag{A.112}$$

$$\rho_{++}^{(2)}(t) = 2\mathrm{Re}\left[\int_{t_0}^{t} d\tau g^*(\tau)\int_{t_0}^{\tau} d\tau' g(\tau')\right] = \left|\int_{t_0}^{t} d\tau g(\tau)\right|^2 = \left|\rho_{g+}^{(1)}(t)\right|^2 , \tag{A.113}$$

which proves the first two identities of Eq. (A.80). The last identity can be shown by employing the relation Eq. (A.69). Using the definitions above, one immediately finds

$$\int_{t_0}^{t} g^*(t,\tau_2)d\tau_2 \int_{t_0}^{t} f(t,\tau_1)d\tau_1 = \rho_{g+}^{(1)}(t)\rho_{-g}^{(1)}(t) \tag{A.114}$$

and, by direct calculation, one can also verify

$$\rho_{-+}^{(2)}(t) = \int_{t_0}^{t} d\tau_2 g^*(t,\tau_2)\int_{t_0}^{\tau_2} d\tau_1 f(t,\tau_1) + \int_{t_0}^{t} d\tau_2 f(t,\tau_2)\int_{t_0}^{\tau_2} d\tau_1 g^*(t,\tau_1) \tag{A.115}$$

$$= \int_{t_0}^{t} g^*(t,\tau_2)d\tau_2 \int_{t_0}^{t} f(t,\tau_1)d\tau_1 = \rho_{g+}^{(1)}(t)\rho_{-g}^{(1)}(t) \tag{A.116}$$

which proves Eq. (A.80) and together with the equivalence Eq. (A.93) also Eq. (6.27). Since the remaining matrix elements up to second order are zero, this also proves the equivalence of the coherences squared and populations up to second order:

$$\rho_{ll}^{(0-2)}(t) = |\rho_{0l}^{(0-2)}(t)|^2 \tag{A.117}$$

In the following, we will use this interesting result to simplify analytical calculations allowing for an interpretation of numerical studies of the coupling dynamics in effective nuclear three-level systems including excited-state coupling. Beyond this specific use in the scope of this thesis, we envision future research of nonlinear and many-body dynamics of Mössbauer nuclei to benefit from similar analysis approaches even beyond the LER since the dressed-state diagonalization approach of the time-evolution operator $\hat{T}_t$ can also be applied in the nonlinear excitation regime. Further, the generalized dressed-state approach may help to interpret complex phenomena and corresponding NRS spectra like similar approaches in traditional quantum optics [SZ97; MS07].

A.8 Unitary similarity transformations for effective three-level systems

Here, we briefly discuss the condition a matrix Λ, defined in Eq. (A.78), has to satisfy such that a unitary similarity transformation $\hat{A}$, i.e. $\hat{A}^{-1} = \hat{A}^\dagger$ can be found to diagonalize Λ. To this end, the matrix Λ has to be normal, i.e.

$$\left[\Lambda^\dagger \Lambda, \Lambda\Lambda^\dagger\right] = 0\,. \tag{A.118}$$

Explicit calculation yields the following form of the two operator products in the commutator

$$\Lambda\Lambda^\dagger = \begin{pmatrix} \omega_2^2 + \Gamma_2^2 + |\Delta_{12}|^2 & -\Delta_{21}\left[\omega_2 + \omega_1 + i(\Gamma_2 - \Gamma_1)\right] & 0 \\ -\Delta_{12}\left[\omega_2 + \omega_1 + i(\Gamma_1 - \Gamma_2)\right] & \omega_1^2 + \Gamma_1^2 + |\Delta_{12}|^2 & 0 \\ 0 & 0 & 1 \end{pmatrix} \tag{A.119}$$

$$\Lambda^\dagger\Lambda = \begin{pmatrix} \omega_2^2 + \Gamma_2^2 + |\Delta_{12}|^2 & -\Delta_{21}\left[\omega_2 + \omega_1 + i(\Gamma_1 - \Gamma_2)\right] & 0 \\ -\Delta_{12}\left[\omega_2 + \omega_1 + i(\Gamma_2 - \Gamma_1)\right] & \omega_1^2 + \Gamma_1^2 + |\Delta_{12}|^2 & 0 \\ 0 & 0 & 1 \end{pmatrix} \tag{A.120}$$

It can be seen that these two expressions become identical if the two decay rates are the same, i.e. $\Gamma_1 = \Gamma_2$ which is the condition under which the decay matrix $\hat{\Gamma}$ and the nuclear Hamiltonian $\hat{H}_{nuc}$ can be diagonalized simultaneously in the case of neglibible cross-damping terms (cf. Sec. A.7).

A.9 Area theorem

We derive the area theorem for two-level systems and time-dependent Rabi-drives. Assume a two-level system with ground state $|g\rangle$ and excited state $|e\rangle$ and transition frequency ω. The system is driven by a Rabi drive of the form $e^{-i\phi}e^{i\nu t}\Omega(t)$ thus leading to an interaction Hamiltonian

$$\hat{V}(t) = \hbar \begin{pmatrix} \omega & -\frac{1}{2}e^{-i\phi}e^{i\nu t}\Omega(t) \\ -\frac{1}{2}e^{i\phi}e^{-i\nu t}\Omega(t) & 0 \end{pmatrix} \tag{A.121}$$

Transforming into a corotating frame with frequency ν, we get the interaction picture Hamiltonian

$$\hat{H}_I(t) = \hbar \begin{pmatrix} \Delta & -\frac{1}{2}e^{-i\phi}\Omega(t) \\ -\frac{1}{2}e^{i\phi}\Omega(t) & 0 \end{pmatrix} \tag{A.122}$$

with detuning $\Delta = \omega - \nu$ and real-valued envelope $\Omega(t)$. In general, the Schrödinger equation

$$i\hbar\partial_t \left|\psi(t)\right\rangle_I = \hat{H}_I \left|\psi(t)\right\rangle_I \tag{A.123}$$

is not analytically solvable. However, if the detuning Δ between driving pulse and two-level system becomes negligible (either because the drive is resonant with the two-level system or because it is short enough such that the two-level is driven in the impulsive limit) the solution to this equation is given by

$$\left|\psi(t)\right\rangle_I = \hat{U}_I(t, t_0) \left|\psi(t_0)\right\rangle_I \tag{A.124}$$

with the time-evolution operator calculated self-consistently as

$$\begin{aligned} \hat{U}_I(t, t_0) =& I + \sum_{n=1}^{\infty} \left(\frac{i}{2}\right)^n \begin{pmatrix} 0 & e^{-i\phi} \\ e^{i\phi} & 0 \end{pmatrix}^n \int_{t_0}^{t} dt_n \Omega(t_n) \int_{t_0}^{t_n} dt_{n-1}\Omega(t_{n-1}) \cdots \int_{t_0}^{t_2} dt_1 \Omega(t_1) \\ =& I + \sum_{n=1}^{\infty} \frac{i^n}{n!} \sigma_\phi^n \left(\frac{1}{2}\mathcal{A}(t)\right)^n \end{aligned} \tag{A.125}$$

where we defined the pulse area $\mathcal{A}(t)$ as

$$\mathcal{A}(t) = \int_{t_0}^{t} \Omega(t')dt' \tag{A.126}$$

and used the identity for real-valued functions f

$$\frac{1}{n!}\int_{t_0}^{t} dt' f(t')\Big[\int_{t_0}^{t'} dt'' f(t'')\Big]^n = \frac{1}{(n+1)!}\Big[\int_{t_0}^{t} dt' f(t')\Big]^{n+1} \tag{A.127}$$

to simplify the nested integrals. Further, we introduced the matrix $\sigma_\phi = \begin{pmatrix} 0 & e^{-i\phi} \\ e^{i\phi} & 0 \end{pmatrix}$. Using that

$$\sigma_\phi^n = \begin{cases} I \ , & n \in 2\mathbb{Z} \\ \sigma_\phi \ , & \text{else} \end{cases} \tag{A.128}$$

the time-evolution operator splits up into

$$\begin{aligned} \hat{U}_I(t,t_0) =& I\sum_{n=0}^{\infty} \frac{(-1)^n}{(2n)!}\left[\frac{1}{2}\mathcal{A}(t)\right]^{2n} + i\sigma_\phi \sum_{n=0}^{\infty} \frac{(-1)^n}{(2n+1)!}\left[\frac{1}{2}\mathcal{A}(t)\right]^{2n+1} \\ =& \begin{pmatrix} \cos\big(\frac{1}{2}\mathcal{A}(t)\big) & ie^{-i\phi}\sin\big(\frac{1}{2}\mathcal{A}(t)\big) \\ ie^{i\phi}\sin\big(\frac{1}{2}\mathcal{A}(t)\big) & \cos\big(\frac{1}{2}\mathcal{A}(t)\big) \end{pmatrix} \end{aligned} \tag{A.129}$$

The key feature of this solution is that the dynamics are essentially independent of the shape of the pulse envelope $\Omega(t)$ but only depend on its integrated value from initial time t_0 until time t. Note that the pulse area $\mathcal{A}$ can be interpreted as the polar angle on the Bloch sphere while ϕ is related to the azimuthal angle. This can be seen by calculating the state of a two-level system, being in its ground state $|g\rangle = \begin{pmatrix} 0 \\ 1 \end{pmatrix}$ initially, under the action of the time evolution operator $\hat{U}(t,t_0)$ which yields

$$\hat{U}_I(t,t_0)\,|g\rangle = ie^{-i\phi}\sin\bigg(\frac{1}{2}\mathcal{A}\bigg)\,|e\rangle + \cos\bigg(\frac{1}{2}\mathcal{A}\bigg)\,|g\rangle \tag{A.130}$$

where we introduced the notation $|e\rangle = \begin{pmatrix} 1 \\ 0 \end{pmatrix}$, similarly to the ground state $|g\rangle$. Comparison whith the polar form of the Bloch representation of state $|\psi\rangle$

$$|\psi\rangle = e^{i\varphi}\sin(\theta/2)\,|e\rangle + \cos(\theta/2)\,|g\rangle \tag{A.131}$$

where θ defines the polar angle and φ the azimuthal angle shows that the pulse area $\mathcal{A}$ corresponds to the polar angle of excitation from the ground state towards the excited state that is covered during the interaction period of the Rabi frequency $\Omega(t)$. The phase ϕ and the system's free unitary time evolution, on the other hand, correspond to drifts along the azimuthal direction.

The density matrix of a two-level system initially in state

$$\rho(t_0) = \begin{pmatrix} \rho_{ee} & \rho_{eg} \\ \rho_{ge} & \rho_{gg} \end{pmatrix} \tag{A.132}$$

after application of a resonant pulse with pulse area $\mathcal{A}(t)$ in the interaction picture can be written as

$$\hat{\rho}_I(t) =\hat{U}_I(t,t_0)\hat{\rho}(t_0)\hat{U}_I^\dagger(t,t_0) = \begin{pmatrix} \rho_{ee}^I(t) & \rho_{eg}^I(t) \\ \rho_{ge}^I(t) & \rho_{gg}^I(t) \end{pmatrix} \tag{A.133}$$

with

$$\rho^I_{ee}(t) = \rho_{ee}\cos^2\frac{1}{2}\mathcal{A} + \rho_{gg}\sin^2\frac{1}{2}\mathcal{A} + i\sin\frac{1}{2}\mathcal{A}\cos\frac{1}{2}\mathcal{A}(e^{-i\phi}\rho_{ge} - e^{i\phi}\rho_{eg}) \tag{A.134}$$

$$\rho^I_{eg}(t) = \rho_{eg}\cos^2\frac{1}{2}\mathcal{A} + e^{-2i\phi}\rho_{ge}\sin^2\frac{1}{2}\mathcal{A} + ie^{-i\phi}\sin\frac{1}{2}\mathcal{A}\cos\frac{1}{2}\mathcal{A}(\rho_{gg} - \rho_{ee}) \tag{A.135}$$

$$\rho^I_{ge}(t) = \rho_{ge}\cos^2\frac{1}{2}\mathcal{A} + e^{2i\phi}\rho_{eg}\sin^2\frac{1}{2}\mathcal{A} + ie^{i\phi}\sin\frac{1}{2}\mathcal{A}\cos\frac{1}{2}\mathcal{A}(\rho_{ee} - \rho_{gg}) \tag{A.136}$$

$$\rho^I_{gg}(t) = \rho_{ee}\sin^2\frac{1}{2}\mathcal{A} + \rho_{gg}\cos^2\frac{1}{2}\mathcal{A} + i\sin\frac{1}{2}\mathcal{A}\cos\frac{1}{2}\mathcal{A}(e^{i\phi}\rho_{eg} - e^{-i\phi}\rho_{ge}) \tag{A.137}$$

For later use in ch. 5 we also write down the result for the coherence and excited state population if the two-level system is initially in its ground state

$$\rho_{ee} = 0\,, \quad \rho_{ge} = 0 = \rho_{eg}\,, \quad \rho_{gg} = 1 \tag{A.138}$$

such that

$$\rho^I_{ee}(t) = \sin^2\left(\frac{1}{2}\mathcal{A}(t)\right) \tag{A.139}$$

$$\rho^I_{ge}(t) = -\frac{i}{2}e^{i\phi}\sin(\mathcal{A}(t)) \tag{A.140}$$

Note, that the angular rotation covered by the coherence at time t is twice the angle of the population at the same time instance. In contrast to the constant-envelope case, however, this does not imply that local maxima of the coherence can be found exactly at twice the time of corresponding maxima since the pulse area is the (time-dependent) Rabi frequency integrated over time and thus subject to temporal changes in the pulse envelope as discussed, e.g. in Sec. 5.5.6.

A.10 Optical Bloch equations of two-level systems

For reference in the main text, here we state the optical Bloch equations for a single two-level atom, that can be derived from the Liouvillian

$$\frac{d}{dt}\hat{\rho} = \frac{1}{i\hbar}\left[\hat{H}, \hat{\rho}\right] + \mathcal{L}[\hat{\rho}]\,, \tag{A.141}$$

with

$$\hat{H} = \hat{H}_{\text{nuc}} + \hat{W}(t)\,. \tag{A.142}$$

Here, the nuclear Hamiltonian is given by

$$\hat{H}_{nuc} = \hbar\omega_0 \left|e\right\rangle \left\langle e\right|\,, \tag{A.143}$$

and the interaction part by

$$\hat{W}(t) = -\frac{\hbar}{2}\left(\Omega(t)\hat{\sigma}^+ + h.c.\right)\,. \tag{A.144}$$

The Linbladian of a two-level system reads

$$\mathcal{L}\left[\hat{\rho}\right] = \frac{\gamma}{2}\left(2\hat{\sigma}^-\hat{\rho}\hat{\sigma}^+ - \left\{\hat{\sigma}^+\hat{\sigma}^-, \hat{\rho}\right\}\right)\,, \tag{A.145}$$

By projection onto the ground and excited states $|g\rangle$ and $|e\rangle$ and defining the excited state population $\rho_{ee} = \langle e|\, \hat{\rho}\, |e\rangle$ and the coherence $\rho_{ge} = \langle g|\, \hat{\rho}\, |e\rangle$, the result reads

$$\dot{\rho}_{ee} = -\gamma\rho_{ee} + \frac{i}{2}\left[\Omega(t)\rho_{ge} - \Omega^*(t)\rho_{eg}\right] \,, \tag{A.146a}$$

$$\dot{\rho}_{ge} = \big(i\omega_0 - \frac{\gamma}{2}\big)\rho_{ge} + \frac{i\Omega^*(t)}{2}\left(2\rho_{ee} - 1\right) \,, \tag{A.146b}$$

$$\rho_{eg} = \rho_{ge}^* \,, \qquad \rho_{gg} = 1 - \rho_{ee} \,, \tag{A.146c}$$

where γ is the total natural linewidth. Note that the same equations of motion govern the dynamics of effective two-level systems in the low-excitation sector of nuclear resonant scattering, however, with collectively modified parameters ω_0, γ and $\Omega(t)$.

Bibliography

[ABE76] W P Aue, E Bartholdi, and R R Ernst. “Two-dimensional spectroscopy. Application to nuclear magnetic resonance”. In: *J. Chem. Phys.* 64.5 (Mar. 1976), pp. 2229–2246.

[Ada+13a] Bernhard W. Adams et al. “X-ray quantum optics”. In: *Journal of Modern Optics* 60.1 (Jan. 2013), pp. 2–21. DOI: `10.1080/09500340.2012.752113`.

[Ada+13b] Bernhard W. Adams et al. “X-ray quantum optics”. In: *Journal of Modern Optics* 60.1 (2013), pp. 2–21. DOI: `10.1080/09500340.2012.752113`.

[Ada+19a] Bernhard Adams et al. “Scientific opportunities with an X-ray free-electron laser oscillator”. In: (2019). DOI: `10.48550/arXiv.1903.09317`.

[Ada+19b] Bernhard Adams et al. *Scientific Opportunities with an X-ray Free-Electron Laser Oscillator*. 2019. arXiv: `1903.09317 [physics.ins-det]`.

[ADR82] Alain Aspect, Jean Dalibard, and Gérard Roger. “Experimental Test of Bell’s Inequalities Using Time-Varying Analyzers”. In: *Phys. Rev. Lett.* 49 (25 1982), pp. 1804–1807. DOI: `10.1103/PhysRevLett.49.1804`.

[AE75] L. Allen and J.H. Eberly. *Optical Resonance and Two-Level Atoms*. New York: Dover Publications INC., 1975.

[AG+17] A. Asenjo-Garcia et al. “Exponential Improvement in Photon Storage Fidelities Using Subradiance and “Selective Radiance” in Atomic Arrays”. In: *Phys. Rev. X* 7 (3 2017), p. 031024. DOI: `10.1103/PhysRevX.7.031024`.

[Aga74] G. S. Agarwal. “Quantum statistical theories of spontaneous emission and their relation to other approaches”. In: *Quantum Optics*. Ed. by G. Höhler. Berlin, Heidelberg: Springer Berlin Heidelberg, 1974, pp. 1–128. DOI: `10.1007/BFb0042382`.

[AKH66] I. D. Abella, N. A. Kurnit, and S. R. Hartmann. “Photon Echoes”. In: *Phys. Rev.* 141 (1 1966), pp. 391–406. DOI: `10.1103/PhysRev.141.391`.

[Alp+03] E. E. Alp et al. “Vibrational Dynamics Studies by Nuclear Resonant Inelastic X-Ray Scattering”. In: *Mössbauer Spectroscopy*. Ed. by P. Gütlich et al. Dordrecht: Springer Netherlands, 2003, pp. 3–20.

[AM22] Neil W Ashcroft and N David Mermin. *Solid state physics*. Cengage Learning, 2022.

[Ama+12] J. Amann et al. “Demonstration of self-seeding in a hard-X-ray free-electron laser”. In: 6 (2012), pp. 693–698. DOI: `10.1038/nphoton.2012.180`.

[Ani10] Vladimir Il’ich Anisimov. “Electronic structure of strongly correlated materials”. In: *AIP Conference Proceedings*. Vol. 1297. 1. American Institute of Physics. 2010, pp. 3–134.

[ANM11] Jens Als-Nielsen and Des McMorrow. *Elements of Modern X-ray Physics*. Chichester, UK: John Wiley & Sons, Ltd, 2011.

[Asp23] Alain Aspect. *The Second Quantum Revolution: From Basic Concepts to Quantum Technologies*. May 2023. DOI: `10.1002/9783527837427.ch2`.

[Aue98] Assa Auerbach. *Interacting electrons and quantum magnetism*. Springer Science & Business Media, 1998.

[B9̈9] U. van Bürck. In: *Hyperfine Interactions* 123/124.1/4 (1999), pp. 483–509. DOI: `10.1023/a:1017080008712`.

[Bar+96] A. Q. R. Baron et al. “Single-nucleus quantum beats excited by synchrotron radiation”. In: *Europhysics Letters* 34.5 (1996), p. 331. DOI: `10.1209/epl/i1996-00460-0`.

[BB20] Robert Bennett and Stefan Yoshi Buhmann. “Inverse design of light–matter interactions in macroscopic QED”. In: *New Journal of Physics* 22.9 (2020), p. 093014. DOI: `10.1088/1367-2630/abac3a`.

[Ber+86] J. C. Bergquist et al. “Observation of Quantum Jumps in a Single Atom”. In: *Phys. Rev. Lett.* 57 (14 1986), pp. 1699–1702. DOI: `10.1103/PhysRevLett.57.1699`.

[BEW05] Donald H Bilderback, Pascal Elleaume, and Edgar Weckert. “Review of third and next generation synchrotron light sources”. In: *Journal of Physics B: Atomic, Molecular and Optical Physics* 38.9 (2005), S773–S797. DOI: `10.1088/0953-4075/38/9/022`.

[BHS94] U. Bergmann, J. B. Hastings, and D. P. Siddons. “Time evolution of incoherent nuclear scattering from ^{57}Fe excited with synchrotron radiation”. In: *Phys. Rev. B* 49 (2 1994), pp. 1513–1516. DOI: `10.1103/PhysRevB.49.1513`.

[BJ89] Brian Harold Bransden and Charles Jean Joachain. “Introduction to quantum mechanics”. In: (1989).

[Boc+21] Lars Bocklage et al. “Coherent control of collective nuclear quantum states via transient magnons”. In: *Sci. Adv.* 7.5 (Jan. 2021), eabc3991. DOI: `10.1126/sciadv.abc3991`.

[Bor+84] Ch J Bordé et al. “Optical Ramsey fringes with traveling waves”. In: *Physical Review A* 30.4 (1984), p. 1836.

[BP08] R.W. Boyd and D. Prato. *Nonlinear Optics*. Elsevier Science, 2008.

[BPW98] Wim P de Boeij, Maxim S Pshenichnikov, and Douwe A Wiersma. “Ultrafast solvation dynamics explored by femtosecond photon echo spectroscopies”. In: *Annual review of physical chemistry* 49.1 (1998), pp. 99–123.

[Bro+16] S. L. Bromley et al. “Collective atomic scattering and motional effects in a dense coherent medium”. In: *Nat Commun* 7.1 (Apr. 2016), p. 11039. DOI: `10.1038/ncomms11039`.

[Bru+96] M. Brune et al. “Quantum Rabi Oscillation: A Direct Test of Field Quantization in a Cavity”. In: *Phys. Rev. Lett.* 76 (11 1996), pp. 1800–1803. DOI: `10.1103/PhysRevLett.76.1800`.

[BS97] George C. Baldwin and Johndale C. Solem. “Recoilless gamma-ray lasers”. In: *Rev. Mod. Phys.* 69 (4 1997), pp. 1085–1118. DOI: `10.1103/RevModPhys.69.1085`.

[BT54] R. Hanbury Brown and R.Q. Twiss. “LXXIV. A new type of interferometer for use in radio astronomy”. In: *The London, Edinburgh, and Dublin Philosophical Magazine and Journal of Science* 45.366 (1954), pp. 663–682. DOI: `10.1080/14786440708520475`. eprint: `https://doi.org/10.1080/14786440708520475`.

[BW07] Stefan Yoshi Buhmann and Dirk-Gunnar Welsch. “Dispersion forces in macroscopic quantum electrodynamics”. In: *Progress in Quantum Electronics* 31.2 (2007), pp. 51 –130. DOI: `https://doi.org/10.1016/j.pquantelec.2007.03.001`.

[Cal+02] R. Callens et al. “Stroboscopic detection of nuclear forward-scattered synchrotron radiation”. In: *Phys. Rev. B* 65 (18 2002), 180404(R). DOI: `10.1103/PhysRevB.65.180404`.

[Cal+03] R. Callens et al. “Principles of stroboscopic detection of nuclear forward-scattered synchrotron radiation”. In: *Phys. Rev. B* 67 (10 2003), p. 104423. DOI: `10.1103/PhysRevB.67.104423`.

[Cal+05] R. Callens et al. “Phase determination in nuclear resonant scattering using a velocity drive as an interferometer and phase shifter”. In: *Phys. Rev. B* 72 (8 2005), p. 081402. DOI: `10.1103/PhysRevB.72.081402`.

[CCL96] R. Coussement, S. Cottenier, and C. L’abbé. “Time-integrated nuclear resonant forward scattering of synchrotron radiation”. In: *Phys. Rev. B* 54 (22 1996), pp. 16003–16009. DOI: `10.1103/PhysRevB.54.16003`.

[CE19] Salvatore Castrignano and Jörg Evers. “Probing Quantum Dynamical Couple Correlations with Time-Domain Interferometry”. In: *Phys. Rev. Lett.* 122 (2 2019), p. 025301. DOI: `10.1103/PhysRevLett.122.025301`.

[Che+22] Yu-Hsueh Chen et al. “Transient nuclear inversion by x-ray free electron laser in a tapered x-ray waveguide”. In: *Phys. Rev. Research* 4 (3 2022), p. L032007. DOI: `10.1103/PhysRevResearch.4.L032007`.

[Cho08] Minhaeng Cho. “Coherent two-dimensional optical spectroscopy”. In: *Chem. Rev.* 108.4 (Apr. 2008), pp. 1331–1418. DOI: `10.1021/cr078377b`.

[Cho19] Minhaeng Cho, ed. *Coherent Multidimensional Spectroscopy*. 1st ed. Springer series in optical sciences. Singapore, Singapore: Springer, Aug. 2019. DOI: `10.1007/978-981-13-9753-0`.

[Chu+18] Aleksandr I. Chumakov et al. “Superradiance of an ensemble of nuclei excited by a free electron laser”. In: *Nature Phys* 14.3 (Mar. 2018), pp. 261–264. DOI: 10.1038/s41567-017-0001-z.

[Chu+86] Steven Chu et al. “Experimental Observation of Optically Trapped Atoms”. In: *Phys. Rev. Lett.* 57 (3 1986), pp. 314–317. DOI: 10.1103/PhysRevLett.57.314.

[Chu+97] A. I. Chumakov et al. “Radiation trapping in nuclear resonant scattering of x rays”. In: *Phys. Rev. B* 56 (14 1997), R8455–R8458. DOI: 10.1103/PhysRevB.56.R8455.

[Cla+69] John F. Clauser et al. “Proposed Experiment to Test Local Hidden-Variable Theories”. In: *Phys. Rev. Lett.* 23 (15 1969), pp. 880–884. DOI: 10.1103/PhysRevLett.23.880.

[CT77] C. Cohen-Tannoudji. “Atoms in strong resonant fields”. In: *Frontiers in Laser Spectroscopy (Les Houches XXVII 1975).* Ed. by Balian R., Haroche S., and Liberman S. Amsterdam: North Holland, 1977, p. 3.

[Deá+06] L. Deák et al. “Synchrotron Mössbauer reflectometry using stroboscopic detection”. In: *Hyperfine Interactions* 167.1 (2006), pp. 709–715. DOI: 10.1007/s10751-006-9479-y.

[Dec+20] W. Decking et al. “A MHz-repetition-rate hard X-ray free-electron laser driven by a superconducting linear accelerator”. In: 14 (2020), pp. 391–397. DOI: 10.1038/s41566-020-0607-z.

[DGK08] Frank De Groot and Akio Kotani. *Core level spectroscopy of solids.* CRC press, 2008.

[Dic54] R. H. Dicke. “Coherence in Spontaneous Radiation Processes”. In: *Phys. Rev.* 93.1 (Jan. 1954), pp. 99–110. DOI: 10.1103/PhysRev.93.99.

[DKW02] Ho Trung Dung, Ludwig Knöll, and Dirk-Gunnar Welsch. “Resonant dipole-dipole interaction in the presence of dispersing and absorbing surroundings”. In: *Phys. Rev. A* 66 (6 2002), p. 063810. DOI: 10.1103/PhysRevA.66.063810.

[DLE22a] O. Diekmann, D. Lentrodt, and J. Evers. “Inverse design in nuclear quantum optics: From artificial x-ray multi-level schemes to spectral observables”. In: *arXiv:2205.06586 [quant-ph]* (2022).

[DLE22b] Oliver Diekmann, Dominik Lentrodt, and Jörg Evers. “Inverse design approach to x-ray quantum optics with Mössbauer nuclei in thin-film cavities”. In: *Phys. Rev. A* 105 (1 2022), p. 013715. DOI: 10.1103/PhysRevA.105.013715.

[DLE22c] Oliver Diekmann, Dominik Lentrodt, and Jörg Evers. “Inverse design in nuclear quantum optics: From artificial x-ray multilevel schemes to spectral observables”. In: *Phys. Rev. A* 106 (5 2022), p. 053701. DOI: 10.1103/PhysRevA.106.053701.

[Emm+10] P. Emma et al. “First lasing and operation of an Angstrom-wavelength free-electron laser”. In: 4 (2010), pp. 641–647.

[Eng07] S Engelberg. *Random Signals and Noise.* CRC Press, 2007.

[Ern92] Richard R Ernst. “Nuclear magnetic resonance Fourier transform spectroscopy (Nobel lecture)”. In: *Angewandte Chemie International Edition in English* 31.7 (1992), pp. 805–823.

[FC72] Stuart J. Freedman and John F. Clauser. “Experimental Test of Local Hidden-Variable Theories”. In: *Phys. Rev. Lett.* 28 (14 1972), pp. 938–941. DOI: 10.1103/PhysRevLett.28.938.

[FHM73] R. Friedberg, S.R. Hartmann, and J.T. Manassah. “Frequency shifts in emission and absorption by resonant systems ot two-level atoms”. In: *Physics Reports* 7.3 (Mar. 1973), pp. 101–179. DOI: 10.1016/0370-1573(73)90001-X.

[FIM05] Michael Fleischhauer, Atac Imamoglu, and Jonathan P. Marangos. “Electromagnetically induced transparency: Optics in coherent media”. In: *Rev. Mod. Phys.* 77.2 (July 2005), pp. 633–673. DOI: 10.1103/RevModPhys.77.633.

[Fr91] D. Fröhlich et al. “Coherent propagation and quantum beats of quadrupole polaritons in Cu_2O”. In: *Phys. Rev. Lett.* 67 (17 1991), pp. 2343–2346. DOI: 10.1103/PhysRevLett.67.2343.

[Fro+85] J. C. Frost et al. “Surface sensitive Mössbauer spectroscopy by the combination of total external reflection and conversion electron detection”. In: *Applied Physics Letters* 47.6 (Sept. 1985), pp. 581–583. DOI: `10.1063/1.96078`. eprint: `https://pubs.aip.org/aip/apl/article-pdf/47/6/581/7757005/581\_1\_online.pdf`.

[Fry+08] J. Frydrych et al. “Conversion Electron Detectors for 57Fe Mössbauer Measurements”. In: *AIP Conference Proceedings* 1070.1 (Oct. 2008), pp. 170–184. DOI: `10.1063/1.3030842`. eprint: `https://pubs.aip.org/aip/acp/article-pdf/1070/1/170/11873803/170\_1\_online.pdf`.

[FS05] Z. Ficek and S. Swain. *Quantum interference and coherence: theory and experiments*. Springer series in optical sciences. Heidelberg: Springer, 2005.

[Fus08] Mizuho Fushitani. “Applications of pump-probe spectroscopy”. In: *Annual Reports Section" C"(Physical Chemistry)* 104 (2008), pp. 272–297.

[Gar11] Barry M. Garraway. “The Dicke model in quantum optics: Dicke model revisited”. In: *Phil. Trans. R. Soc. A.* 369.1939 (Mar. 2011), pp. 1137–1155. DOI: `10.1098/rsta.2010.0333`.

[Ger19] Miriam Lena Gerharz. *Dynamical polarization control in X-ray quantum optics*. 2019.

[Ger21] Miriam Gerharz. “Temporal phase and polarization interferometry at x-ray energies: Reconstruction of phase-related observables and temporal pulse shaping”. MA thesis. Ruprecht-Karls-Universität Heidelberg, 2021.

[Ger+85a] E. Gerdau et al. “Nuclear Bragg diffraction of synchrotron radiation in yttrium iron garnet”. In: *Phys. Rev. Lett.* 54 (8 1985), pp. 835–838. DOI: `10.1103/PhysRevLett.54.835`.

[Ger+85b] E. Gerdau et al. “Nuclear Bragg diffraction of synchrotron radiation in yttrium iron garnet”. In: *Physical Review Letters* 54.8 (Feb. 1985), pp. 835–838. DOI: `10.1103/PhysRevLett.54.835`.

[GH82] M. Gross and S. Haroche. “Superradiance: An essay on the theory of collective spontaneous emission”. In: *Physics Reports* 93.5 (Dec. 1982), pp. 301–396. DOI: `10.1016/0370-1573(82)90102-8`.

[Gla06] Roy J. Glauber. “Nobel Lecture: One hundred years of light quanta”. In: *Rev. Mod. Phys.* 78 (4 2006), pp. 1267–1278. DOI: `10.1103/RevModPhys.78.1267`.

[Gla63] Roy J. Glauber. “The Quantum Theory of Optical Coherence”. In: *Phys. Rev.* 130 (6 1963), pp. 2529–2539. DOI: `10.1103/PhysRev.130.2529`.

[Goe+19] Stephan Goerttler et al. “Time-resolved sub-Ångström metrology by temporal phase interferometry near X-ray resonances of nuclei”. In: *Phys. Rev. Lett.* 123.15 (Oct. 2019), p. 153902. DOI: `10.1103/PhysRevLett.123.153902`.

[GRK17] W. Guerin, M.T. Rouabah, and R. Kaiser. “Light interacting with atomic ensembles: collective, cooperative and mesoscopic effects”. In: *Journal of Modern Optics* 64.9 (May 2017), pp. 895–907. DOI: `10.1080/09500340.2016.1215564`.

[GS22] Walther Gerlach and Otto Stern. “Der experimentelle Nachweis der Richtungsquantelung im Magnetfeld”. In: *Zeitschrift fuer Physik* 9.1 (Dec. 1922), pp. 349–352. DOI: `10.1007/bf01326983`.

[GW96] T. Gruner and D.-G. Welsch. “Green-function approach to the radiation-field quantization for homogeneous and inhomogeneous Kramers-Kronig dielectrics”. In: *Phys. Rev. A* 53 (3 1996), pp. 1818–1829. DOI: `10.1103/PhysRevA.53.1818`.

[GW99] “Nuclear resonant scattering of synchrotron radiation”. In: *Hyperfine Interact.* 123-125 (1999/2000). Ed. by E Gerdau and H de Waard.

[Hab+16] Johann Haber et al. “Collective strong coupling of X-rays and nuclei in a nuclear optical lattice”. In: *Nature Photonics* 10.7 (July 2016), pp. 445–449. DOI: `10.1038/nphoton.2016.77`.

[Hab+17] Johann Haber et al. “Rabi oscillations of X-ray radiation between two nuclear ensembles”. In: *Nature Photonics* 11.11 (2017), pp. 720–725. DOI: `10.1038/s41566-017-0013-3`.

[Has+91] J. B. Hastings et al. “Mössbauer spectroscopy using synchrotron radiation”. In: *Phys. Rev. Lett.* 66 (6 1991), pp. 770–773. DOI: `10.1103/PhysRevLett.66.770`.

[HE13] Kilian P Heeg and Jörg Evers. “X-ray quantum optics with Mössbauer nuclei embedded in thin-film cavities”. In: *Phys. Rev. A* 88.4 (Oct. 2013), p. 043828. doi: 10.1103/PhysRevA.88.043828.

[HE15a] Kilian P. Heeg and Jörg Evers. “Collective effects between multiple nuclear ensembles in an x-ray cavity-QED setup”. In: *Phys. Rev. A* 91 (6 2015), p. 063803. doi: 10.1103/PhysRevA.91.063803.

[HE15b] Kilian P. Heeg and Jörg Evers. “Collective effects between multiple nuclear ensembles in an x-ray cavity-QED setup”. In: *Phys. Rev. A* 91 (6 2015), p. 063803. doi: 10.1103/PhysRevA.91.063803.

[HE20] Benedikt Herkommer and Jörg Evers. “Phase-sensitive nuclear target spectroscopy”. In: *Phys. Rev. Research* 2 (2 2020), p. 023397. doi: 10.1103/PhysRevResearch.2.023397.

[Hee+13] Kilian P. Heeg et al. “Vacuum-Assisted Generation and Control of Atomic Coherences at X-Ray Energies”. In: *Phys. Rev. Lett.* 111 (7 2013), p. 073601. doi: 10.1103/PhysRevLett.111.073601.

[Hee14a] K. P. Heeg. “X-Ray Quantum Optics With Mößbauer Nuclei In Thin-Film Cavities”. PhD thesis. Heidelberg University, 2014. doi: 10.11588/heidok.00017869.

[Hee14b] Kilian Peter Heeg. “X-Ray quantum optics with Mössbauer nuclei in thin-film cavities”. PhD thesis. 2014.

[Hee+15a] K P Heeg et al. “Interferometric phase detection at x-ray energies via Fano resonance control”. In: *Phys. Rev. Lett.* 114.20 (May 2015), p. 207401. doi: 10.1103/PhysRevLett.114.207401.

[Hee+15b] K. P. Heeg et al. “Interferometric phase detection at x-ray energies via Fano resonance control”. In: *Phys. Rev. Lett.* 114 (20 2015), p. 207401. doi: 10.1103/PhysRevLett.114.207401.

[Hee+15c] Kilian P Heeg et al. “Tunable subluminal propagation of narrow-band X-ray pulses”. In: *Phys. Rev. Lett.* 114.20 (May 2015), p. 203601. doi: 10.1103/PhysRevLett.114.203601.

[Hee+17] K P Heeg et al. “Spectral narrowing of x-ray pulses for precision spectroscopy with nuclear resonances”. In: *Science* 357.6349 (July 2017), pp. 375–378. doi: 10.1126/science.aan3512.

[Hee19] K P Heeg. *Software Package* pynuss. unpublished. 2019.

[Hee+21] Kilian P Heeg et al. “Coherent X-ray-optical control of nuclear excitons”. In: *Nature* 590.7846 (Feb. 2021), pp. 401–404. doi: 10.1038/s41586-021-03276-x.

[Hee+22] Kilian P. Heeg et al. “Reply to: On yoctosecond science”. In: *Nature* 608.7922 (2022), E18–E19. doi: 10.1038/s41586-022-04871-2.

[Hel+91] P. Helistö et al. “Gamma echo”. In: *Phys. Rev. Lett.* 66 (15 1991), pp. 2037–2040. doi: 10.1103/PhysRevLett.66.2037.

[HKE16a] K. P. Heeg, C. H. Keitel, and J. Evers. “Inducing and detecting collective population inversions of Mössbauer nuclei”. In: *arXiv:1607.04116 [quant-ph]* (2016).

[HKE16b] K. P. Heeg, C. H. Keitel, and J. Evers. “Inducing and detecting collective population inversions of Mössbauer nuclei”. In: *arXiv:1607.04116 [quant-ph]* (2016).

[Hol+00] R. Holzwarth et al. “Optical Frequency Synthesizer for Precision Spectroscopy”. In: *Phys. Rev. Lett.* 85 (11 2000), pp. 2264–2267. doi: 10.1103/PhysRevLett.85.2264.

[HT99a] J Hannon and G Trammell. “Coherent γ-ray optics”. In: *Hyperfine Interact.* 123 (1999), pp. 127–274. doi: 10.1023/A:1017011621007.

[HT99b] J. P. Hannon and G. T. Trammell. “Coherent γ-ray optics”. In: *Hyperfine Interactions* 123.1 (1999), pp. 127–274. doi: 10.1023/A:1017011621007.

[HZ11] Peter Hamm and Martin Zanni. *Concepts and methods of 2D infrared spectroscopy.* Cambridge, England: Cambridge University Press, Aug. 2011. doi: 10.1017/CBO9780511675935.

[Ino+19] Ichiro Inoue et al. “Generation of narrow-band X-ray free-electron laser via reflection self-seeding”. In: 13 (2019), pp. 1749–4893. doi: 10.1038/s41566-019-0365-y.

[Ish+12] Tetsuya Ishikawa et al. “A compact X-ray free-electron laser emitting in the sub-Angström region”. In: 6 (2012), pp. 540–544. doi: 10.1038/nphoton.2012.141.

[Jae+16] Eberhard J Jaeschke et al., eds. *Synchrotron light sources and free-electron lasers*. 1st ed. Synchrotron Light Sources and Free-Electron Lasers. Cham, Switzerland: Springer International Publishing, Apr. 2016. DOI: `10.1007/978-3-319-14394-1`.

[Jam58] Reginald William James. *The Optical Principles of the Diffraction of X-rays*. London: G. Bell and Sons, 1958.

[Jia15] Hong Jiang. "First-principles approaches for strongly correlated materials: A theoretical chemistry perspective". In: *International Journal of Quantum Chemistry* 115.11 (2015), pp. 722–730.

[JNN12] J.R. Johansson, P.D. Nation, and Franco Nori. "QuTiP: An open-source Python framework for the dynamics of open quantum systems". In: *Computer Physics Communications* 183.8 (2012), pp. 1760–1772. DOI: `https://doi.org/10.1016/j.cpc.2012.02.021`.

[JNN13] J.R. Johansson, P.D. Nation, and Franco Nori. "QuTiP 2: A Python framework for the dynamics of open quantum systems". In: *Computer Physics Communications* 184.4 (2013), pp. 1234–1240. DOI: `https://doi.org/10.1016/j.cpc.2012.11.019`.

[Joa75] C. J. Joachain. *Quantum collision theory*. Netherlands: North-Holland, 1975.

[Jon+00] David J. Jones et al. "Carrier-Envelope Phase Control of Femtosecond Mode-Locked Lasers and Direct Optical Frequency Synthesis". In: *Science* 288.5466 (Apr. 2000), pp. 635–639. DOI: `10.1126/science.288.5466.635`.

[Kag99] Yu. Kagan. In: *Hyperfine Interactions* 123/124.1/4 (1999), pp. 83–126. DOI: `10.1023/a:1017059504169`.

[KAH64] NA Kurnit, ID Abella, and SR Hartmann. "Observation of a photon echo". In: *Physical Review Letters* 13.19 (1964), p. 567.

[KAK79] Yu Kagan, A M Afanas'ev, and V G Kohn. "On excitation of isomeric nuclear states in a crystal by synchrotron radiation". In: *J. Phys. C: Solid State Phys.* 12.3 (Feb. 1979), pp. 615–631. DOI: `10.1088/0022-3719/12/3/027`.

[KCP20a] Xiangjin Kong, Darrick E. Chang, and Adriana Pálffy. "Green's-function formalism for resonant interaction of x rays with nuclei in structured media". In: *Phys. Rev. A* 102.3 (Sept. 2020), p. 033710. DOI: `10.1103/PhysRevA.102.033710`.

[KCP20b] Xiangjin Kong, Darrick E. Chang, and Adriana Pálffy. "Green's-function formalism for resonant interaction of x rays with nuclei in structured media". In: *Phys. Rev. A* 102 (3 2020), p. 033710. DOI: `10.1103/PhysRevA.102.033710`.

[Kea+12] J. Keaveney et al. "Cooperative Lamb Shift in an Atomic Vapor Layer of Nanometer Thickness". In: *Phys. Rev. Lett.* 108.17 (Apr. 2012), p. 173601. DOI: `10.1103/PhysRevLett.108.173601`.

[Kif+10] Martin Kiffner et al. "Vacuum-induced processes in multi-level atoms". In: *Progress in Optics*. Vol. 55. Burlington: Elsevier Science, 2010, pp. 85–197.

[KK12] G. Kalvius and P. Kienle, eds. Berlin, Heidelberg: Springer-Verlag, 2012.

[KK17a] Elena Kuznetsova and Olga Kocharovskaya. "Quantum optics with X-rays". In: *Nature Photonics* 11.11 (Oct. 2017), pp. 685–686. DOI: `10.1038/s41566-017-0034-y`.

[KK17b] Elena Kuznetsova and Olga Kocharovskaya. "Quantum optics with X-rays". In: *Nature Photonics* 11.11 (Nov. 2017), pp. 685–686. DOI: `10.1038/s41566-017-0034-y`.

[KKR99] Olga Kocharovskaya, Roman Kolesov, and Yuri Rostovtsev. "Coherent Optical Control of Mössbauer Spectra". In: *Phys. Rev. Lett.* 82 (18 1999), pp. 3593–3596. DOI: `10.1103/PhysRevLett.82.3593`.

[KSR08] Kwang-Je Kim, Yuri Shvyd'ko, and Sven Reiche. "A Proposal for an X-Ray Free-Electron Laser Oscillator with an Energy-Recovery Linac". In: *Phys. Rev. Lett.* 100 (24 2008), p. 244802. DOI: `10.1103/PhysRevLett.100.244802`.

[L'a+00] C L'abbé et al. "Experimental demonstration of time-integrated synchrotron-radiation spectroscopy with crossed polarizer and analyzer". In: *Physical Review B* 61.6 (2000), p. 4181.

[Lax51] Melvin Lax. "Multiple Scattering of Waves". In: *Rev. Mod. Phys.* 23 (4 1951), pp. 287–310. DOI: `10.1103/RevModPhys.23.287`.

[LE14a] Paolo Longo and Jörg Evers. “Far-Field Signatures of a Two-Body Bound State in Collective Emission from Interacting Two-Level Atoms on a Lattice”. In: *Phys. Rev. Lett.* 112 (19 2014), p. 193601. DOI: 10.1103/PhysRevLett.112.193601.

[LE14b] Paolo Longo and Jörg Evers. “Probing few-excitation eigenstates of interacting atoms on a lattice by observing their collective light emission in the far field”. In: *Phys. Rev. A* 90 (6 2014), p. 063834. DOI: 10.1103/PhysRevA.90.063834.

[LE20] Dominik Lentrodt and Jörg Evers. “Ab Initio Few-Mode Theory for Quantum Potential Scattering Problems”. In: *Phys. Rev. X* 10 (1 2020), p. 011008. DOI: 10.1103/PhysRevX.10.011008.

[Lee23] Junhee Lee. “Shaping waveform of X-ray Mössbauer scattering into short pulses”. MA thesis. Ruprecht-Karls-Universität Heidelberg, 2023.

[Len+20] Dominik Lentrodt et al. “*Ab initio* quantum models for thin-film x-ray cavity QED”. In: *Physical Review Research* 2 (June 2020), p. 023396. DOI: 10.1103/PhysRevResearch.2.023396.

[Len21] Dominik Lentrodt. “Ab initio approaches to x-ray cavity QED: From multi-mode theory to nonlinear dynamics of Mössbauer nuclei”. PhD thesis. Ruprecht-Karls-Universität Heidelberg, 2021.

[Len+23] Dominik Lentrodt et al. “Certifying Multimode Light-Matter Interaction in Lossy Resonators”. In: *Phys. Rev. Lett.* 130 (26 2023), p. 263602. DOI: 10.1103/PhysRevLett.130.263602.

[LHH60a] F. J. Lynch, R. E. Holland, and M. Hamermesh. “Time Dependence of Resonantly Filtered Gamma Rays from Fe57”. In: *Phys. Rev.* 120.2 (Oct. 1960), pp. 513–520. DOI: 10.1103/PhysRev.120.513.

[LHH60b] F. J. Lynch, R. E. Holland, and M. Hamermesh. “Time Dependence of Resonantly Filtered Gamma Rays from Fe^{57}”. In: *Phys. Rev.* 120 (2 1960), pp. 513–520. DOI: 10.1103/PhysRev.120.513.

[Lip+95] M. Lippmaa et al. “Mössbauer-NMR double resonance”. In: *Phys. Rev. B* 52 (14 1995), pp. 10268–10277. DOI: 10.1103/PhysRevB.52.10268.

[Liu+] Shan Liu et al. *Cascaded hard X-ray self-seeded free-electron laser at MHz-repetition-rate, 26 January 2023, PREPRINT (Version 1) available at Research Square [https://doi.org/10.21203/rs.3.rs-2487501/v1].* DOI: 10.21203/rs.3.rs-2487501/v1.

[LKE16a] Paolo Longo, Christoph H Keitel, and Jörg Evers. “Tailoring superradiance to design artificial quantum systems”. In: *Scientific reports* 6.1 (2016), pp. 1–7.

[LKE16b] Paolo Longo, Christoph H. Keitel, and Jörg Evers. “Tailoring superradiance to design artificial quantum systems”. In: *Scientific Reports* 6.1 (2016), p. 23628. DOI: 10.1038/srep23628.

[LP17] Wen-Te Liao and Adriana Pálffy. “Optomechanically induced transparency of x-rays via optical control”. In: *Scientific Reports* 7.1 (2017), p. 321. DOI: 10.1038/s41598-017-00428-w.

[LPK11] Wen-Te Liao, Adriana Pálffy, and Christoph H. Keitel. “Nuclear coherent population transfer with X-ray laser pulses”. In: *Physics Letters B* 705.1 (2011), pp. 134–138. DOI: https://doi.org/10.1016/j.physletb.2011.09.107.

[LPK12] Wen-Te Liao, Adriana Pálffy, and Christoph H Keitel. “Coherent storage and phase modulation of single hard-x-ray photons using nuclear excitons”. In: *Phys. Rev. Lett.* 109.19 (Nov. 2012), p. 197403. DOI: 10.1103/PhysRevLett.109.197403.

[Lu+18] W Lu et al. “Development of a hard X-ray split-and-delay line and performance simulations for two-color pump-probe experiments at the European XFEL”. In: *Rev. Sci. Instrum.* 89.6 (June 2018), p. 063121. DOI: 10.1063/1.5027071.

[Lud+15] Andrew D. Ludlow et al. “Optical atomic clocks”. In: *Rev. Mod. Phys.* 87 (2 2015), pp. 637–701. DOI: 10.1103/RevModPhys.87.637.

[Ma+22] Zi-Ru Ma et al. “First Observation of New Flat Line Fano Profile via an X-Ray Planar Cavity”. In: *Phys. Rev. Lett.* 129 (21 2022), p. 213602. DOI: 10.1103/PhysRevLett.129.213602.

[Man10] Jamal T. Manassah. “Giant Cooperative Lamb Shift in a density-modulated slab of two-level atoms”. In: *Physics Letters A* 374.19 (2010), pp. 1985–1988. DOI: `https://doi.org/10.1016/j.physleta.2010.03.010`.

[Mas+08] Ryo Masuda et al. “Development of neV-Resolution Spectroscopy Using Synchrotron-Based ^{57}Fe Mössbauer Radiation”. In: *Japanese Journal of Applied Physics* 47.10 (Oct. 2008), pp. 8087–8090. DOI: `10.1143/JJAP.47.8087`.

[McH17] Jeanne L McHale. *Molecular spectroscopy*. CRC Press, 2017.

[Mor+12] Emilia Morosan et al. “Strongly Correlated Materials”. In: *Advanced Materials* 24.36 (Aug. 2012), pp. 4896–4923. DOI: `10.1002/adma.201202018`.

[Mös12] Rudolf L. Mössbauer. “Recoilless Nuclear Resonance Absorption of Gamma Radiation”. In: *The Rudolf Mössbauer Story: His Scientific Work and Its Impact on Science and History*. Ed. by Michael Kalvius and Paul Kienle. Berlin, Heidelberg: Springer Berlin Heidelberg, 2012, pp. 3–17. DOI: `10.1007/978-3-642-17952-5_1`.

[Mös58] Rudolf L. Mössbauer. “Kernresonanzfluoreszenz von Gammastrahlung in Ir191”. In: *Zeitschrift für Physik* 151.2 (1958), pp. 124–143. DOI: `10.1007/BF01344210`.

[MS07] Pierre Meystre and Murray Sargent. *Elements of Quantum Optics*. Berlin, Heidelberg: Springer Berlin Heidelberg, 2007. DOI: `10.1007/978-3-540-74211-1`.

[MT10] Brian W. J. McNeil and Neil R. Thompson. “X-ray free-electron lasers”. In: *Nature Photonics* 4.12 (Nov. 2010), pp. 814–821. DOI: `10.1038/nphoton.2010.239`.

[Muk95] Shaul Mukamel. *Principles of Nonlinear Optical Spectroscopy*. Oxford Univ. Press, 1995.

[Nam+21] Inhyuk Nam et al. “High-brightness self-seeded X-ray free-electron laser covering the 3.5 keV to 14.6 keV range”. In: 15 (2021), pp. 435–441. DOI: `10.1038/s41566-021-00777-z`.

[New82] Roger G. Newton. *Scattering Theory of Waves and Particles*. Springer Berlin Heidelberg, 1982. DOI: `10.1007/978-3-642-88128-2`.

[Ney+98] G. Neyens et al. “Energy-resolved Mössbauer spectroscopy with broad-band synchrotron radiation”. In: *Hyperfine Interact.* 111 (1998), pp. 341–344.

[NH06] Lukas Novotny and Bert Hecht. *Principles of Nano-Optics*. Cambridge: Cambridge University Press, 2006. DOI: `10.1017/CBO9780511813535`.

[Nom99] Kiyoshi Nomura. “Conversion Electron Mössbauer Spectroscopy”. In: *Mössbauer Spectroscopy in Materials Science*. Ed. by Marcel Miglierini and Dimitris Petridis. Dordrecht: Springer Netherlands, 1999, pp. 63–78. DOI: `10.1007/978-94-011-4548-0_7`.

[Pag06] David Paganin. *Coherent X-ray optics*. 6. Oxford University Press, USA, 2006.

[Pan+98] Jian-Wei Pan et al. “Experimental Entanglement Swapping: Entangling Photons That Never Interacted”. In: *Phys. Rev. Lett.* 80 (18 1998), pp. 3891–3894. DOI: `10.1103/PhysRevLett.80.3891`.

[Par07] William W Parson. *Modern optical spectroscopy*. Vol. 2. Springer, 2007.

[Pet] *PETRA III - Facility Information*. `https://photon-science.desy.de/facilities/petra_iii/facility_information/index_eng.html`.

[Pey+18] T. Peyrot et al. “Collective Lamb Shift of a Nanoscale Atomic Vapor Layer within a Sapphire Cavity”. In: *Phys. Rev. Lett.* 120.24 (June 2018), p. 243401. DOI: `10.1103/PhysRevLett.120.243401`.

[PKE09] Adriana Pálffy, Christoph H. Keitel, and Jörg Evers. “Single-Photon Entanglement in the keV Regime via Coherent Control of Nuclear Forward Scattering”. In: *Phys. Rev. Lett.* 103 (1 2009), p. 017401. DOI: `10.1103/PhysRevLett.103.017401`.

[Pot+12] Vasily Potapkin et al. “The ^{57}Fe Synchrotron Mössbauer Source at the ESRF”. In: *Journal of Synchrotron Radiation* 19.4 (2012), pp. 559–569. DOI: `10.1107/S0909049512015579`.

[PR60] R. V. Pound and G. A. Rebka. “Apparent Weight of Photons”. In: *Phys. Rev. Lett.* 4 (7 1960), pp. 337–341. DOI: `10.1103/PhysRevLett.4.337`.

[PS95] Michael E. Peskin and Daniel V. Schroeder. “An Introduction To Quantum Field Theory”. In: New York: Avalon Publishing, 1995.

[R9̈9] R. Röhlsberger. In: *Hyperfine Interactions* 123/124.1/4 (1999), pp. 301–325. DOI: 10.1023/a:1017063605078.

[Rab+39] I. I. Rabi et al. "The Molecular Beam Resonance Method for Measuring Nuclear Magnetic Moments. The Magnetic Moments of ${}_3\mathrm{Li}^6$, ${}_3\mathrm{Li}^7$ and ${}_9\mathrm{F}^{19}$". In: *Phys. Rev.* 55 (6 1939), pp. 526–535. DOI: 10.1103/PhysRev.55.526.

[Ram50] Norman F. Ramsey. "A Molecular Beam Resonance Method with Separated Oscillating Fields". In: *Phys. Rev.* 78 (6 1950), pp. 695–699. DOI: 10.1103/PhysRev.78.695.

[Ram90] Norman F Ramsey. "Experiments with separated oscillatory fields and hydrogen masers". In: *Reviews of modern physics* 62.3 (1990), p. 541.

[R.C+00] R.Coussement et al. "Heterodyne detection of synchrotron radiation". In: *Hyperfine Interact.* 125 (Mar. 2000), pp. 113–132. DOI: 10.1023/A:1012669200960.

[RE21a] Ralf Röhlsberger and Jörg Evers. "Quantum Optical Phenomena in Nuclear Resonant Scattering". In: *Modern Mössbauer Spectroscopy: New Challenges Based on Cutting-Edge Techniques*. Ed. by Yutaka Yoshida and Guido Langouche. Singapore: Springer Singapore, 2021, pp. 105–171. DOI: 10.1007/978-981-15-9422-9_3.

[RE21b] Ralf Röhlsberger and Jörg Evers. "Quantum Optical Phenomena in Nuclear Resonant Scattering". In: *Modern Mössbauer Spectroscopy*. Ed. by Yutaka Yoshida and Guido Langouche. Vol. 137. Series Title: Topics in Applied Physics. Singapore: Springer Singapore, 2021, pp. 105–171.

[RES20a] Ralf Röhlsberger, Jörg Evers, and Sharon Shwartz. "Quantum and nonlinear optics with hard x-rays". In: *Synchrotron light sources and free-electron lasers: accelerator physics, instrumentation and science applications* (2020), pp. 1399–1431.

[RES20b] Ralf Röhlsberger, Jörg Evers, and Sharon Shwartz. "Quantum and Nonlinear Optics with Hard X-Rays". In: *Synchrotron Light Sources and Free-Electron Lasers*. Ed. by Eberhard J. Jaeschke et al. Cham: Springer International Publishing, 2020, pp. 1399–1431. DOI: 10.1007/978-3-030-23201-6_32.

[RJ16] Janne Ruostekoski and Juha Javanainen. "Emergence of correlated optics in one-dimensional waveguides for classical and quantum atomic gases". In: *Phys. Rev. Lett.* 117.14 (Sept. 2016), p. 143602. DOI: 10.1103/PhysRevLett.117.143602.

[Röh+00] R Röhlsberger et al. "Coherent resonant x-ray scattering from a rotating medium". In: *Physical Review Letters* 84.5 (2000), p. 1007.

[Röh04] R. Röhlsberger. *Nuclear Condensed Matter Physics with Synchrotron Radiation*. Berlin Heidelberg: Springer, 2004.

[Röh+10] Ralf Röhlsberger et al. "Collective Lamb shift in single-photon superradiance". In: *Science* 328.5983 (June 2010), pp. 1248–1251. DOI: 10.1126/science.1187770.

[Röh+12] Ralf Röhlsberger et al. "Electromagnetically induced transparency with resonant nuclei in a cavity". In: *Nature* 482.7384 (Feb. 2012), pp. 199–203. DOI: 10.1038/nature10741.

[Roo+16] S. J. Roof et al. "Observation of Single-Photon Superradiance and the Cooperative Lamb Shift in an Extended Sample of Cold Atoms". In: *Phys. Rev. Lett.* 117.7 (Aug. 2016), p. 073003. DOI: 10.1103/PhysRevLett.117.073003.

[Sak+17] S. Sakshath et al. "Optical pump - nuclear resonance probe experiments on spin crossover complexes". In: *Hyperfine Interactions* 238.1 (2017), p. 89. DOI: 10.1007/s10751-017-1461-3.

[SB08] S. Scheel and S. Y. Buhmann. "Macroscopic quantum electrodynamics - concepts and applications". In: *Acta Phys. Slovaca* 58 (5 2008), p. 675.

[SB09] Stefan Scheel and Stefan Yoshi Buhmann. "Macroscopic QED-concepts and applications". In: *arXiv preprint arXiv:0902.3586* (2009).

[SBH99] D. Siddons, U. Bergmann, and J. Hastings. "Polarization effects in resonant nuclear scattering". In: *Hyperfine Interact.* 123 (Mar. 1999), pp. 681–719. DOI: 10.1023/A:1017096512347.

[SC95] Jun John Sakurai and Eugene D Commins. *Modern quantum mechanics, revised edition*. 1995.

[Sch+02a] P. Schindelmann et al. “Radiative decoupling and coupling of nuclear oscillators by stepwise Doppler-energy shifts”. In: *Phys. Rev. A* 65 (2 2002), p. 023804. doi: `10.1103/PhysRevA.65.023804`.

[Sch+02b] P. Schindelmann et al. “Radiative decoupling and coupling of nuclear oscillators by stepwise Doppler-energy shifts”. In: *Phys. Rev. A* 65 (2 2002), p. 023804. doi: `10.1103/PhysRevA.65.023804`.

[Scu09a] Marlan O. Scully. “Collective Lamb Shift in Single Photon Dicke Superradiance”. In: *Phys. Rev. Lett.* 102 (14 2009), p. 143601. doi: `10.1103/PhysRevLett.102.143601`.

[Scu09b] Marlan O. Scully. “Collective Lamb Shift in Single Photon Dicke Superradiance”. In: *Phys. Rev. Lett.* 102.14 (Apr. 2009), p. 143601. doi: `10.1103/PhysRevLett.102.143601`.

[Ser+06] I. Sergueev et al. “Synchrotron-radiation-based perturbed angular correlations used in the investigation of rotational dynamics in soft matter”. In: *Phys. Rev. B* 73 (2 2006), p. 024203. doi: `10.1103/PhysRevB.73.024203`.

[Set+09] Makoto Seto et al. “Synchrotron-Radiation-Based Mössbauer Spectroscopy”. In: *Phys. Rev. Lett.* 102 (21 2009), p. 217602. doi: `10.1103/PhysRevLett.102.217602`.

[She12] G.K. Shenoy. “Dreams with Synchrotron Radiation”. In: *The Rudolf Mössbauer Story: His Scientific Work and Its Impact on Science and History*. Ed. by G. Kalvius and P. Kienle. Berlin, Heidelberg: Springer-Verlag, 2012, pp. 359–372.

[Shv04] Yuri Shvyd’Ko. *X-ray optics: high-energy-resolution applications*. Vol. 98. Springer Science & Business Media, 2004.

[Shv+23] Yuri Shvyd’ko et al. “Resonant X-ray excitation of the nuclear clock isomer 45Sc”. In: *Nature* (Sept. 2023). doi: `10.1038/s41586-023-06491-w`.

[Shv94] Yu V Shvyd’ko. “Perturbed nuclear scattering of synchrotron radiation”. In: *Hyperfine Interact.* 90.1 (Dec. 1994), pp. 287–299. doi: `10.1007/BF02069133`.

[Shv+94] Yu. V Shvyd'ko et al. “Fast Switching of Nuclear Bragg Scattering of Synchrotron Radiation by a Pulsed Magnetic Field”. In: *Europhysics Letters (EPL)* 26.3 (1994), pp. 215–220. doi: `10.1209/0295-5075/26/3/010`.

[Shv+96] Yu. V. Shvyd’ko et al. “Storage of Nuclear Excitation Energy through Magnetic Switching”. In: *Phys. Rev. Lett.* 77 (15 1996), pp. 3232–3235. doi: `10.1103/PhysRevLett.77.3232`.

[Shv+98] Yu V Shvyd’ko et al. “Hybrid beat in nuclear forward scattering of synchrotron radiation”. In: *Phys. Rev. B Condens. Matter* 57.6 (Feb. 1998), pp. 3552–3561. doi: `10.1103/PhysRevB.57.3552`.

[Shv99] Yuri V. Shvyd’ko. “Nuclear resonant forward scattering of x rays: Time and space picture”. In: *Phys. Rev. B* 59 (14 1999), pp. 9132–9143. doi: `10.1103/PhysRevB.59.9132`.

[Sie82] Kai Siegbahn. “Electron spectroscopy for atoms, molecules, and condensed matter”. In: *Rev. Mod. Phys.* 54 (3 1982), pp. 709–728. doi: `10.1103/RevModPhys.54.709`.

[SK99] W. Sturhahn and V.G. Kohn. In: *Hyperfine Interactions* 123/124.1/4 (1999), pp. 367–399. doi: `10.1023/a:1017071806895`.

[SM85] Donna Strickland and Gerard Mourou. “Compression of amplified chirped optical pulses”. In: *Optics Communications* 56.3 (1985), pp. 219–221. doi: `https://doi.org/10.1016/0030-4018(85)90120-8`.

[Smi+05] G. V. Smirnov et al. “Propagation of nuclear polaritons through a two-target system: Effect of inversion of targets”. In: *Phys. Rev. A* 71 (2 2005), p. 023804. doi: `10.1103/PhysRevA.71.023804`.

[Smi+07] Gennady Smirnov et al. “Currents and fields reveal the propagation of nuclear polaritons through a resonant target”. In: *Physical Review A* 76 (Oct. 2007), pp. 043811–12. doi: `10.1103/PHYSREVA.76.043811`.

[Smi86] G. V. Smirnov. “Coherent effects in resonant diffraction: experiment”. In: *Hyperfine Interactions* 27.1 (1986), pp. 203–218. doi: `10.1007/BF02354756`.

[Smi+97a] G. V. Smirnov et al. “Synchrotron Mössbauer source”. In: *Phys. Rev. B* 55 (9 1997), pp. 5811–5815. doi: `10.1103/PhysRevB.55.5811`.

[Smi+97b] G. V. Smirnov et al. “Synchrotron Mössbauer source”. In: *Phys. Rev. B* 55 (9 1997), pp. 5811–5815. DOI: 10.1103/PhysRevB.55.5811.

[Smi99] G.V. Smirnov. In: *Hyperfine Interactions* 123/124.1/4 (1999), pp. 31–77. DOI: 10.1023/a:1017007520099.

[SP84] Francesc Salvat and Joan Parellada. “Theory of conversion electron Mössbauer spectroscopy (CEMS)”. In: *Nuclear Instruments and Methods in Physics Research Section B: Beam Interactions with Materials and Atoms* 1.1 (1984), pp. 70–84. DOI: https://doi.org/10.1016/0168-583X(84)90481-6.

[SR08] G K Shenoy and R Röhlsberger. “Scientific opportunities in nuclear resonance spectroscopy from source-driven revolution”. In: *Hyperfine Interact.* 182.1-3 (Feb. 2008), pp. 157–172. DOI: 10.1007/s10751-008-9720-y.

[SS22] Yuri Shvyd’ko and Peter Schindelmann. “On yoctosecond science”. In: *Nature* 608.7922 (2022), E16–E17. DOI: 10.1038/s41586-022-04870-3.

[SS89a] Yu Shvyd’ko and Gennady Smirnov. “Experimental study of time and frequency properties of collective nuclear excitations in a single crystal”. In: *Journal of Physics Condensed Matter* 1 (Jan. 1989), pp. 10563–10584.

[SS89b] Yu V Shvyd’ko and G V Smirnov. “Experimental study of time and frequency properties of collective nuclear excitations in a single crystal (gamma-ray resonance)”. In: *Journal of Physics: Condensed Matter* 1.51 (1989), p. 10563. DOI: 10.1088/0953-8984/1/51/025.

[SS92] Yu V Shvyd’ko and GV Smirnov. “Enhanced yield into the radiative channel in Raman nuclear resonant forward scattering”. In: *Journal of Physics: Condensed Matter* 4.10 (1992), p. 2663.

[Stu00a] W. Sturhahn. “CONUSS and PHOENIX: Evaluation of nuclear resonant scattering data”. In: *Hyperfine Interact.* 125 (2000), p. 149. DOI: 10.1023/A:1012681503686.

[Stu00b] WCONUSS Sturhahn. “CONUSS and PHOENIX: Evaluation of nuclear resonant scattering data”. In: *Hyperfine Interactions* 125.1-4 (2000), pp. 149–172.

[Stu01] W. Sturhahn. “Phase problem in synchrotron Mössbauer spectroscopy”. In: *Phys. Rev. B* 63 (9 2001), p. 094105. DOI: 10.1103/PhysRevB.63.094105.

[Stu04] Wolfgang Sturhahn. “Nuclear resonant spectroscopy”. In: *J. Phys. Condens. Matter* 16.5 (Feb. 2004), S497–S530. DOI: 10.1088/0953-8984/16/5/009.

[Stu+96] W. Sturhahn et al. “Electron emission from ^{57}Fe nuclei excited with synchrotron radiation”. In: *Phys. Rev. B* 53 (1 1996), pp. 171–175. DOI: 10.1103/PhysRevB.53.171.

[SVK13] R. N. Shakhmuratov, F. Vagizov, and O. Kocharovskaya. “Single gamma-photon revival from sandwich absorbers”. In: *Phys. Rev. A* 87 (1 2013), p. 013807. DOI: 10.1103/PhysRevA.87.013807.

[SZ97] Marlan O. Scully and M. Suhail Zubairy. *Quantum Optics*. Cambridge: Cambridge University Press, 1997. DOI: 10.1017/CBO9780511813993.

[Tan08] Howe-Siang Tan. “Theory and phase-cycling scheme selection principles of collinear phase coherent multi-dimensional optical spectroscopy”. In: *J. Chem. Phys.* 129.12 (Sept. 2008), p. 124501. DOI: 10.1063/1.2978381.

[Tay03] Garry Taylor. “The phase problem”. In: *Acta Crystallographica Section D* 59.11 (2003), pp. 1881–1890. DOI: 10.1107/S0907444903017815.

[Tit+93] Ilkka Tittonen et al. “Stepwise phase modulation of recoilless gamma radiation in a coincidence experiment: Gamma echo”. In: *Phys. Rev. B* 47 (13 1993), pp. 7840–7846. DOI: 10.1103/PhysRevB.47.7840.

[Toe+95] T S Toellner et al. “Polarizer/analyzer filter for nuclear resonant scattering of synchrotron radiation”. In: *Appl. Phys. Lett.* 67.14 (Oct. 1995), pp. 1993–1995. DOI: 10.1063/1.114764.

[Tom95] M. S. Tomaš. “Green function for multilayers: Light scattering in planar cavities”. In: *Phys. Rev. A* 51 (3 1995), pp. 2545–2559. DOI: 10.1103/PhysRevA.51.2545.

[Tra62] G. T. Trammell. “Elastic Scattering at Resonance from Bound Nuclei”. In: *Phys. Rev.* 126 (3 1962), pp. 1045–1054. DOI: 10.1103/PhysRev.126.1045.

[Vag+14] Farit Vagizov et al. “Coherent control of the waveforms of recoilless γ-ray photons”. In: *Nature* 508.7494 (Apr. 2014), pp. 80–83.

[Vag90] F. G. Vagizov. “The splitting of hyperfine lines of ^{57}Fe nuclei in RF magnetic field”. In: *Hyperfine Interactions* 61.1 (1990), pp. 1359–1362. DOI: `10.1007/BF02407625`.

[VB86] U. Van Bürck. “Coherent effects in resonant diffraction: theory”. In: *Hyperfine Interactions* 27.1 (1986), pp. 219–230. DOI: `10.1007/BF02354757`.

[Vir+20] Pauli Virtanen et al. “SciPy 1.0: Fundamental Algorithms for Scientific Computing in Python”. In: *Nature Methods* 17 (2020), pp. 261–272. DOI: `10.1038/s41592-019-0686-2`.

[VRD09] Guido Van Rossum and Fred L. Drake. *Python 3 Reference Manual.* Scotts Valley, CA: CreateSpace, 2009.

[WE23a] Lukas Wolff and Jörg Evers. “Unraveling time- and frequency-resolved nuclear resonant scattering spectra”. In: *Phys. Rev. Res.* 5 (1 2023), p. 013071. DOI: `10.1103/PhysRevResearch.5.013071`.

[WE23b] Lukas Wolff and Jörg Evers. *A characterization and detection method for x-ray excitation of Mössbauer nuclei beyond the low-excitation regime.* 2023. arXiv: `2308.07644 [quant-ph]`.

[Wei] E W Weisstein. *Cross-Correlation Theorem.* From Mathworld - A Wolfram Web Resource. `https://mathworld.wolfram.com/Cross-CorrelationTheorem.html`.

[Wil+10] H-C Wille et al. “Nuclear resonant scattering at PETRA III : Brillant opportunities for nano – and extreme condition science”. In: *Journal of Physics: Conference Series* 217 (2010), p. 012008. DOI: `10.1088/1742-6596/217/1/012008`.

[Wit+20] Andreas Wituschek et al. “Tracking attosecond electronic coherences using phase-manipulated extreme ultraviolet pulses”. In: *Nat. Commun.* 11.1 (Feb. 2020), p. 883. DOI: `10.1038/s41467-020-14721-2`.

[WL18] Guan-Ying Wang and Wen-Te Liao. “Generation of Short Hard-X-Ray Pulses of Tailored Duration Using a Mössbauer Source”. In: *Phys. Rev. Applied* 10 (1 2018), p. 014003. DOI: `10.1103/PhysRevApplied.10.014003`.

[Zha+19] Xiwen Zhang et al. “Nuclear Quantum Memory and Time Sequencing of a Single γ Photon”. In: *Phys. Rev. Lett.* 123 (25 2019), p. 250504. DOI: `10.1103/PhysRevLett.123.250504`.